

Stellingen behorende bij het proefschrift van Aswin Draad

1. Het draaien van de aarde kan leiden tot een sterke asymmetrie van het axiale snelheidsprofiel in een laminaire buisstroming (dit proefschrift, appendix C).
2. Het is een tekortkoming dat in de meeste numerieke codes voor het rekenen aan stromingsproblemen alleen de mogelijkheid bestaat om een drukgradiënt op te leggen, terwijl voor het rekenen aan omslagverschijnselen in stromingen het van essentieel belang is om een constant debiet te kunnen opleggen (dit proefschrift, hoofdstuk 4 en appendix C).
3. De 'information super-highway' dreigt een file-gevoelige polderweg te worden.
4. De term Assistent In Opleiding is een zeer juiste benaming voor promovendi die tijdens hun promotie-onderzoek veel tijd moeten steken in het opbouwen van een onderzoeksopstelling en juist op het moment dat ze als volleerd onderzoeker de vruchten van hun werk kunnen gaan plukken, gedwongen worden met hun onderzoek te stoppen.
5. Onderzoek bestaat voor 1% uit inspiratie en voor 99% uit frustratie. Ziehier, het belang van motivatie.
6. Klussende medewerkers zijn vaak erger dan bijklussende hoogleraren.
7. Een van de grootste problemen bij het maken van een planning is dat de wens vaak de vader is van de gedachte.
8. Als je zelf geen keuzes maakt, dan maakt Vadertje Tijd ze wel voor je.
9. Personen die, bij het doorrekenen van een stromingsprobleem op een supercomputer, spreken van een 'numeriek experiment' diskwalificeren zichzelf als experimentator.
10. Een goed zakmes, tape, touw, en ijzer-/koperdraad zijn onmisbaar bij het experimenteren. Dit wil niet zeggen dat een basisopstelling van het type 'houtje-touwtje' voldoende is.
11. De uitspraak 'meten is weten' is een onderschatting van de complexiteit van metingen. Het is daarom beter het devies van Kamerlingh Onnes: 'Door meten tot weten' te gebruiken en het zou goed zijn de van Dale op dit punt te wijzigen.
12. Hoewel veel Nederlanders zeggen dat ze tijdens hun wintersportvakantie gaan langlaufen, beoefenen slechts weinigen deze tak van sport; de meesten gaan skiwandelen.
13. Sporten is niet alleen ontspanning door inspanning maar ook een 'way of living'.
14. Geluk moet je een handje helpen.



**TR diss
2779**

660466

1390887

TR diss 2779

**LAMINAR-TURBULENT TRANSITION
IN PIPE FLOW FOR NEWTONIAN
AND NON-NEWTONIAN FLUIDS**



Laminar-Turbulent Transition in Pipe Flow
for Newtonian and non-Newtonian Fluids

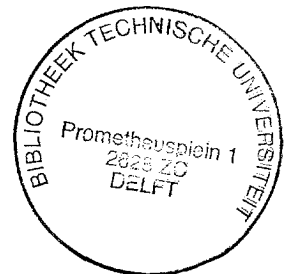
De Omslag van Laminair naar Turbulent in Pijpstroming
voor Newtonse en niet-Newtonse Vloeistoffen

PROEFSCHRIFT

ter verkrijging van de graad van doctor
aan de Technische Universiteit Delft,
op gezag van de Rector Magnificus Prof. ir. K.F. Wakker,
in het openbaar te verdedigen ten overstaan van een commissie,
door het College van Dekanen aangewezen,
op dinsdag 25 juni 1996 te 16.00 uur

door

ADRIANUS ANTONIUS DRAAD
werktuigbouwkundig ingenieur,
geboren te Oss.



Dit proefschrift is goedgekeurd door de promotor:
Prof. dr. ir. F.T.M. Nieuwstadt

Toegevoegd promotor:
Dr. ir. G.D.C. Kuiken

Samenstelling promotiecommissie:

Rector Magnificus, voorzitter
Prof. dr. ir. F.T.M. Nieuwstadt, Technische Universiteit Delft, promotor
Dr. ir. G.D.C. Kuiken, Technische Universiteit Delft, toegevoegd promotor
Prof. dr. R.B. Bird, University of Wisconsin, USA
Prof. dr. ir. B.H.A.A. van den Brule, Technische Universiteit Delft
Prof. dr. ir. G.J. van Heijst, Technische Universiteit Eindhoven
Prof. dr. ir. W.M.J. Schlösser, Technische Universiteit Eindhoven
Prof. dr. F. Verhulst, Rijksuniversiteit Utrecht

Copyright ©1996 by A.A. Draad
All rights reserved.

ISBN 90-370-0140-8

Printed by Ponsen & Looijen, The Netherlands.

*Toen ik klein was ging ik naar zee, en alleen mijn grote broer mocht mee,
En de goudvis, en mijn oma, want die had een zwemdiploma,
En mijn vader zei, hé goeie vaart, en mijn moeder zei, goeie vaart,
Harrie, stuur je wel met kerst een kaart.*

*Toen ik klein was werd ik piloot, net als de buurman, die was dood,
Maar zijn vliegpak hing nog in de kast,
Mijn God, ik heb die pet wel duizend keer gepast,
En mijn vader zei, goeie vlucht, en mijn moeder zei, goeie vlucht,
Harrie schrijf wel je naam als afscheid in de lucht.*

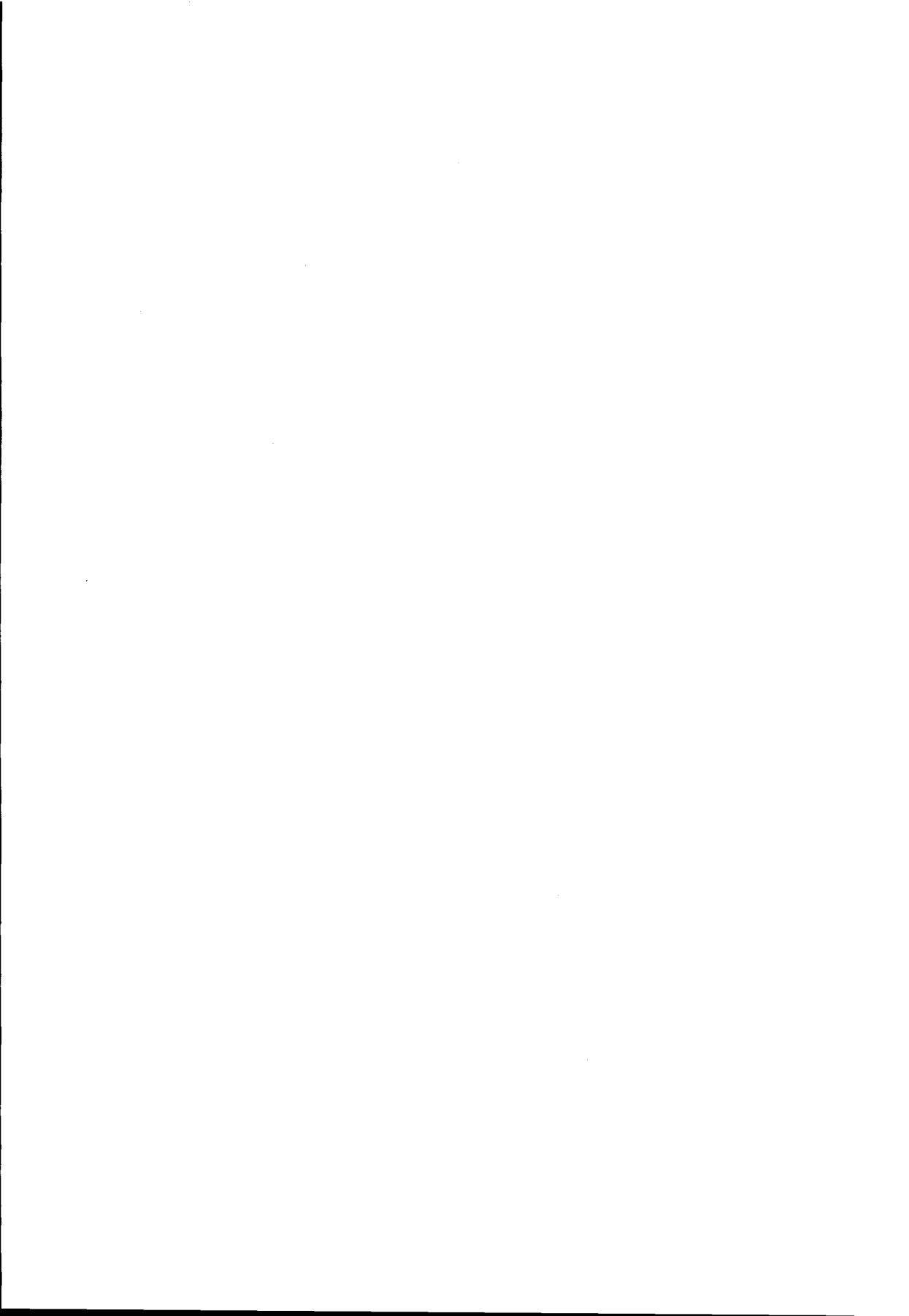
*En ik weet nu dat ik groot ben, en natuurlijk geen piloot ben,
En ook geen zeeman ben geworden,
Dat je moet vliegen in je dromen, om later van de grond te komen,
En heel misschien had ik hier nooit gestaan,
Als ik toen niet van mijn ouders naar zee had mogen gaan,
Als ik toen niet met mijn goudvis naar zee toe was gegaan.*

*Toen ik klein was werd ik astronaut, ik had mijn Spoetnik zelf gebouwd,
En ik zou in alle, in alle kranten staan, Harrie Jekkers, als eerste op de maan,
En mijn vader zei, dat lukt vast jongen, goeie reis,
En mijn moeder zei, goeie reis,
Harrie, vergeet je niet een maansteen als bewijs.*

*En ik weet nu dat ik groot ben, geen zeeman of piloot ben,
En ook zelfs wel niet op de maan zal staan,
Dat je de ruimte moet krijgen, om boven jezelf uit te stijgen,
Heel misschien had ik hier nooit gestaan,
Als ik toen niet van mijn ouders naar de maan had mogen gaan,
Als ik toen niet met mijn goudvis naar zee toe was gegaan.*

Harrie Jekkers Uit "Met een goudvis naar zee"

dedicated to ons pap en ons mam



Acknowledgements

This thesis is based on more than five years of research at the Laboratory of Aero- & Hydrodynamics of the Delft University of Technology. This thesis is about laminar-turbulent transition in pipe flows, a subject that has been tackled for more than a century and still poses a great challenge. When combining this with rheology, we obtain the playing field for the study presented here.

The emphasis is on performing stability measurements in pipe flows with water and polymer solutions as working fluids. For this purpose, a new facility has been constructed in the course of this Ph.D.-project. Building a large experimental setup is an incredible amount of work, the extend of which can only be fully appreciated by those who have gone through such a process themselves. Also, it represents a great lesson on many different subjects, both scientific and non-scientific.

Over the years, many people have contributed to the work presented in this thesis, in particular my colleagues at the lab, for which I am very grateful. Several of them deserve special attention.

Frans Nieuwstadt and Gerard Kuiken for giving me the opportunity to perform this study, and their guidance and continuing support have been a big stimulation. The freedom they have given me to direct my project is very much appreciated. Proof-reading of this manuscript by Frans Nieuwstadt completely redefines the expression 'met de Franse slag'.

I have greatly benefitted from the work of and discussions with Martien Hulsen. It would not be an exaggeration to say that without him, chapter 4 would not have existed.

A special word of appreciation is in order for Ruud van den Boom. Time and time again, he came up with solutions to the large amount of problems that we encountered during the design and construction of the experimental facility. It has been a pleasure and a privilege to work with him. The many discussions, both professional and personal, have helped me to keep on going, especially when the going got tough.

Over a great many years, Joop Bodde, Cor Gerritsen, Wietse Kracht, and Wout van Sorge have contributed a great deal through a lot of work and craftsmanship, and it has been a pleasure to work with them. They also trusted me to operate machines and equipment, a privilege which has tremendously contributed to this Ph.D.-work and without this, chapter 7 most certainly would not have existed.

I thank my former students Lourens Aanen and Jan-Willem Boere, who contributed a great deal in the course of their graduation work, in which they shared in the problems encountered when trying to obtain a good experimental setup. Working with them was a lot of fun and I learned a great deal.

I also thank Jacobiene van der Hoeven, Sjaak van Oord, and Jerry Westerweel for being able to work with them in the PIV-field and all the fun we had during the experiments.

I am also thankful to Bendiks-Jan Boersma for incorporating the Coriolis force in a numerical pipe code and to Jan Verhelst, who performed the viscosity measurements on the polymer solutions used in the experiments.

I would like to thank Jaap den Toonder for the valuable discussions we had on rheology and turbulence and for his work with the LDV-system.

My roommates René Delfos and Arjan van Dijk have left a permanent mark through their "Utrecht" approach of physics, which is very much appreciated. I would like to thank them for all the fun we had, but also for sharing in the frustrations that come with experiments. I am greatly indebted to René Delfos. He has contributed a great deal to this work through the countless fruitful discussions and the helping hands he lend me over the past five years. I wish him and my other fellow Ph.D.-students the best of luck in finishing their work.

In 1994, I have had the pleasure of meeting Bob Bird during his stay of several months at our Lab as a 'Burgers-professor'. The discussions at the dinner table in the Aula are unforgettable and some of the basic Japanese words he taught me turned out to come in very handy. His suggestions for improvements of the manuscript are greatly appreciated. I am honored to have him in my graduation committee and I am looking forward to meeting him again. Hopefully, I am able to master the 'J'-stroke in our next canoe trip.

Finally, I am deeply thankful to my mum & dad, and my sister Myriam for their never-ending understanding and support and for trying to protect me from myself.

Delft, May 1 1996

This work has been made possible by the financial support of the 'Koninklijke Shell Exploratie en Productie Laboratorium' (KSEPL) which is gratefully acknowledged. For the time of this Ph.D.-work, a PC-version of the program SEPRAN was made available to the author by Ingenieursbureau SEPRA b.v. which is also gratefully acknowledged.

Contents

Acknowledgements	vii
Summary	xiii
Samenvatting	xvii
List of symbols	xxi
1 General introduction	1
1.1 Context of project	1
1.2 Laminar-Turbulent transition	2
1.3 Non-Newtonian fluid flow	3
1.4 Aim and outline of this thesis	4
2 Newtonian flow stability	7
2.1 Introduction	7
2.2 Plane Poiseuille Flow	7
2.2.1 Linear Instability Theory	7
2.2.2 Nonlinear Instability Theory	9
2.2.3 Secondary Instability	11
2.2.4 Direct Numerical Simulations	13
2.2.5 Experiments	16
2.3 Cylindrical Poiseuille Flow	17
2.3.1 Linear Instability Theory	18
2.3.2 Nonlinear Instability Theory	18
2.3.3 Asymptotic Theory	19
2.3.4 Secondary Instability	19
2.3.5 Experiments	21
2.4 Transient Growth	24
2.5 Summary & Discussion	26
3 Non-Newtonian flow stability	29
3.1 Introduction	29
3.2 Experimental	30
3.2.1 Polymer solutions	30
3.2.2 Coiled vs. stretched conformation	33
3.2.3 Fibers	36
3.3 Stability Analysis	36
3.3.1 Introduction	36
3.3.2 Visco-elastic fluids	37

3.3.3	Dilute Fiber Suspension	39
3.4	Discussion	40
4	Stability of plane Poiseuille flow	43
4.1	Introduction	43
4.2	Problem definition	44
4.2.1	Introduction	44
4.2.2	Flow geometry	44
4.2.3	Governing equations	45
4.2.4	Constitutive equations	45
4.2.5	Boundary Conditions	46
4.3	The Upper Convected Maxwell fluid model	47
4.3.1	Dimensionless groups for the UCM fluid	47
4.3.2	The UCM model in steady shear flow	48
4.4	Numerical Techniques	49
4.4.1	Introduction	49
4.4.2	Numerical Method	49
4.4.3	Mesh	50
4.4.4	The initial disturbance	50
4.5	Linear Stability	51
4.5.1	Introduction	51
4.5.2	Newtonian linear stability	52
4.5.3	Upper Convected Maxwell Fluids	55
4.5.4	Linear disturbance field	56
4.6	Nonlinear stability for Newtonian fluids	56
4.6.1	Introduction	56
4.6.2	Constant Pressure Gradient	58
4.6.3	Constant Flow Rate	61
4.7	Nonlinear stability for UCM fluids	63
4.8	Summary and discussion	68
5	Experimental setup	73
5.1	Introduction	73
5.2	Existing pipe-flow facilities	75
5.3	Requirements	78
5.4	Pumping polymers	79
5.5	Overview of new facility	83
5.6	Mechanical backbone	87
5.7	Measurement pipe and components	89
5.7.1	Introduction	89
5.7.2	Measurement pipe	89
5.7.3	Test sections	91
5.8	Settling Chamber	96
5.8.1	Introduction	96
5.8.2	Convection	97

5.8.3	Contraction design	100
5.8.4	Settling chamber setup	104
5.9	Discharge chamber and return pipe	108
5.10	Dispersing and storage vessels	109
5.11	Measurement equipment	111
5.11.1	Introduction	111
5.11.2	Pressure drop transducer	111
5.11.3	Flow meter	111
5.11.4	Thermometer	112
5.11.5	Laser Doppler Velocimetry	112
5.11.6	Digital Particle Image Velocimetry	113
5.12	Flow quality	117
5.13	Disturbance mechanism	120
5.13.1	Introduction	120
5.13.2	Eccentric disturbance mechanism	122
6	Newtonian stability measurements	125
6.1	Introduction	125
6.2	Measurement method	126
6.2.1	Introduction	126
6.2.2	Transition detection	126
6.2.3	Measurement location	128
6.2.4	Measurement procedure	130
6.2.5	Dimensionless quantities	132
6.3	Slug- Re -range	133
6.3.1	Introduction	133
6.3.2	Single and multiple transitions	133
6.3.3	Scaling rules	139
6.3.4	Negative pressure drops	141
6.4	Puff- Re -range	143
6.4.1	Introduction	143
6.4.2	Velocity time-traces	144
6.4.3	Discussion	152
7	Non-Newtonian stability measurements	155
7.1	Introduction	156
7.2	The effect of salt	157
7.3	Non-Newtonian viscosity	158
7.3.1	Introduction	158
7.3.2	Viscosity function	159
7.4	Non-Newtonian Moody diagram	162
7.4.1	Introduction	162
7.4.2	Modified Reynolds number	164
7.4.3	Moody diagram measurements	167
7.5	Stability Measurements	170

7.5.1	Introduction	170
7.5.2	Stability measurements	172
7.6	Discussion	179
7.6.1	Introduction	179
7.6.2	Natural transition Reynolds number	182
7.6.3	Triggered transition in Moody diagram	183
7.6.4	Applications	186
8	Main conclusions and discussion	189
A	Disturbance energy	197
B	Contraction design	201
C	Coriolis force	205
C.1	Historical background	205
C.2	Direction of the Coriolis force	206
C.3	Linear theory	208
C.3.1	Introduction	208
C.3.2	Basic equations	208
C.4	Numerical computations	215
C.4.1	Introduction	215
C.4.2	Numerical techniques	216
C.4.3	Comparison with the linear solution	216
C.4.4	Comparison with measurements	219
C.5	Curved pipe	222
D	Multiple transition points	227
D.1	Introduction	227
D.2	Stability measurements	227
E	Non-Newtonian Moody diagram	233
E.1	Introduction	233
E.2	Viscosity curves	233
E.3	Viscosity corrected Moody diagram	236
	Bibliography	247
	Curriculum vitae	255

Summary

Laminar-Turbulent transition in pipe flow for Newtonian and non-Newtonian fluids

Aswin A. Draad

Dissolving a minute amount of long-chain polymers in a turbulent flow can have very large effects on the turbulence. An example is the spectacular drag reduction in turbulent pipe flow of such dilute polymer solutions, with reductions up to 80%. The central theme of this thesis is to throw light on the influence of polymers on the transition process. This transition process has even for a Newtonian fluid many unsolved questions and for non-Newtonian fluids the situation is even less clear. For instance, in most cases the results seem to indicate that the transition occurs at the same Reynolds number as for the solvent. Sometimes a delay in transition to higher Reynolds numbers is found and occasionally transition occurs at lower Reynolds numbers than what is found for the solvent. Information on transition is important because, when the flow becomes turbulent, flow features like mixing, heat transfer and flow resistance are considerably increased and for many applications it is therefore necessary to know beforehand whether the flow will be laminar or turbulent.

In this thesis we aim to identify the most important parameters that govern laminar-turbulent transition in general and for polymer solutions in particular. In order to reach this goal, we have performed strongly nonlinear stability calculations in plane Poiseuille flow for a visco-elastic fluid described by the Upper Convected Maxwell model. The results of these computations are discussed in the first part of this thesis, and show that elasticity destabilizes until the Weissenberg number (We), i.e. the ratio of the relaxation time of the fluid to the flow time scale, reaches unity. Increasing We further leads to an increase in the critical Reynolds number which can be interpreted as a stabilizing effect.

In the remainder of the thesis, we will be occupied with stability measurements for water and polymer solutions in pipe flow. In particular, the effect of the polymer configuration on the flow stability is elucidated. To carry out the measurements on transition, we constructed an experimental pipe-flow facility especially suited to perform stability measurements on Newtonian and non-Newtonian fluids. To be able to study the flow behavior in detail we use a pipe with a diameter of 40 mm. The length of 800 diameters (32 m) ensures that the flow is fully developed till high Reynolds numbers ($Re=14\ 300$). Fully developed flow facilitates comparison with theory and numerical simulations. By suppressing entrance disturbances, we can increase the natural transition Reynolds number in our pipe for water, a Newtonian fluid, from the common value of 2 300 to more than 60 000. However, at these large Reynolds numbers, the laminar velocity profile is no longer parabolic, i.e. Poiseuille flow. There are several reasons for this non-parabolic velocity profile. First, our pipe is too short for these Reynolds numbers to

allow the flow to develop fully. Second, we found that small temperature differences between the water and the ambient air significantly skew the laminar velocity profile. Third, it appears that the Coriolis force resulting from the rotation of the earth strongly deforms the laminar velocity profile, an effect which increases strongly with the Reynolds number.

To trigger transition to turbulence in this laminar flow, we added a well controlled disturbance to the flow. Both the frequency (related to the wave number) and the amplitude of the disturbance could be varied. In this way we can determine the disturbance magnitude and wave number combinations that trigger transition for a wide range of Reynolds numbers. Comparing the measurements for a Newtonian fluid with those for polymer solutions, gives information on the effect that polymers have on the stability of pipe flow and on the Reynolds number at which transition to turbulence occurs.

In our experimental study, we first investigated the stability of water, which is a Newtonian fluid. The critical relative disturbance velocity ($v_{i,c}^*$), i.e. the ratio of disturbance velocity that triggers transition to the bulk velocity, decreases when the Reynolds number is increased. The sensitivity of $v_{i,c}^*$ to the dimensionless wave number (α^*) is small for large α^* . We find that for low Reynolds numbers, the flow is most sensitive to long-wave disturbances. For $Re \geq 30\,000$, the flow becomes increasingly more sensitive to disturbances with $0.5 \lesssim \alpha^* \lesssim 1$. This suggests that depending on the Reynolds number, different modes are involved in the transition process. Multiple transition points, found for $2 < \alpha^* < 6$, seem to be related to this. Here, the term 'multiple transition point' indicates the sequence of laminar-turbulent transition, relaminarization, and next a second transition to turbulence as a function of increasing $v_{i,c}^*$. Apart from the transition points, we also study how the critical disturbance amplitude varied with Re as this plays a role in various theoretical studies of transition. For large wave numbers, we find that $v_{i,c}^*$ scales according to Re^{-1} , while for small wave numbers $v_{i,c}^* \sim Re^{-2/3}$. The latter is in agreement with weakly nonlinear stability calculations.

Second, we investigated the pipe flow stability of polymer solutions (non-Newtonian fluids). For the concentrations that we investigated (20 - 40 ppm) we found that the viscosity of the solutions is significantly increased by the polymers and also that shear thinning is present. In particular, shear thinning occurs for those solutions where the polymers adopt a stretched conformation. We accounted for these viscosity effects by defining the Reynolds number with the viscosity at the wall, which gives good results for the Moody diagram, i.e. friction factor as a function of Reynolds number. From the stability measurements, it follows that the polymers reduce the natural transition Reynolds number and at the same time have a stabilizing effect, viz. the critical relative disturbance velocity $v_{i,c}^*$ for the polymers solutions is larger than for water. The stabilization is stronger for fresh polymer solutions and it is also larger when the polymers become more extended. However, a *delay* in transition, i.e. the critical Reynolds number below which the flow remains laminar at any disturbance, is increased to values larger than that for Newtonian fluids, was only found for fresh polymers that adopt an extended conformation.

In a related research project on drag reduction (Toonder 1995) it was shown that the key property for drag reduction is the anisotropic stress which is introduced by extended polymers, whereas elasticity has an adverse effect on drag reduction. This complements our findings for transition and the picture that arises is that the polymers have to adopt the extended conformation in order to influence the transition to turbulence as well as to generate drag reduction in turbulent flows. Our nonlinear stability calculations for plane Poiseuille flow show that elasticity has a destabilizing effect for $We < 1$, while for $We > 1$ a stabilizing effect can be observed as well as large stretching in the flow direction. Thus, also stability computations for plane Poiseuille flow seem to indicate that the stabilizing effect of elasticity is related to the stretching of the polymers by the flow. The decrease in natural transition Reynolds number caused by the polymers remains unclear, but it may be related to a destabilizing effect of the elasticity on the developing boundary layers in the entry region of the flow.

Samenvatting

De omslag van laminair naar turbulent in pijpstroming voor Newtonse en niet-Newtonse vloeistoffen

Aswin A. Draad

Het oplossen van zeer kleine hoeveelheden polymeren met hele lange ketens in een turbulente stroming kan zeer grote effecten hebben op de turbulentie. Bijvoorbeeld, in deze verdunde polymeeroplossingen kan de stromingsweerstand soms wel met 80% gereduceerd worden. Het centrale thema van dit proefschrift is het krijgen over meer duidelijkheid van het effect dat deze polymeren hebben op het omslagpunt van een laminaire naar een turbulente stroming. Zelfs voor Newtonse vloeistoffen zijn nog veel zaken niet goed begrepen, wat in nog sterkere mate geldt voor niet-Newtonse vloeistoffen. Om een voorbeeld te geven, in de meeste gevallen is geen verandering merkbaar in vergelijking tot het oplosmiddel. Soms wordt de omslag uitgesteld tot hogere waarden van het Reynoldsgetal maar een enkele keer vindt er ook omslag plaats bij waarden van het Reynoldsgetal die lager zijn dan die voor het oplosmiddel. Kennis over het omslagproces is belangrijk, omdat zaken als mixen, warmte-overdracht en stromingsweerstand sterk toenemen wanneer de stroming turbulent wordt, en het is daarom voor veel toepassingen erg belangrijk om van te voren te kunnen voorspellen of de stroming laminair dan wel turbulent zal zijn.

In dit proefschrift willen we duidelijkheid krijgen over wat de meest belangrijke parameters zijn die de omslag bepalen van laminair naar turbulent in het algemeen en voor polymeeroplossingen in het bijzonder. Om deze doelstelling te realiseren hebben we sterk niet-lineaire stabiliteitsberekeningen uitgevoerd voor een twee-dimensionale stroming tussen twee vlakken platen van een visco-elastische vloeistof waarvan het gedrag beschreven wordt door het Upper Convected Maxwell-model. De resultaten van deze berekeningen worden beschreven in het eerste deel van dit proefschrift en laten zien dat elasticiteit destabiliserend werkt voor $We < 1$. Hierbij staat We voor het Weissenberggetal en beschrijft de verhouding van de relaxatietijd van het polymeer tot de tijdschaal van de stroming. Wanneer het Weissenberggetal wordt verhoogd tot waarden groter dan 1, neemt het kritisch Reynoldsgetal voor deze verstoringen weer toe. Dit kan worden gezien als een stabiliserende werking.

In het overige deel van dit werk beslaat uit het meten van de stabiliteit van polymeeroplossingen in een buisstroming. Hierbij is vooral gekeken naar de invloed die de gestrektheid van de polymeren heeft op de stromingsstabiliteit. Voor het uitvoeren van deze metingen hebben we een nieuwe buisopstelling gebouwd die speciaal geschikt is voor het doen van stabiliteitsmetingen aan stromingen van Newtonse en niet-Newtonse vloeistoffen. Hierbij hebben we gekozen voor een buisdiameter van 40 mm, zodat ook de details van de stroming goed onderzocht kunnen worden. Met een lengte van 800 pijpdiameters (32 m) is de buis tevens lang

genoeg om tot hoge Reynoldsgetalen ($Re=14\,300$) nog steeds een volledig ontwikkelde stroming te krijgen. Dit laatste is vooral gedaan om de vergelijking tussen de resultaten van de metingen en die van theorieën en numerieke simulaties te vergemakkelijken. Door verstoringen bij de instroming zo goed mogelijk te onderdrukken is het mogelijk om voor water (een Newtonse vloeistof) in onze buis het Reynoldsgetal waarbij de stroming van nature omslaat van laminair naar turbulent, te verhogen van de normale waarde van $\pm 2\,300$ naar meer dan $60\,000$. Echter, bij deze hoge Reynoldsgetalen is het axiale snelheidsprofiel niet langer parabolisch, d.w.z. een Poiseuille stroming. Dit wordt veroorzaakt door een aantal factoren. Ten eerste is voor deze hoge Reynoldsgetalen de buis niet lang genoeg om een volledig ontwikkelde stroming te krijgen. Ten tweede blijkt dat een klein temperatuurverschil tussen het water en de omringende lucht al een forse vervorming van het laminaire snelheidsprofiel oplevert. Een derde oorzaak is dat de Coriolis-kracht, die het gevolg is van het draaien van de aarde, groot genoeg is om het laminaire snelheidsprofiel enorm scheef te drukken, een effect dat snel toeneemt met de verhoging van het Reynoldsgetal.

Om de omslag van laminair naar turbulent te induceren wordt een goed gecontroleerde verstoring aanbracht in een laminaire stroming. De frequentie en de amplitude van de verstoring zijn beide instelbaar. Hiermee zijn we in staat om voor een groot bereik van Reynoldsgetalen de combinatie van verstoringssnelheid en -frequentie te bepalen die omslag veroorzaken. Door vervolgens de resultaten voor een Newtonse vloeistof te vergelijken met die van polymeeroplossingen, krijgen we informatie over het effect dat de polymeren hebben op de stabiliteit van de stroming en het omslag-Reynoldsgetal bepalen.

Allereerst hebben we in onze proefopstelling de stabiliteit van de Newtonse vloeistof water bestudeerd. Verhoging van het Reynoldsgetal leidt tot een daling van de kritieke relatieve verstoringssnelheid ($v_{i,c}^*$), de verhouding van de verstoringssnelheid tot de bulksnelheid waarbij omslag van laminair naar turbulent plaats vindt. De gevoeligheid van $v_{i,c}^*$ voor het dimensieloze golfgetal (α^*) is klein voor grote α^* . Bij lage Reynoldsgetalen is de stroming het gevoeligst voor langgolvige verstoringen. Boven $Re \approx 30\,000$ laat de pijpstroming een verhoogde gevoeligheid zien voor verstoringen met $0.5 \lesssim \alpha^* \lesssim 1$. Dit suggereert dat afhankelijk van het Reynoldsgetal, andere modes betrokken zijn bij het omslagproces. Dit lijkt gerelateerd te zijn aan de meervoudige omslagpunten die optreden bij $2 < \alpha^* < 6$. De term 'meervoudig omslagpunt' betekent dat wanneer $v_{i,c}^*$ wordt verhoogd, er eerst omslag van laminair naar turbulent optreedt, vervolgens bij een hogere waarde relaminarisatie gevonden wordt om bij nog hogere waarden van $v_{i,c}^*$ toch weer turbulent te worden. Uit de stabiliteitsmetingen kan ook worden bekeken hoe $v_{i,c}^*$ varieert met het Reynoldsgetal. Voor grote golfgetallen suggereren de metingen dat $v_{i,c}^*$ schaalt met Re^{-1} terwijl bij lage golfgetallen $v_{i,c}^* \sim Re^{-2/3}$. Deze laatste wordt ook voorspeld door zwak niet-lineaire stabiliteitsberekeningen.

Als tweede hebben we de stabiliteit van polymeeroplossingen (niet-Newtonse vloeistoffen) bestudeerd. Voor de gebruikte concentraties (20 - 40 ppm) blijkt dat de viscositeit van de oplossing duidelijk toeneemt door het toevoegen van polymeren en tevens vertoont de oplossing afschuifverdunnend gedrag. Dit gedrag komt vooral sterk naar voren in die oplossingen waarin de polymeren gestrekt zijn. Deze effecten zijn niet te verwaarlozen en door een Reynoldsgetal

te definiëren gebaseerd op de viscositeit aan de wand, is hiervoor te corrigeren wat prima werkt voor Moody-diagram metingen (frictiefactor als functie van het Reynoldsgetal). Uit de stabiliteitsmetingen volgt dat de polymeren in het algemeen het natuurlijk omslag-Reynoldsgetal verlagen en tegelijkertijd een stabiliserend effect hebben, d.w.z. dat de kritieke relatieve verstoringsnelheid $v_{i,c}^*$ groter is voor de polymeeroplossingen dan voor water. De stabilisatie is sterker voor verse polymeeroplossingen en naarmate de polymeren meer gestrekt zijn. Echter, *uitstel* van omslag, d.w.z. het kritieke Reynoldsgetal waaronder geen omslag van laminair naar turbulent kan plaatsvinden, ongeacht de verstoring, verschuift naar waarden die groter zijn dan die voor het oplosmiddel, wordt alleen gevonden voor verse polymeeroplossingen waarin de polymeren gestrekt zijn.

Een nauw gerelateerd promotie-onderzoek naar weerstandsvermindering door polymeer-toevoeging laat zien dat de pure anisotrope viskeuze spanning die wordt veroorzaakt door gestrekte polymeren de belangrijkste eigenschap is voor weerstandsvermindering, terwijl elasticiteit een verminderend effect heeft op weerstandsvermindering (Toonder 1995). Dit complementeert onze bevindingen betreffende de omslag van laminair naar turbulent en het plaatje dat ontstaat is dat de polymeren gestrekt moeten zijn om de omslag van een laminaire naar turbulente stroming te kunnen beïnvloeden en tevens om voor weerstandsvermindering in turbulente stromingen te kunnen zorgen. Onze niet-lineaire stabiliteitsberekeningen voor een stroming tussen vlakke platen laat zien dat elasticiteit een destabiliserend effect heeft wanneer $We < 1$, terwijl voor $We > 1$ een stabiliserend effect is gevonden gecombineerd met een sterke elastische rek in stromings richting. Dus ook de berekeningen voor vlakke Poiseuille stroming lijken te wijzen op een stabiliserend effect van de elasticiteit welke is gerelateerd aan het gestrekt worden van de polymeren door de stroming. De oorzaak voor de reductie in natuurlijk omslag-Reynoldsgetal blijft vooralsnog onduidelijk. Het zou gerelateerd kunnen zijn aan een destabiliserende werking van elasticiteit in de zich ontwikkelende grenslaag in het intreegebied van de stroming.

List of symbols

symbol	description	definition in formula or at page
Italic symbols		
A	initial disturbance amplitude	(4.18)
A	amplitude of disturbance oscillation	(5.28)
A_∞	disturbance amplitude	Fig. 2.4
A_{rms}	rms disturbance amplitude	(4.20)
\underline{b}	conformation tensor	(4.16)
b_{ij}	component of conformation tensor \underline{b}	p. 67
b_s	width of injection slit	p. 123
c	wave speed	(2.1)
c_e	elastic shear wave speed	(4.11)
CR	area contraction ratio	p. 76, 97
D	pipe diameter	(5.1)
D_s	diameter of injection syringes	(5.27)
DR	amount of drag reduction	(5.2)
e	base of natural logarithms (≈ 2.718282)	(2.1)
\underline{e}_i	unit vector in i -direction	p. 48
E	elasticity number	(4.8)
E'	disturbance energy	p. 9
E_{Herbert}	disturbance energy	(4.20)
Ek	Ekman number	(5.25)
f	disturbance frequency	(5.28)
f_M	Moody friction factor	(5.3), (7.3)
G	Görtler number	(5.13)
h	half-distance between the plates	p. 45
h_s	height of injection slit	p. 123
h_{so}	height of blockage in injection slit	p. 123
i	purely imaginary number ($\sqrt{-1}$)	(2.1)
\underline{I}	unit tensor	(4.16)
k	order of finite-element polynomials	p. 49
K	consistency index in power-law fluid	(7.4)
L	length of the computational domain	p. 45, 47
L	length of pipe section or entire pipe	p. 76
$L_{99\%}$	entrylength for pipe flow	(5.1)

m	dimensionless azimuthal wave number	p. 18
n	power-law index	(7.4)
O_{ring}	surface of injection+extraction	(5.26)
p	dimensionless pressure	(2.1)
Pr	Prandtl number	(5.8)
Q	flow rate	(5.2)
r	dimensionless radial direction	p. 18
R	radius of curvature	(5.13)
Ra	Rayleigh number	(5.8)
Re	Reynolds number in plane Poiseuille flow	(4.6), (7.2)
Re_n	modified Reynolds number (Metzner & Reed 1955)	(7.10)
Re_p	Reynolds number based on pressure gradient	p. 9
Re_w	modified Reynolds number based on wall viscosity	(7.11)
$Re_{99\%}$	maximum Re for fully developed flow in a pipe	(5.1)
Ro	Rossby number	(5.25)
s	stream-wise boundary layer position	(5.13)
s_h	shift length	(5.20)
t	time	(2.1)
t^*	dimensionless time	p. 51
ΔT	temperature difference	(5.8)
\underline{u}'	dimensionless disturbance velocity vector	(2.1)
\hat{u}	dimensionless disturbance amplitude	(2.1)
U	mean stream-wise velocity in plane Poiseuille flow	(2.2)
\underline{v}	velocity vector	(4.1)
v_i	disturbance velocity	(5.28)
v_i^*	relative disturbance velocity	(6.2)
$v_{i,c}^*$	critical relative disturbance velocity	p. 132
ΔV	displacement volume of disturbance	(5.28)
W	mean axial velocity	(2.7)
\overline{W}	bulk velocity in pipe flow	(5.3)
W_∞	free stream velocity	(5.13)
We	Weissenberg number	(4.7)
x	stream-wise direction in plane Poiseuille flow	(2.1)
y	wall-normal direction in plane Poiseuille flow	(2.1)
z	spanwise direction in plane Poiseuille flow	(2.1)
z	stream-wise direction in cylindrical Poiseuille flow	p. 18

Greek symbols

α	dimensionless stream-wise wave number	(2.1)
α^*	dimensionless stream-wise wave number	p. 48, (6.4)
β	dimensionless spanwise wave number	(2.1)
$\dot{\underline{\gamma}}$	rate-of-deformation tensor	(4.3)
$\dot{\gamma}$	shear rate	(4.13)
δ_r	boundary layer length scale	(5.13)
ϵ	related to pseudo-modes	p. 25
η	viscosity	(4.3), (7.1)
η_w	viscosity at the wall	(7.11)
η_0	zero-shear-rate viscosity	(7.1)
η_∞	infinite-shear-rate viscosity	(7.1)
θ	azimuthal coordinate	p. 18
κ	thermal diffusivity	(5.8)
λ	relaxation time in UCM model	(4.4)
λ	time constant in Carreau model	(4.4)
Λ	Lambda-shaped vortices	p. 12
ν	kinematic viscosity	(4.6)
ρ	density	(4.1)
$\underline{\underline{\sigma}}$	Cauchy stress tensor	(4.2)
$\underline{\underline{\tau}}$	extra-stress tensor	(4.1)
τ_{ij}	component of stress tensor $\underline{\underline{\tau}}$	(4.12)
τ_w	wall shear stress	p. 164
ϕ	amplitude of stream function	(2.4)
ψ	stream function	(2.3)
Ψ	stream function	(5.15)
Ψ_1	first normal stress coefficient	(4.15)

Calligraphic symbols

\mathcal{D}	differentiation to dimensionless y -coordinate	(2.2)
\mathcal{L}	differential operator	(2.7)
\mathcal{O}	order function	p. 12

Miscellaneous symbols

∇	nabla-operator	(4.1)
$D(\)/Dt$	material derivative	(4.1)
$(\)^{\dagger}$	transpose	(4.3)
$(\)_{\nabla}$	upper-convective derivative	(4.5)
$(\)_{cl}$	quantity at the centerline	
$(\)_w$	quantity at the wall	

Abbreviations

2-D	two-dimensional	
3-D	three-dimensional	
20 + 10 ppm	10 ppm of fresh polymer added to 20 ppm solution	p. 157
A-110	PAMH: Superfloc A-110	
ABB	Asea Brown Boveri	
Ar ⁺	Argon-ion laser	
BSA	Burst Spectrum Analyzer (Dantec)	
DPIV	digital particle image velocimetry	
DNS	direct numerical simulation	
FVA	Flow Velocity Analyzer (Dantec)	
HeNe	Helium-Neon laser	
LDV	laser Doppler velocimetry	
LE	leading edge	
M	Molar; mol ⁻¹	
MW	molecular weight	p. 80
PAM	polyacrylamide	p. 80
PAMH	partially hydrolyzed polyacrylamide	p. 80
PEO	polyethyleneoxide	p. 80
PIV	particle image velocimetry	
ppm	weight parts per million	
PVC	polyvinylchloride	
rms	root-mean-square	
TE	trailing edge	
TS	Tollmien-Schlichting	
UCM	Upper Convected Maxwell fluid	
wppm	weight parts per million	

Chapter 1

General introduction

1.1 Context of project

Research on transition started with the publication of Reynolds (1883) on the study of the transition to turbulence in pipe flow. He found that transition to turbulence occurred when a dimensionless group, now called the Reynolds number (Re), exceeds a certain critical value. The Reynolds number is the ratio of the nonlinear inertia forces to the viscous forces. For small values of Re , the viscous forces dominate the flow behavior and fluid particles move through the pipe following straight lines, i.e. the flow is laminar. For flows with a Reynolds number above the critical value, nonlinear inertia forces control the behavior of the fluid and an irregular chaotic motion emerges, which we call turbulence.

With respect to a laminar flow, turbulence causes large changes in flow-related processes, e.g. mixing, the transfer of heat, and the resistance or drag are dramatically increased. However, these processes are precisely the key ingredients of the flow problems that we encounter in every day life and in industrial applications. For example, we stir our tea to enhance mixing, we design a heat exchanger with turbulent flow to promote heat transfer, and we shape our cars, ships, and airplanes aerodynamically to reduce drag. An industrial application where accurately predicting pressure losses caused by drag becomes increasingly important is drilling for oil and gas. Since the present thesis follows from the questions asked in this field of research, let us take a more detailed look at this application.

During a drilling operation, drilling fluid is pumped down through the drill pipe to the drill bit, and flows up in the annular space between the drill pipe and the well casing. At the drill bit the fluid should remove excess heat caused by the drilling operation. So here heat transfer properties are important. The upward flow through the annulus is used to remove the cuttings. Also, the drilling fluid is used to counterbalance the pressure in the drilling zone. This pressure has to be kept within its sometimes narrow margin. The minimum (hydrostatic) pressure of the fluid is regulated by adjusting its density, and should be larger than the pressure of the oil/gas present at the drill bit. This prevents inflow of oil/gas that would lead to a danger of explosion at the surface. The maximum pressure should be lower than the stress at which the rock fractures, to avoid the loss of drilling fluid. Apart from the hydrostatics, the pressure at the drill bit is also influenced by the flow circulation. The total pressure, i.e. the sum of these two contributions could exceed the maximum pressure, leading to a breakdown of the drilling operation. For this reason, it is important to accurately predict the flow resistance. In pursuit of cost reduction, attempts are made to decrease the size of the drill hole, so-called slim hole drilling, which considerably increases the flow resistance. Since the latter is directly related to the type of flow, we need to be able to predict whether the flow will be laminar or turbulent.

For flows of, for example, water and air, empirical correlations exist with which we can

predict the type of flow and the related pressure losses for the conditions encountered in practical applications. For drilling fluids, prediction of laminar-turbulent transition is more difficult, the reason being their complex composition. Drilling fluids consist of a mixture of water, clay, polymers, chemicals, and sometimes oil. These mixtures behave differently from water and therefore unexpected behavior can occur. Drilling fluid is not the only fluid that displays this behavior. In fact, water-like fluid behavior is an exception. For example, blood, polymer solutions, polymer melts, suspensions, paints, glue, and many every day fluids that can be found in our kitchens, like yoghurt, ketchup, jam, and butter all show complex behavior and are known as non-Newtonian fluids, to distinguish them from Newtonian fluids like water. The field of science which deals with these non-Newtonian fluids is called rheology.

This explains the main goal of this thesis: The prediction of laminar-turbulent transition in fluids with rheological properties similar to drilling fluids. In view of this longterm goal, we set ourselves to this study in which we have to combine two more or less separate scientific issues; i.e. laminar-turbulent transition and non-Newtonian fluid flow.

1.2 Laminar-Turbulent transition

In the previous section we have highlighted the direct application of transition in non-Newtonian fluids to drilling operations. Here we will study this transition process for the idealized geometry of a fully developed cylindrical pipe flow. The theoretical understanding of laminar-turbulent transition, in particular transition in pipe flow, is still rather poor despite the vast amount of work which has been done in this field over past century. The understanding of laminar-turbulent transition mechanisms active in non-Newtonian fluid flows has progressed even less due to the complex nature of these fluids. Hence, in order enhance the understanding of laminar-turbulent transition for non-Newtonian fluids much work still needs to be done in two very exciting fields of fluid mechanics, being laminar-turbulent transition and rheology.

Since Reynolds (1883) published his results of the "... the circumstances which determine whether the motion of water shall be direct or sinuous ... ", many investigators have tackled the transition problem in pipes as well as in other flow geometries. The classical theoretical approach is to linearize the equations of motion and study the growth of very small disturbances. For 2-D Poiseuille flow between parallel plates, it has been found that these small disturbance grow above a critical value of the Reynolds number, i.e. Re_c . This results has been confirmed experimentally (Nishioka *et al.* 1975). However, the value of Re_c found from linear stability theory is more than 5 times as high as the critical value that is obtained in practical conditions. From the fact that the flow becomes turbulent at values of Re where infinitesimal disturbances are stable, it was concluded that in general finite amplitude disturbances are responsible for the transition to turbulence. Although calculations show that for finite amplitude disturbances the critical Reynolds number is indeed much lower, the disagreement with experiments remains still more than a factor of 2. Stability theory for cylindrical Poiseuille flow is even less successful. Although no rigorous proof exists, the theory indicates that infinitesimal disturbances are stable (e.g. Davey & Drazin 1969 and Salwen & Grosch 1972). Calculations for finite amplitude disturbances show no critical Reynolds number values above which disturbances will grow. Indirectly, by calculating Landau constants, the threshold amplitudes above which finite amplitude disturbances can grow have been calculated (e.g. Davey & Nguyen 1971 and Sen *et al.* 1985).

An alternative to solving (linearized) stability equations is direct numerical simulation (DNS) of the three-dimensional equations of motion. Although extremely computationally expensive, excellent results have been achieved for transitional flow between parallel plates and for boundary layers (Kleiser & Zang 1991). Also, for pipe flow, DNS of fully turbulent flows emerged (Eggels *et al.* 1994) but transition calculations in this geometry have not reached the stage where they can be considered as reliable. This is mainly due to the very high resolution that is required.

Recently, using DNS, Trefethen *et al.* (1993) showed that a small disturbance which consists of a combination of (linearly stable) eigenmodes, can grow during a finite period of time before it decays as is predicted by linear stability theory. This initial growth is a result of the non-orthogonality of the linear Navier-Stokes operator and such behavior of disturbances is called transient growth. The results of Trefethen *et al.* (1993) have been extended to pipe flows by O'Sullivan & Breuer (1994a, 1994b), who find a nonlinear disturbance which shows transient growth and develops into a transitional flow structure which is similar to the transitional flow structure called puff, observed experimentally by Wygnanski *et al.* (1975). Unfortunately, the Reynolds number in their calculations is slightly too small and after initial growth the flow decays to a laminar state. Given the continuing increase in computing power and the development of massively parallel computers, one may expect considerable progress from numerical simulations of transition within the next decade or so.

In this thesis we will primarily concentrate on an experimental study on transition since theory is unable to predict transition for Newtonian pipe flow, let alone for flows of non-Newtonian fluids. For this we have constructed a new and specialized experimental pipe flow setup to be discussed in detail in this thesis. Developments of measurement techniques has also evolved significantly. A non-intrusive measurement technique like Laser Doppler Velocimetry has more or less become established techniques and allow for a very detailed study of flow characteristics. Unfortunately, with this technique the velocity can only be measured at one location in the flow. A very promising new technique in this respect is Particle Image Velocimetry (PIV). PIV can measure velocity fields in a plane or even in a volume of the flow as a function of time (Westerweel 1993). Application of PIV to turbulent and transitional pipe flows has already shown exciting results (Westerweel *et al.* 1994, Draad *et al.* 1995), and will no doubt lead to more information in the future. Probably the largest potential for this technique is that it permits a direct comparison between velocity fields obtained in experiments and those from DNS.

1.3 Non-Newtonian fluid flow

Our application area forces us to look not only to transition of Newtonian flow, which is a problem in itself, but also to transition of non-Newtonian fluids. Basically, all materials that show behavior which is in between that of a purely viscous fluid with a constant viscosity and an elastic solid fall in the category of non-Newtonian fluids. Very often, materials that possess both viscous and elastic behavior, are designated by the term visco-elastic fluids.

Non-Newtonian fluids can show some astonishingly different behavior from Newtonian fluids like water. Most non-Newtonian fluids have a viscosity that is not constant but depends on the shear rate. More spectacular differences are rod-climbing and the tubeless-siphon effects. When a rod is rotated in a beaker, strongly elastic fluids can climb the rod whereas no climbing

occurs for Newtonian fluids. When a siphon is retracted above the free surface, the flow for Newtonian fluids will stop whereas for strongly elastic fluids it will continue to flow! Such elastically behaving fluids can be obtained by dissolving several weight percent of a high-molecular weight polymer in water. Another surprising effect occurs when we dissolve minute amounts of these polymers (typically 0.001%) in a turbulent flow. The drag of the flow can then be decreased by as much as 80%. A more extensive review of such differences in behavior between Newtonian and non-Newtonian fluids is given in Bird *et al.* (1987a).

Laminar-turbulent transition in non-Newtonian fluids can also be different from that in Newtonian fluids. For many dilute polymer solutions, transition in pipe flow occurs at roughly the same Reynolds number as for Newtonian fluids (Virk *et al.* 1967), but also delay in transition has been reported (e.g. Chung & Graebel 1972) as well as 'early' transition (e.g. Zakin *et al.* 1977). Stability calculations for non-Newtonian fluids in plane Poiseuille flow show a reduction in critical Reynolds number when elasticity is added (e.g. Porteous & Denn 1972a and Sureshkumar & Beris 1995b) or an increase for suspended rods (Bark & Tinoco 1978)). The results of the stability calculations vary considerably with the choice of the constitutive equation, which describes the relationship between the stresses and the deformation rates. However, validation of such a relationship is possible only in very simple flows. The choice of the constitutive equation which best describes the behavior of polymers in such a complex flow as transition is very difficult, viz. it is not even known if any of the existing models performs satisfactorily in such flows.

Thus, no clear picture is presently available on whether and how non-Newtonian fluid behavior affects laminar-turbulent transition.

1.4 Aim and outline of this thesis

The aim of the work described in this thesis is to disclose some characteristics and properties that accompany the transition from laminar to turbulent pipe flow in both Newtonian and non-Newtonian fluids, where we are interested in the difference in behavior between both fluids. For this we concentrate on performing detailed stability measurements in laminar pipe flow of Newtonian and non-Newtonian fluids. For the Newtonian fluid we have used water and for non-Newtonian fluids dilute polymer solutions. Also, numerical simulation of two-dimensional visco-elastic fluid flow has been used to study the nonlinear stability of laminar flow between parallel plates.

The outline of this thesis is as follows. In chapter 2 and 3 we present a review of the literature on laminar-turbulent transition for Newtonian and non-Newtonian fluids respectively. Results on flow between parallel plates as well as in pipes are discussed. In chapter 4 we will discuss the results of the numerical computations that we carried out of the stability of flow between parallel plates. For the visco-elastic fluid we have taken the Upper Convected Maxwell model. We explore the range of Reynolds number-wave number combinations for which saturated two-dimensional disturbances exist. We compare the results for various levels of elasticity with those of a Newtonian fluid in order to explore the difference in transition behavior between both fluids.

In the following chapters, we focus on the experimental investigation of pipe flow stability. In chapter 5 we give a detailed description of the flow facility that we have designed with the aim to perform a study of pipe-flow stability. The flow in this facility can be maintained

laminar up to high Reynolds numbers ($Re > 60\,000$) and transition to turbulence is triggered by adding a well controlled disturbance. Special attention is given to details and features of the settling chamber and the measurement pipe which are necessary to obtain a very stable flow. Also, the disturbing influence of convection and the rotation of the earth on laminar pipe flow is measured and discussed. The results of the stability experiments are presented in chapters 6 and 7 for water (Newtonian) and dilute polymer solutions (non-Newtonian) respectively. We show results of the disturbance magnitude which is needed to trigger transition from laminar to turbulence flow as a function of a large range of disturbance frequencies and Reynolds numbers. For the non-Newtonian solutions, the effect of the polymer configuration, i.e. coiled or extended, on the flow stability is investigated. Also, the shear-rate-dependence of the viscosity of these dilute solutions is measured and a method to correct the experimental results for this effect is presented. We end this thesis with our main conclusions and suggest some possible directions for future research in chapter 8.

Chapter 2

Newtonian flow stability

Abstract

In this chapter we will briefly review the literature on theory and experiments of transition in both plane and cylindrical Poiseuille flow for Newtonian fluids.

2.1 Introduction

Transition to turbulence in a cylindrical pipe goes back more than one-hundred years when Osborne Reynolds in 1883 performed his famous experiments. His findings, which are still not explained satisfactorily by theory, showed that smooth laminar flow of Newtonian fluid in a pipe becomes unstable if a dimensionless number exceeds a certain critical value. This number $U_{\max}R/\nu$ is known as the Reynolds number, where U_{\max} is the maximum velocity, R the radius of the pipe and ν the kinematic viscosity of the fluid. Presently, after more than a century, we still know relatively little about the processes and mechanisms of the transition in pipe flow. More progress has been made for Poiseuille flow between parallel plates. In this overview, the results on 2-D Poiseuille flow will be presented in section 2.2 and the results dealing with cylindrical Poiseuille flow in section 2.3. The more recent developments concerning transient growth phenomena are the subject of section 2.4 as far as they are important for both plane and cylindrical Poiseuille flow.

2.2 Plane Poiseuille Flow

First, we discuss some theory concerning plane Poiseuille flow rather than starting with the much more complicated case of cylindrical Poiseuille flow. Much of the material presented here can also be found in the book by Drazin & Reid (1981) and in the excellent review papers on ‘Instability mechanisms in shear-flow transition’ (Bayly *et al.* 1988) and ‘Numerical simulation of transition in wall-bounded shear flows’ (Kleiser & Zang 1991). All quantities that we use in this section are made dimensionless with the centerline velocity and the channel half-width.

2.2.1 Linear Instability Theory

The most obvious and direct route to investigate the stability of a flow is linear instability theory. In this theory, the solution to the Navier–Stokes equation is disturbed by infinitesimal disturbances which have the following form:

$$\underline{u}'(x, y, z, t) = \hat{u}(y)e^{i(\alpha x + \beta z - \alpha ct)} \quad (2.1)$$

in which the real part of this expression represents the physical quantity. x and z are the homogeneous streamwise and spanwise direction respectively, and y is the inhomogeneous wall normal direction, where homogeneous indicates that flow properties are not a function of the

spatial coordinate and inhomogeneous means the opposite. From the assumption of homogeneity in the x and z -directions follows that α and β are real wave numbers. The wave speed c may be complex. If the imaginary part of c becomes positive the linear disturbance will grow exponentially and the flow is then by definition unstable. Substitution of $\underline{u} + \underline{u}'$ and $p + p'$ in the Navier–Stokes equations, where \underline{u}' and p' are disturbances, and keeping only the linear terms in the disturbances gives a set of linearized stability equations; one continuity equation and the Navier–Stokes equation. For plane shear flows it can be shown (Squire's theorem) that only two-dimensional disturbances have to be considered (Drazin & Reid 1981, pp. 129 & 155).

Consider plane shear flow between two rigid boundaries. After elimination of the pressure and u' , follows the famous Orr–Sommerfeld equation, which reads:

$$[U - c](\mathcal{D}^2 - \alpha^2)\hat{v} - U''\hat{v} = \frac{1}{i\alpha Re}(\mathcal{D}^2 - \alpha^2)^2\hat{v} \quad (2.2)$$

where $U(y)$ is the dimensionless velocity profile, \hat{v} is the y -component of the dimensionless amplitude of the velocity disturbance, and \mathcal{D} is an operator which stands for differentiating to the dimensionless y -coordinate. An alternative form which is often encountered, can be obtained by introducing in equation 2.2 the streamfunction $\psi'(x, y, t)$ such that the two velocity components of the disturbance are given by:

$$u' = \frac{\partial\psi'}{\partial y} \quad \text{and} \quad v' = -\frac{\partial\psi'}{\partial x} \quad (2.3)$$

Let the disturbance be of the form:

$$\psi'(x, y, t) = \phi(y)e^{i\alpha(x-ct)} \quad (2.4)$$

Then it follows that $\phi(y)$ also satisfies the Orr–Sommerfeld equation:

$$[U - c](\mathcal{D}^2 - \alpha^2)\phi - U''\phi = \frac{1}{i\alpha Re}(\mathcal{D}^2 - \alpha^2)^2\phi \quad (2.5)$$

For inviscid flow can be obtained by simply ignoring the term with the Reynolds number. We then obtain the Rayleigh equation which is identical to the Taylor–Goldstein equation (Nieuwstadt 1992, p. 28 and Drazin & Reid 1981, p. 329) for homogeneous temperature fields. Analysis of the Rayleigh equation leads to a well known criterion for instability (Drazin & Reid 1981, pp. 131–132): Rayleigh's inflection-point theorem. It implies that a necessary condition for instability is that the basic profile $U(y)$ should have an inflection point. Note that the criterion gives only a necessary condition for instability, viz. an inflection point does not always lead to instability in an inviscid flow. However, plane Poiseuille flow has no inflectional velocity profile, but the flow is nevertheless unstable at finite Reynolds numbers. This indicates that inviscid theory is not always sufficient and we have to consider solutions of the full Orr–Sommerfeld equation.

The Orr–Sommerfeld equation applied to plane Poiseuille flow gives a critical Reynolds number of $Re_c = 5772.22$ and $\alpha_c = 1.021$ (Drazin & Reid 1981, p. 192), where Re is based on half the distance between the plates and the maximum velocity. These unstable modes are called Tollmien–Schlichting (TS) waves since these same waves were predicted by Tollmien and

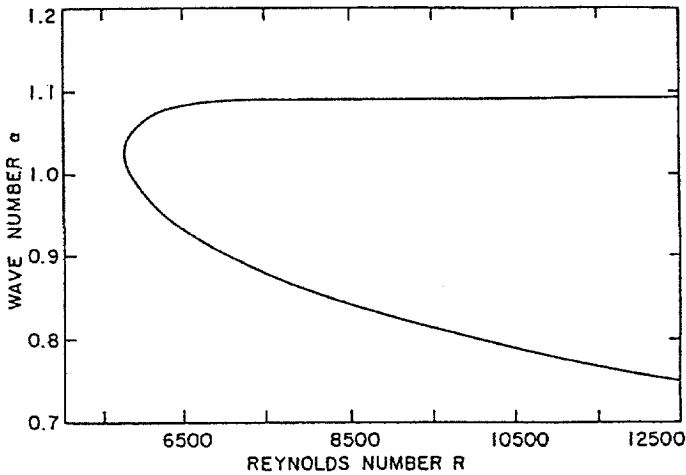


Figure 2.1: Linear stability diagram for plane Poiseuille flow. From Porteous & Denn (1972a).

Schlichting in the early 1930's for boundary layer instability. The linear stability diagram for plane Poiseuille flow is shown in figure 2.1. The shape of the disturbance will be discussed in more detail in chapter 4 in relation to the numerical calculations for plane Poiseuille flow of Newtonian and non-Newtonian fluids.

2.2.2 Nonlinear Instability Theory

As we have seen in the previous section, linear stability theory for plane Poiseuille flow gives a critical Reynolds number of 5772.22. On the other hand, in experiments we find transition to turbulence at Reynolds numbers as low as 1000. As infinitesimal disturbances are stable at this Re , clearly, finite amplitude disturbances must be relevant. The idea is that for larger amplitude disturbances the critical Reynolds number decreases (Drazin & Reid 1981, pp. 370–375), see figure 2.2. Chen & Joseph (1973) showed that the finite-amplitude solutions which bifurcate from the linear stability diagram can be subcritical, i.e. finite-amplitude instability exists for Reynolds numbers smaller than the linear critical Reynolds number. Therefore, the diagram in figure 2.2 is known as subcritical bifurcation. For small disturbance amplitudes, behavior as depicted in figure 2.2 has been found for the plane Poiseuille flow by Porteous & Denn (1972a) (see also figure 3.7 on page 39.). Zahn *et al.* (1974) and Herbert (1976) showed that a nonlinear neutral surface in the parameter space (Re, α, E') exists as is shown in figure 2.3. E' is the disturbance energy. The top neutral surface is attracting (upper-branch solutions are stable) whereas the bottom part of the surface (lower branch) is unstable. Herbert gives for the critical Reynolds number for these 2-D nonlinear disturbances, located at the nose of this nonlinear neutral surface; the value $Re_{p,NL}=2935$ and $\alpha=1.32$. Note that here the Reynolds number is based on the pressure gradient, as is indicated by the subscript p . However, due to the effect of the large nonlinear disturbances the corresponding flow rate has decreased by roughly 10%, so that the critical Reynolds number based on flow rate becomes $Re_{NL}\approx 2640$. This latter value

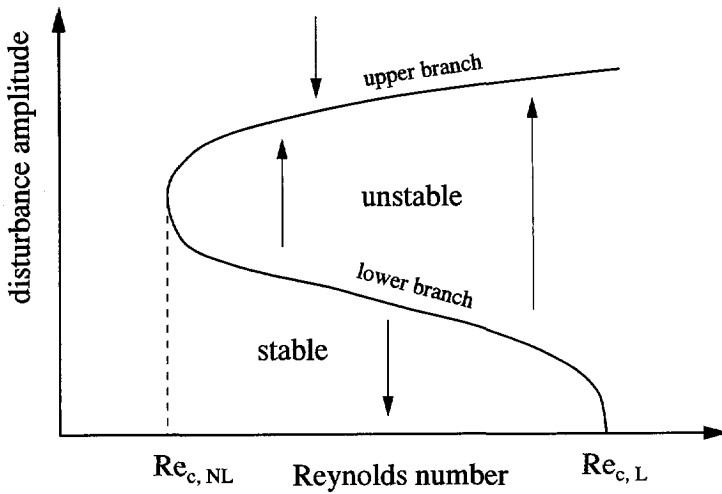


Figure 2.2: Sketch of the dependence of the critical Reynolds number on the disturbance amplitude. $Re_{c,L}$ denotes the linear critical Reynolds number and $Re_{c,NL}$ is the nonlinear critical Reynolds number.

is in broad agreement with results presented by Jiménez (1990).

Weakly nonlinear theory, which extends the linear eigenfunction to finite amplitude solutions, is able to give the lower-branch solutions for small amplitudes, i.e. near Re_c . Essentially these are horizontal cross-sections for $E' = \text{constant}$ in figure 2.3. A plot of α versus Re for weakly nonlinear constant amplitude solutions is given in figure 2.4.

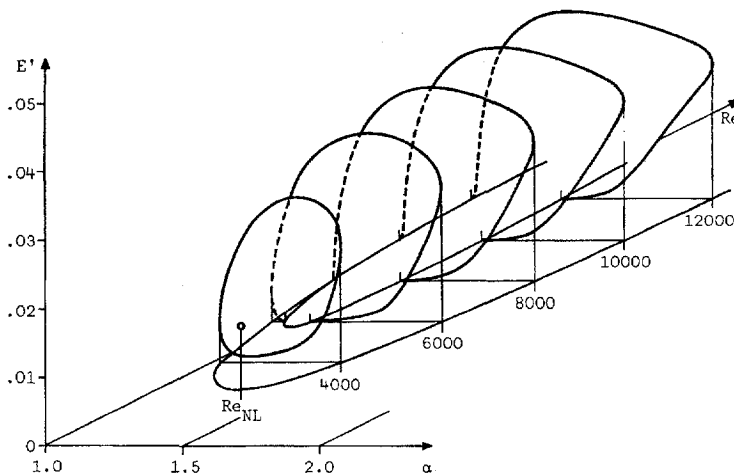


Figure 2.3: Nonlinear neutral surface for finite-amplitude two-dimensional waves in plane Poiseuille flow. From Herbert (1980).

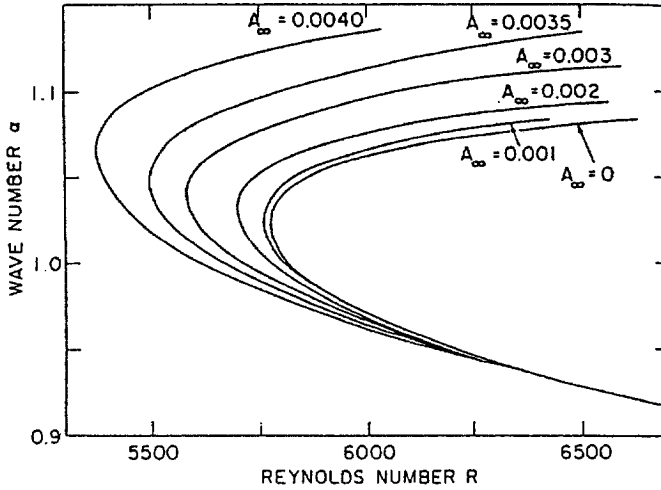


Figure 2.4: Finite amplitude neutral stability curves (lower branch) obtained by weakly nonlinear theory. A_∞ designates the disturbance magnitude. From Porteous & Denn (1972b).

Apart from linear and nonlinear stability equations, these 2-D disturbances have been also studied by numerical simulation, e.g. the Direct Numerical Simulation of 2-dimensional Poiseuille flow by Jiménez (1987, 1990). Since transition to turbulence is essentially 3-dimensional, 2-dimensional transition cannot give the complete picture. However, Jiménez found a sweep-ejection cycle which is shown in figure 2.5, and he shows that a group of waves travels at a higher speed than an individual wave. The active front of the group triggers new waves, which produces a strong ejection. After that, the wave immediately begins to decay. The vorticity of the ejection is enough to trigger another new wave in the undisturbed flow in front of the first wave and so the wave group propagates.

Recently, Price *et al.* (1993) presented the existence of stable localized wave packets which are created through a saddle-node bifurcation at $Re=2330$. This Reynolds number is lower than the critical Reynolds number for the finite-amplitude TS-waves described above but still a large gap remains with the experimentally found critical Reynolds numbers of approximately 1000 (Nishioka & Asai 1985).

2.2.3 Secondary Instability

In the last decade, numerical calculations have revealed an interesting mechanism in the transition to turbulence. Shear flows can be divided into three groups according to their linear stability characteristics. The first group of flows that have an inflectional velocity profile is inviscidly unstable to infinitesimal disturbances. The second group consists of flows that are inviscidly linearly stable, but can be unstable to infinitesimal viscous disturbances. Examples of such flows are plane Poiseuille flow and boundary layer flow. The third group includes flows that are linearly stable to all infinitesimal disturbances. Prototypes are cylindrical Poiseuille flow and plane Couette flow.

We have seen in the previous section, that in plane Poiseuille flow finite amplitude solutions

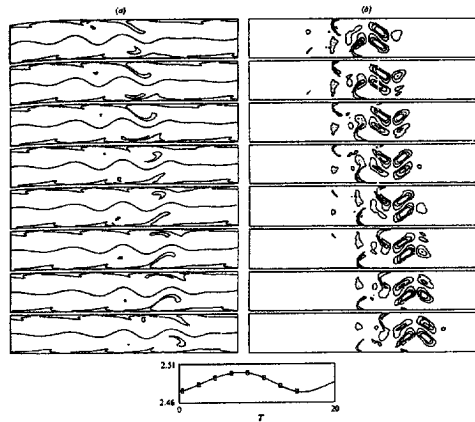


FIGURE 12. Time evolution of flow (u, v) for the propagation cycle of a permanent wave packet. $Re = 4000$, $\alpha = 0.25$. Flow from left to right and time from top to bottom. Frames are keyed to wall stream plot at bottom. (a) Vorticity: isolines, $\omega = 0, \pm 1, 2$. (b) Reynolds stress: isolines, $-v'v' = 0, \pm 0.02, \pm 0.05, \pm 0.08$. Shaded area is below -0.02 .

Figure 2.5: Sweep–ejection cycle in 2–D Poiseuille flow. From Jiménez (1990).

(oscillating flows) which are neutrally stable exist for $Re \gtrsim 2640$. These are called secondary flows (the primary flow is the parabolic Poiseuille flow itself). Orszag & Patera (1983) study the linear stability of three–dimensional disturbances in plane Poiseuille flow in the presence of non-linear two-dimensional disturbances. They show that the growth rate for 3–D disturbances in such a flow can reach values of 0.12, which is very fast compared with the TS–waves and which is close to the convective time scale (i.e. $\mathcal{O}(1)$ in this nondimensional notation). Also, below $Re \approx 2640$ ($Re_p \approx 2900$) (where no neutral finite amplitude TS–waves exist, and where thus the analysis can be regarded only as an approximation) three–dimensional disturbances grow above $Re_p \approx 400$. Applying direct numerical simulation techniques of time dependent flows, Orszag & Patera (1983) showed that the three–dimensional disturbances grow for Reynolds numbers exceeding 1000. This critical Reynolds number cannot be taken as a precise number since the number of modes in the y -direction in their simulation is limited. Also, in the simulation by Orszag & Patera, the three–dimensional disturbance does not influence the two–dimensional finite amplitude disturbance and as all two–dimensional states decay for $Re_p < 2900$ the infinitesimal three–dimensional disturbances will eventually also have to decay for $t \rightarrow \infty$. Continuing the calculations beyond the point where three–dimensional disturbances can be considered as linear does not result in a saturated tertiary state but results in chaotic behavior normally associated with turbulent flow. This shows that when the initially small three-dimensional disturbances are able to grow large enough, and they might trigger transition to turbulence at Reynolds numbers close to those found in experiments. This suggests a scenario of linear disturbances growing to become nonlinear, which in turn are linearly unstable to 3-D disturbances. The latter may grow and eventually trigger transition.

The growth of 3–D disturbances on top of the large amplitude 2-D waves is known as secondary instability. The secondary instabilities can in appear in several modes. They may take the form of a double periodic array of Λ -shaped vortices (Klebanoff modes) as is shown in

figure 2.6. These Klebanov modes (also named K-type instabilities) have the same wavelength as the fundamental TS-wave. They occur for the upper-branch TS-waves. For the unstable lower-branch TS-waves, Herbert (1983) discovered subharmonic secondary instabilities, i.e. their wavelength is twice that of the fundamental TS-wave. These so-called Herbert modes (or H-type instabilities) consist of staggered Λ -vortices (see figure 2.6).

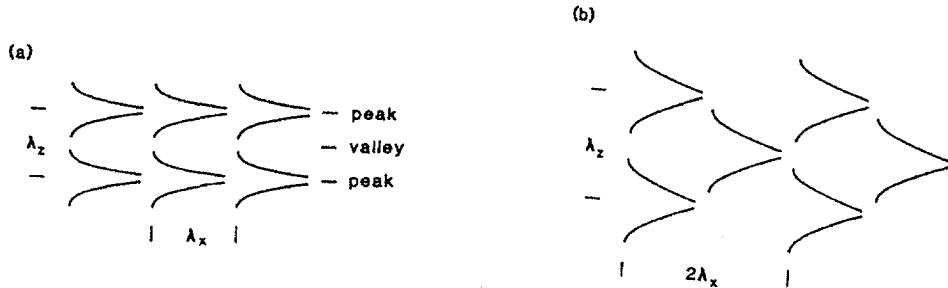


Figure 2.6: Schematic of Λ -vortex patterns resulting from secondary instability: (a) fundamental modes known as Klebanov-modes (K-type) and (b) subharmonic modes known Herbert-modes (H-type). From Herbert (1983).

Bayly *et al.* (1988) give a review of instability mechanisms in shear flows and also discuss a time-scale which is important for our nonlinear stability calculations on plane Poiseuille flow presented in chapter 4. They show that the 2-D nonlinear waves approach their saturated amplitudes on a viscous time-scale. This requires long calculation times in numerical simulations, a point to which we will return in chapter 4.

2.2.4 Direct Numerical Simulations

As we have seen above, Orszag & Patera used Direct Numerical Simulation (DNS) of the Navier–Stokes equation already in 1983 to investigate the growth of secondary instabilities. However, Gilbert & Kleiser were the first to provide an accurate simulation of the complete transition process from laminar to turbulence in a channel flow. They distinguish three phases in the transition process (see Kleiser & Zang 1991):

1. The initial two- and three-dimensional disturbance growth (dimensionless time smaller than 100),
2. The formation and development of 3-D transitional flow structures, such as Λ -vortices and high shear layers ($100 < t < 150$), and
3. The breakdown phase ($150 < t < 200$), in which the transitional flow structures on the scale of the TS-wave disappear and turbulence sets in.

In figure 2.7 the lambda-vortex structure is shown and in figure 2.8 the break-down phase is shown.

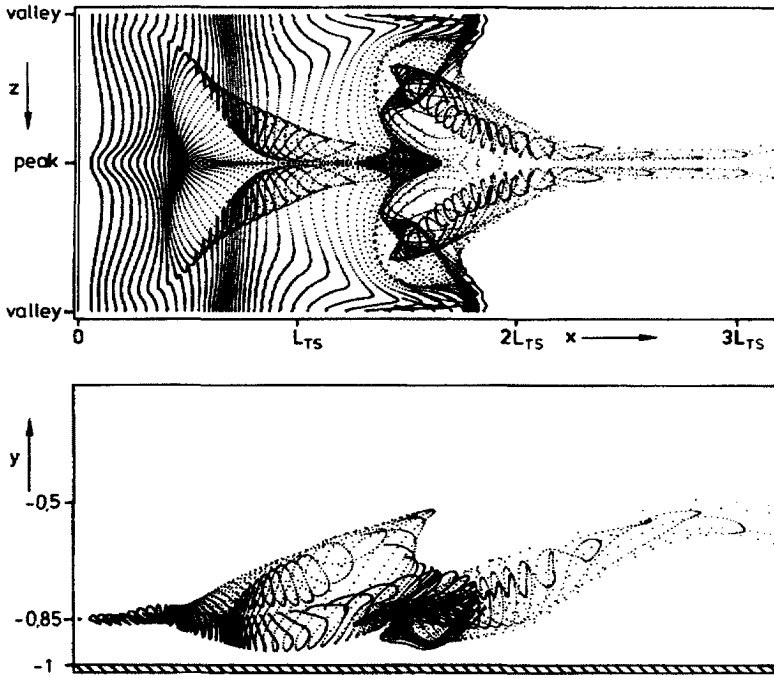


Figure 2.7: Lambda-vortex structures as computed by Gilbert. From Kleiser & Zang (1991).

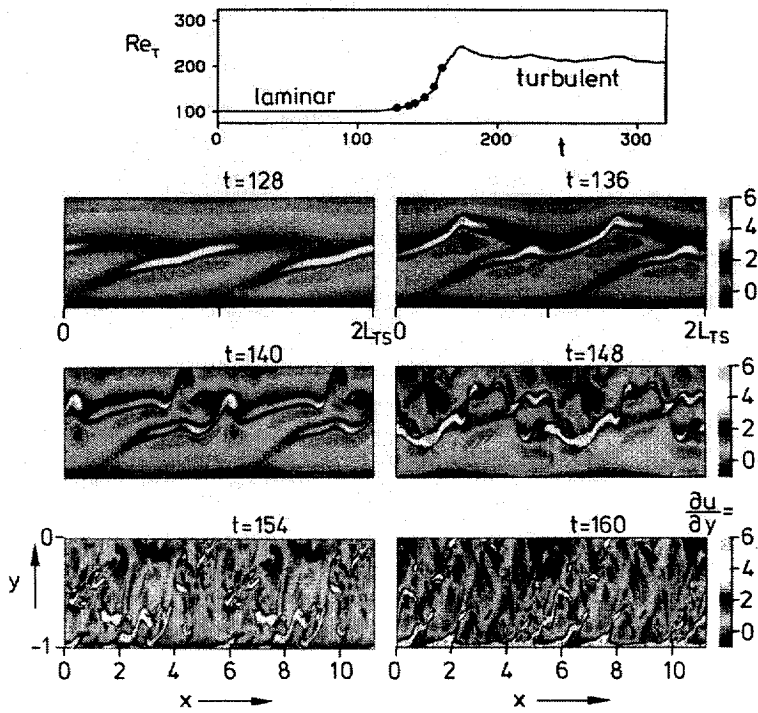


Figure 2.8: Breakdown process in plane Poiseuille flow. From Kleiser & Zang (1991).

2.2.5 Experiments

From the Orr–Sommerfeld equation it was deduced that linear instabilities should be present in a boundary layer, known as Tollmien–Schlichting waves. However, it remained uncertain whether or not these waves exist in actual flows. Only after Schubauer and Skramstad strongly reduced the background turbulence level, in their facility 0.0459% (see Drazin & Reid 1981, p. 239), actual TS-waves could be detected. A similar landmark for plane Poiseuille flow were the measurements by Nishioka, Iida & Ichikawa (1975). The experiments by Nishioka *et al.* were done in a low turbulence air channel flow with a background turbulence level of only 0.05%. The height of their channel was 14.6 mm. The channel was 27.4 heights wide and 411 heights long. They roughly confirmed the neutral stability curve for plane Poiseuille flow, as shown in figure 2.9.

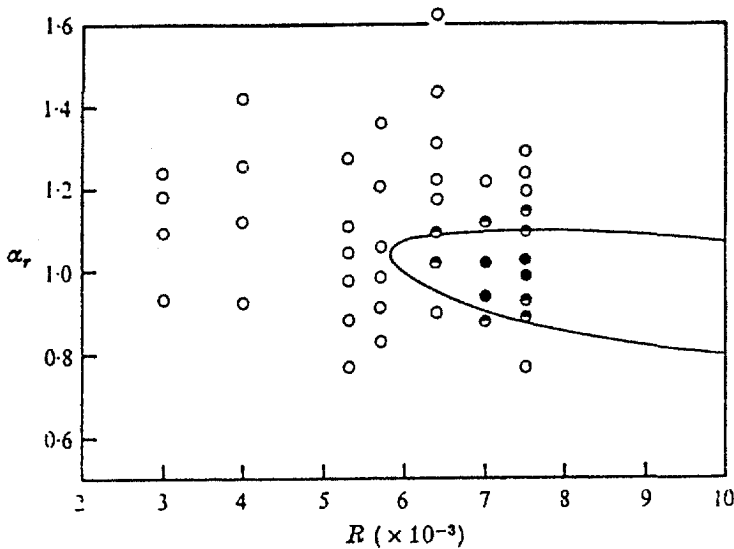


Figure 2.9: Neutral stability curve for linear disturbances in plane Poiseuille flow as measured by Nishioka *et al.* (1975).

Kozlov & Ramazanov (1984a, 1984b) visualized both the fundamental (Klebanov or K-type) and the subharmonic (Herbert or H-type) secondary instability modes as depicted in figure 2.6. One of their results is depicted in figure 2.10.

For small amplitudes of the 2-D wave, theory predicts that the Herbert modes will dominate transition. For larger amplitudes of the 2-D wave, the fundamental and subharmonic modes compete. However, most experiments show that the fundamental Klebanov modes prevail even in conditions where theory predicts the domination of subharmonic Herbert modes. Singer *et al.* (1989) performed calculations using DNS and show that the presence of weak streamwise vortices can cause the K-type structure to dominate transition. An alternative explanation is offered by Kim & Moser (1989). Their simulations show that the initial growth of the streamwise velocity of the spanwise modes (which they call “minus” modes) acts as a forcing for the fundamental (K-type) modes.

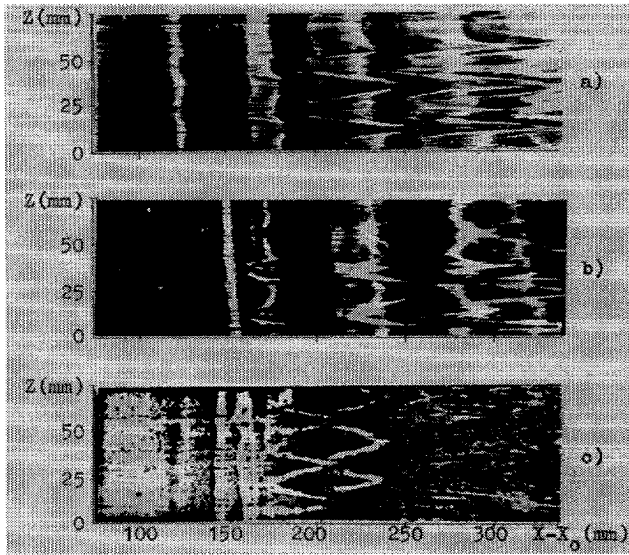


Figure 2.10: Secondary instabilities as visualized by Kozlov & Ramazanov (1984b). $Re=3850$, (a) 73 Hz, (b) 55 Hz and (c) 57 Hz. (a) and (b) depict fundamental modes (K-type) whereas (c) is an example of a subharmonic (H-type) secondary instability.

When experimental investigations in relation to the minimum transition Reynolds number in plane Poiseuille flow are discussed, mostly the work of Davies & White (1928) and Patel & Head (1969) is mentioned. Both these experiments give minimum transition Reynolds number of around 1000 (1080 and 1035 respectively). Since in both experiments the inlet flow was disturbed by possible flow separation on the right-angled entrance corners. Therefore, some uncertainty remained about the validity of this minimum transition Reynolds number. However, Nishioka & Asai (1985) also found a transition number of 1000 using three types of disturbance generators, viz. placing 1 or 6 cylinders at the entrance or periodic injection from a hole in the wall. The threshold intensity of the external disturbance that is able to trigger the transition, is comparable to the maximum intensity of u -fluctuations in fully turbulent channel flows (i.e. 13-15%).

2.3 Cylindrical Poiseuille Flow

In this section we will briefly discuss the literature of transition in cylindrical pipe flow transition. As we will see, our understanding of pipe-flow transition is much less progressed than for plane Poiseuille flow. This is mainly due to the problems related to linear stability theory, as we will see in the next section.

2.3.1 Linear Instability Theory

In cylindrical Poiseuille flow, Squire's transformation can be used only for axisymmetric disturbances (Drazin & Reid 1981, p. 217). Thus, for axisymmetric disturbances it is sufficient to consider disturbances having velocity components $(0, u'_r, u'_z)$. Here the z -axis coincides with the axial flow direction. In analogy to plane Poiseuille flow, a streamfunction $\psi'(r, z, t) = \phi(r)e^{i\alpha(z-ct)}$ is introduced related to the disturbance velocities by:

$$u'_z = \frac{1}{r} \frac{\partial \psi'}{\partial r} \quad \text{and} \quad u'_r = -\frac{1}{r} \frac{\partial \psi'}{\partial z} \quad (2.6)$$

The real part of this equation represents the physical disturbance velocity. It can be shown that $\phi(r)$ satisfies the equation:

$$[W - c](\mathcal{L}^2 - \alpha^2)\phi - \frac{1}{r} \left(\frac{W'}{r} \right)' \phi = \frac{1}{i\alpha Re} (\mathcal{L}^2 - \alpha^2)^2 \phi \quad \text{with} \quad \mathcal{L} = \frac{d^2}{dr^2} - \frac{1}{r} \frac{d}{dr} \quad (2.7)$$

Here W designates the axial velocity component. Davey & Drazin (1969) studied this equation numerically and found stability for all axisymmetric disturbances. Investigation of non-axisymmetric disturbances is important since for plane Poiseuille flow is stable to disturbances having the same symmetry as the base flow but nonsymmetric ones are unstable. Salwen & Grosch (1972) performed numerical calculations for non-axisymmetric disturbances (disturbances varying like $e^{im\theta}$) and found stable solutions for azimuthal wave numbers $m=0, \dots, 5$, axial wave numbers α between 0.1 and 10.0, and $\alpha Re \leq 50\,000$. Furthermore, the least stable mode for large Reynolds number is a fast mode (dimensionless wave speed approaches unity) whereas for plane Poiseuille flow the least stable mode is a slow mode (dimensionless wave speed approaches zero).

As we will see later, experiments show that by suppressing disturbances, pipe flow can be maintained laminar up to very high Reynolds numbers and values of 100 000 have been reported in the literature. Combined with the results from linear stability theory, this has led to the hypothesis (not strictly proven using linear stability theory) that cylindrical Poiseuille flow is stable to all linear disturbances. Thus nonlinear disturbances are needed to bridge the gap between $Re=\infty$ and the experimentally observed value of $Re \approx 2\,300$.

2.3.2 Nonlinear Instability Theory

Several results have been reported in the literature regarding the (weakly) nonlinear instability of cylindrical Poiseuille flow. The scenario of subcritical instability as illustrated in figure 2.2 is not obvious for cylindrical Poiseuille flow since this flow is believed to be stable to all linear disturbances. Rosenblat & Davis (1979) suggested that bifurcations from infinity could indeed be applicable to pipe flow but not in the classical sense. They studied nonlinear diffusion equations as model equations and show that an infinite number of small finite amplitude disturbances bifurcates from infinity and they all are of the same order of magnitude. The spatial structure of the eigenfunctions of the linear stability problem for the null solution (stable) and the spatial structure of the bifurcating solutions are inherently different. Since classical stability theories assume the same spatial structure for the bifurcating solutions as for the eigenfunctions in the linear stability problem, classical theory could be inapplicable to the stability problem of cylindrical Poiseuille flow. This may explain why the present weakly nonlinear stability theories are unable to give accurate quantitative results.

Davey & Nguyen (1971) studied stability of pipe flow to finite amplitude axisymmetric disturbances. They found that the first Landau constant for axisymmetric disturbances is negative, which gives rise to a subcritical bifurcation and an equilibrium amplitude (for an explanation see e.g. Drazin & Reid 1981, pp. 370-376. Disturbances having a smaller amplitude than the equilibrium value will decay while for larger amplitudes the solution will break down at finite time, suggesting a transition to turbulence. Davey & Nguyen found that the minimum energy of a critical center-mode disturbance is smaller than that of a critical disturbance close to the wall. Hence, the flow containing axisymmetric disturbances is expected to become unstable at the center first. In the appendix of Davey & Nguyen's paper, Gill shows that, when using as scaling parameters quantities defined at the center of the pipe, i.e. the kinematic viscosity ν and the curvature of the velocity profile $|d^2W/dr^2|$, the scaling 'laws' for the energy and the wave number found by Davey & Nguyen are indeed correct. The velocity scale of the disturbance is demonstrated to be:

$$w_c \sim (\nu^2 |d^2W/dr^2|)^{\frac{1}{3}} \sim \overline{W} Re^{-\frac{2}{3}} \quad (2.8)$$

These results are extended by Sen *et al.* (1985) to include non-axisymmetric disturbances with azimuthal wave number of unity.

2.3.3 Asymptotic Theory

Smith & Bodonyi (1982) show the existence of finite amplitude neutral modes in Hagen-Poiseuille (pipe) flow with the use of asymptotic theory. Their solution is a helical wave having a fully nonlinear and *three-dimensional* critical layer. In the critical layer, where the wave speed equals the average flow velocity, the disturbance magnitude scales as $\delta = \mathcal{O}(Re^{-1/3})$. Neutral solutions are found only for nondimensional wave speeds $0.248 < c < 1$ and $m = 1$, where m is the azimuthal wave number. They believe that these neutral modes are linked to upper-branch properties. Furthermore, they suggest that in a numerical or experimental study of Hagen-Poiseuille flow instability, the critical disturbance amplitude would be about 1% for $Re=10^6$ (according to scaling as $Re^{-1/3}$) with azimuthal wave number 1. A 3-D plot of the axial disturbance velocity according to Smith & Bodonyi is shown in figure 2.11.

2.3.4 Secondary Instability

For plane Poiseuille flow the secondary instability analysis could be extended below $Re_p=2900$ where no stationary secondary flow exists. For pipe Poiseuille flow no such two-dimensional secondary flow equilibria are known to exist. However, although the analysis is less precise than in plane Poiseuille flow, secondary instability does explain some aspects of cylindrical pipe-flow transition. To be able to study the secondary instability in pipe flow, Orszag & Patera (1983) used direct numerical simulation. The initial velocity field is a two-dimensional (i.e. axisymmetric) least stable wall mode (energy is 4% of the mean flow) combined with a three-dimensional (i.e. non-axisymmetric) linear disturbance. At high Reynolds numbers the strong exponential growth of the 3-D disturbances persists for long times. At low Reynolds numbers this growth is rapidly cut off by the decay of the 2-D disturbances, as is illustrated in figure 2.12. These results suggest that secondary instability mechanisms can play a role in pipe flow transition if large two-dimensional disturbances are initially present.

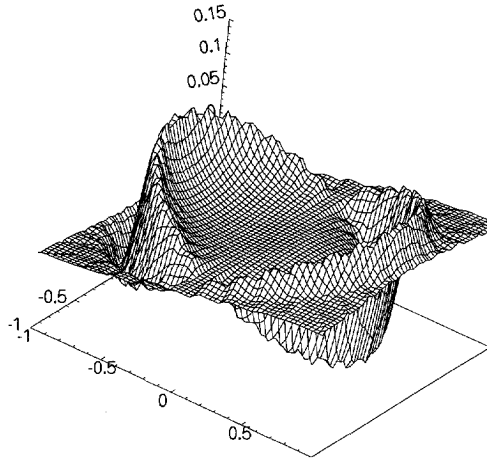


Figure 2.11: A 3-D plot of the axial disturbance velocity of the Smith & Bodonyi type over the cross section of the pipe. Only the solution for $r/R \leq 1$ is meaningful. The solution at the critical surface is singular and as chopped to finite values. From Aanen (1995).

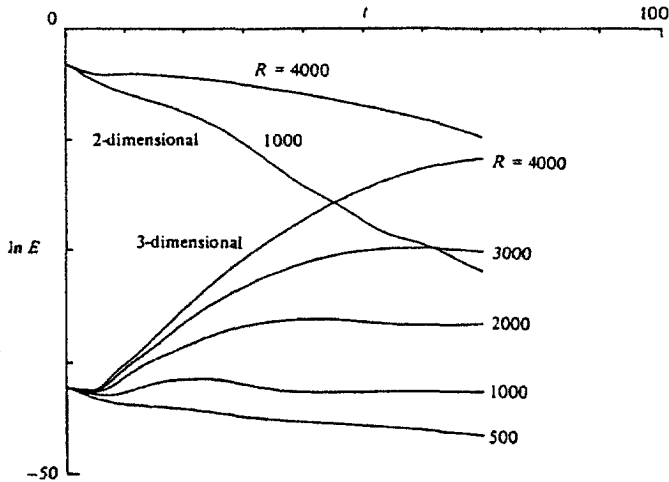


Figure 2.12: Reynolds number dependence of the three-dimensional growth rate for flow at $\alpha = \beta = 1$. Note the very strong two-dimensional decay. From Orszag & Patera (1983).

2.3.5 Experiments

Most of the experiments concerned with pipe-flow transition study triggered transition, i.e. the transition to turbulence is triggered by adding a disturbance to a laminar flow. In this way, the magnitude and other parameters of the disturbances can be varied in a controlled way and their influence on the transition evaluated. A brief review of these experiments will be given below, but first we will discuss the two structures that have been found in transitional pipe flows, i.e. puffs for $Re \lesssim 2700$ and turbulent slugs for $Re \gtrsim 3000$.

Puffs and slugs

The most extensive experimental work on puffs and turbulent slugs has been done by Wygnanski and coworkers (Wygnanski & Champagne 1973, Wygnanski *et al.* 1975, Rubin *et al.* 1980). Recently, Darbyshire & Mullin (1995) extended this work to constant mass-flux flows. Let us recapitulate the main results of these and some other investigations on transitional flow structures in cylindrical pipes.

- The characteristic shape of the centerline-velocity time-trace for a puff and a turbulent slug are sketched in figure 2.13 from which it is clear that the centerline-velocity time-trace is quite different for puffs and turbulent slugs. The leading edge (LE) of a puff is not very well defined, i.e. velocity traces at the pipe axis show a gradual decrease in velocity. The trailing edge (TE) of a puff can be fairly well determined as a sharp increase in velocity. Turbulent slugs have a clear interface at both the leading and trailing edges.

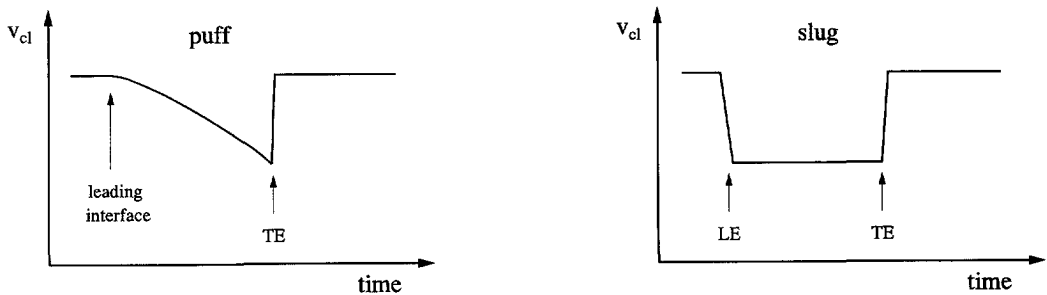


Figure 2.13: Sketch of the centerline-velocity time-trace of a puff and a turbulent slug. LE=leading edge and TE=trailing edge.

- By means of ensemble averaging over many slugs, it is found that profiles of the leading and trailing edge interface of slugs are on average axisymmetric and identical in shape. Also, the ensemble-averaged interfaces extend over approximately 3 pipe diameters, when comparing the axial location of the edge at the centerline and close to the wall, and are blunt around the pipe axis (Wygnanski & Champagne 1973).
- Streamwise velocity fluctuations in a puff are strongest in the central region of the pipe and rather small near the pipe wall whereas for slugs fluctuations are present across the entire cross section of the pipe (Wygnanski & Champagne 1973, Rubin *et al.* 1980). Ensemble averaged streamline patterns for puffs closely resemble that of turbulent slugs

at low Reynolds numbers when only the leading and trailing interfaces are considered (Rubin *et al.* 1980). This suggests that puffs and slugs are related structures.

- Wagnanski & Champagne (1973) have observed puffs in the range $2000 \leq Re \leq 2700$. Wagnanski *et al.* (1975) showed that puffs decay as a function of distance below $Re \approx 2200$. Above $Re \approx 2300$ the puffs grow as they move downstream at almost the bulk velocity. As a puff grows, it can split into new puffs to a maximum of four new puffs at $Re = 2600$. When Re is further increased, the number of puffs decreases until at $Re \approx 2800$ a single turbulent region resembling a turbulent slug was found. This is caused by the merging of puffs which leads to the formation of turbulent slugs (Rubin *et al.* 1980). A schematic diagram of the regions in which puffs and slugs occur is shown in figure 2.14. Recently,

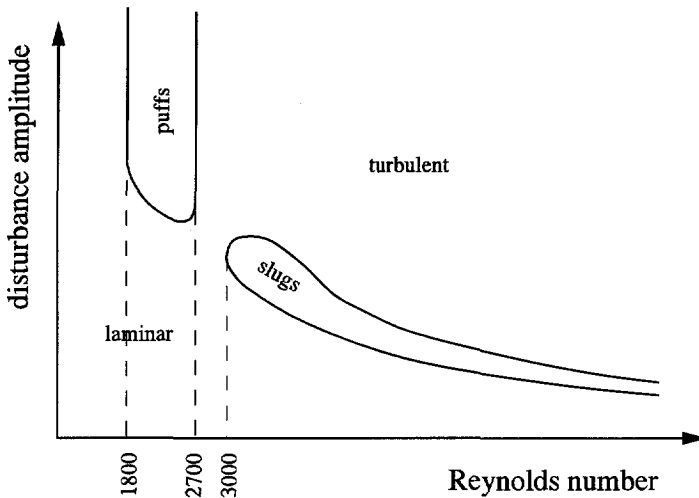


Figure 2.14: Sketch of the regions where the puffs and turbulent slugs can be found.

Darbyshire & Mullin (1995) found that below $Re \approx 1760$ no turbulent structures can be sustained. However, it is not clear from their results whether or not these structures decay when moving downstream and if their relatively short pipe has affected the results. Compared to most of the other experiments, this value is rather small.

- Wagnanski & Champagne (1973) found that in their experiment the puffs originated from large disturbances already present in the inlet of the pipe and that turbulent slugs originate from the developing boundary layer in the pipe inlet. Another method to generate puffs and slugs is to inject fluid in a developing flow (Wagnanski *et al.* 1975) or in a fully developed pipe flow (Rubin *et al.* 1980, Teitgen 1980, and Darbyshire & Mullin 1995). Thus, the puffs and turbulent slugs appear to be universal structures in the sense that they are relatively insensitive to the instability generating source, be it natural or triggered.
- The propagation speed of the leading interface and trailing edge of puffs approach the bulk velocity. In contrast, the leading and trailing edges of slugs propagate at a velocity of

roughly 1.5 and 0.5 times the bulk velocity respectively (however, some dependence with Re is present Wygnanski & Champagne 1973). As a result, the slug strongly grows as it moves downstream and the length of the slug becomes proportional to the distance that it has traveled. The natural transition mechanism in a smooth pipe seems to be a result of the slugs that are generated in the developing boundary layer in the pipe inlet flow; the difference in propagation speed between the leading and trailing edge then results in turbulent slug lengths comparable to the pipe length. For artificially generated puffs and slugs, Teitgen (1980) showed that the propagation speeds of the interfaces are identical to those found in natural transition.

The strong growth of turbulent slugs when moving downstream can also explain why turbulent slugs only appear for a small range of disturbance velocities at a certain location downstream of a source which continuously generates disturbances. For a certain minimum disturbance velocity, transition occurs just upstream of the measurement location and a train of slugs can be observed in e.g. the signal of a Laser Doppler Velocimeter. When the disturbance velocity above this minimum value, the turbulent slugs are generated further upstream leaving them more time to grow before they reach the LDV-position. When the disturbance velocity is large enough such that consecutive slugs can grow and merge, a full turbulent flow will be seen at the measurement station far downstream of the disturbance mechanism.

- In a recent experiment, Darbyshire & Mullin (1995) showed that transition in a constant mass-flux system results in the same puffs and slugs as those found in pressure-driven systems of Wygnanski & Champagne (1973), Wygnanski *et al.* (1975), and Rubin *et al.* (1980), in which the Reynolds number varies. From this they conclude that relaminarization at the trailing edge of puffs and slugs is not related to the decrease in Reynolds number as a result of the increase in flow resistance due to turbulence. We note that this mechanism has been put forward as an explanation for the relaminarization in the trailing interfaces of puffs and slugs and is thus has been shown to be false. The facility that we used is also a constant mass-flux system.

In conclusion we may summarize that these literature results show that in the range $2000 \lesssim Re \lesssim 3500$ puffs and turbulent slugs are related structures. Puffs occur for the lower Reynolds number ranges ($Re \lesssim 2700$). When the Reynolds number is increased to e.g. $Re = 3000$, they transform into slugs, a process which consist of splitting, growing, and merging of puffs. Perhaps, every slug is born as a puff but is very rapidly transformed into a turbulent slug provided that the Reynolds number is large enough to permit such transformation.

Triggered transition

In order to investigate the magnitude of the disturbance that is needed to trigger transition to turbulence, well-controlled disturbances are added to a laminar flow. The response of the flow is monitored by means of pressure gauges, LDV, and injection of dye. A more detailed description of the various experimental facilities that have been used in the past to perform transition experiments, is given in the chapter on the design of our experimental pipe-flow facility in section 5.2. Here, some main results will be discussed.

Leite (1959) performed experiments in a horizontal pipe with a length of 700 diameters, operated with air. The flow was found to be stable up to Reynolds numbers of 20 000 (the maximum capacity of the system). Due to thermal problems, his velocity profile was not parabolic, and he used a heating element in the top-half the pipe to generate a symmetric profile. The background turbulence level was about 0.01%. Leite introduced small disturbances by oscillating a cylindrical sleeve at the wall. The amplitude of the disturbance was in the order of 0.1% to 1% of the maximum velocity. No transition to turbulence was found and all disturbances decayed. The disturbances were not axisymmetric and some evidence was given that the non-axisymmetric part of the disturbance decays more rapidly than the axisymmetric part. Large disturbances were introduced by a ring airfoil which triggered transition for $Re \geq 8000$.

Fox *et al.* (1968) studied the stability of pipe flow to non-axisymmetric disturbances for a range of frequencies with $2000 \leq Re \leq 4000$. The maximum disturbance velocity was less than 2% of the centerline velocity of the laminar flow. They find a cigar-shaped instability region as is shown in figure 2.15. From their results they estimate the minimum Reynolds number to be $Re \approx 2130$.

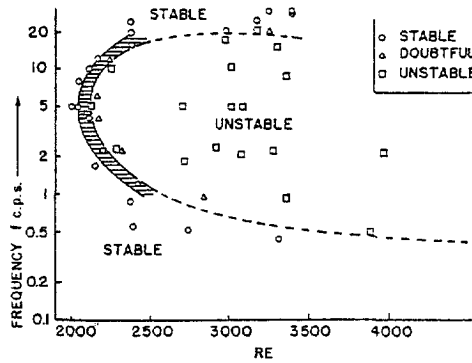


Figure 2.15: Neutral stability curve in the frequency–Reynolds number plane. From Fox *et al.* (1968).

Recently, Darbyshire & Mullin (1995) used a constant-mass-flux system to investigate transition to turbulence and concentrated their experiments in the range $1700 \leq Re \leq 2800$. Comparing these results with several measurements they performed up to $Re \leq 10000$, a significant increase in critical disturbance amplitude was found when the Reynolds number was decreased below $Re \approx 2800$. They do not find a large dependence on the actual form of the disturbance. Darbyshire & Mullin use a single disturbance as opposed to a continuous forcing. No turbulent structures were sustained below $Re \approx 1760$. However, it is not clear from their paper whether puffs decay for $Re \lesssim 2200$ as is found by Wygnanski *et al.* (1975).

2.4 Transient Growth

From the discussions above, both for plane and cylindrical Poiseuille flow, we have seen that linear stability theory cannot predict the transition Reynolds numbers which are found in experiments. For plane Poiseuille flow, nonlinear theory and secondary instability mechanisms appear to be able to describe the development of structures found in experiments. However,

secondary instabilities require the presence of 2-D nonlinear waves which decay for $Re \lesssim 2640$ and this value is much larger than the experimentally observed Reynolds numbers. For cylindrical Poiseuille flow, the discrepancy between theory and experiments is even larger. This is mainly related to the stability of the pipe flow to linear disturbances. Due to this linear stability, the scenario of secondary instability cannot be applied to the cylindrical pipe and any theory must by necessity be fully nonlinear.

In recent years, the mechanism known as transient growth is proposed as a possible explanation which could bridge the gap between theory and experiments. In the remainder of this section, the basic ideas behind this theory are briefly recapitulated and some results are discussed. An excellent introduction on transient growth and related effects is given by Trefethen *et al.* (1993).

The mechanism of transient growth has its origin in the property of the linear operators. For instance, the linear operators that arise in the Bénard convection and Taylor–Couette flow have orthogonal eigenfunctions and predictions of eigenvalue analysis are in good agreement with experiments. However, for the plane and cylindrical Poiseuille flow, the eigenfunctions of the linear operator are not orthogonal. For these flows, extremely large amplification of small disturbances can occur through interaction of the non-orthogonal eigenfunctions. Plane and cylindrical Poiseuille flow as well as Couette flow fall into these categories and amplification factors of many thousands are reported. The flow features associated with this amplification process have a distinctive form: A perturbation to the velocity field in the form of a streamwise vortex evolves into a higher amplitude streamwise streak, i.e. an elongated region of high or low velocity. These disturbances are essentially three dimensional and thus cannot be captured by the commonly used two-dimensional analysis, based on the Squires theorem. The streaks are not eigenmodes of the linearized flow problem but they are called pseudomodes.

An unstable eigenvalue of a linear operator is a value for which the accompanying eigenfunctions can be amplified unboundedly. If one replaces infinity with $1/\epsilon$, we obtain an “ ϵ -pseudoeigenvalue” and the corresponding “ ϵ -pseudomode”. Thus, if ϵ is small, an ϵ -pseudomode can grow to large values. At $Re=5\,000$, for example, a streamwise streak is an ϵ -pseudomode of the linearized plane Poiseuille flow for $\epsilon \approx 1.2 \cdot 10^{-5}$. This shows that such a streak can be excited by a streamwise vortex that is five orders of magnitude weaker. Small disturbances, that are linearly stable, can grow by several orders of magnitude, but also pseudoresonance can occur. For an orthogonal linear operator, resonance occurs when the frequency is close to an eigenvalue. For non-orthogonal operators, strong resonance can occur even when the frequency is far from an eigenvalue. When a nonlinear term feeds back some of the energy to the original pseudomode, even larger growth can occur than for linear disturbances. Combined, these mechanisms may cause a very small disturbance to grow to a magnitude where it can trigger transition to turbulence.

Quite a number of papers have been published already on transient growth in plane and cylindrical Poiseuille flow. Here, we will only summarize some of the main results for cylindrical Poiseuille flow. Bergström (1993) shows analytically that the largest amplification through transient growth is obtained for disturbances with zero streamwise wave number and with an azimuthal wave number of unity. Axisymmetric disturbances display almost no transient growth. Small disturbances can grow four to five orders in magnitude (O’Sullivan & Breuer 1994a). Transient growth attains a maximum at dimensionless times $t/Re \approx 0.05$ and the amplitude

magnification scales with Re both for $\alpha=0$ (Bergström) and for non-zero α . To continue the calculations into the nonlinear range, O'Sullivan & Breuer (1994b) perform a direct numerical simulation of a pipe flow at $Re=2200$. They study the transient growth of a pair of helical waves with long streamwise wave length. For the calculation with the largest disturbance that they use, i.e. the *energy* is $1.6 \cdot 10^{-3}$ compared to the basic flow, they can generate transition and they find a structure resembling a puff. However, the Reynolds number is just too low and the flow seems to decay to a laminar state. This is in good agreement with the results by Wygnanski *et al.* (1975) on the puffs, who show that the puffs only grow for $Re \gtrsim 2300$. A higher initial disturbance does not always result in a higher disturbance energy peak. The reason is that the disturbances displaying transient growth become so large such that nonlinear effects become important. This is caused by the transfer of energy from the mean flow to the disturbance which has an adverse effect for the transient growth process.

Schmid & Henningson (1994) construct the shape of the linear disturbance that gives the maximum possible transient growth. For $\alpha=0$, such a disturbance is a pair of counter-rotating vortices near the centerline embedded in a strongly azimuthal flow near the wall. For $\alpha=1$, the optimal disturbance consists of a swirling flow field leading to an overall helical motion. These shapes are rather complex and difficult to realize in an experiment. Nevertheless, also other disturbances that do not attain the maximum possible growth, still show very large amplification. Transient growth of experimental disturbances could therefore play an important role in transition to turbulence in pipe flow. More research, in particular experimental in nature, is needed to test the importance of transient growth for laminar-turbulent transition.

2.5 Summary & Discussion

For plane Poiseuille flow, the results of stability theory, experiments, and DNS have led to a picture which is fairly clear and one may say that many aspects of transition to turbulence are understood. Although in experiments not all phases can be separated, the transition process to turbulence in a low disturbance environment is thought to be given by the following sequence:

1. The basic parabolic profile is disturbed with two-dimensional TS-waves which grow slowly. The critical Reynolds number is 5772 for infinitesimal TS-waves, but finite amplitude (nonlinear) TS-waves can exist down to $Re \approx 2600$ (i.e. based on flow rate), and $Re_p = 2900$ (based on pressure drop). For $2600 < Re < 5772$, threshold amplitudes exist (lower branch of the stability curve) above which the solution grows and saturates as an upper-branch disturbance.
2. The saturated TS-waves are subject to three-dimensional instabilities which are characterized by much larger growth rates than TS-waves. These so called secondary instabilities form lambda-shaped vortices and cause layers with high shear rates.
3. These three-dimensional structures do not saturate and they eventually break down into small scale structures which eventually result in fully developed turbulence.

Most of the characteristics described above, have also been found in experiments. However, the scenario described above relies on the existence of saturated nonlinear 2-D disturbances, which do not exist for $Re \lesssim 2600$ while transition to turbulence is found for $Re \gtrsim 1000$. Perhaps

the concept of transient growth can provide large disturbances which slowly decay but on which other disturbances can grow and trigger transition.

The results for plane Poiseuille flow cannot be applied to cylindrical pipe flow. A cylindrical pipe flow is generally believed to be linearly stable to all 2-D and 3-D disturbances. The route of infinitesimal disturbances that grow exponentially to become nonlinearly saturated and on which secondary instabilities can grow cannot exist. No 2-D saturated disturbances have been observed in pipe flow. Nonetheless, calculations of Orszag & Patera (1983) in which they artificially prevent the 2-D disturbances from decaying, do show that 3-D disturbances can grow in such flows. Another possible mechanism is transient growth and direct numerical simulations of this phenomenon may be of help to bridge the large gap between theory and experiments. The results presented by O'Sullivan & Breuer (1994b) look very promising in this respect.

Experiments show that so-called puffs and turbulent slugs are the characteristic flow structures that are present in transitional pipe flows. The mechanisms involved the generation and propagation of these structures are still far from being understood. Also, only limited data are available regarding frequency and Reynolds number dependence of the threshold disturbance needed that is needed to trigger transition. Much work remains to be done in this area.

In the next chapter we will give a brief review of the literature related to laminar-turbulent transition for non-Newtonian fluids.

Chapter 3

Non-Newtonian flow stability

Abstract

In this chapter we briefly review the literature that is related to stability and transition for non-Newtonian fluids. Most of the material can be classified into two categories; the stability theory/simulations for plane Poiseuille flow, and transition experiments in pipe Poiseuille flow. With regard to the latter, it should be stated that only a limited amount of literature on non-Newtonian pipe flows deals specifically with transition. Most of the experiments focus on drag reduction by polymer additives and only a few brief remarks are devoted to transition.

Also, a very extensive body of work is present for stability measurements and theory at extremely low Reynolds numbers. Such work is commonly associated with concentrated polymer solutions and polymer melts and their manufacturing processes like extrusion. As these flows are extremely viscous and elastic, but generally not turbulent we will disregard them in this review.

3.1 Introduction

The term 'Newtonian fluid' is used for fluids that obey the constitutive equation Eq. 18.4-1 of Transport Phenomena (Bird *et al.* 1960, p. 565). All other fluids are 'non-Newtonian fluids'. By stating that a fluid does not behave as a Newtonian one does not give a clue how these non-Newtonian fluids then behave. When one is used to Newtonian fluids, non-Newtonian fluids can be regarded to misbehave, i.e. the effects encountered in non-Newtonian fluids are very often radically different from Newtonian flows. Water and air are well-known Newtonian fluids and their viscosity is constant, i.e. independent of shear rate. In contrast, most non-Newtonian fluids have a viscosity that depends on the shear rate. Other, more spectacular properties of non-Newtonian fluids are rod-climbing and the tubeless-siphon effects. The first effect occurs when a rod is rotated in a beaker. Strongly elastic fluids can then climb the rod whereas no climbing occurs for Newtonian fluids. The second effect applies to a siphon when it is retracted above the free surface. The flow for Newtonian fluids will then stop whereas for strongly elastic fluids it will continue to flow! Both effects are caused by the elasticity which is present in some non-Newtonian fluids. These elastic fluids can be obtained by dissolving several percent of a high-molecular weight polymer in a solvent such as water. Another surprising effect occurs when dissolving a minute amount of these polymers (typically 0.001%). In that case, the drag in a turbulent flow can be decreased by as much as 80%. For a more extensive review of such differences in behavior between Newtonian and non-Newtonian fluids see Bird *et al.* (1987a).

Non-Newtonian fluids could be defined in general terms as all materials that display behavior in between that of a Newtonian fluid and a purely elastic solid. The field of fluid mechanics

involved with the description of non-Newtonian fluid behavior is called rheology¹. Besides the term non-Newtonian fluids, very often the name 'visco-elastic' fluids is used. This stresses the presence in the fluid of both viscous and elastic behavior. Which of the two prevails, depends strongly on the type and rate of deformation. On the other hand, the term 'generalized Newtonian' fluid is used for models of fluids that exhibit only a shear-rate-dependent viscosity behavior of the fluid and no elasticity. These models are particularly useful for laminar flow in simple geometries. The power-law model and the Carreau-model are well known examples of generalized Newtonian models.

To illustrate the wide variety of flow behavior that can be found for non-Newtonian fluids, even in a non-complex flow geometry like a straight pipe, we will begin with a brief overview of the transition experiments in pipe flows in section 3.2. In particular, the difference in flow behavior for polymers and fibers will be addressed. Related to this is the effect of the conformation of the polymer. Then, in section 3.3, the results are reviewed obtained from theory and numerical simulations. Following the trend in literature, this section will almost entirely deal with plane Poiseuille flow. Finally, a brief discussion follows in section 3.4 in which we present the ideas that form the basis of the research direction in the present thesis.

3.2 Experimental

3.2.1 Polymer solutions

Already for several decades, researchers have been doing flow rate–pressure drop measurements for non-Newtonian fluids. The motivation is the shear-thinning behavior and the drag-reduction found in dilute polymer solutions. The latter is known since 1949 and which is still an object of study (see den Toonder (1995)). For Newtonian fluids, data on pressure drop/flow rate are commonly presented in a Moody diagram, i.e. a dimensionless pressure drop as a function of dimensionless flow rate in the form of a Reynolds number. The details of the Moody diagram will be further discussed in section 5.12 and 7.4 for Newtonian fluids and non-Newtonian fluids respectively. In 1955 Metzner & Reed introduced a generalized Reynolds number for shear thinning fluids described with the power-law model (for a definition see also section 7.4.2) which collapsed all laminar flow data to the Newtonian curve. In figure 3.1 we show data of Dodge & Metzner (1959) of a 0.3% CarboxyMethylCellulose (CMC) solution. For laminar flow, because of the choice of the modified Reynolds number, the laminar flow data are forced to fall on the Newtonian laminar curve ($f = 16/Re$).

However, it is also clear that for turbulent flow, the data of this CMC solution do not fall on the Newtonian flow curve and that different curves are obtained when varying the diameter of the pipe. With decreasing pipe diameter, the reduction in drag when compared to the Newtonian case increases and also a delay of transition to turbulence towards higher generalized Reynolds numbers occurs. The fact that different curves for the same fluid are found is an indication that the Reynolds number alone is no longer sufficient to completely characterize the flow behavior, as is the case for Newtonian fluids. At least one additional parameter besides a Reynolds number is needed to describe this flow.

Other evidence is given by White & McEligot (1970) used the long unbranched polymers Polyox WSR-35 (molecular weight $MW=2 \cdot 10^5$), Polyox WSR-301 ($MW=4 \cdot 10^6$) and Separan

¹Rheology is not restricted to the behavior of fluids but includes also the behavior of solid materials.

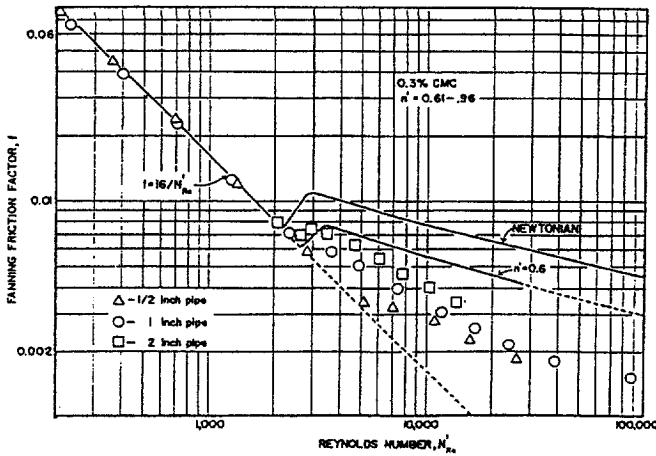


Figure 3.1: Flow data of CMC-solution for 3 pipe diameters illustrating the influence of the pipe diameter. Note that for Newtonian fluids no such dependence on pipe diameter is present. From Dodge & Metzner (1959).

AP-30 ($MW=2 - 3 \cdot 10^6$) for their transition experiments. Some of their results are shown in figure 3.2. They detected transition to turbulence from the usual jump in the Moody diagram and by using oscillograph traces of the pressure measurements. These two detection criteria were found to give approximately the same result.

In order to minimize degradation effects, White & McEligot used a syringe rather than a pump to achieve the desired flow rate. The diameter of their pipe section was 0.0235 inch (0.60 mm). The Moody diagrams of Polyox WSR-35 and Separan AP-30 are displayed in figures 3.2a and b respectively. As can be seen, for Polyox WSR-35 with the small molecular weight, drag reduction can be observed to increase with higher concentrations but no delay in transition Reynolds number is found. For Separan AP-30 (and Polyox WSR-301 not shown here), which have both approximately a ten times larger molecular weight, not only more drag reduction is found in the turbulent flow regime but also a delay in transition Reynolds number which increases with increasing concentration. By mixing polymers with different molecular weights, White & McEligot show that the delay in transition is dominated by the higher molecular weight polymers, while the effect on drag reduction is roughly additive.

Chung & Graeble (1972) used Polyox WSR-301 in their transition experiments. They also find a delay in transition Reynolds number. However, the transition Reynolds number increases most for the solutions having a small concentration of polymer, which is different from the results by White & McEligot. From this experimental evidence, it seems as if a delay in laminar-turbulent transition for dilute polymer solutions is found only for height molecular weight in small pipe diameters, typically less than 1 cm (Castro & Squire 1967, White & McEligot 1970, Chung & Graebel 1972, Wójs 1993). A delay in transition has also been reported for concentrated solutions of low molecular weight polymers (e.g. Sá Pereira & Pinho 1994).

A very different behavior was found by Paterson & Abernathy (1972) who used a smooth-nozzle inlet for a 6.3 mm pipe. For water, the nozzle inlet provides a smooth inflow and the

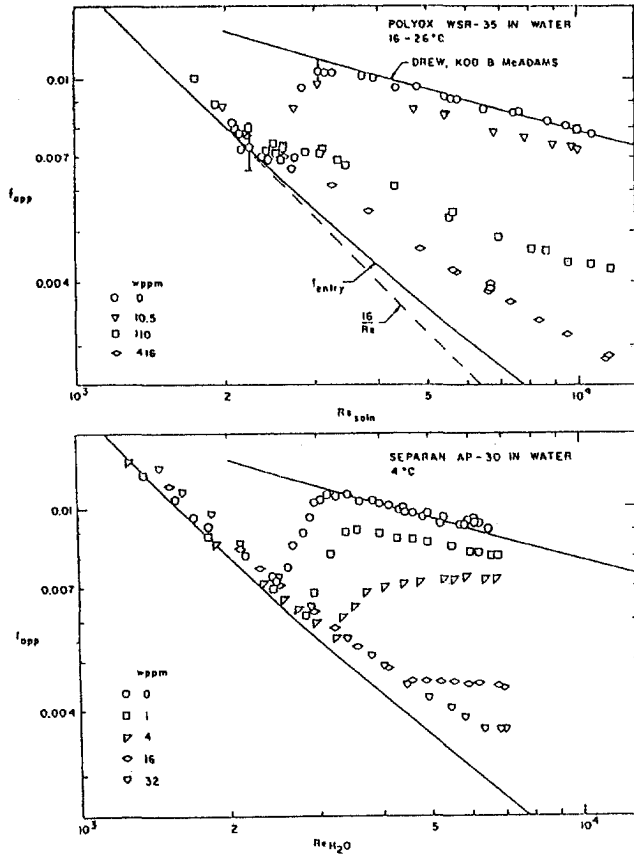


Figure 3.2: Flow measurements in a 0.6 mm diameter pipe for two linear unbranched polymers of which Separan has a ten times larger molecular weight. From White & McEligot (1970).

flow remained laminar till $Re \approx 10\,000$. Adding polyethylene polymers results in a decrease in natural transition Reynolds number. The effect of decrease in natural transition Re number increases with the polymer concentration. However, using a pipe inlet with squared corners, they found that the transition Reynolds numbers for all polymer solution were approximately the same and equal to that found for water. Paterson & Abernathy have also studied the propagation velocity of the leading and trailing edges of turbulent slugs in polymer flows and they found good agreement with the values reported for Newtonian fluids.

A transition Reynolds number *smaller* than the Newtonian minimum of approximately 2 300 is reported by Forame *et al.* (1972). This effect is known as 'early transition'. Earlier studies have also reported this effect for dilute solutions in capillary tubes. By increasing the viscosity of the solvent, Forame *et al.* find onset of turbulence for Reynolds numbers as low as 500 in pipes of approximately 6 mm diameter. The transition Reynolds number seems only weakly dependent on polymer concentration but increases almost linearly with the viscosity. Zakin *et al.* (1977) performed Laser Doppler Velocimetry (LDV) measurements of early turbulence and show that the mean velocity profile becomes progressively flatter with increasing flow rate. The rms of the axial velocity fluctuations is about half of the value for turbulent flow of Newtonian fluids. Recently, early turbulence has been reported in a 26.2 mm pipe for 200 to 1 000 ppm solutions of polyacrylamide in deionized water (Li & McCarthy 1995). They used time averaged nuclear magnetic resonance imaging techniques to study the velocity profile.

Transition by controlled disturbances in non-Newtonian flow has been performed by Berman & Cooper (1972) who studied the response of 20 ppm solutions of Separan AP-30 and Polyox WSR-301 to disturbances generated by an oscillating sleeve at the wall. The response of the dilute polymer solutions to the sleeve is different when compared to water. Fewer higher frequencies were generated in the wake. They found that the wake spreads faster in water and that the turbulence far downstream was less developed for the polymer solutions. Since they performed measurements for $Re \leq 2\,000$, proper transition could not be studied since the turbulence decayed far downstream.

Mizunuma & Kato (1988) investigated the transition in plane Poiseuille flow of a 200 ppm Separan AP-30 solution in water and found no delay in transition. They also found that polymers reduce the spreading angle of an artificially generated turbulent spot.

With respect to the extent of the transition region, i.e. the range of Reynolds number in which the flow changes from laminar to fully turbulent, different effects have been reported. Park *et al.* (1989) find a shorter transition regime for a non-Newtonian slurry whereas Pinho & Whitelaw (1990) find a delay in transition and an extended transition region for a sodium CMC solution.

3.2.2 Coiled vs. stretched conformation

Several pieces of evidence point to the importance of polymer conformation in flow dynamics. In drag reduction research of dilute polymer solutions, polyethyleneoxide (Polyox family by Union Carbide) and polyacrylamide (Separan family by Floerger/France and previously Dow Chemical) are commonly used. These polymers are forced to have, on the average, a randomly-coiled conformation in the rest state where no deformation is imposed. Virk (1975) and Virk & Wagger (1990) show some very interesting results using a partially hydrolyzed polyacrylamide (PAMH) of high molecular weight. In the absence of salt these polymers are forced to have,

on the average, an extended conformation whereas adding salt forces the polymers to assume the randomly-coiled conformation. They show that the configuration of the polymer has a very large effect on the drag reduction capability, as is displayed in figures 3.3 and 3.4. Since extended polymers also seem to show quite different behavior from randomly coiled polymers, Virk introduced the terms 'type-A' and 'type-B' to distinguish between the drag reduction behavior of randomly-coiled and extended polymers respectively.

To summarize here both cases, as can be expected, in the presence of salt, PAMH displays the same behavior that we know for random coiled polymers; known as drag reduction type-A (see figure 3.3). For this type of drag reduction the transition point is located at the same Reynolds number as for the solvent ($Re_c \approx 2300$). In the turbulent flow regime, the Blasius friction line is followed up to the point of onset of drag reduction. When Prandtl-Kármán (P-K) coordinates are being used, i.e. $1/\sqrt{f}$ as a function of $Re\sqrt{f}$, the Prandtl-Kármán line (labeled 'N' in figures 3.3 and 3.4) is followed up to the onset point and then the lines fan out with increasing slope for higher concentrations. Drag reduction increases with increasing $Re\sqrt{f}$. In type-B drag reduction, a family of polymer solutions yields segments that are roughly parallel to, but displaced upwards from the P-K line. The drag reduction increases in this case with increasing concentration but is essentially independent of $Re\sqrt{f}$. Type-B drag reduction is commonly found for fiber solutions, soaps, clays and extended polyelectrolytes such as PAMH and is displayed in figure 3.4.

Besides effects on drag reduction, the polymer conformation also affects the viscosity. Interestingly enough, the solutions in the presence of salt leading to a coiled polymer conformation show hardly any increase in viscosity when compared to the solvent while in the absence of salt, the polymers are forced to have the extended conformation and cause a significant increase in viscosity compared with the solvent. In the case of extended polymers, the laminar flow curve stays parallel to the solvent line, this indicates that the indeed the viscosity is increased but no shear thinning is present. For very low concentrations (<2 ppm), no appreciable difference in transition Reynolds number can be found. If for the higher concentrations the curves are corrected for the increase in viscosity, i.e. shifting the curves to the left in the P-K plot until they collapse on the solvent line, then for the 10 ppm solution the transition Reynolds number can be estimated to be 6500. After this correction, the flow curves are also in between the laminar flow curve and the maximum drag reduction asymptote named after Virk. Without correction, the curves seem to touch the maximum drag reduction asymptote. Virk (1975) does not mention this delay in transition. Note that Virk & Wagger (1990) find a delay in transition for dilute polymer solution in a relatively large diameter pipe (14.6 mm).

PAMH is not the only polymer showing type-B drag reduction. Another example is Xanthan gum which is a high-molecular weight polysaccharide which has a rigid helical structure. Bewersdorff & Singh (1988) used Xanthan gum in concentrations ranging from 250 to 1000 ppm in pipe-flow experiments. Such solutions show a distinct shear thinning behavior and they use the viscosity at the wall in their definition of Re in the Moody diagram. A clear delay in transition is found which increases with concentration as is shown in figure 3.5.

The configuration of Xanthan gum is found to be also sensitive to the salt concentration, although not as sensitive as PAMH. A delay in transition for Xanthan gum without salt has been also found by Rochefort & Middleman (1985) in a glycerin/water mixture in a 2.4 mm pipe. Adding salt decreases the delay.

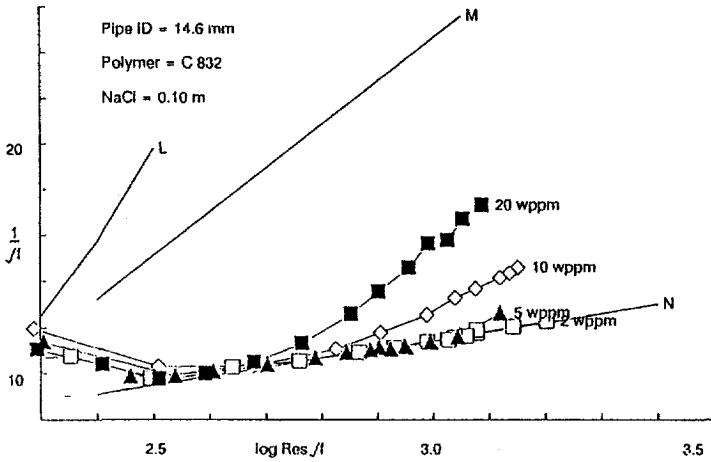


Figure 3.3: Type-A drag reduction for PAMH in the presence of salt: randomly coiled polymer configuration. From Virk & Wagger (1990). The lines labeled 'L', 'N', and 'M' represent laminar Poiseuille flow, turbulent pipe flow, and Virk's maximum drag-reduction asymptote for polymer solutions respectively.

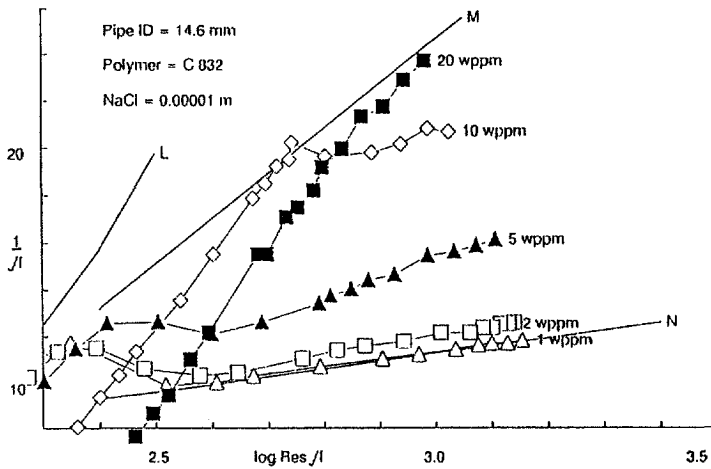


Figure 3.4: Type-B drag reduction for PAMH in the absence of salt: extended polymer conformation. From Virk & Wagger (1990).

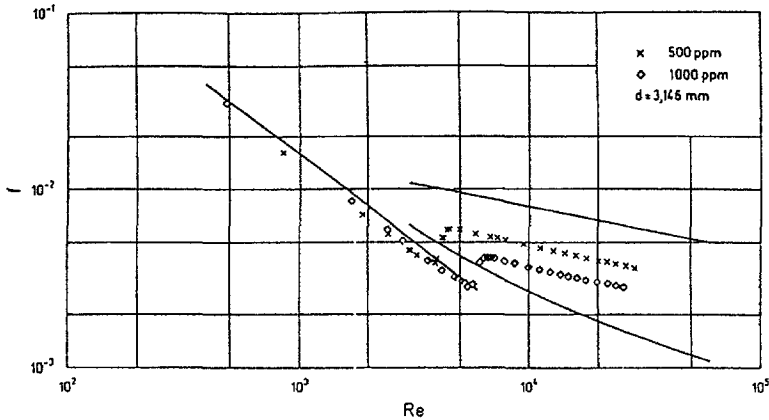


Figure 3.5: Moody diagram for Xanthan gum. From Bewersdorff & Singh Bewersdorff & Singh 1988.

3.2.3 Fibers

We have seen that extended polymers seem to be able to delay the transition. Taking this idea one step further, one could speculate that fibers will also show similar behavior to stretched polymers. For a 5000 ppm solution of asbestos fibers, Vaseleski & Metzner (1974) indeed find a delay in transition. The flow is laminar till $Re > 2 \cdot 10^5$, corresponding to the maximum flow rate of the experimental setup. However, they use the solvent viscosity in their definition of the Reynolds number. Estimating the viscosity from their data to be 12 times as high as the solvent, results in a delay of transition to $Re > 16\,000$. In contrast to polymer solutions, they do not find a dependence of drag reduction on the pipe diameter, indicating that fibers and extended polymers show similar but not identical flow behavior.

Rod-like particles can also be generated by some surface active agents (surfactants). Above a certain concentration, some surfactants form so-called rod-like micelles. The advantage of surfactants is that they can recuperate from mechanical degradation, something polymers are unable to do. Bewersdorff (1990) is able to delay transition till $Re = 4\,000 - 5\,000$. Sabadell (1988) who used rod-like micelles in a boundary layer flow, showed that the surfactants suppressed the development of a turbulent spot which results in a delay in transition.

3.3 Stability Analysis

3.3.1 Introduction

In this section we review the stability calculations and their results that have been reported in the literature. Basically, stability analysis and more in particular a linear stability analysis for non-Newtonian fluid models is not very different from the Newtonian case. Again, the behavior is studied for infinitesimal disturbances superimposed on steady state base flows. In the linear case the equations of motion are linearized and an equation similar to the Orr-Sommerfeld equation is found. For some simple visco-elastic fluid models this exercise has been performed and the results will be reviewed in section 3.3.2, together with some additional nonlinear analyses.

The experiments discussed in the previous section, have shown the influence of the conformation of the polymer on the drag reduction and transition. Long rigid molecules seem to be more effective for transition delay than flexible molecules. It is thus interesting to look at the stability analysis for rods suspended in a fluid. This is the subject of section 3.3.3.

3.3.2 Visco-elastic fluids

On of the earliest attempts to study the stability of visco-elastic fluids is work by Walters (1962). He shows that the derivation of a generalized Orr-Sommerfeld equation is possible only for fluids having a short memory. For plane Poiseuille flow, elasticity is found to have a destabilizing effect, viz. the critical Reynolds number above which linear disturbances can grow decreases with increasing elasticity (Chan Man Fong & Walters 1965). This result has been confirmed many times.

Most of the stability calculations have been performed for plane Poiseuille flow and for one of the most simple visco-elastic fluids: the Upper Convected Maxwell (UCM) model. The UCM model describes the relationship between the extra-stress tensor $\underline{\underline{\tau}}$ and the rate-of-deformation tensor $\underline{\underline{\dot{\gamma}}}$ in the following way:

$$\underline{\underline{\tau}} + \lambda \underline{\underline{\overset{\nabla}{\tau}}} = \eta \underline{\underline{\dot{\gamma}}} \quad (3.1)$$

Here, λ is a time constant, often called the relaxation time, and η is the viscosity taken to be constant. Thus, the Maxwell model does not describe shear thinning behavior which is found for most non-Newtonian fluids. As a result, the UCM model gives as laminar solution the parabolic velocity profile in plane Poiseuille flow. The time derivative ($\overset{\nabla}{\tau}$) in equation 3.1 is a special so-called upper-convected time derivative (Bird *et al.* 1987a, p. 342) which is needed to ensure objectivity of the stress. For a more detailed discussion of the Maxwell model we refer to the next chapter, section 4.3.

For the discussion of the literature results on stability we need only to know two dimensionless numbers in addition to the Reynolds number. Both can be defined for a Maxwell fluid flow. They are the elasticity number E and the Weissenberg number We :

$$We = \frac{U\lambda}{h} \quad E = \frac{\eta\lambda}{\rho h^2} \quad (3.2)$$

where U is the centerline velocity and h is the channel half-width. The relationship between the Reynolds number and these two numbers is:

$$We = Re \cdot E \quad (3.3)$$

The Weissenberg number is the ratio of the relaxation time of the polymer to the time-scale of the flow. The elasticity number can be interpreted as the ratio of elastic forces to viscous forces. Note that for a given flow geometry, E depends solely on fluid parameters. A line for constant E can therefore be interpreted as a line describing the behavior of a polymer solution in a given flow geometry.

For plane Poiseuille flow, Porteous & Denn (1972a) calculated the neutral curves for linear disturbances for $E=0$ (Newtonian) up to $E=5 \cdot 10^{-3}$, i.e. $We \approx 10$. They find a continuing destabilization with increasing E . For $E \geq 2.5 \cdot 10^{-3}$, they find second and third instability

modes. The results up to $E=10^{-3}$ have been confirmed by for example Ho & Denn (1978) and Sureshkumar & Beris (1995b). The latter also find the second eigenmodes. However, as opposed to the monotonic decrease in critical Reynolds found by Porteous & Denn, Sureshkumar & Beris find a minimum of $Re_c \approx 1670$ for $E \approx 2.5 \cdot 10^{-3}$, as is illustrated in figure 3.6.

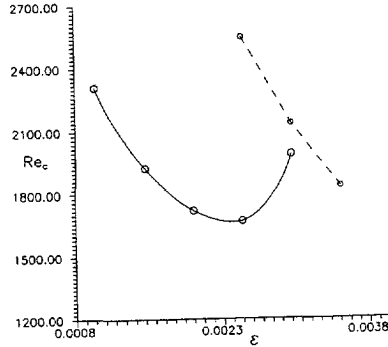


Figure 3.6: The critical Reynolds number as a function of the elasticity number for the Upper Convected Maxwell model. Solid lines: first eigenfunction, dashed lines: second eigenfunction. Here ε is equal to our elasticity number E . Results from Sureshkumar & Beris (1995b).

The corresponding Weissenberg number of the minimum value is $We \approx 4$, i.e. a stabilizing effect occurs for linear disturbances once the flow time-scale is more than four times the relaxation time of the fluid. Sureshkumar & Beris (1995b) also studied the Oldroyd-B model and the Chilcott-Rallison model. The Oldroyd-B model has an additional solvent viscosity which has a pronounced stabilizing effect on the flow. Introducing finite extensibility of the polymer through the Chilcott-Rallison model results in further stabilization. Note that all these calculations have been performed for two-dimensional disturbances. This is based on the Squire's theorem which states that it is sufficient to study 2-D linear disturbances. Proof for the applicability of the Squire's theorem to non-Newtonian fluids is possible for an Oldroyd-B fluid (Maulik 1989) but not for the Chilcott-Rallison model, so care should be taken. Since the UCM model is a special case of the Oldroyd-B fluid, calculations for 2-D disturbances give the correct picture of the linear stability behavior.

Porteous & Denn (1972b) continued their work on linear stability to weakly non-linear disturbances. Also for nonlinear disturbances, elasticity was found to destabilize the flow when compared to Newtonian fluids as shown in figure 3.7 where the critical Reynolds number is plotted as a function of the disturbance amplitude for various elasticity numbers. However, when the results shown in this figure for $E=0$ and $E=10^{-4}$ are extrapolated to larger disturbance amplitudes, the visco-elastic fluid may be more stable than Newtonian fluids. Sureshkumar & Beris (1995a) have applied a three-dimensional numerical code to perform direct numerical simulations for visco-elastic fluids. Unfortunately, their calculations become numerically unstable for high Weissenberg values. By introducing a rather large artificial stress diffusivity, they can suppress numerical instabilities.

Another three-dimensional calculation for the Oldroyd-B fluid is reported by Maulik (1989). This computations also suffered from numerical instabilities for high Weissenberg numbers.

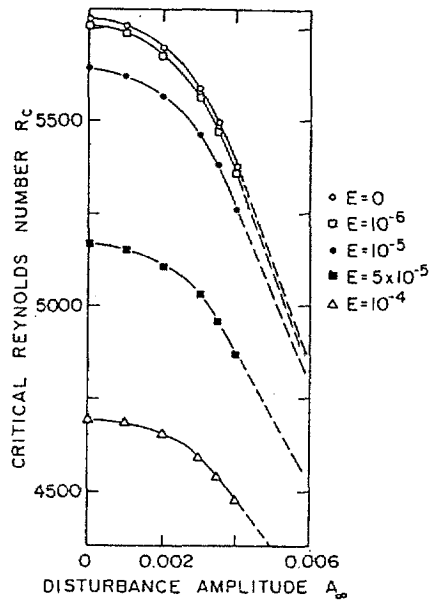


Figure 3.7: Critical Reynolds number as a function of disturbance amplitude for a second order fluid. From Porteous & Denn (1972b).

For a modest value of the elasticity parameter, Maulik simulated a K-type transition (see section 2.2.3) and no qualitative difference from the Newtonian behavior is found.

With respect to cylindrical pipe flows, we may refer to Hansen (1973) who performed a stability analysis of axisymmetric disturbances. To simplify the analysis, he considers only disturbances with high phase velocities for the Oldroyd-B model (which also includes the Maxwell model). Hansen is able to obtain an analytical expression which is valid for all wave numbers, pipe diameters, and fluid parameters. All axisymmetric disturbances decay, but when the elasticity number is small enough, the decay rate of the disturbance is larger than that for the Newtonian fluid, i.e. elasticity has a stabilizing effect. However, when the elasticity number is increased above a certain value (depending on the wave number), the decay rate is smaller than for disturbances in a Newtonian fluid and elasticity becomes destabilizing.

So far, all models that have been studied are visco-elastic. However, also studies have been done for other types of fluids. For instance linear stability analysis for a Bingham fluid, i.e. a non-elastic fluid with a yield stress, suggests a very large stabilizing effect (Frigaard *et al.* 1994). However, the Reynolds number in this case is based on the limiting viscosity (viscosity at very high shear rates). When a more appropriate viscosity is used, the effect of the yield stress is much less, but still stabilizing.

3.3.3 Dilute Fiber Suspension

The experiments for polymer solutions, have demonstrated that the conformation of the polymers has a large effect on the flow behavior. Therefore, it seems appropriate to analyze the

effects of rigid rod-like particles on the flow stability. A stretched polymer can be regarded as a rod-like particle. However, it should be born in mind that a polymer can be deformed and compressed whereas a rod maintains its shape. Thus, the comparison does not hold completely.

Landahl (1973) has studied the effect of fibers on the stability of a flow with an inflectional velocity profile and showed that the fibers have a stabilizing influence. A linear stability analysis for a dilute suspension of slender fibers in plane Poiseuille flow has been performed by Bark & Tinoco (1978). They used the constitutive equation derived by Batchelor to model the rheological properties of the suspension. In this model, the direction of the suspended fibers is described by a vector field $\vec{p}(\vec{x}, t)$, where \vec{x} is the position vector and t is the time. The extra-stress tensor τ_{kl} , in Cartesian coordinates is given in terms of the vector $\vec{p}(\vec{x}, t)$ field and the velocity field $\vec{u}(\vec{x}, t)$ by:

$$\tau_{kl} = 2\mu d_{kl} + \frac{\mu\Phi r^2}{\ln 2r - \frac{3}{2}} p_k p_l p_m p_n d_{mn} \quad (3.4)$$

where $d_{kl} = \frac{1}{2}(u_{k,l} + u_{l,k})$ is the rate-of-deformation tensor, μ the viscosity of the Newtonian solvent, Φ the volume fraction of the suspended fibers and r their aspect ratio. Note that the contribution of the fibers to the stress has the form of a purely viscous stress term, i.e. no relaxation time is present. The results can be represented with the use of a dimensionless parameter B , which appears in equation 3.4 for the stress tensor and is defined as

$$B = \frac{\Phi r^2}{\ln 2r - \frac{3}{2}} \quad (3.5)$$

In a plane Poiseuille flow the fibers will be completely aligned in the flow direction and have no dynamical effect at all. Therefore, the velocity profile for this case remains parabolic. Linear disturbance theory shows that the only perturbation stress caused by the fibers is a normal stress in the flow direction. As for the Newtonian case, the most unstable mode is found to be a symmetric mode in the normal velocity component. In figure 3.8 the neutral stability curves in terms of wave number versus Reynolds number are shown for various values of the parameter B . The aspect ration r can be very large for some fibers, e.g. asbestos fibers values as large as 10^4 have been reported (see also Vaseleski & Metzner 1974). For this aspect ratio, a B -value of 200 can be obtained with a volume fraction of only $\Phi = 17 \cdot 10^{-6}$. For fibers with densities close to that of the solvent, this results in concentrations of approximately 20 ppm. Such concentrations are often encountered in drag-reduction and transition-delay experiments using polymers. This shows that large effects on the flow behavior can be expected for fibers with large aspect ratios. In this respect, polymers can be regarded as the ultimate fibers given their extremely large aspect ratio when they are fully extended.

3.4 Discussion

Summarizing the results of this chapter, it will be clear that the transition to turbulence in a non-Newtonian fluid can differ from that of Newtonian fluids. A delay in transition as well as early transition can occur, but (in most cases) no change in transition is reported (e.g. Virk *et al.* 1967). A possible explanation for the latter could be that many of the experiments

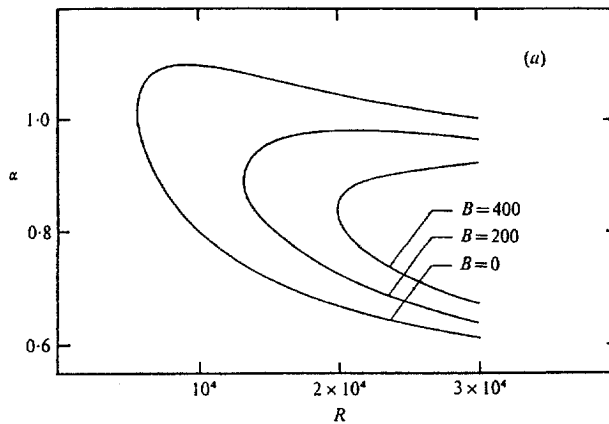


Figure 3.8: Neutral linear stability curves for plane Poiseuille flow of slender fibers that are suspended in a Newtonian fluid. From Bark & Tinoco (1978).

are performed in pipes with diameters larger than a few millimeters, in which the results on delay in transition are commonly found. An explanation for this influence of pipe diameter on experimental data may be that the elasticity number E for a given fluid depends on pipe diameter as D^{-2} . Thus, the elasticity number in pipes with a very small diameter is much larger than in pipes with a large diameter and consequently, the influence of elasticity is stronger in small diameter pipes. However, the stability calculations show a destabilization with an increase in E . This difference in the effect of elasticity found in experiments and stability calculations may be explained when in such flows the polymers are stretched. This can result in a stabilizing effect, as is shown by the experiments (Virk & Wagger 1990) and in linear stability calculations for fibers (Bark & Tinoco 1978). The possibility of polymer stretching has been shown by Massah *et al.* (1993) who performed numerical simulations. They also show that the polymers stretch in shear flows only when the shear rate at the wall is larger than the relaxation time of the polymer. When we keep the Reynolds number constant, the shear rate at the wall varies with the pipe diameter as D^{-2} , viz. for small pipe diameters both the elasticity number and the shear rate at the wall are strongly increased. This indicates that the hypothesis that the delay in transition which is found in pipes with small diameters can be due to the stretching of the polymer. This effect will not occur in large pipes and as a result no effect on the transition can be observed.

Recently, den Toonder (1995) showed that the key property for drag reduction is the purely viscous anisotropic stresses that are introduced by stretched polymers. This indicates the type-B drag reduction is the fundamental mechanism for drag reduction rather than type-A, as is suggested by Virk & Wagger (1990). The onset-point of drag reduction of type-A is then related to the conditions in which the turbulent flow can stretch the polymers. When stretching can occur in a laminar flow, no onset of drag reduction exists and drag reduction should be present as soon as the flow becomes turbulent. This type of behavior is indeed found in experiments.

We will test the hypothesis that stretched polymers are important for a delay in transition by performing stability measurements in a 40 mm pipe and change the conformation of the PAMH

polymers by varying the salt concentration. These results will be presented in chapter 7.

Another result which comes out of this review is adding elasticity results in a destabilization for linear and weakly nonlinear disturbances in plane Poiseuille flow (Porteous & Denn 1972a, 1972b). However, they speculate that for larger nonlinear disturbances, visco-elastic fluids may become more stable than Newtonian fluids. To check whether this is the case, we performed 2-D nonlinear stability calculations in plane Poiseuille flow for an Upper Convected Maxwell model. The area in the wave number-Reynolds number plane where 2-D saturated disturbances exist has been investigated for several values of the elasticity number. We will discuss these results in chapter 4.

Chapter 4

Stability of plane Poiseuille flow

Abstract

In this chapter we will present results of numerical stability computations of plane Poiseuille flow of Newtonian and non-Newtonian fluids. We have used the finite element method to solve the complete equations of motion of the two-dimensional flow. The non-Newtonian fluid model that is used in the computations is the Upper Convected Maxwell (UCM) model which is one of the most simple models to incorporate visco-elastic behavior.

With help of higher-order elements, we can accurately capture the growth rates of linear disturbances for both the Newtonian as well as the UCM model flow as follows from comparison with existing data. Also, the results for the saturated nonlinear two-dimensional disturbances agree very well with literature results (Herbert 1976). Our simulations of the saturated two dimensional disturbances show, that the critical Reynolds number decreases from $Re_c \approx 2650$ for the Newtonian fluid to a minimum at $Re_c \approx 1920$ when the elasticity of the UCM model is increased until the Weissenberg number approaches unity. When the elasticity is further increased, the critical Reynolds number increases again and the disturbance amplitude is strongly decreased.

4.1 Introduction

Two-dimensional stability calculations for plane Poiseuille flow have been performed in various previous studies. The first attempts for Newtonian fluids were asymptotic approximations of the Orr–Sommerfeld equation. In 1953, Thomas solved the Orr–Sommerfeld equation using a finite difference scheme. Subsequently, it was found that the accuracy can be strongly increased by the use of spectral methods. Orszag (1971) for instance, presented an accurate solution of the Orr–Sommerfeld equation for $Re=10\,000$. He also found the critical Reynolds number for infinitesimal perturbation to be $Re_c=5\,772.22$ with dimensionless wave number $\alpha_c^*=1.02056$.

The linear stability problem can be extended to weakly nonlinear calculations (Chen & Joseph 1973, Davey & Drazin 1969, Sen *et al.* 1985). Spectral methods have also been used for solving the full 3-D Navier–Stokes equation for plane Poiseuille flow (Kleiser & Zang 1991). Spectral methods are highly suited for stability and transition calculations because of their numerical accuracy. This is because, transition problems require very accurate calculations since they are (inherently) sensitive to small perturbations. Very few calculations have been performed for non-Newtonian fluids, especially those solving the equations of motions rather than solving the stability problem. Linear stability calculations show a reduction in critical Reynolds number when the elasticity of the fluid is increased (Porteous & Denn 1972a, Sureshkumar & Beris 1995b). However, weakly nonlinear calculations suggest, when the results are extrapolated to disturbance amplitudes of several percent of the centerline velocity, that a visco-elastic fluids might show higher critical Reynolds number values than the Newtonian fluid (Porteous

& Denn 1972b). Some attempts have been made to perform three-dimensional calculations of visco-elastic fluids but for large Weissenberg numbers numerical instability caused the computations to break down (Maulik 1989, Sureshkumar & Beris 1995a).

For our computations we have used the program DYNAFLOW that has been developed by Hulsen (1996) and it can perform 2-D time dependent numerical computations of incompressible flows of inviscid, viscous or visco-elastic fluids. This program is partly based on the SEPRAN finite element package (by Ingenieursbureau SEPRA). It has been used to perform stability computations of two-dimensional plane Poiseuille flow of Newtonian and visco-elastic fluids of which the results will be presented in the following sections.

We will begin with a description of the type of flow, the fluid models and the governing equations. Then, a brief discussion of the behavior of the visco-elastic fluid model that we used, i.e. the Upper Convected Maxwell (UCM) model, in plane Poiseuille flow is given in section 4.3. The numerical techniques employed are the subject of section 4.4. We have first tested the program for the linear stability problem of plane Poiseuille flow of Newtonian and UCM fluids, which is the subject of section 4.5, where it is found that the results agree very well with those in the literature. This is also true for strongly nonlinear disturbances for Newtonian fluids, as is shown in section 4.6. Accurate results for the saturated 2-D disturbances have been presented by Herbert (1976) for flows with constant pressure gradient. We performed some calculations for a constant pressure gradient to check the accuracy of our code for nonlinear disturbances. Then we calculate the Reynolds number-wave number combinations for which saturated 2-D disturbances exist in Newtonian flow. Here we concentrate on locating the minimum Reynolds number for which these saturated disturbances can be sustained. We performed these calculations for constant flow rate conditions, since it gives a much faster convergence in time to the steady state disturbances.

These results are then compared with those for the UCM model fluids in section 4.7. From this comparison we can check the suggestion by Porteous & Denn (1972b) that visco-elastic fluids could be more stable than Newtonian fluids for large amplitude disturbances. In the final section, we present a discussion and show how our results may be linked to the delay in transition found experimentally in small diameter pipes.

4.2 Problem definition

4.2.1 Introduction

In this section we will describe the flow problem that we studied in relation to the stability of the flow between parallel plates, i.e. plane Poiseuille flow. The geometry that we studied, the governing equations and the boundary conditions are discussed in the next sections. Also, the dimensionless quantities and the dimensionless numbers that arise will be explained.

4.2.2 Flow geometry

We studied two-dimensional flow between parallel plates, which is also known as 2-D plane Poiseuille flow. The coordinate system is chosen such that the x -axis is aligned with the mean flow direction and the y -coordinate represents the wall normal direction, with its origin at the centerline, as is shown in figure 4.1. The distance between the plates is $2h$ and the length of the computational domain is L .

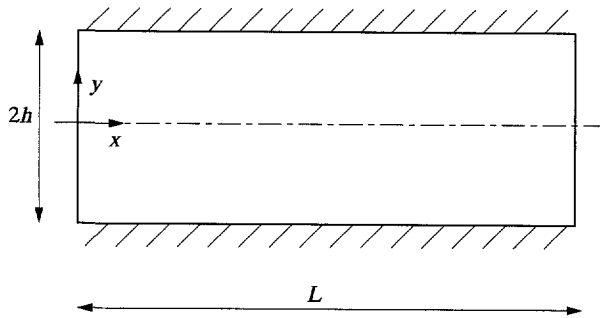


Figure 4.1: The flow geometry that we used for the stability calculations of plane Poiseuille flow together with the coordinate system.

4.2.3 Governing equations

We study the flow of incompressible fluids, thus $\nabla \cdot \underline{v} = 0$, where \underline{v} is the velocity vector. For incompressible fluids the equations of motion are:

$$\rho \frac{D\underline{v}}{Dt} + \nabla p - \nabla \cdot \underline{\tau} = \underline{0} \quad (4.1)$$

Here, ρ is the fluid density, $D/Dt = \partial/\partial t + (\underline{v} \cdot \nabla)$ denotes the material derivative. p is the pressure and $\underline{\tau}$ is the extra-stress tensor. The extra-stress tensor is related to the Cauchy stress tensor $\underline{\sigma}$ in the following way:

$$\underline{\sigma} = -p\underline{I} + \underline{\tau} \quad (4.2)$$

The extra-stress tensor $\underline{\tau}$ vanishes at equilibrium. To solve the equations of motion, we have to provide additional equations for $\underline{\tau}$. These additional equations describe the behavior of the fluid and are called constitutive equations.

4.2.4 Constitutive equations

One of the simplest constitutive equations is that of the Newtonian fluid in which the extra-stress varies linearly with the rate of deformation. Only one fluid parameter is needed to describe such behavior; the viscosity η . For an incompressible Newtonian fluid, the constitutive equation describing the relationship between the extra-stress tensor $\underline{\tau}$ and the rate-of-deformation tensor $\underline{\dot{\gamma}}$ is given by

$$\underline{\tau} = \eta \underline{\dot{\gamma}} \quad \text{where} \quad \underline{\dot{\gamma}} = \nabla \underline{v} + (\nabla \underline{v})^\dagger \quad (4.3)$$

in which $(\nabla \underline{v})^\dagger$ is the transpose of the tensor $\nabla \underline{v}$ and η is the viscosity. Substitution of equation 4.3 in equation 4.1 results in the well known Navier–Stokes equation which governs Newtonian fluid flow.

One of the simplest non-Newtonian fluids is the generalized Newtonian fluid, in which the viscosity is no longer constant but a function of the rate of deformation. For an overview of the proposed generalized Newtonian fluid models see chapter 4 of Bird (1987a). Generalized Newtonian fluid models are frequently used in practical applications of laminar flows.

The generalized Newtonian fluids are still purely viscous fluid models, and no elasticity is present. For visco-elastic fluids the constitutive equation is a differential or integral equation in time. Many visco-elastic fluid models have been proposed of varying in complexity. We have used one of the simplest models that incorporates visco-elastic behavior; the Upper Convected Maxwell (UCM) model. The choice for the UCM model is based on several considerations. The UCM model is widely used and we can compare our results to those presented in the literature. Also, the UCM model exaggerates the effects of elasticity so that deviations in behavior from Newtonian fluids is emphasized. However, the UCM does not describe the material functions commonly found for non-Newtonian fluids. Most non-Newtonian fluids show material functions, for example the viscosity function, that are shear-rate-dependent whereas for the UCM model these are constant. Although the results for the UCM model are therefore unlikely to describe actual non-Newtonian fluid behavior, this also has a major advantage. The constant viscosity results in parabolic velocity profiles in Poiseuille flows which facilitates the comparison with Newtonian flows. The UCM model is an one-parameter extension to the Newtonian fluid. So the effect of visco-elasticity can be studied by varying only one parameter. Despite the simplicity of the model, however, it is one of the most difficult ones to solve numerically.

Mechanically, one can interpret the UCM model as an elastic spring and dash-pot connected in series. For slow motions, the behavior is governed by the dash-pot and the model simplifies to the Newtonian model. For sudden changes in the stress, the elastic spring dominates the behavior, and the fluid behaves as an elastic solid. The constitutive equation for such an UCM fluid model, which gives the relation between the extra-stress $\underline{\underline{\tau}}$ and the rate-of-deformation tensor $\dot{\underline{\underline{\gamma}}}$ reads (Bird *et al.* 1987a, p. 345):

$$\underline{\underline{\tau}} + \lambda \overset{\nabla}{\underline{\underline{\tau}}} = \eta \dot{\underline{\underline{\gamma}}} \quad (4.4)$$

Here, λ is a time constant and is often referred to as relaxation time, and η is the viscosity, which is constant. The time derivative ($\overset{\nabla}{\underline{\underline{\tau}}}$) is a special time derivative (Bird *et al.* 1987a, p. 342):

$$\overset{\nabla}{\underline{\underline{\tau}}} = \frac{D}{Dt} \underline{\underline{\tau}} - (\nabla \underline{\underline{v}})^\dagger \cdot \underline{\underline{\tau}} - \underline{\underline{\tau}} \cdot \nabla \underline{\underline{v}} \quad (4.5)$$

called the upper-convected derivative. The upper-convected time derivative is frame indifferent, thus making the constitutive equation frame indifferent. For a comprehensive overview see Bird *et al.* (1987a). The behavior of the UCM model in plane Poiseuille flow will be analyzed in section 4.3.

4.2.5 Boundary Conditions

For the velocity the following boundary conditions are used:

- Normal velocity v equals zero at both plates: $v(y=\pm h)=0$,
- No-slip condition $u(y=\pm h)=0$ for the velocity in flow direction is applied through the vorticity-equation.

In stability theory it is common practice to use Fourier modes in the stream-wise direction. In finite element codes this is not possible. When we want to study the dependence of the

stability on the wave number, we have to use the length of our computational domain, i.e. L , to introduce a wave number in our calculations. When we consider a wave with wave number α : $\text{Re}(e^{i(\alpha x + \omega t)})$, we adjust L so that exactly one wave length fits in our computational domain. This gives $L = \frac{2\pi}{\alpha}$. By using periodical boundary conditions in the stream-wise direction we can study the behavior of Fourier modes with wave number α , i.e. the base function, and its higher harmonics. We use periodical boundary conditions at the inflow and outflow boundaries for the velocities, stresses, and the pressure disturbances. Note that the total pressure is not periodic due to the pressure gradient.

4.3 The Upper Convected Maxwell fluid model

In this section, we will review the dimensionless groups that describe the flow behavior of the Upper Convected Maxwell (UCM) model and the steady shear flow of the UCM fluid between two parallel plates (plane Poiseuille¹ flow) is analyzed.

4.3.1 Dimensionless groups for the UCM fluid

With the introduction of the relaxation time λ to describe the elastic behavior of the visco-elastic fluid, the Reynolds number alone is no longer sufficient to characterize the flow. Therefore, the Weissenberg number, (We), or the elasticity number, (E), are commonly used to introduce an additional dimensionless group. For the plane Poiseuille flow of an UCM fluid these groups can be defined based on the centerline velocity of the undisturbed parabolic profile (U), and half the distance between the plates (h) (Joseph 1990, pp. 171–174):

$$Re = \frac{\rho U h}{\eta} \quad (4.6)$$

$$We = \frac{U \lambda}{h} \quad (4.7)$$

$$E = \frac{\eta \lambda}{\rho h^2} \quad (4.8)$$

The relationship amongst these groups is:

$$We = E \cdot Re \quad (4.9)$$

The Weissenberg number can be regarded as a ratio of time scales²:

$$We = \frac{\lambda}{h/U} = \frac{\text{relaxation time}}{\text{flow time scale}} \quad (4.10)$$

Note that the Weissenberg number can also be defined using the shear rate at the wall to define a flow time scale. Then, the Weissenberg number can be defined as $We = \lambda \dot{\gamma}_w$ where $\dot{\gamma}_w$ is the shear rate at the wall. In plane Poiseuille flow of an UCM model this Weissenberg number is twice that defined in equation 4.7.

¹Although the name Poiseuille refers to fully developed two-dimensional laminar flow for a Newtonian fluid, we will also use this designation for non-Newtonian fluids.

²This ratio of time scales is also known as the Deborah number, see e.g. Bird *et al.* 1987a, pp. 92–94.

The elasticity number depends only on the geometry of the flow and the fluid parameters. Thus, for a given flow geometry, a line $E=\text{constant}$ can be interpreted as a line for a specific polymer solution, viz. changing the concentration of the polymer or the polymer type would change the elasticity number. Therefore, the elasticity number is the most natural parameter next to the Reynolds number when comparing the flow behavior of several non-Newtonian fluids. E can also be interpreted as the ratio of the diffusion velocity to the elastic wave velocity:

$$E = \frac{\eta\lambda}{\rho h^2} = \frac{(\eta/\rho)^2 h^{-2}}{\eta/(\rho\lambda)} = \left(\frac{\eta/\rho h}{c_e} \right)^2 = \left(\frac{\text{diffusion velocity}}{\text{elastic shear wave speed}} \right)^2 \quad (4.11)$$

Here, $c_e = \sqrt{\frac{\eta}{\rho\lambda}}$ is the elastic shear wave speed.

We will present the results of our numerical computations using the Reynolds number and the elasticity number, analogous to Porteous & Denn (1972a). All quantities are non-dimensionalized using the centerline velocity of the undisturbed flow (U) and the half-distance between the plates, i.e. h . The dimensionless wave number can then be defined as $\alpha^* = \alpha h$.

4.3.2 The UCM model in steady shear flow

Let us consider plane Poiseuille flow for an UCM model, based on equation 4.4. The orientation of the coordinate system is such that the x -axis is aligned in the flow direction, the y -axis is aligned in the direction normal to the wall, and the z -axis denotes the spanwise direction. For plane Poiseuille flow, the velocity vector reduces to $\underline{v} = u(y)\underline{e}_x$, which results in $D/Dt=0$. For the other terms in the convected derivative, we need an expression for $\underline{\tau} \cdot \nabla \underline{v}$. When we write the several tensors in algebraic form, using the symmetry of $\underline{\tau}$, $\partial/\partial x=0$, $\partial/\partial z=0$, and the two-dimensionality of the flow, we obtain:

$$\nabla \underline{v} = \begin{pmatrix} 0 & 0 & 0 \\ \frac{\partial u}{\partial y} & 0 & 0 \\ 0 & 0 & 0 \end{pmatrix} \quad \underline{\tau} = \begin{pmatrix} \tau_{xx} & \tau_{yx} & 0 \\ \tau_{yx} & \tau_{yy} & 0 \\ 0 & 0 & 0 \end{pmatrix} \quad (4.12)$$

Multiplication of these two tensors and substitution in equation 4.5 gives the expression for the upper-convected derivative of $\underline{\tau}$:

$$\frac{\nabla}{\underline{\tau}} = -\dot{\gamma} \begin{pmatrix} 2\tau_{yx} & \tau_{yy} & 0 \\ \tau_{yy} & 0 & 0 \\ 0 & 0 & 0 \end{pmatrix} \quad (4.13)$$

where, $\dot{\gamma} = \partial u / \partial y$ denotes the shear rate. Substitution in equation 4.4 results in the following set of equations for the stress in a steady shear flow of an UCM fluid:

$$\begin{pmatrix} \tau_{xx} & \tau_{yx} & 0 \\ \tau_{yx} & \tau_{yy} & 0 \\ 0 & 0 & 0 \end{pmatrix} - \lambda \dot{\gamma} \begin{pmatrix} 2\tau_{yx} & \tau_{yy} & 0 \\ \tau_{yy} & 0 & 0 \\ 0 & 0 & 0 \end{pmatrix} = \eta \begin{pmatrix} 0 & 1 & 0 \\ 1 & 0 & 0 \\ 0 & 0 & 0 \end{pmatrix} \dot{\gamma} \quad (4.14)$$

Equation 4.14 points to some important characteristics of the UCM model. For τ_{yy} immediately follows $\tau_{yy}=0$. The equation for τ_{yx} yields $\tau_{yx}=\eta\dot{\gamma}$, i.e. the Newtonian relationship between the shear stress and the shear rate and this results in the same parabolic velocity profile that we find for the Newtonian fluid. For the normal stress in x -direction, equation 4.14 yields $\tau_{xx}=2\eta\lambda\dot{\gamma}^2$. With $\tau_{yy}=0$, this gives for the first normal stress coefficient:

$$\Psi_1 = \frac{\tau_{xx} - \tau_{yy}}{\dot{\gamma}^2} = 2\eta\lambda \quad (4.15)$$

Thus, like the shear viscosity, also the first normal stress coefficient is constant whereas for (concentrated) polymer solutions and melts both normally decrease with increasing shear rate.

The program DYNFLOW uses in its computation a tensor $\underline{\underline{b}}$, the so-called conformation tensor³, which is defined as:

$$\underline{\underline{b}} = \frac{\lambda\tau}{\eta} + \underline{\underline{I}} \quad (4.16)$$

where $\underline{\underline{I}}$ is the unit tensor. Using the result for τ found above gives us:

$$\underline{\underline{\tau}} = \eta\dot{\gamma} \begin{pmatrix} 2\lambda\dot{\gamma} & 1 & 0 \\ 1 & 0 & 0 \\ 0 & 0 & 0 \end{pmatrix} \quad \text{and} \quad \underline{\underline{b}} = \begin{pmatrix} 1 + 2(\lambda\dot{\gamma})^2 & \lambda\dot{\gamma} & 0 \\ \lambda\dot{\gamma} & 1 & 0 \\ 0 & 0 & 1 \end{pmatrix} \quad (4.17)$$

The tensor $\underline{\underline{b}}$ can be regarded as a measure of the elastic deformation. If the rate of deformation is much smaller than the relaxation time λ , i.e. $\lambda\dot{\gamma} \ll 1$, then $\underline{\underline{b}}$ reduces to the unit tensor. We will use the tensor $\underline{\underline{\tau}}$ when we discuss the results of the nonlinear stability calculations.

Before we discuss the results we will first briefly review the numerical techniques that we used to perform the stability calculations.

4.4 Numerical Techniques

4.4.1 Introduction

The calculations have been performed with the program DYNFLOW (Hulsen 1996). In the next sections, we will briefly review some details on the numerical method which is used, the boundary conditions, and the mesh. Also, the shape of the initial disturbance is discussed.

4.4.2 Numerical Method

To implement visco-elastic models in the finite element program, special elements had to be defined. These are needed to accommodate the additional stresses due to the visco-elastic behavior of the fluids. A brief summary of the numerical schemes used in the program are given below. For more details see Hulsen (1996).

The problem is treated using the following elements:

- *Velocity-pressure discretization*: Raviart-Thomas mixed triangular elements with polynomials of order k where k can be varied between 1 and 3,

³ $\underline{\underline{b}}$ reduces to the Finger tensor, a finite strain tensor (see e.g. Bird *et al.* 1987a, p. 427), when the deformation is fast enough such that no relaxation occurs.

- *Viscous terms*: discrete mixed vorticity/velocity with vorticity piece wise continuous of $k + 1$ order,
- *Visco-elastic stresses*: piece-wise discontinuous of order k ,
- *Hyperbolic 1st order terms*: discontinuous Galerkin,
- *Time-dependent equations*: explicit Runge–Kutta of order $k + 1$.

The incompressibility is handled with a penalty method. Details of the numerical schemes are outside the scope of this thesis.

4.4.3 Mesh

The linearly most unstable modes have a maximum in u' close to the wall. To be able to model these modes correctly, the mesh should be finer close to the wall and coarser in the center. Our code has an option to define the ratio of largest to the smallest grid cell. In the center of the flow, an equidistant mesh was used to prevent excessively large size differences between the mesh around the centerline and close to the wall. A typical mesh used for the calculations is shown in figure 4.2. The mesh is symmetrical around $y = 0$.

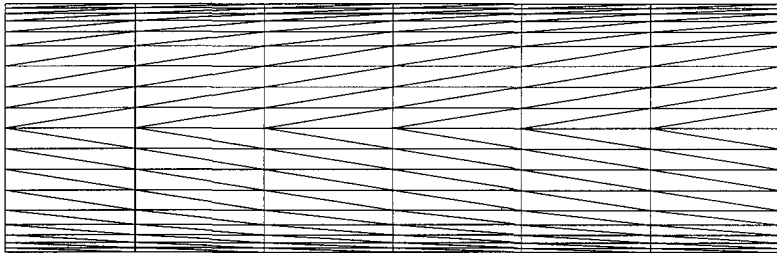


Figure 4.2: Mesh used for most calculations: Mesh size: 6×18 .

4.4.4 The initial disturbance

From the literature, we know that the first eigenmode which becomes linearly unstable above a certain Reynolds number has a wave number close to unity (non-dimensionalized in terms of h). It is a symmetric mode in disturbance stream function and the y -component of the disturbance velocity. From the continuity equation, it then follows that the disturbance in the flow direction, u' , is anti-symmetric in the normal coordinate y . The flow is periodic in the flow direction with period $L=2\pi/\alpha$ and the plates (i.e. walls) are located at $y=\pm h$. To study the linear stability of disturbances with wave number α , we adjusted the length of our computational domain to the corresponding wave length: $L=2\pi/\alpha$. As an initial condition we used a disturbance which roughly resembles the linearly most unstable mode. In stream-wise direction it varies as a sine-function with wave number α and in y -direction a polynomial form was chosen. After a short transient, the flow quickly transforms the initial disturbance into the most unstable eigenmode which starts to grow exponentially.

The initial disturbance that we used in stream-wise direction, i.e. u' , has the following form:

$$\frac{u'}{U} = A \frac{y}{h} \left[1 - \left(\frac{y}{h} \right)^{2n} \right] \sin \left(\frac{2\pi x}{L} \right) \quad (4.18)$$

Here U is the centerline velocity. This form ensures the anti-symmetric properties as well as the periodicity. The power $2n$ in the equation determines the location of the maximum value for the u' disturbance. For $2n = 30$ the disturbance has roughly the shape of the eigenfunctions described in literature. From 4.18 an expression for v' can be derived with help of the continuity equation:

$$\frac{v'}{U} = -A \frac{2\pi h}{L} \left[\frac{1}{2} \left(\frac{y}{h} \right)^2 - \frac{1}{2n+2} \left(\frac{y}{h} \right)^{2n+2} - \frac{n}{2n+2} \right] \cos \left(\frac{2\pi x}{L} \right) \quad (4.19)$$

Only disturbances in the velocities were introduced and not in the stresses. This disturbance field does not represent an unstable mode exactly, but this is not a problem because, due to the growth of the instability mode, the flow quickly adjusts itself and approaches quickly the most unstable mode as will be shown in the next section.

Disturbances described by equations 4.18 & 4.19 with the dimensionless disturbance amplitude A of order 10^{-4} are used for linear stability calculations. For the nonlinear calculations, the initial disturbance was also chosen of the form (4.18) & (4.19) but with A of the order 10^{-1} and also up to nine higher harmonics were added having an amplitude of 10% of the base functions (4.18) & (4.19).

All results for Newtonian and UCM fluids are presented in terms of dimensionless variables based on centerline velocity U and channel half-width h ; e.g. dimensionless time $t^* = tU/h$. In the next section, we compare our calculations for the linear stability with results presented in the literature. Typical dimensionless time-steps in the numerical computations are 0.01–0.05.

4.5 Linear Stability

4.5.1 Introduction

Our ultimate aim is to check whether the UCM model is or is not more stable than a Newtonian fluid when the disturbance amplitude is increased. This is illustrated in figure 4.3, where we sketch roughly the results obtained by Porteous & Denn (1972b)⁴ together with extrapolated lines that suggest that the UCM model with $E=10^{-4}$ may be more stable than a Newtonian fluid for $A \gtrsim 0.01$. Before we can perform any numerical simulations to study the stability behavior of visco-elastic fluids, we first have to establish the suitability of our program for stability calculations. This is not obvious, since stability calculations require very accurate codes in order to give precise predictions of e.g. disturbance growth rates. Therefore, we perform first some linear stability calculations for Newtonian and UCM fluids.

For plane Poiseuille flow, the linear stability problem for a Newtonian fluid is well known. Therefore, we have tested our code against literature results for some of the standard Reynolds number–wave number combinations.

⁴Porteous & Denn (1972b) actually performed weakly non-linear calculations for a second-order fluid. In their linear stability study they showed that a second-order fluid and a Upper Convected Maxwell model behave identically up to $E=5 \cdot 10^{-4}$. To facilitate the discussion, we will refer to their results as if they were obtained for an UCM model.

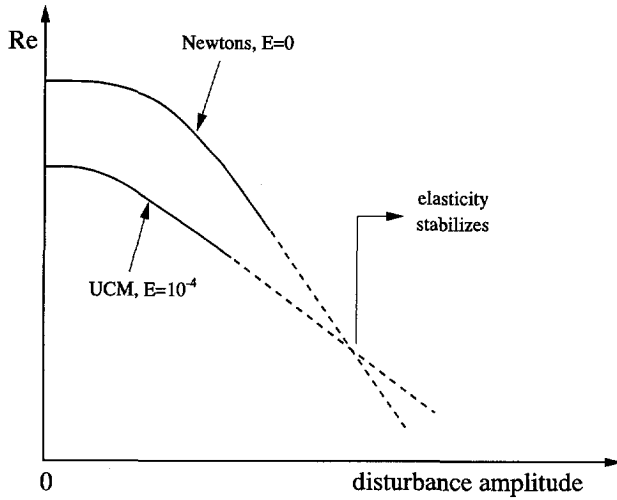


Figure 4.3: A sketch of the weakly nonlinear results obtained by Porteous & Denn (1972b) (solid lines) together with the extrapolations (dotted lines) that suggest a possible stabilizing effect of the UCM model for larger disturbance amplitudes A .

The first linear stability calculations were performed using elements with linear base functions, i.e. $k=1$, which at that time were the only elements available in the code. The growth rates calculated with these low-order elements were accurate till 2 significant digits. To achieve this, very large (fine) meshes and long calculation times were necessary. Performing such calculations on our HP-735 workstation was not practical. Memory limits and calculation times in the order of days limited the obtainable accuracy, viz. growth rates for a 20×60 grid still deviated by -2% . Through Richardson extrapolation based on calculations at several mesh sizes, a more accurate estimate could be obtained of maximal 0.5% difference. However, details in the flow were not resolved accurately enough. Therefore, we concluded that the first-order elements were not accurate enough for our purpose. For transition calculations, it is generally believed that 3 to 5 significant digits in the linear growth rate of Tollmien-Schlichting waves should be achieved in order to obtain a good representation of the instability mode.

The results of these plane Poiseuille flow stability calculations and other flows lead to the implementation of higher order elements in our code. All results in the remaining part of this chapter have been obtained with higher order elements with third-order polynomials ($k=3$). For the time integration a 4th order Runge-Kutta scheme is used. The results for the linear stability calculations using these elements for Newtonian and UCM fluids are shown in the next sections.

4.5.2 Newtonian linear stability

The three "benchmark" cases for linear stability calculations of Newtonian plane Poiseuille flow are Reynolds numbers 7500 and 10000, both for dimensionless wave number $\alpha^*=1$, and the so called critical Reynolds number. Orszag (1971) was the first to obtain very accurate growth rates by using spectral methods to solve the Orr-Sommerfeld equation for $Re=10,000$ and

$\alpha^*=1$. The growth rate of this disturbance is found to be 0.00373967. For a Reynolds number of 7500, linear disturbances with $\alpha^*=1$ are unstable and grow at a rate of 0.00223497 (see e.g. Canuto *et al.* 1988 and Liu *et al.* 1991). Also, the critical Reynolds number that Orszag found was $Re_c=5772.22$ and the corresponding wave number $\alpha_c^*=1.02056$.

When small disturbances are introduced in the flow with $Re > Re_c$, with an dimensionless amplitude of order 10^{-4} , the linearly instable Tollmien-Schlichting (TS) wave starts growing. Some transient behavior is present for times smaller than $t^*=30$, as shown in figure 4.4. A_{rms} is the root-mean-square amplitude of the disturbance averaged over the entire computational domain. This is probably caused by the difference in shape of the initial disturbance and the TS-wave.

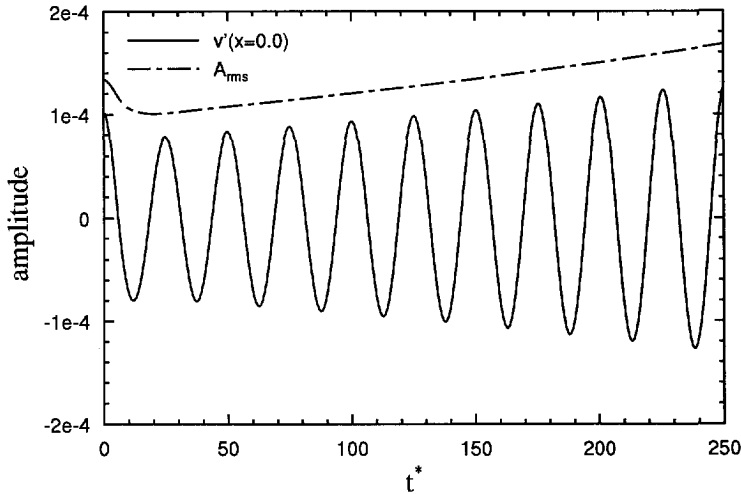


Figure 4.4: v' and A_{rms} of the disturbance versus time for $Re=7500$ and $\alpha^*=1$, mesh size 6×18 .

Table 4.1: Growth rates for linear disturbances for various meshes with $k=3$. $Re=7500$ and $\alpha^*=1$. The value obtained with spectral methods is also listed.

mesh size	growth rate: spectral: 0.00223497
2×6	-0.004614
4×12	0.0022093
6×18	0.00223456
10×30	0.00223503

The growth rates are determined by fitting an exponential function to the A_{rms} time-trace after the transient behavior has died out, typically after $t^*=50$. The linear growth rates obtained in this way for $Re=7500$ with several meshes are given in table 4.1. The mesh 4×12 gives a

growth rate comparable to the one with mesh 20×60 for $k=1$. The number of points for $k = 1$ per element side is 2 whereas for $k=3$ this is 4. This means that for a 4×12 mesh with $k=3$ the number of points amounts to 16×48 whereas a 20×60 mesh with $k=1$ results in 40×120 points. This clearly demonstrates the advantage of using higher order elements. For mesh sizes 6×18 or finer, 3 to 4 significant digits in growth rate are obtained directly; no Richardson extrapolation is necessary. Using the values in table 4.1, the order of the present numerical scheme can be estimated to be 4.8, which is not bad and is larger than the typical $k + 1=4$ that would be expected in finite elements. However, the growth rate for the mesh 10×30 exceeds the exact value whereas the others all underestimate it. A possible reason for this can be that the penalty method limits the number of possible significant digits.

Using a 8×24 grid for $Re=10\,000$ and $\alpha^*=1$, a growth rate of 0.0037403 is obtained. This is 0.017% different from the result obtained by Orszag (1971) (0.00373967).

The growth rate calculations can also be used to determine the critical Reynolds number. From the results in literature we know that this critical Reynolds number ($Re_c=5772.22$) occurs for a wave number $\alpha_c^*=1.021$. By calculating growth rates for linear disturbances at several Reynolds numbers for this wave number, and by interpolating the results, we find the critical Reynolds number at which the growth is zero. The results of these calculations on a 6×18 mesh are shown in figure 4.5.

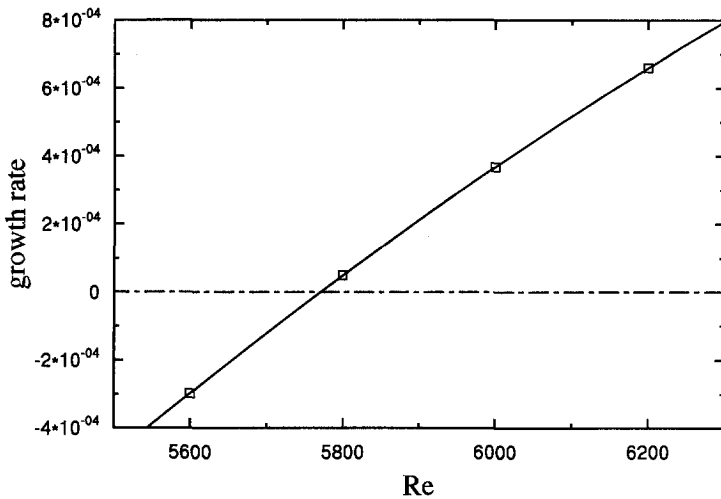


Figure 4.5: Growth rates at several Reynolds numbers for the critical wave number $\alpha_c^*=1.021$. Mesh size 6×18 .

For computations on a 6×18 mesh, a critical Reynolds number of $Re_c=5770.7$ is found and for a 8×24 mesh $Re_c=5772.6$ which deviate -0.026% and 0.0065% respectively from the much more accurate values found in spectral calculations. In our opinion, these linear instability calculations for Newtonian fluids show that our code is able to accurately calculate linear disturbances of order 10^{-5} to 10^{-4} on top of a parabolic base profile and also give growth rates within a few hundreds of a percent of the exact values. With the higher-order elements, these calculations on a 6×18 mesh are expected to be accurate enough for the nonlinear calculations,

Table 4.2: Comparison between our linear stability calculations and literature results for an UCM fluid.

	critical Re	growth rate	growth rate
	$We=1$ & $\alpha^*=1.15$ $E=2.7 \cdot 10^{-4}$	$Re=7500$ & $\alpha^*=1$ $E=10^{-5}$	$Re=7500$ & $\alpha^*=1$ $E=10^{-4}$
reference	Lee & Finlayson 1986	Porteous 1971	Renardy 1993
literature	3650	0.00262	0.005010778
mesh 6×18	3657	0.0025322	0.0050165
mesh 10×30			0.005010835

given the number of significant digits in the linear stability problem, that follow. These can be carried out within a reasonable time frame allowing for a wide parameter range to be studied.

4.5.3 Upper Convected Maxwell Fluids

We have also performed stability calculations for Upper Convected Maxwell fluids. Since much of the attention in rheology is focused on polymer melts, many of the stability calculations reported in literature are performed only for Reynolds numbers of the order 1 and smaller. Let us first review some of the earlier results obtained for Reynolds number much larger than 1. Some of the earliest weakly nonlinear calculations for visco-elastic fluids were performed by Porteous & Denn (1972b). In appendix C of his Ph.D. thesis, Porteous (1971) included the tables with data of his calculations on linear and nonlinear disturbances. For wave number $\alpha^*=1$ and $Re=7500$, Porteous obtained a growth rate of 0.00262 for $E=10^{-5}$ and 0.00508 for $E=10^{-4}$. These growth rates still changed approximately ± 0.0001 in the last iteration step given in his table. Lee & Finlayson (1986) presented mostly results of low Reynolds numbers, but they also give a critical Reynolds number for $\alpha^*=1.15$ and $We=1$ of $Re_c=3650$. Y. Renardy (1993) has developed a code using spectral methods for a multilayer UCM flow. Using this code for 2 identical fluids and 45 Chebyshev polynomials for each fluid, she could reproduce Lee & Finlayson's critical Reynolds number. For $Re=7500$ and $\alpha^*=1$ she found a growth rate of 0.005010778.

All these test cases were also investigated in this study. The calculations were performed for the same meshes as the Newtonian calculations. As initial conditions either equations 4.18 and 4.19 were used or calculations were restarted from a computed Newtonian flow field. The program has a built-in numerical stability criterion. For Newtonian fluids this works fine. For the UCM model, we found that only a slightly smaller time-step has to be used to prevent numerical stability problems. The smallest fraction that we used was 80% of the stability criterion. The results for the linear stability calculations can be found in table 4.2.

We find that the results for a 6×18 mesh are accurate to 0.1% whereas the result for a 10×30 mesh is accurate till 0.001%. The results obtained by Porteous agree with our results well within the accuracy of his calculations. The accuracy of the growth rate for $Re=7500$ and $E=10^{-4}$ obtained with the finest mesh is comparable to the result for Newtonian fluids. The results for the mesh 6×18 are approximately a factor 4 less accurate than the Newtonian results (see table 4.1). Nevertheless, these results give us confidence that the code can accurately represent

linear disturbances of an UCM fluid on top of the base profile and in our opinion, the accuracy is sufficient to proceed to nonlinear calculations. By the way, note that the growth rate of the disturbances is higher than the one for Newtonian fluids. At $Re=7500$ and $E=10^{-5}$ it is 13% higher and for $E=10^{-4}$ it is already more than a factor of two in the (exponential) growth rate. Also critical Reynolds numbers are lower for higher elasticity numbers. This is in agreement with the results obtained by Porteous & Denn (1972a).

4.5.4 Linear disturbance field

To get an impression of the form of the linear disturbance mode, we plot the disturbance velocity in x and y -direction as a function of the y -coordinate in figures 4.6 and 4.7 respectively for $Re=7500$ and $\alpha^*=1$ for a Newtonian fluid. These disturbance velocity profiles closely resemble those in the literature (e.g. Liu *et al.* 1991). For the Upper Convected Maxwell model the instability modes are very similar to those found for Newtonian fluids as long as $E \leq 0.0025$ (Sureshkumar & Beris 1995b).

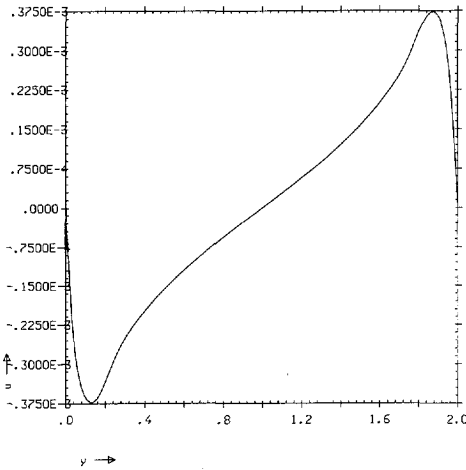


Figure 4.6: $u'(x=\pi/2)$, $Re=7500$, $\alpha^*=1$, $E=0$.

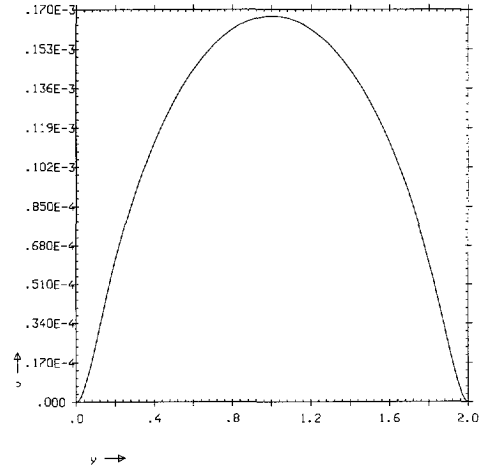


Figure 4.7: $v'(x=0)$, $Re=7500$, $\alpha^*=1$, $E=0$.

In figures 4.8 and 4.9 we plot the disturbance stream function and velocity vector field respectively. Clearly, the instability mode consists of two counter rotating cells.

4.6 Nonlinear stability for Newtonian fluids

4.6.1 Introduction

Now that we have established the accuracy of the code with respect to linear stability problems, we can proceed to perform nonlinear calculations. These calculations can be done in two essentially different ways. First, weakly nonlinear calculations for small finite amplitude disturbances for which the linear stability problem is the starting point. Porteous & Denn (1972b) performed such type of calculations for Newtonian and UCM fluids. The second possibility is to solve the complete equations of motion which allows for strongly nonlinear disturbances. Zahn

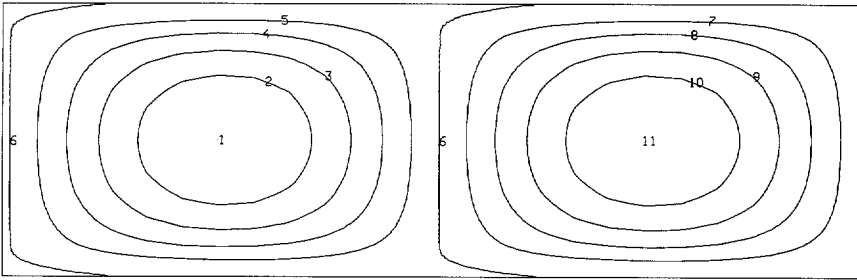


Figure 4.8: Contour levels of disturbance stream function. $Re=7500$, $\alpha^*=1$, $E=0$. The 11 contour levels are evenly spaced between $-1.672 \cdot 10^{-4}$ and $1.672 \cdot 10^{-4}$.

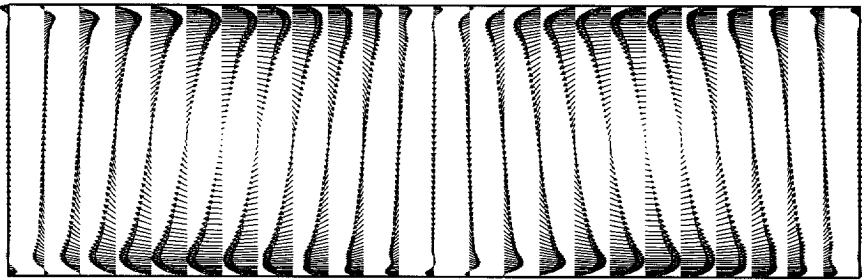


Figure 4.9: Disturbance velocity field. $Re=7500$, $\alpha^*=1$, $E=0$.

et. al (1974) and Herbert (1976) performed such calculations for Newtonian fluids. Jiménez (1990) extended these calculations to higher Reynolds numbers and showed the existence of solutions which vary either periodically or chaotically in time.

Zahn and Herbert performed calculations for constant pressure gradient conditions. We have checked our code against their results and this is presented in section 4.6.2. However, convergence to a steady state value is very slow and for the parameter study, the constant flow rate driven flow is to be preferred. This is particularly the case for instability and transition studies, as will be explained in section 4.6.3. In this section, also the Reynolds number–wave number combinations for which the 2-D saturated-amplitude disturbances exist will be determined. These also serve as a reference for the nonlinear calculations for the UCM model.

4.6.2 Constant Pressure Gradient

Following the good agreement for the linear stability calculations, we continue by investigating the accuracy of our code for nonlinear stabilities. This is done by trying to reproduce the results obtained by Herbert (1976). Herbert calculated the curve for $Re=4000$ at which the disturbance amplitudes are neutrally stable. He obtained different curves when he varied the number of higher harmonics used to describe the disturbance. These neutral curves are egg-shaped, as is sketched⁵ in figure 4.10. The top part is called the upper branch (UB) and the bottom part the lower branch (LB). Solutions on the lower branch are neutral, however not attracting, i.e. disturbances having a smaller amplitude will decay whereas an amplitude above the lower branch will cause the disturbance to grow and saturate at the upper-branch value. Therefore, in a time dependent code, the lower-branch solutions are not stable and cannot be reproduced. The upper-branch solutions are attracting and can thus be reproduced with our code.

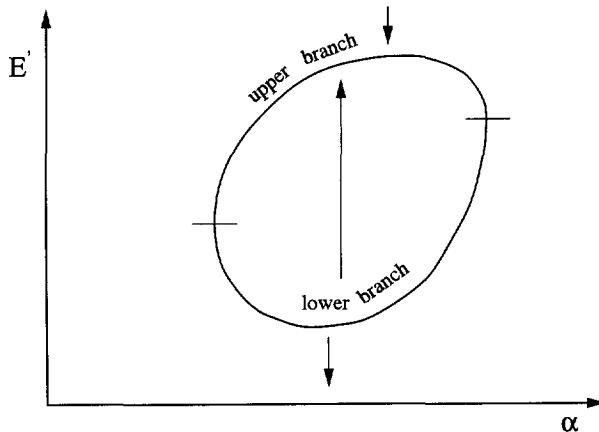


Figure 4.10: A sketch of the curve at which the nonlinear disturbance amplitudes are neutrally stable, and it consists of an upper branch and a lower branch. The disturbance energy E' is plotted as a function of the wave number α of the base mode. The arrows indicate the directions in which the disturbances will grow.

For our calculations we use the initial conditions given by equations 4.18 and 4.19 using an

⁵The result obtained by Herbert (1976) will be shown in figure 4.13 together with the result of our calculations.

amplitude of 10% of the centerline velocity and we added as much as nine higher harmonics of the same form having an amplitude that is 10% of the base function. Although this disturbance is far from the final solution, the higher harmonics are just added to put energy into the higher wave numbers in order to speed up the energy transfer to these wave numbers.

As it turns out, the calculations are very tedious and time consuming. This is due to the fact that a constant pressure gradient is applied. An increase in disturbance amplitude results normally in an increase of the pressure gradient. Under constant-pressure-gradient conditions, the flow rate will then decrease. But at a lower flow rate, the flow can sustain only smaller disturbances since the Reynolds number is lower. Therefore the disturbance has to decrease again. This process results in a very slow convergence to a final time-independent amplitude disturbance. To give an example, these calculations took in the order of several weeks on a workstation HP-735. The same time estimate applies to the Convex at Delft University of Technology. As the finite element code allows almost no vectorization, the Convex, which is like the Cray a vector machine, cannot handle these problems efficiently.

For $Re_c=4000$, we performed two calculations where the wave numbers of the base functions are $\alpha^*=1.15$ and $\alpha^*=1.45$. Herbert presents his results in terms of the total energy of the saturated disturbance averaged over the computational domain. In this energy, the disturbance with zero frequency, i.e. the distortion of the average velocity profile, is not included. From figures 4.11 and 4.12, where we show the rms disturbance amplitude as a function of time, it seems that excluding the base flow distortion component has a large influence on the disturbance amplitude. However, the base flow distortion also includes the decrease in flow rate which is a result of the increase in drag due to the growth of the disturbance. After subtraction of the base flow distortion, the relationship between the energy plotted by Herbert and the rms amplitude of the disturbance (A_{rms}) provided by the finite element code DYNAFLOW is found to be (for a derivation of equation 4.20 see appendix A):

$$E_{Herbert} = \frac{15}{8} A_{rms}^2 \quad (4.20)$$

After the base flow distortion is subtracted, many crossing lines in figure 4.11 exist till $t^* \approx 6200$. This is caused by the procedure that is followed to subtract the average velocity profile. The user has to supply the time period over which the velocities have to be averaged. If this period is not equal to the actual one, oscillations in A_{rms} are formed and combined with the sampling interval this gives rise to these intertwined lines. After adjusting the time period for averaging at $t^* \approx 6200$, the oscillations in A_{rms} disappear.

In figure 4.11 and even more pronounced in figure 4.12, we can see the extremely slow oscillation of A_{rms} . A typical period for this oscillation is 2000 dimensionless time-scales. This is related to the decrease in flow rate for these pressure gradient driven flows. Under constant flow rate conditions, the period of these oscillations is roughly ten times smaller (as will be shown in the next section).

The asymptotic values of the rms disturbance amplitudes can be estimated from the graphs, and for the two cases we find 0.08295 and 0.1026 for $\alpha^*=1.15$ and $\alpha^*=1.45$ respectively. From equation 4.20 the disturbance energy values according to Herbert become 0.0129 and 0.0197 respectively. These values lie right on top of Herbert's curve for 4 Fourier modes (3 higher harmonics), as we show in figure 4.13.

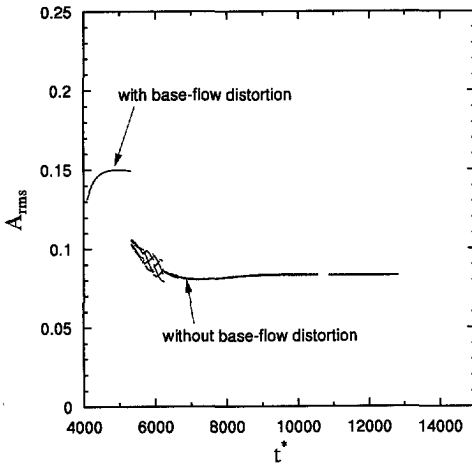


Figure 4.11: Disturbance amplitude as a function of time for $Re=4000$ and $\alpha^*=1.15$. Constant pressure gradient.

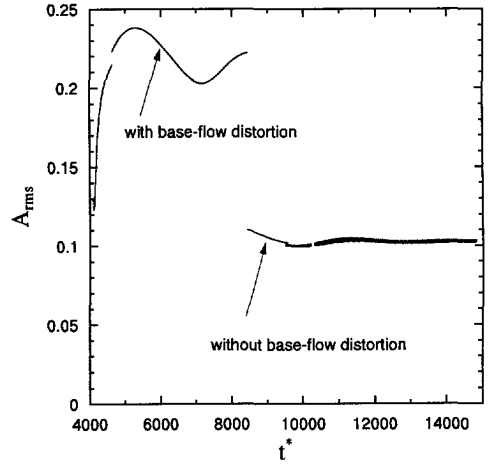


Figure 4.12: Disturbance amplitude as a function of time for $Re=4000$ and $\alpha^*=1.45$. Constant pressure gradient.

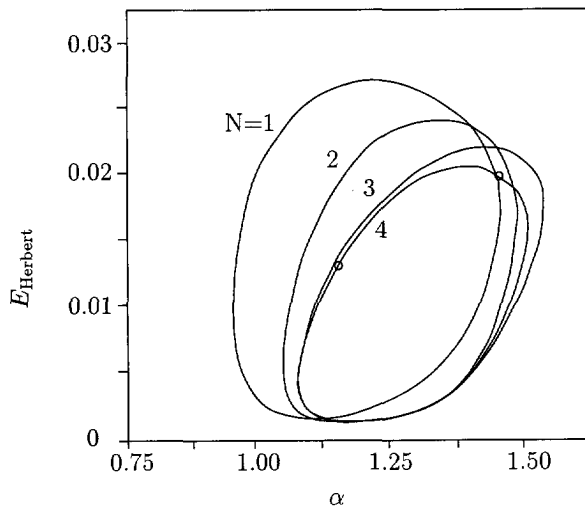


Figure 4.13: The neutral curves for the disturbance amplitude as presented by Herbert (1976) for $Re=4000$. Herbert varied the number of Fourier modes (N) to describe the nonlinear disturbance. The two circles indicate the energy that we found in our calculations for $\alpha^*=1.15$ and $\alpha^*=1.45$.

Since the calculations are performed under constant pressure gradient, the flow rate decreases significantly relative to the undisturbed flow. The dimensionless flow rate for the undisturbed flow (parabolic velocity profile) is $Q^*=4/3$ whereas for $\alpha^*=1.15$ it stabilizes at $Q^*=1.1384$ (85%) and for $\alpha^*=1.45$ at $Q^*=0.9845$ (73%). Thus, when we define the Reynolds number based on flow rate, Re_Q , instead of the pressure gradient, then the Reynolds numbers for these cases would be $Re_Q=3\,415$ and $Re_Q=2\,954$ respectively. For the undisturbed flow, the Reynolds number is still $Re_Q=4\,000$. The good agreement between Herbert's results and our results gives us confidence that the program can handle nonlinear saturated disturbances.

The stream-wise averaged velocity profiles have been determined for the two cases discussed here. A parabolic velocity profile with the same flow rate is subtracted, thus giving the distortion of the parabolic velocity profiles and these are plotted in figure 4.14. We see that the average velocity is increased close to the wall and in the center with a decrease in between. Similar effects were found by Jiménez (1990). This distortion of the average velocity profile is about 2% of the centerline velocity. Close to the wall, this means a large increase in the velocity gradient and under constant pressure gradient conditions, this results in a strong decrease in flow rate.

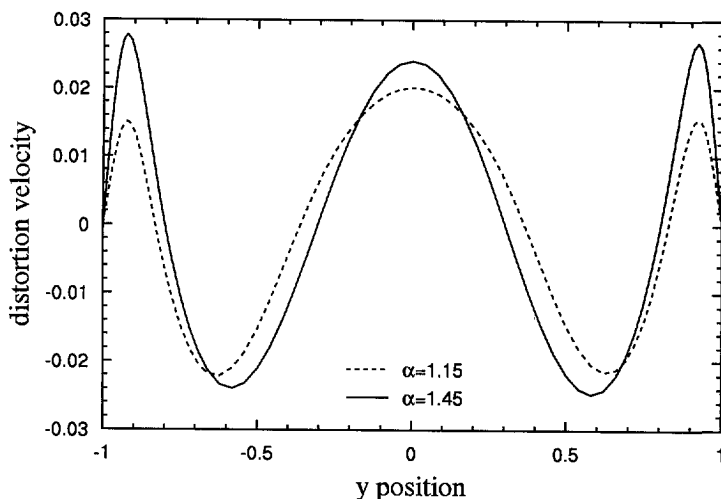


Figure 4.14: Distortion of the parabolic profile caused by saturated nonlinear two-dimensional disturbances at $Re=4\,000$ for two wave numbers under constant pressure gradient conditions.

4.6.3 Constant Flow Rate

In the previous section, we have seen that under constant pressure gradient conditions, very slow oscillations in the disturbance amplitude are found and that convergence in time to the asymptotic values is slow. This is unacceptable for a wide range parameter study. Another disadvantage of a constant pressure gradient condition is the fact that the flow rate decreases during the growth of the disturbance. This means that a calculation from linear to nonlinear disturbances will not take place at a constant Reynolds number. This makes the interpretation of the results more complicated and as a result comparison with experimental transition

experiments carried out under constant Reynolds number becomes difficult.

For these reasons, all calculations that will be presented in the next sections have been performed using a constant flow rate. This ensures a much faster convergence to a steady saturated solution. We varied the wave number and the Reynolds number we determine whether or not the nonlinear disturbance decays, i.e. the flow becomes laminar. In case the 2-D disturbance is sustained, it will grow towards the upper branch and the amplitude will saturate. We are particularly interested in the minimum Reynolds number for which such saturated 2-D disturbance exists.

To speed up the convergence in time, we used rescaling of the disturbance amplitude. If we find that in a calculation the disturbance energy keeps growing in time, this magnitude of disturbance velocity field is increased. After some short time oscillating behavior, the disturbance energy will either continue to increase or decrease with time and another rescaling can take place, as is illustrated in figures 4.15 and 4.16. Figure 4.15 shows the beginning of the calculation where the level of the disturbance is still far removed from the saturated value. When getting closer to this situation, smaller steps are used and thus the oscillations in the solution almost disappear as is shown in figure 4.16. Note that the two figures show calculations for different Reynolds numbers.

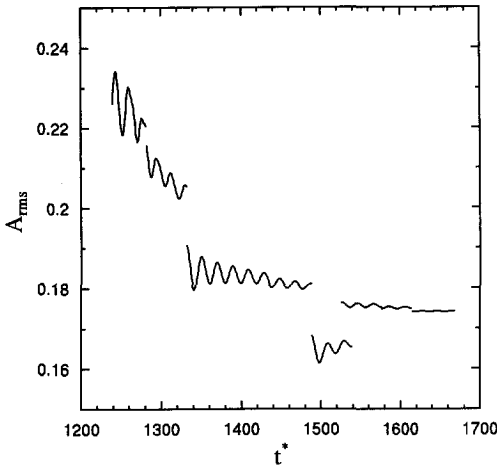


Figure 4.15: Rescaling of disturbance using large steps. $Re=5\,500$ and $\alpha^*=1.15$.

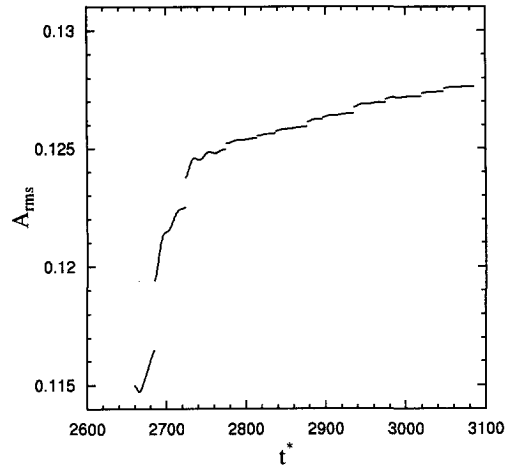


Figure 4.16: Rescaling of disturbance using smaller steps at the end. $Re=3\,000$ and $\alpha^*=1.30$.

Using the technique described above, a large parameter study was performed to locate the minimum critical Reynolds number, i.e. the smallest Reynolds number for which the 2-D saturated disturbances exist. The Reynolds number–wave number combinations for which saturated 2-D nonlinear disturbances in plane Poiseuille flow exist, are marked with a (\circ) in figure 4.17. A (\bullet) indicates the combinations where the disturbance decays and the flow returns to the parabolic velocity profile. The area where the saturated disturbances exist, has the familiar cigar-shape also found by Zahn (1974), Herbert (1976), and Jiménez (1990). Jiménez found a minimum Reynolds number for these saturated 2-D disturbances between 2 500 and 2 800 based on flow rate, which agrees well with the results of figure 4.17. Herbert found a minimum

critical Reynolds number of $Re=2935$ for $\alpha^*=1.32$. However, this Reynolds number is based on the pressure gradient, viz. based on flow rate it would have been lower. He finds an average dimensionless centerline velocity of 0.917 which includes the increase as a result of the distortion of the average velocity profile. Thus, the flow rate may have decreased approximately 10% giving a minimum Reynolds number of 2640. The latter is very close to minimum critical Reynolds number estimated from the data presented in figure 4.17; $Re_c \approx 2650$ and $\alpha^* \approx 1.35$.

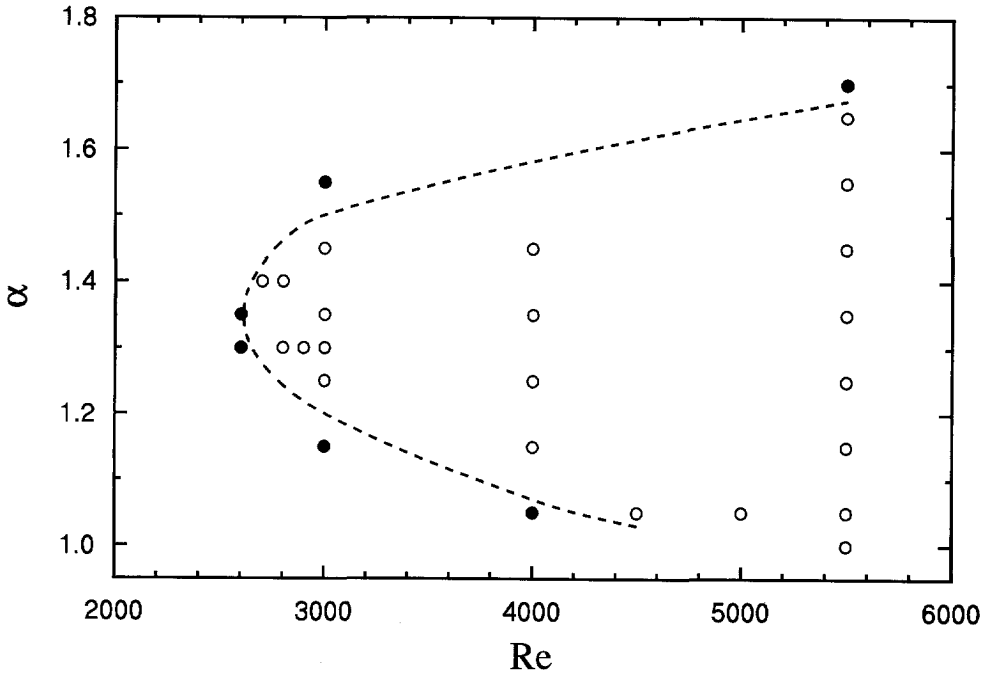


Figure 4.17: Nonlinear 2-D saturated disturbances exist (o) or the flow decays to a laminar parabolic flow profile (•) for a Newtonian fluid.

To summarize, in our opinion it is now established that our code can accurately reproduce linear stability calculations for Newtonian and UCM fluids as well as the saturated 2-D nonlinear disturbances in Newtonian flow. Therefore, we feel confident to study the nonlinear stability behavior of plane Poiseuille flow for an UCM fluid, which we will discuss in the next section.

4.7 Nonlinear stability for UCM fluids

To start our nonlinear stability study of an UCM fluid, we first check the suggestion by Porteous & Denn (1972b), who speculate the UCM model with $E=10^{-4}$ may become more stable than a Newtonian fluid for disturbance velocities larger than approximately 1%. They performed weakly nonlinear stability calculations, i.e. study lower-branch solutions. Since these are not attracting, we take our calculations one step further, and check the suggestion by Porteous

& Denn for the largest 2-D disturbances that can be sustained in plane Poiseuille flow, i.e. we study upper-branch (saturated) solutions. Then, the UCM fluid would be less stable than a Newtonian fluid when the minimum critical Reynolds number for which these saturated disturbances exist is smaller for the UCM fluid than for the Newtonian fluid and vice versa.

All calculations are performed using a constant flow rate condition, and rescaling of the disturbance is used to speed up convergence, as is explained in the previous section. The results for $E=10^{-4}$ are shown in figure 4.18, where the existence of the saturated disturbances is depicted using open markers and decay to a laminar parabolic flow is indicated by solid markers. To facilitate comparison with the Newtonian results, we have included the estimated critical line for $E=0$, i.e. the Newtonian fluid from figure 4.17.

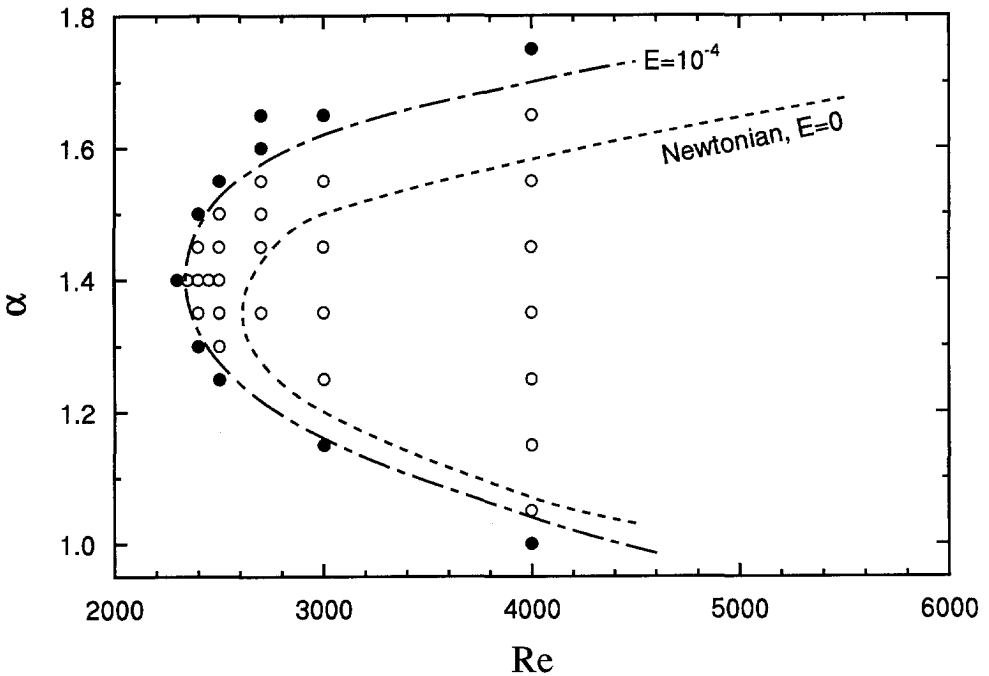


Figure 4.18: Nonlinear 2-D saturated disturbances exist (open markers) or decay to a laminar parabolic flow profile (solid markers) for an UCM model with $E=10^{-4}$. The results for the Newtonian calculations are incorporated in the form of the estimated critical line also drawn in figure 4.17.

Comparing the results for Newtonian and UCM fluids for $E=10^{-4}$, we may note several differences. For the UCM fluid saturated 2-D disturbances exist for a wider span of wave numbers at each Reynolds number than for the Newtonian case. Also, the lowest Reynolds number which still sustains a 2-D saturated disturbance at a certain wave number value is smaller for the UCM fluid than for the Newtonian fluid. In short, the lowest Reynolds number for which saturated disturbances exist is smaller for an UCM fluid than for a Newtonian fluid. Furthermore, the critical condition seems to occur at a slightly larger wave number for UCM fluids than for Newtonian fluids. Estimating the critical Reynolds number from the data presented

here gives: $Re_c \approx 2350$ and $\alpha_c^* \approx 1.40$ for UCM fluids compared with $Re_c \approx 2650$ and $\alpha_c^* = 1.35$ for Newtonian fluids. Consequently, the UCM model is found to destabilize the channel flow for $E=10^{-4}$.

Porteous & Denn (1972b) suggested, on the basis of their *weakly* nonlinear calculations that for larger disturbance amplitudes, the UCM model might become more stable than the Newtonian fluid (see figure 3.7 on page 39). They suggested this on the basis of extrapolating the curve of the critical Reynolds number versus disturbance amplitude for $E=10^{-4}$. Our calculations show that this is not the case, at least not anywhere near the tip of the stability curve for $E=10^{-4}$. Since the overall critical Reynolds number is considered when discussing stabilizing or destabilizing behavior of certain rheological models, the conclusion has to be that for two-dimensional flow, adding elasticity to the fluid has a destabilizing effect.

We have repeated the calculations shown in figure 4.18 for large values of E . Our calculations for the finite amplitude disturbances for UCM fluids do not show numerical instability for the range of Weissenberg numbers studied. Our maximum Weissenberg number calculations has been 2.5, i.e. $Re=2500$ and $E=10^{-3}$. We continued our calculations for several thousand dimensionless time units without any numerical instabilities. No artificial stress diffusivity as proposed by Sureshkumar & Beris (1995a) is needed.

Let us look at the results in terms of Re_c . When we further increase the elasticity number, we find a decrease in minimum critical Reynolds number for $E=3 \cdot 10^{-4}$ till $Re_c \approx 2000$ at $\alpha_c^* \approx 1.40$. The minimum critical Reynolds number for $E=6 \cdot 10^{-4}$ is slightly lower, $Re_c \approx 1925$ with a corresponding critical wave number of $\alpha_c^* = 1.34$. Further increasing the elasticity number to $E=10^{-3}$, *increases* the minimum critical Reynolds number to $Re_c \approx 2150$ with a critical wave number of $\alpha_c^* \approx 1.30$. In table 4.3 we give the critical parameters for the various elasticity numbers. With equation 4.9 we can also calculate We at the critical points and these are also included in the table and in figure 4.19 we show the corresponding instability regions. In figure 4.20 we plot the minimum critical Reynolds number as a function of the Weissenberg number. Clearly, elasticity shows a stabilizing tendency for $We \geq 1.0$ but it should be noted that the minimum critical Reynolds number for $E=10^{-3}$ is still smaller than that for the Newtonian fluid, viz. the flow is more unstable than for a Newtonian fluid. The minimum of the spline-curve connecting the points is located at $We \approx 1.04$ for which the minimum critical Reynolds number is 1920. This change in behavior for $We \gtrsim 1$ is unlikely to be caused by the coarseness of the mesh. We also performed some calculations on a 8×24 mesh for $E=10^{-3}$ and found that the amplitude values for the saturated disturbances deviated by less than 2% and also the location in the $Re-\alpha^*$ plane was accurately reproduced.

It is striking, that the stabilization occurs almost exactly at $We=1$, for which the relaxation time of the fluid equals the time scale of the flow. For We larger than unity the elastic effects come into play and cause a stabilizing effect.

When we plot A_{rms} (with the mean flow distortion included) as a function of the Weissenberg number, figure 4.21, we see that A_{rms} decreases when We is increased. The wave number at the critical condition seems to reach a maximum for $We \approx 0.35$, as is depicted in figure 4.22. For linear disturbances, such a maximum generally is located near the value of We for which the minimum in critical Reynolds number is found (Sureshkumar & Beris 1995b). In our case, it seems to be located at a somewhat smaller We value, but the inaccuracy in critical wave

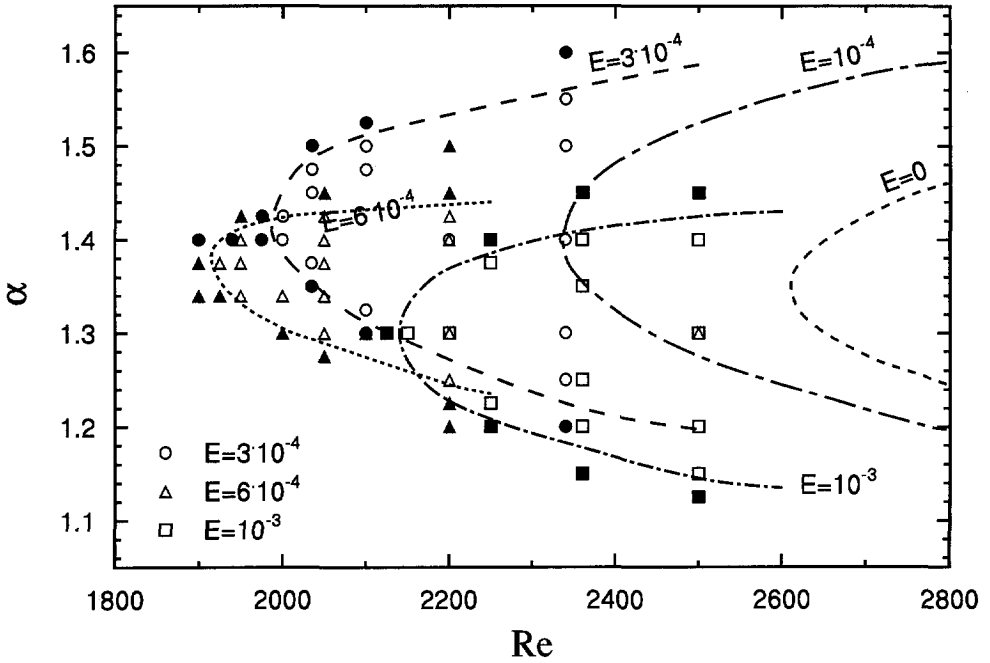


Figure 4.19: Nonlinear 2-D saturated disturbances exist (open markers) or decay to a laminar parabolic flow profile (solid markers) for an UCM model at various elasticity numbers; $E=3 \cdot 10^{-4}$, $E=6 \cdot 10^{-4}$, and $E=10^{-3}$. The results for the Newtonian calculations and those for the UCM model with $E=10^{-4}$ are incorporated in the form of the estimated critical lines also drawn in figure 4.18.

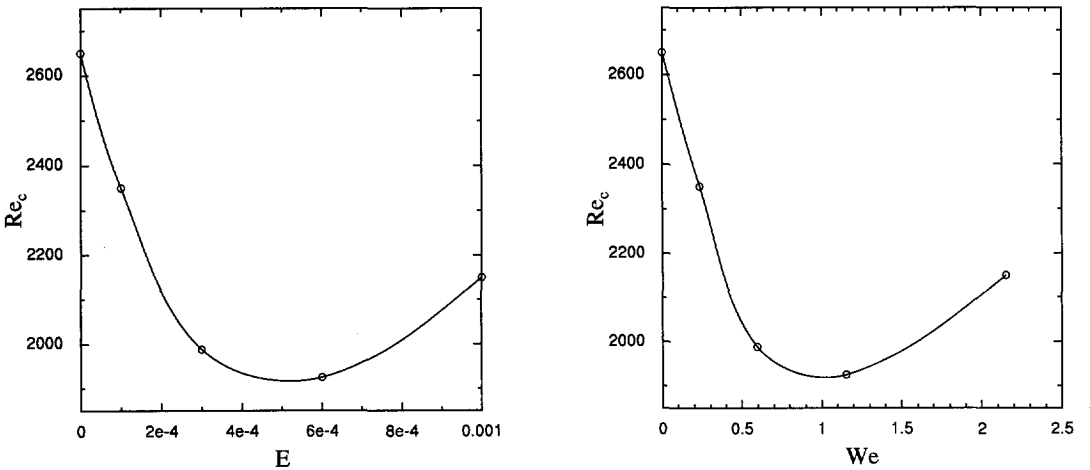


Figure 4.20: The minimum critical Reynolds number for the Upper Convected Maxwell model as a function of the elasticity number, E , and the Weissenberg number We .

Table 4.3: Critical parameters for the Upper Convected Maxwell fluid. We included the maximum value of b_{11} in the parabolic flow which is located at the wall. From its definition, it can be deduced that the following relationship applies: $b_{11, \max \text{ base flow}} = 1 + 8We^2$.

E	Re_c	We	α_c^*	$b_{11, \max \text{ baseflow}}$	$b_{11, \max}$
0	2650	0	1.35	0	0
0.0001	2350	0.235	1.40	1.4	5.0
0.0003	2000	0.600	1.40	3.9	17.3
0.0006	1925	1.155	1.38	12.5	44.7
0.0010	2150	2.150	1.30	37.9	57.3

number is relatively large, so this observation should be treated with caution.

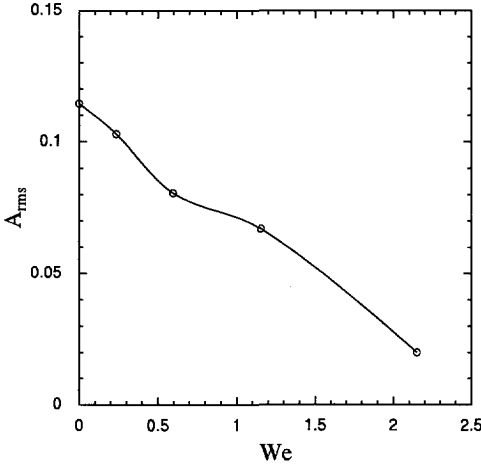


Figure 4.21: A_{rms} , including the mean flow distortion, at the minimum critical Reynolds number as a function of the Weissenberg number, We .

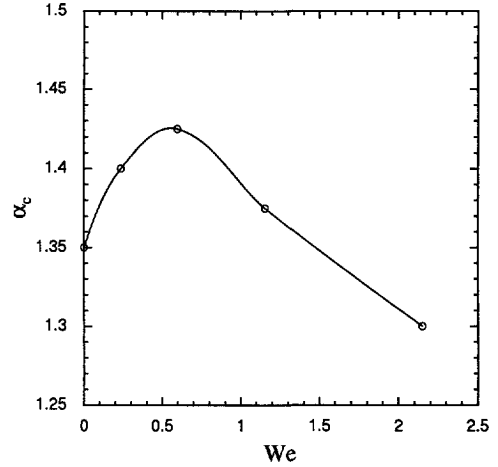


Figure 4.22: α_c^* at the minimum critical Reynolds number as a function of the Weissenberg number.

Comparing the disturbance stream functions at the minimum critical Reynolds numbers for various elasticity numbers, figure 4.23, shows that the shape of the disturbances does not change significantly with an increase in elasticity, and is very similar to the Newtonian saturated disturbances.

A different picture arises when we plot in figure 4.24 the $(1,1)$ -component of the conformation tensor \underline{b} , i.e. b_{11} . To interpret these contour plots, the solution for the parabolic Poiseuille flow is useful. Equation 4.17 gives $b_{11} = 1 + 2(\lambda\dot{\gamma})^2$ for the parabolic base flow. Since the largest shear rate is found at the wall, the maximum value for b_{11} occurs at the wall. Substitution of the shear rate at the wall in equation 4.17 gives $b_{11} = 1 + 8We^2$. These values together with the maxima found at the minimum critical Reynolds numbers are listed in table 4.3. When we compare the values of b_{11} for the base flow with that for the critical flow, we see that the

disturbances roughly cause an increase in b_{11} , viz. in elastic deformation in flow direction, by a factor of 4 and is highly localized. For $E=10^{-3}$ this increase is only 50%, which is mainly caused by the drastic reduction in disturbance amplitude, and is much more spread out in the flow. Since b_{11} shows a quadratic dependence on the Weissenberg number, the maximum in b_{11} increases rapidly for $We \geq 1$. Thus, large elastic deformation in the flow directions is found close to the wall for high We . This can be interpreted as stretching of the polymers close to the wall. These results suggest that randomly coiled polymers cause a destabilization of the flow. When the polymers are stretched at high Weissenberg numbers, a stabilizing influence is found for polymer solutions.

4.8 Summary and discussion

In this chapter, we have shown that our program can accurately predict linear stability for both Newtonian as well as UCM fluids in plane Poiseuille flow, as follows from a comparison with results previous published by (Orszag 1971), (Liu *et al.* 1991), (Porteous 1971), and (Lee & Finlayson 1986). To obtain this accuracy, we found that higher order finite elements are required. Next we extended the computations to 2-D finite amplitude disturbances in plane Poiseuille flow for a Newtonian fluid. The results for the upper-branch solutions, which have an amplitude that is saturated, are in excellent agreement with results published by Herbert (1976).

Based on these good results, we were confident that our computation could be extended the calculation of nonlinear disturbances of an UCM fluid. Subsequently, a large parameter study has been performed to investigate the existence of saturated 2-D disturbances both in Newtonian and non-Newtonian fluids. This has yielded several interesting results:

- The minimum Reynolds number for which saturated 2-D disturbances exist in a Newtonian medium is $Re_c \approx 2650$ for dimensionless wave number $\alpha_c^* \approx 1.35$. This result is in good agreement with calculations by Jiménez (1990) and Herbert (1976). From Jiménez' results, it can be estimated that in his case $2500 \leq Re_c \leq 2800$ where Re_c is based on flow rate. Herbert found $Re_c = 2935$ for $\alpha^* = 1.32$ based on the pressure gradient. If we try to correct this to the corresponding flow rate, it can be estimated that $Re_c = 2640$. The latter is very close to our result.
- Similar behavior has been reported for linear calculations by Sureshkumar & Beris (1995b), but for the linear case the minimum critical Reynolds number is $Re \approx 1672$ at $We \approx 4.18$. Thus, for the nonlinear saturated disturbances, stabilization occurs at a smaller Weissenberg number and at a higher Reynolds number than for linear disturbances. The linear critical Reynolds number reported by Sureshkumar & Beris for $E=10^{-3}$ is $Re_c = 2310$, which is larger than the $Re = 2150$ for the saturated 2-D disturbances, i.e. the flow is still more unstable to nonlinear disturbances than to linear disturbances. However, if Re_c continues to increase with the elasticity number above 10^{-3} , the critical Reynolds number in the linear case would become smaller than that for saturated 2-D nonlinear disturbances studied here. This could suggest that above a certain elasticity number, the subcritical transition (finite amplitude disturbance exist below the linearly critical Reynolds number) for small E changes into a supercritical transition, i.e. finite amplitude disturbances exist only above the critical Reynolds number for linear disturbances. But this is very

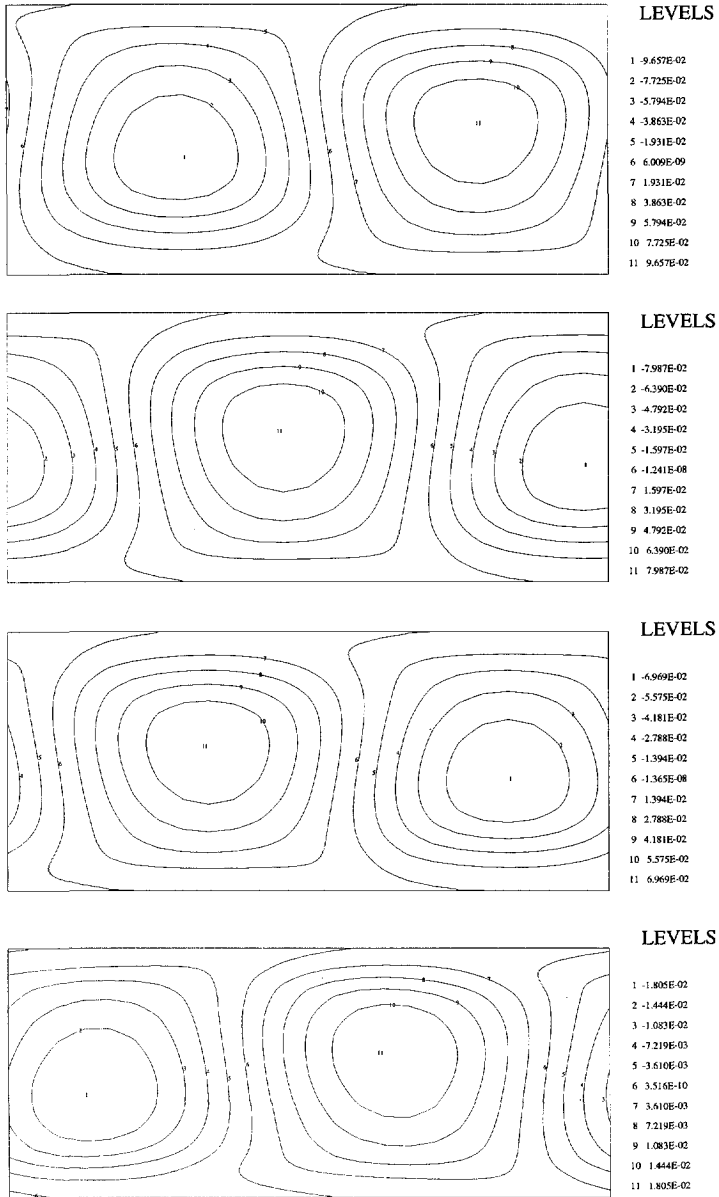


Figure 4.23: Disturbance stream functions at the minimum critical Reynolds numbers for $E = 10^{-4}$, $3 \cdot 10^{-4}$, $6 \cdot 10^{-4}$, and 10^{-3} from top to bottom respectively.

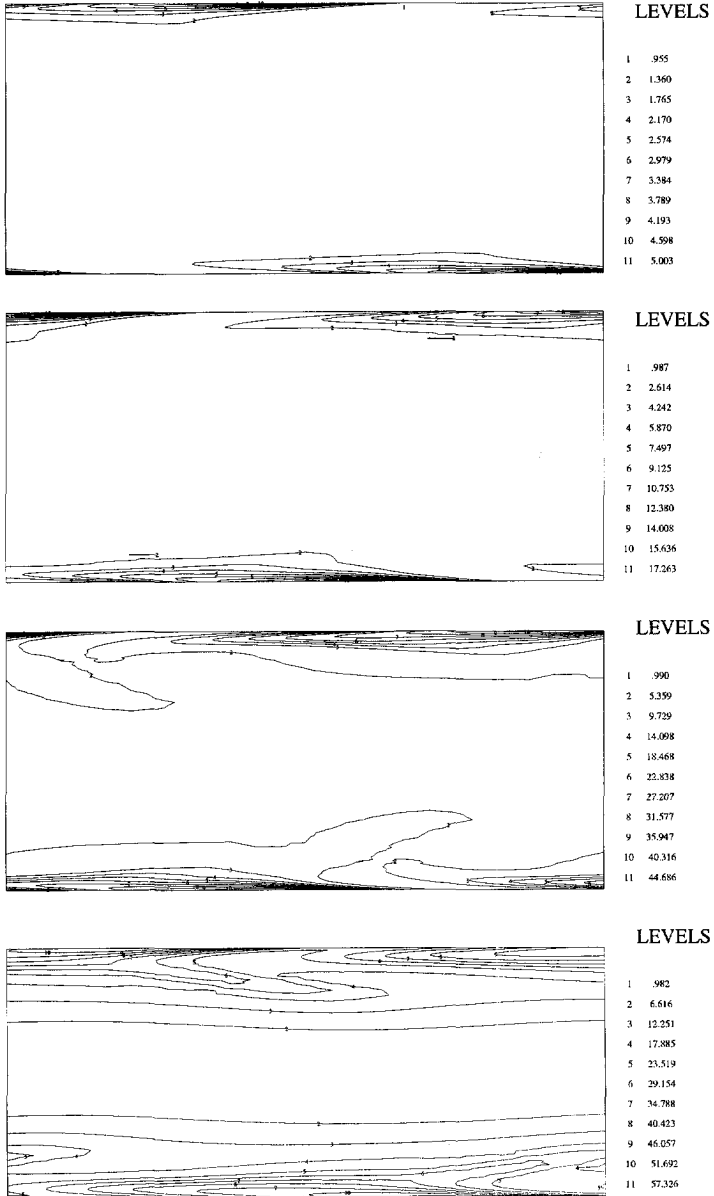


Figure 4.24: Contourplots of b_{11} at the minimum critical Reynolds numbers for $E = 10^{-4}$, $3 \cdot 10^{-4}$, $6 \cdot 10^{-4}$, and 10^{-3} from top to bottom respectively.

speculative, since the disturbances considered in our investigation are strongly nonlinear whereas the sub/supercritical transition is determined governed by the behavior of weakly nonlinear disturbances.

- The speculation by Porteous & Denn (1972b), based on their weakly nonlinear stability calculations for second-order fluids, that for larger amplitudes elasticity might be stabilizing rather than destabilizing cannot be confirmed by our computations of the saturated 2-D finite amplitude disturbances for the Upper Convected Maxwell model.
- The position of the ‘cigar’-like area where the 2-D saturated disturbances exist for the UCM model depends on the value of the Weissenberg number. For $We < 1.04$, we find that the introduction of elasticity destabilizes the flow and Re_c decreases when the We is increased. The minimum in the critical Reynolds number is $Re \approx 1920$ and occurs for $We = 1.04$. For $We \geq 1.0$, elasticity has a stabilizing effect so that Re_c increases again. The conformation tensor \underline{b} , which is a measure of the elastic deformation of a visco-elastic fluid, reveals that stretching in the flow direction is strongly increased at these high Weissenberg numbers. Translated to the polymer conformation, this could suggest that for stabilization, the polymers have to be stretched in order to show a stabilizing effect.

In the light of the present results of our stability calculations, it is interesting to look at some of the experiments with coiled polymers. The majority of the non-Newtonian transition literature, where mostly dilute solutions of flexible, linear, high-molecular weight polymers like Polyox (Polyethyleneoxide) or Separan (Polyacrylamide) are used, reports no change in transition behavior. These polymers are forced to have, on the average, a coiled conformation. However, many experiments in pipe diameters of several millimeters to one centimeter show a *delay* in transition (e.g. Castro & Squire 1967, White & McEligot 1970, Chung & Graebel 1972, Wójs 1993). Also, when experiments are performed for several pipe diameters, the delay in transition is larger for the smaller pipe diameters.

This behavior might be explained when we consider the definition of the elasticity number:

$$E = \frac{\eta\lambda}{\rho h^2} \quad (4.21)$$

For a given fluid, i.e. η and λ are constant, a reduction in channel half-width (or pipe diameter) increases the elasticity number quadratically. The Weissenberg number is related to the elasticity number as $We = Re \cdot E$. Therefore, when for a given Reynolds number the pipe diameter is decreased, this will strongly increase E and with it We .

From our strongly nonlinear stability calculations, we see that stabilization begins at $We = 1$. As a result, stabilization can occur in small pipe diameters leading to a delay in transition, whereas in large diameter pipes for the same Reynolds number We is too low and no stabilization can occur. Our non-linear stability calculations show that for $We > 1$, the elastic deformation in flow direction increases rapidly with We . Under such conditions, polymers can be stretched. Thus, the delay in transition which is found in small diameter pipes for randomly coiled polymers may be seen as ‘circumstantial evidence’ for the view that the polymers need to be stretched in order to delay the transition to turbulence to higher Reynolds numbers.

That shear flows can indeed stretch polymers is illustrated in calculations on the behavior of a FENE-bead spring polymer model in a turbulent flow by Massah *et al.* (1993). They show that the polymers stretch both in the viscous sublayer as well as in the buffer layer if the time constant of the polymer is large enough compared to the rate of shear at the wall⁶. In the viscous sublayer, the stretching is constant and the polymer is almost aligned in the flow direction, resulting in large additional normal stresses in the flow direction, which is very similar to what we find in our simulations. In this respect, it is also interesting to look at the results obtained by den Toonder (1995) for turbulent flow in pipes. He used Direct Numerical Simulation techniques and used some simple fluid models to investigate the effect of elasticity and stretched polymers on drag reduction. He shows that the key property for drag reduction is the purely viscous anisotropic stress which is introduced by the extended polymers, and elasticity has an adverse effect on drag reduction.

Based on these findings, we conjecture that stretching of the polymers is vital to achieve a delay in laminar-turbulent transition to higher Reynolds numbers. In order to pursue this line of research, we designed and constructed a pipe facility to study the transition behavior of fully developed pipe flow of polymer solutions. The design of the experimental setup is discussed in detail in the next chapter. The stability measurements of Newtonian and non-Newtonian fluids are presented in chapters 6 and 7 respectively.

⁶For plane Poiseuille flow of an UCM model, the dimensionless shear rate at the wall is 2 whereas the flow time-scale used in the definition of the Weissenberg number is 1. Thus, when the shear rate at the wall is used in the definition of We , the minimum critical Reynolds number in our nonlinear stability calculation would be located at $We=2$.

Chapter 5

Experimental setup

Abstract

In this chapter, we will focus on the design and construction of a pipe-flow facility, specially designed for the study of transitional and turbulent pipe flows, both for the Newtonian fluid water and for polymer solutions. The pipe length to diameter ratio is very long ($L/D=800$) and the laminar flow is fully developed for $Re \lesssim 14\,300$. It has been designed as a recirculatory facility which is very unusual for transition flow facilities. Nevertheless, its natural transition Reynolds number (based on bulk velocity and diameter) of more than 60 000.

We found that the flow is very sensitive to small differences in temperature between the water and the ambient air which may cause secondary buoyancy drive secondary circulations. Also, we found that the influence of the earth's rotation on the laminar pipe flow is not negligible for $Re > 5\,000$ which leads to strongly asymmetric axial velocity profiles.

As we are able to maintain laminar flow up to very high Reynolds numbers, we can study the stability of the flow to artificially added disturbances. We constructed a disturbance mechanism that generates a non-axisymmetric disturbance of which the magnitude and the frequency of the disturbance can be changed continuously over a wide range. To detect transition to turbulence, we used pressure drop measurements and Laser Doppler Velocimetry techniques.

5.1 Introduction

Transition to turbulence is caused by disturbances that grow until they are large enough to trigger transition. Some flows are linearly unstable, which means that very small disturbances will grow above a certain Reynolds number (examples are plane Poiseuille and boundary layer flow). Other flows, like cylindrical Poiseuille flow are believed to be stable to all linear disturbances. However, in practical applications, pipe flows are likely to be turbulent above $Re \gtrsim 2\,300$. This means that transition must be caused by large disturbances which show nonlinear growth. Such disturbances may be introduced into the flow by bends, pumps, sudden contractions or expansions, or other irregularities in the pipe geometry.

So, the common view is that in the absence of linear instability, transition is caused by large nonlinear disturbances directly, i.e. transition does not originate from linear disturbances that first must grow to become large and nonlinear. This transition mechanism is also known as by-pass transition, and is still poorly understood. Most nonlinear theories which describe transition, depart from linear instability. The fact that linear instability does not exist in this case, makes the theoretical approach much more difficult and as yet no theory has been able to resolve the problem. This leaves only two routes open to be followed; i.e. numerical simulation and experiments.

Numerical simulation techniques applied to transition problems have shown very nice results in the past, and it promises to solve many present mysteries of the transition process in the future. Particularly, in boundary-layer and plane Poiseuille flows, numerical simulations of transition have been very successful (for a review see e.g. Kleiser & Zang 1991). Both the temporal as well as spatial development of disturbances have been studied. Direct numerical simulations in pipe flows are somewhat more complicated due to the cylindrical geometry. However, in the past few years progress has been made on the direct numerical simulation (DNS) of fully developed pipe flow (Eggels *et al.* 1994). It is to be expected that numerical simulations of pipe-flow transition will soon be able to study disturbed pipe flows at high enough Reynolds numbers so that the actual transition to turbulence can be captured. Also, numerical simulations of non-Newtonian turbulent pipe flows emerge (e.g. Toonder 1995). This requires even more computer power than for Newtonian flow simulations, so that numerical simulation of non-Newtonian transition will take a few years more to become established. Nevertheless, we expect it to be available in the next millennium.

Research in transition, and particularly transition in pipe flow, started with the publication of Reynolds (1883). Ever since, many investigators have tackled the transition problem in pipes. Although, progress has been made, the problem is still far from being solved. Recent advances in numerical simulations and nonlinear dynamical systems theory as well as the discovery of so-called algebraic or transient growth of disturbances, has renewed the interest in transition research. All these developments call for detailed experiments on flow stability in Newtonian fluids and should preferably be also extended to non-Newtonian fluids.

Laminar-turbulent transition in e.g. industrial applications normally occurs at the minimum critical Reynolds number because large flow disturbances are present. Given the fact that the details of these disturbances are generally not known, it seems preferable to study pipe-flow transition under more controlled circumstances. This is possible when the flow is maintained laminar up to high Reynolds numbers (e.g. Wygnanski & Champagne 1973 and Pfenniger 1961) and the transition to turbulence is triggered by adding a well controlled disturbance. In this manner, we know the characteristics of the disturbance that actually triggers transition and are also in a position to easily change parameters like frequency and magnitude of the disturbance so that we can study the development of transition as a function of the disturbance.

Our first step has been to review existing experimental pipe-flow facilities that have been used in the past to perform such studies, which is the subject of section 5.2. Against this background we have designed a new experimental pipe-flow facility which is especially suited for the study of laminar-turbulent transition, in particular also at Reynolds numbers much larger than the minimum transition Reynolds number and that can be used for Newtonian and non-Newtonian fluids. The specifications, the design and construction of this new facility is the main subject of this chapter. The following sections are dedicated to a detailed discussion of the various vital components in the setup, e.g. the settling chamber, the pipe sections and the LDV-measurement sections, the pump and polymer mixing facilities. The characteristics of the measurement equipment are reviewed in section 5.11. The overall flow characteristics of our pipe-flow facility will be discussed in section 5.12 to illustrate the quality of the experimental setup. its quality. Finally, the mechanism used to generate the disturbances that trigger the transition is described in section 5.13.

This chapter contains many details which are directed to fellow experimenters and thus a warning to those not falling in this category is in place before reading is continued: Those who find the material presented in this chapter boring, are strongly advised to refrain from any actions even vaguely resembling experiments. In particular any activities involving pipe geometries and definitely, those concerning water and polymers are to be avoided at all costs.

Nevertheless, non-experimentalists may find it eye-opening to completely read this chapter, just to get some taste of what a painstaking process the construction of a new experimental facility is.

5.2 Existing pipe-flow facilities

We will give a brief overview of some of the experimental facilities that have been used in the past to study pipe-flow transition. All of the facilities mentioned here used a carefully designed entrance, e.g. in the form of a settling chamber or a trumpet entrance. In this way, a low turbulence entry flow is generated which then could develop to a laminar flow above the minimum transition Reynolds number. The most important geometrical characteristics of these facilities are listed in table 5.1 together with the maximum Reynolds for which laminar flow was achieved, i.e. Re_{\max} . Also, the maximum Reynolds number is listed for which the flow can be considered as fully developed at the outlet of the pipe, i.e. $Re_{99\%}$. We use the common definition for fully developed flow that the centerline velocity has reached 99% of the corresponding theoretical value of the parabolic profile. The length which is necessary for the flow to develop from a flat entry profile to this stage is called the entrylength. It depends linearly on the pipe diameter D and the Reynolds number Re (based on bulk velocity and D) according to Christiansen & Lemmon (1965):

$$L_{99\%} = 0.056 Re \cdot D \quad (5.1)$$

When $L_{99\%}$ in equation 5.1 is replaced with the length of the pipe, $Re_{99\%}$ is obtained and is listed in table 5.1. Both Reshotko (1958) and Pfenniger (1961) used a vacuum pump to suck air through the pipe. An adjustable sonic throat was used to regulate the flow rate and to avoid any upstream influence of pressure fluctuations or acoustical disturbances originating from the pump. Also, care was taken to insulate the pipe from mechanical vibrations. Reshotko used an aluminum pipe which consisted of 7 sections of which the inner surface was honed smooth. Connecting section ends have internal diameters which are equal to within $5 \mu m$. In the settling chamber five screens were placed to break-up large scale flow disturbances. The tests were conducted in a completely enclosed, windowless room. The temperature ranged between 20.6 and 25°C with no more than 1.5°C variation during any one day. Careful alignment of the pipe sections was found to be extremely important. Reshotko claims that "changes of as little as 0.010 in. (0.25 mm) in the lateral position of the pipe can cause asymmetries in the flow of the order of 5%", which were attributed to centrifugal effects. He suspected that elongation of the pipe due to thermal expansion resulted in such lateral deflection. This could lead to centrifugal affects. This hypothesis is in agreement with his findings that the deviations from the parabola increase with Reynolds number. Reshotko also found secondary circulations due to buoyancy for very-low-speed flows, leading to an asymmetric axial velocity profile.

Table 5.1: Main characteristics of pipe-flow facilities used to study transition to turbulence. The contraction ratio CR is defined as the ratio of the cross sectional area of the settling chamber to that of the pipe. For comparison, the features of the old short facility and the newly constructed pipe-flow facility are already listed.

Researcher	D mm	L m	L/D	CR	Re_{max}	$Re_{99\%}$	medium
Reynolds 1883	26	1.4	55	tr ^c	13 000	1 000	water
Ekman 1909 ^b	26	1.4	55	tr ^c	45 500	1 000	water
Reshotko ^e 1958	51.3	41	800	36	23 000 ^a	14 300	air
Leite 1959	32	22	700	64	20 000 ^a	12 500	air
Pfenniger 1961	50.8	22.8	450	16	100 000	8 000	air
Fox <i>et al.</i> 1968	13	3.3	250	tr ^c	5 000	4 500	water
Wynanski & C. 1973	33	16.5	500	340 ^d	45 000	8 900	air
Barker & Gile 1981	102	6.1	60	36	250 000	1 100	water
Darbyshire & M. 1995	20	3.8	190	tr ^c	17 000 ^a	3 400	water
Draad 1996	40	32	800	9	63 400	14 300	water

^aLaminar flow existed at the maximum obtainable Reynolds numbers.

^bInformation on Ekman was taken from Pfenniger (1961).

Ekman performed his experiments in Reynolds' original setup.

^cInstead of a settling chamber a trumpet entrance was used.

^dA tandem of a trumpet entrance and a settling chamber was used with a total $CR=340$.

^eThe equipment was designed and the experiments directed by John Laufer.

Further evidence for asymmetric velocity profiles is given by Leite (1959), who found asymmetry in the vertical direction due to thermal convection. The symmetry was restored by the placement of a heating element in the top half of the pipe.

The experimental facility of Pfenninger (1961) used twelve damping screens in the settling chamber. The pipe is made of extruded aluminum alloy tubes of which the inner diameter did not vary more than 0.02 mm. "In order to maintain an uniform temperature distribution at the inlet, the test setup was mounted in a bomb shelter. During the afternoon the temperature gradient was generally slightly stable, thus minimizing the possibility of convection currents in the contraction cone downstream of the screens." Fox *et al.* used a water storage tank and a glass pipe with a trumpet entrance with a contraction ratio of 75:1.

A particularly interesting and widely quoted experiment has been performed by Wygnanski & Champagne (1973). They used a seamless aluminum pipe consisting of five sections. These were chosen out of approximately 100 similar sections in order to minimize and match their eccentricity. After the pipe was fixed and aligned, the entire pipe was honed. Tolerance on the alignment was better than ± 1 mm over the entire length of the pipe. Wygnanski & Champagne thermally insulated the entire pipe assembly and did not take measurements when the temperature deviated more than 0.5°C of the prescribed value. They stress the necessity of maintaining a constant temperature along the entire pipe: "Room air-conditioner vents discharging 8 ft away from the bare pipe or a 100 W bulb placed 60 cm away from the uninsulated plenum chamber could distort the parabolic profile beyond recognition." They used one screen and a honeycomb in their second stage of the settling chamber.

The experiment of Barker & Gile (1981) was aimed at the study of the heat-stabilization of the boundary layer in a laminar pipe flow. They used a 'blow-down' type facility, i.e. the water is not recirculated, for two reasons. First, as heat must be added continuously, a heat exchanger would be needed to maintain a constant temperature. Second, they want the entrance free-stream turbulence level to be less than 0.05% which they found difficult to achieve in a closed water facility. Therefore, they used water from a reservoir which was run through their pipe facility and discharged into a lake below the laboratory. The settling chamber that contained several screens, honeycombs and porous foam and has been operated with two contractions. In the conventional contraction, a suction section right in front of the contraction was used to completely remove the turbulent boundary layer that existed in the settling chamber at high velocities. Barker & Gile found a wave like dependence of the boundary layer velocity in the azimuthal direction. They suggested that this was a result of the generation of Görtler vortices in the concave part of the contraction. However, replacement of the conventional contraction with a bell-mouth shaped inlet did not remove these wave like variation of the velocities. Thus, Görtler vortices did not cause these variations after all.

Finally, Darbyshire & Mullin (1995) perform a pipe-flow transition experiment with a Perspex pipe consisting of sections with a length of 158 mm. These sections were individually machined and assembled to a total pipe length of 3.8 m. This machining was done to ensure a uniform cross section over the entire pipe. The fluid was sucked through the pipe by a cylindrical piston, driven at a constant speed, so a constant mass flux rate system was achieved.

When we compare the maximum Reynolds number for which laminar flow could be maintained, i.e. Re_{\max} , to the highest Reynolds number for which the flow is considered to be fully developed, i.e. for $Re_{99\%}$, big differences can be seen. The most extreme values are found

for Barker & Gile (1981). They achieved laminar flow for a magnificent $Re=250\,000$ but the flow is only fully developed up to $Re=1\,100$. However, fully developed flow at their maximum Reynolds number would require a pipe length of over 1 400 m! In their experiments this was no problem as they wanted to study only boundary layer flow at the wall. Also, Reynolds 1883, Ekman, Fox *et al.* 1968, and Darbyshire & Mullin 1995 used relatively short pipes leaving them little or no variation in Reynolds number to study triggered transition to turbulence in fully developed pipe flow.

Reshotko, Leite, and Darbyshire & Mullin all achieved laminar flow up to the maximum flow rate capacity of their system. Given the care with which their facility was manufactured, it is likely that the quality of the pipe was sufficient to sustain laminar flow at much higher Reynolds numbers.

5.3 Requirements

In this section we will discuss the requirements which can be formulated for our experimental setup. The goal is to successfully measure laminar-turbulent transition in pipe flow for Newtonian and non-Newtonian fluids.

Let us discuss the most important considerations for several of the main features of the pipe-flow facility.

1. *Pipe diameter and length:* These two parameters cannot be considered separately. For the study of triggered transition in pipe flow, it is preferred to have a fully developed flow, since this facilitates comparison with theory and numerical simulations. From equation 5.1 it is then clear that research on triggered transition at high Reynolds numbers for fully developed flow requires a large length/diameter ratio. Since transition can be triggered only for $Re \gtrsim 1\,800$ (Darbyshire & Mullin 1995), $Re_{99\%} \geq 10\,000$ is desirable to have a reasonable range of Reynolds number to perform experiments on fully developed flow. Equation 5.1 then implies $L/D \geq 560$ which can be realized with a short pipe for a small diameter or with a long pipe for a large diameter. When details of the flow have to be measured, a large pipe diameter is preferable. Also, scaling rules for polymer solution flows are still not well understood and pipe diameters of several centimeters or larger would give results that are closer to application conditions than much smaller tubes. Our requirements lead to a large pipe diameter and a long pipe length.
2. *Re-range:* For measurements on triggered transition to turbulence, a Reynolds number range of 2 000 to 10 000 would be a minimum requirement. An extension to larger Reynolds numbers would be desirable, especially when we want to study scaling rules of e.g. minimum disturbance amplitude needed for transition with Reynolds number.
3. *Measurement time:* Accurate measurements of statistics of fluctuating quantities, such as occurring during transition and turbulent flow of water and polymer solutions, implies a long measurement duration. For turbulence measurements, the required measurement time increases rapidly when increasing the order of the statistics, and measuring times may have to become as long as several hours.

For triggered transition measurements, measuring times can even become longer. This is mainly caused by the many parameters that can be varied, i.e. Reynolds number,

disturbance magnitude, and disturbance frequency. This results in a large number e.g. Reynolds number–disturbance amplitude combinations for which the frequency at which transition to turbulence occurs has to be determined. These measurements typically take several days.

The combination of a large pipe diameter and the Reynolds numbers mentioned in item 2. leads to fairly large fluid quantities that have to be pumped through the pipe. With this large fluid volume, pre-mixing the amount of polymer solutions required, makes a ‘blow-down’ type facility practically impossible. Thus, a recirculatory flow facility is needed. However, recirculation may lead to polymer degradation. Therefore, we must optimize our experimental set-up in order to minimize degradation of the polymer solution such that the properties of the polymer solutions are fairly constant during a measurement.

4. *Constant flow rate vs. constant pressure gradient:* For a constant-pressure-gradient driven flow system, oscillation in flow rate can occur when the flow is near the transition. If transition to turbulence occurs, this leads to a decrease in flow rate when the constant pressure drop remains constant. At this lower flow rate, relaminarization may occur, accompanied by a low pressure drop. Thus the flow rate increases again which in turn results in transition. Such behavior is highly undesirable. Also, the Reynolds number decreases during a transition to turbulence. For these reasons, we prefer to use a constant flow rate.
5. *Cleaning:* Polymer solutions can be used only for a limited amount of time. Thus, the solutions have to be changed regularly. In order to clean the experimental setup and to remove old polymer solutions, the flow facility should be designed such that the polymer solutions can be easily discharged. The amount of solution that stays behind should be minimized and filling the facility with a fresh polymer solutions should be easy.

These are the most important requirements for the new experimental setup. Many of the other requirements and choices will be discussed while we discuss the details of our setup. Before starting this discussion, we should begin with some background on the polymer solutions and in relation to this a discussion on the pump. This will be the subject of the next section which also includes some of the degradation tests that we performed within the framework of the design process.

5.4 Pumping polymers

The reason for discussing the polymers in combination with the pump is the fact that polymer solution degrades by mechanical action both by the flow and the pump. Let us first define mechanical degradation as the process of breaking of the polymers by mechanical actions. Highly turbulent flows and pumps (in particular several types of pumps) can cause mechanical degradation, and the result is a reduction of the molecular weight of the polymer. This in return has a strong effect on e.g. its non-Newtonian properties. Since we plan to use a recirculatory facility, special attention should be paid to mechanical degradation. This will in principle determine the maximum measuring time, because severe mechanical degradation would lead to unacceptable changes in the measurement conditions.

To select a suitable combination of polymer and pump, we performed several degradation tests to find out which combination of polymer and pump would minimize mechanical degradation. For experiments with dilute polymer solutions, polyethylene-oxide (PEO) and polyacrylamide (PAM) are probably the polymers that are most often used, in particular Polyox WSR-301 (Union Carbide) and Separan AP-273 (Dow Chemical Company; presently delivered by Floerger (France), under the name Flocculant AP-273). In addition to these two polymers, we studied also Superfloc A-110 (Cytec Industries, formerly American Cyanamid Company) which is a partially hydrolyzed polyacrylamide (PAMH). Superfloc A-110 was mainly included in the tests because it changes its conformation depending on the salt concentration which results in spectacular changes in flow behavior and possibly in transition behavior as well (Virk & Waggar 1990 and also section 7.2 on page 157).

All three polymers mentioned above are commercially available bulk products mainly used as flocculants in water treatment facilities. PEO is a linear, flexible molecule which is commercially available in a range of molecular weights (MW). Polyox WSR-301 has a MW of $4 \cdot 10^6$ g/mol. Separan AP-273 (PAM) has a molecular weight of $4 - 6 \cdot 10^6$ g/mol. PAM differs from PEO in that it has a side chain. Superfloc A-110 is partially hydrolyzed polyacrylamide (PAMH) having a molecular weight of $6 - 8 \cdot 10^6$ g/mol, where hydrolysis is a chemical process of decomposition involving splitting of a bond and addition of the elements of water. As a result, PAMH has two possible side chains. The chemical structures of the three polymers are shown in figure 5.1.

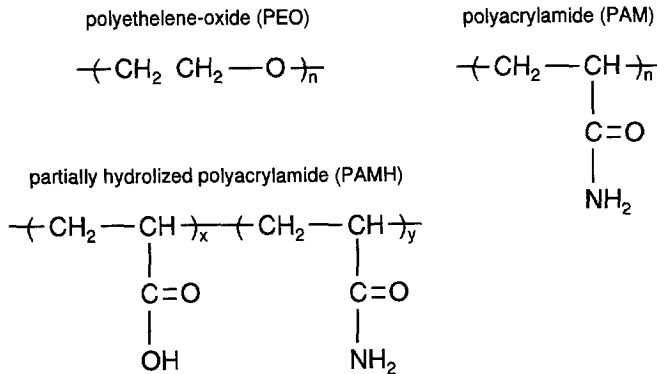


Figure 5.1: Chemical structures of the polymers used in the preliminary investigation on mechanical degradation.

Polymers can be subject to oxidative degradation by e.g. chlorine and peroxides. Furthermore, metal ions such as copper, iron and nickel enhance oxidative degradation. Polyacrylamide solutions are noncorrosive to most common construction materials, but galvanized (zinc) or aluminum equipments should be avoided for corrosion reasons. It is therefore advisable to minimize the use of metals in the facility in components which have direct contact with the solution.

The type of pump is clearly very important with respect to mechanical degradation. Pump types which are known to be 'polymer friendly' are positive displacement pumps, i.e. gear and Moyno pumps (progressive cavity pump). However, these pumps give a pulsating flow. Moreover they are very expensive, especially when no metal interior parts are allowed. On

the other end of the spectrum stands the centrifugal pump which is notorious for its high mechanical degradation of polymers. An alternative pump type is the disc pump (Discflo Corporation, California USA). A disc pump is essentially a centrifugal pump with discs instead of fans. The fluid enters the pump through the central orifices in the discs (see figure 5.2). Since the blades of a centrifugal pump are absent, the flow through a disc pump is much less vigorous. This pump type is used in industry where damaging of solids in the fluid needs to be avoided, e.g. pumping corn or strawberries.

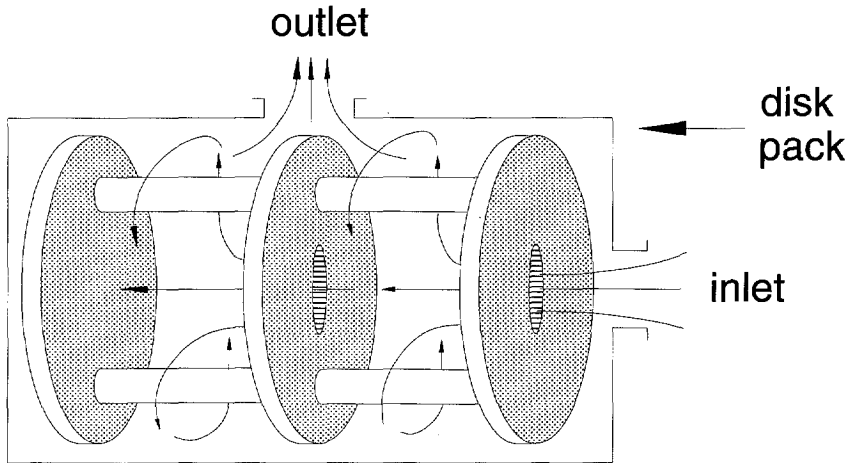


Figure 5.2: Sketch of the disc pump.

We studied the mechanical degradation of the centrifugal and the disc pump in combination with the three polymers mentioned earlier. To estimate degradation, we measured the drag reduction capability of the polymer solution as a function of time in a turbulent pipe flow, because drag reduction is directly dependent on the quality of the polymers. Before discussing the results we need an indicator for the amount of mechanical degradation that has occurred. For this we use the amount of drag reduction capability of the polymers. We use the following definition for the amount of drag reduction:

$$DR = \left(\frac{f_{M,s} - f_{M,a}}{f_{M,s}} \right) \times 100\% \quad \text{at constant } Re \quad (5.2)$$

where $f_{M,a}$ is the friction factor for the additive solution and $f_{M,s}$ is the friction factor for the solvent alone. The Moody friction factor f_M is defined as

$$f_M = \left| \frac{dp}{dx} \right| \frac{D}{\frac{1}{2}\rho\bar{W}^2} \quad (5.3)$$

Where $|dp/dx|$ denotes the pressure gradient, ρ the density of the solution, and \bar{W} the bulk velocity. If the viscosity is not increased by the addition of polymers, keeping Re constant is

equivalent to a constant flow rate Q . For coiled polymers, assuming that the viscosity does not change is a reasonable approximation¹. Then, equation 5.2 is equivalent to

$$DR = \left(\frac{\Delta p_s - \Delta p_a}{\Delta p_s} \right) \times 100\% \quad \text{at constant } Q \quad (5.4)$$

where Δp is the pressure drop measured between two pressure measuring holes.

Detailed information on the degradation experiments can be found in Toonder *et al.* (1995). Here, we present only some of the most important results. Comparing the measurements for a 20 ppm Separan AP-273 solution with the centrifugal and the disc pump, clearly affirms the severe mechanical degradation caused by the centrifugal pump. A disc pump is clearly to be preferred over a centrifugal pump as follows from figure 5.3.

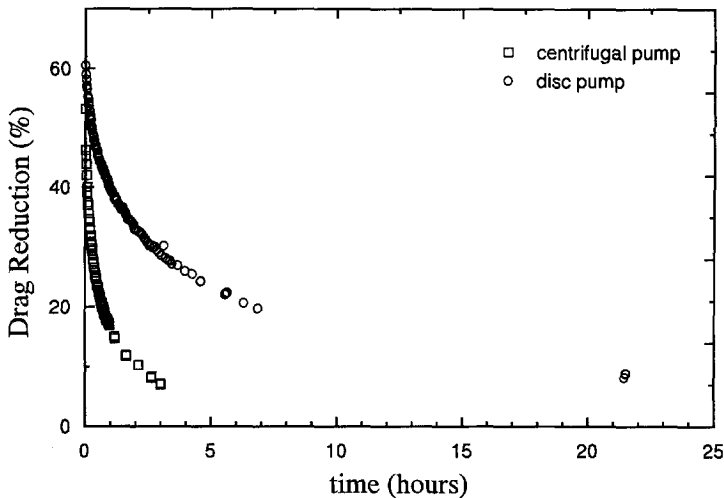


Figure 5.3: Degradation of 20 ppm solution of Separan AP-273 in tap water for different pump types. $Re=19\,500$ and $Q=151/\text{min}$. The volume of the closed flow loop is 13 l.

Thus, the pump type strongly influences the amount of mechanical degradation, but also the polymers themselves display a large difference in resistance to mechanical degradation, which we illustrate in figure 5.4. The Polyox solution shows a fast degradation; i.e. within 20 minutes, the drag reduction was reduced to a few percent. Clearly, Polyox is not suited for use in recirculatory facilities. The Separan solution is much more stable. After 21.5 hours of recirculation still 9% drag reduction remained and thus degradation was relatively slow. The Superfloc solution is clearly the most stable solution. After about 20 hours of recirculation, a plateau² of about 18% drag reduction seems to be retained.

Also, the amount of drag reduction shown in figure 5.4 shows a reasonable correlation with

¹Even at these concentrations of 20 ppm a small increase in viscosity can be observed. For stretched polymers such an assumption is certainly no longer valid. For a more detailed discussion and measurements see chapter 7 and appendix E.

²Such a plateau was not found in the newly built experimental setup (Toonder 1995).

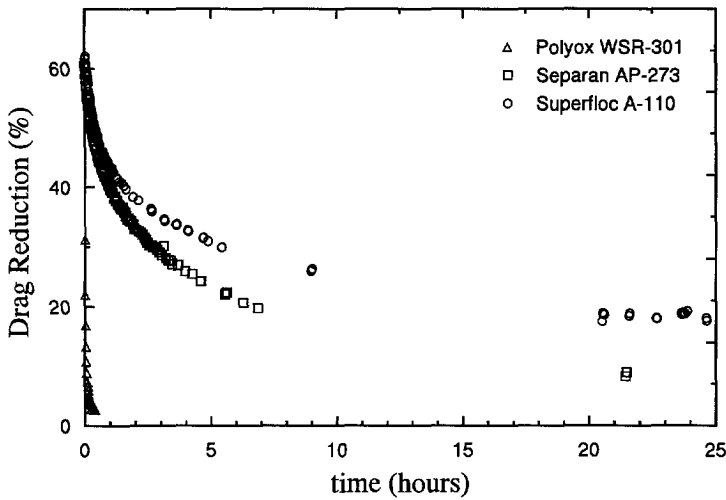


Figure 5.4: Degradation of different 20 ppm polymer solutions in tap water. $Re=19\,500$ and $Q=151/\text{min}$. The volume of the closed flow loop is 131.

the number of passes through the system. This indicates that a large system volume reduces the rate of mechanical degradation, and thus results in fairly constant conditions during the measurements of e.g. a velocity profile.

Summarizing, we have seen that the combination of the partially hydrolyzed polyacrylamide, Superfloc A-110, and a disc pump leads to the smallest mechanical degradation. Furthermore, the use of metals in the facility should be minimized and a large system volume slows down the decrease in drag reduction capability. In the next section, a general overview of the new setup will be given. In the sections thereafter, a detailed description of some of the most important components in the facility is given together with the main design criteria and considerations.

5.5 Overview of new facility

Next, we will give an overview of the experimental pipe-flow facility, which has been designed for the study of the effects of polymer addition on transition to turbulence.

The considerations on the pipe diameter and L/D as presented in section 5.3, lead to a length/diameter ratio of $L/D \geq 560$ and a diameter of at least several centimeters. Given the available space, the pipe diameter of 40 mm was chosen with options to accommodate 20 mm and 80 mm in future. For the length of the facility a maximum of 36 m was available. The settling chamber, discharge chamber, and the flow meter are also to be placed on the same support, thus leaving a net length of approximately 32 m for the pipe. This results in $L/D=800$, viz. the facility places itself among the longest transition facilities (see table 5.1).

A schematic overview of the pipe-flow facility is given in figure 5.5. The facility has two storage vessels, each having a capacity of 0.59 m^3 . A disc flow pump (Discflo corporation, California USA) is used circulate the solution through the settling chamber into the pipe. The settling chamber is used to eliminate swirl and suppress disturbances such that a laminar flow

can be maintained up to high Reynolds numbers. In the pipe, test sections can be placed at any location to study the flow using e.g. Laser Doppler Velocimetry (LDV) or Digital Particle Image Velocimetry (DPIV). At the downstream end of the pipe, a magnetic inductive flow meter (Krohne-Altometer) is used to monitor the flow rate. Finally the flow enters the discharge chamber, which is relatively big, again to increase the volume of the system. A 150 mm return pipe takes the flow back to the storage vessels.

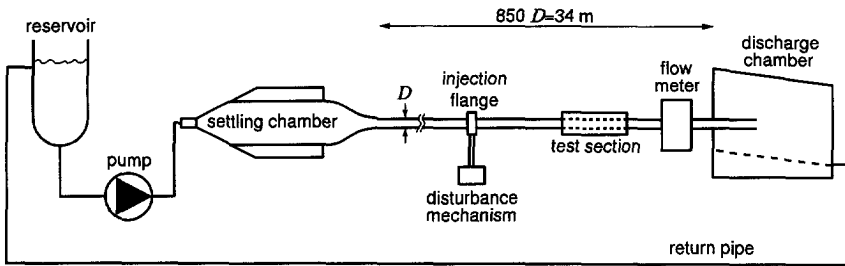


Figure 5.5: Sketch of the new pipe-flow facility for research on the effects of polymer addition on drag reduction and transition. The inner diameter of the pipe is 40 mm.

The disc pump was delivered by Begemann Pompen (presently EnviroTech pumpsystems). They manufactured disc pumps under license of Discflo Corp., California USA. The entire pump housing and the discs are made of epoxy resin in order to avoid any metal contact with the polymer solution. The six discs have an outer diameter of 210 mm and a spacing of 2 mm. The fluid enters the pump through a central orifice in the discs of 80 mm and leaves the discs at the perimeter as a result of the centrifugal force (see figure 5.2). The disc pump is driven by a 2.2 kW electric motor (ABB Motors MT100LB04). The motor is controlled by a frequency regulator (ABB Drives, SAMI-GS-ACS-501004/3) which allows various control options. The motor can be operated at a constant rotational speed. Alternatively, the measured flow rate or pressure drop can be used as an input control signal for the frequency regulator, hence keeping either the flow rate or the pressure gradient constant during an experiment.

To meet the various operational demands, we equipped the facility with an extensive network of pipes. This gives us maximum operating flexibility. The components with the network of pipes and valves is shown in figure 5.6.

To minimize mechanical degradation, the pipes connected to the suction side of the pump, i.e. the pipes connected with valves #1 to #3, and the pipe connecting the return pipe with the reservoir all have an inner diameter of 80 mm. Because of limitations in available space, the pressure side of the pump consists of 40 mm piping and valves.

Before discussing the various operating configurations, we first give the fluid capacities of the various components in table 5.2.

Let us now take a look at some of flow loops that can be realized with network shown in figure 5.6.

- Under normal operating conditions, all valves would be closed except for #1, #5, and #9. In this case the fluid is pumped from the reservoir to the settling chamber, through the measurement pipe, the discharge chamber, and via the return pipe back to the reservoir.

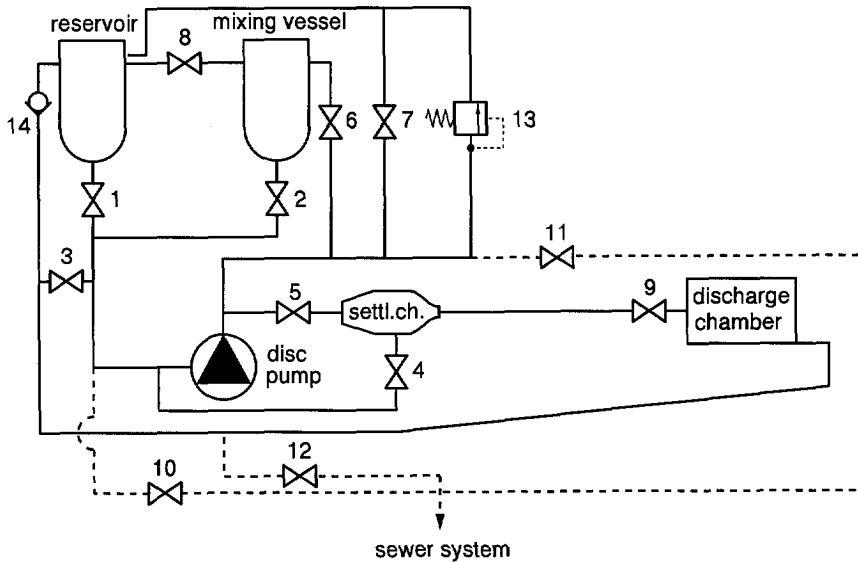


Figure 5.6: Pipe network lay-out with the main components and the location of the valves for the new pipe-flow facility. The two storage vessels are denoted 'reservoir' and 'mixing vessel' after their most common use. #1 to #12 are spherical valves, #13 (how appropriate) is a pressure-relief valve, and #14 is a one-way valve.

Table 5.2: Capacity of the various components in the flow facility in m³. The total system volume with the mixing vessel excluded (normal operating condition) is 1.51 m³. Including the mixing vessel maximizes the system volume to nearly 2 m³. Raising the levels in the vessels may even result in an extra 0.1 m³ per vessel.

Component	Capacity (m ³)
Reservoir	0.48 ^a
Mixing vessel	0.48 ^a
Settling chamber	0.05
Measurement pipe	0.04
Discharge chamber	0.25
Return pipe	0.64
Piping network	0.05

^aThis is the value for the standard level in the vessel.
 Filled till 2 cm of the edge, the capacity becomes 0.59 m³.

This results in a system volume of 1.5 m^3 . Closing valve #1 and opening valves #2 and #8 includes the mixing vessel in the flow loop increasing the system volume to 2.0 m^3 .

- In order to minimize the system volume, the flow facility can be operated without the use of the two vessels. In this case, all valves would be closed except for #3, #5, and #9. In the case that the entire discharge chamber and the return pipe is filled, which is not necessary, the system volume amounts to 1.0 m^3 . Operating with an empty discharge chamber and only partly filling the return pipe, one could further reduce the system volume to something like 0.4 m^3 .
- When filling the pipe with a polymer solution, the typical procedure would be the following. First operate the facility with water. This is necessary to get rid of dissolved air in the water which likes to accumulate at low velocity places. The place where the problems are encountered is in the settling chamber, where small air bubbles stick to the contraction wall and also block the fine screens. Normally, circulation for one or two days is needed to eliminate these bubbles. Then, after closing all valves and opening valves #3, and #6 or #7, the water can be pumped back into the storage vessels. This is the configuration where the one-way valve #14 is needed to prevent air from entering the suction side of the pump. Then, after closing #3, depending on the position of valves #1, #2, #6, #7, and #8, the fluid can be circulated in each vessel separately or between the two storage vessels. In this situation, concentrated polymer solution can be added to the water to produce the dilute polymer solution. The impeller mixer can also be placed in a vessel to enhance the mixing process.

After the mixing of the dilute solution is finished, all valves are closed and #2 is opened to release the content of the mixing vessel into the return pipe. Then, closing valve #2 and opening valves #1, #5, and #9 in this order will start the flow of the dilute polymer solution while the water in the settling chamber and the measurement pipe, is mixed in. In this way, the polymer solution does not have to circulate for one or two days to eliminate the air bubbles that would have been present if fresh water was used to make the dilute polymer solution.

- When all valves at the pressure side of the pump are closed, a dangerous situation can emerge. Particularly dangerous is the situation where the pump is regulated to give a constant flow rate and suddenly the last open valve on the pressure side of the pump is closed. This would cause the pump to accelerate to its maximum rotational speed (which can be programmed in the pump control unit). Then, the pressure-relief valve #13 opens and discharges into the reservoir to prevent any damage to the facility.
- The outlet of the settling chamber is connected to the suction side of the pump by means of valve #4. By opening this valve, we can use the disc pump to (partly) empty the settling chamber into one of the storage vessels.
- Valve #9 is added to be able to isolate the measurement pipe from the rest of the facility, e.g. when making the dilute polymer solution. It can also be used as a throttle valve. This can stabilize the control of the pump at very low flow rates by introducing extra

resistance. Such a throttle valve has to be located before the discharge chamber in order to prevent exposure to large pressures which could overload the chamber.

- Valves #10 through #12 are drain valves used to discharge the fluid into the sewer system. The polymers we used are non-toxic and at the quantities that we use they do not disturb the waste-water purification process.
- To prevent any large dirt particles to enter the pump and the settling chamber, we placed a filter element in the pipe at the suction side of the pump. The screen size that we used in this filter element is 0.5 mm.
- A large amount of three-part threaded couplings have been used for easy assembly and access of the various piping sections. Also, all spherical valves have threaded ends. In this way, the valves do not have to be glued to the piping and can be reused when changing the piping layout.

Now that we have presented an overview of the new facility, we will further discuss the most important components in the system separately. The mechanical construction that constitutes the backbone of the pipe-flow facility is discussed in section 5.6. The central part of the facility is of course the pipe itself. This, the test sections, and the flow meter are reviewed in section 5.7. In order to obtain laminar flow at high Reynolds numbers, a high-quality pipe is needed together with a carefully designed settling chamber. The design of the latter is presented in section 5.8. In the section thereafter, the features of the discharge chamber and the return pipe are explained. The dispersing vessel, i.e. the smaller vessel in which the concentrated master polymer solution is prepared, is discussed together with the two storage vessels in section 5.10. In section 5.11, we will discuss some of the measurement equipment that we used, like the pressure drop transducer, the flow meter, LDV and DPIV equipment, and thermometers. Then we will present some of the results to give an indication of the quality of the pipe and some of its peculiarities. Finally, the design of the disturbance mechanism that we used to trigger the transition to turbulence is considered.

5.6 Mechanical backbone

The mechanical support for the measurement pipe constitutes the backbone of the facility and is 36 m long. It consists of 6 H-beams (HE-A 200, 200 mm wide and 190 mm in height, each 6 m long), that are placed on supporting beams, mounted on 0.7 m high concrete fence posts (Heras Hekwerk) as shown in figure 5.7. A total of 20 fence posts is used, placed every 2 m, three for each H-beam and an additional one at each end of the facility, where the settling and the discharge chamber are placed. The settling chamber and the discharge chamber are mounted on the H-beams as well. For this, two 1 m long H-beams are placed next to the central H-beam on the support beams at each end of the 36 m long support structure. As the discharge chamber is placed directly on the three H-beams (the central one plus two 1 m H-beams at each side), we constructed a leveled the top surface using epoxy resin.

To insulate the facility from mechanical vibrations³, we placed the concrete fence posts on 6

³As support for this, we quote that modern traffic in the streets of Manchester made the critical Reynolds number in Reynolds' original apparatus lower than the value of 13 000 found by Reynolds (Dyke 1982, p. 61).

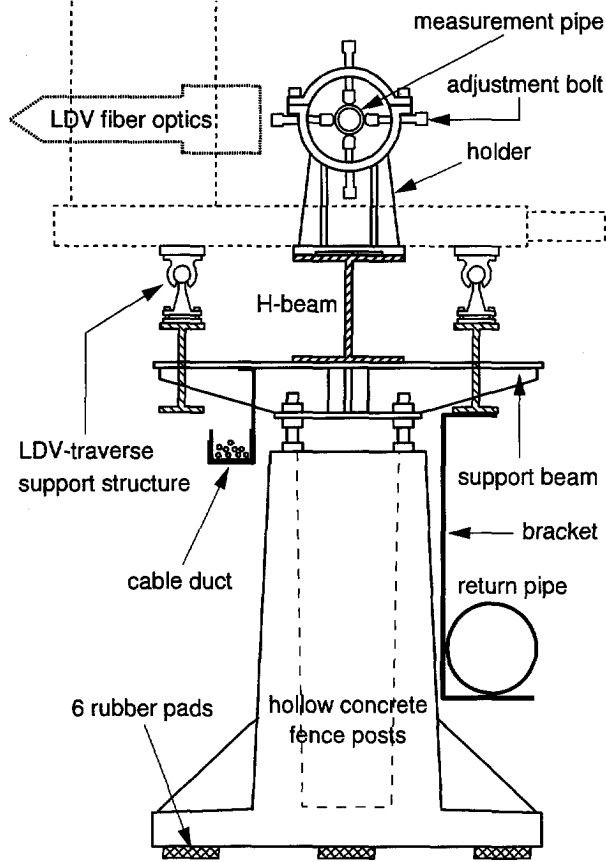


Figure 5.7: The mechanical support structure of the pipe-flow facility which in essence functions as the backbone on which all components are mounted, except for the disc pump and the storage vessels. Here, the pipe is drawn without the insulation material which is used to suppress convection. The brackets for the return pipe are not drawn.

sponge-rubber pads (diameter=100 mm and height=15 mm). These rubber pads also compensate for irregularities in the concrete of the posts and the basement floor. Four threaded bushes (M20) are casted in the concrete fence posts. The threaded ends are used to adjust and fix the supporting beams. The H-beams were not entirely straight and the two flanges not exactly parallel. Therefore, the H-beams are placed such that on average a reasonably straight and horizontal top surface is obtained on which the holders for the measurement pipe can be placed. The 6 m H-beams are connected to each other with three steel plates, one is bolted to the top flange and the other two are placed at each side of the vertical core of the H-beam. In this way, we obtained a very stiff construction that is mechanically insulated from the environment and which provides a good platform on which all the components of the flow loop can be mounted. The pump and the two vessels (mixing vessel and reservoir) have a separate support structure.

A rubber bellow is placed at the suction side of the pump. The pressure side of the pump is connected to the settling chamber through a rubber hose. Similarly, a rubber hose is used to connect the return pipe to the pipe section in which the one-way valve is placed. The bellow and the rubber hoses are used to mechanically insulate the measurement pipe from the rest of the piping system.

We used casted aluminum holders for the support of the measurement pipe. All together, the measurement pipe is mounted at approximately 1.1 m above the ground, which provides a convenient working height. We placed these holders at every 0.5 m, viz. a 2 m pipe section is supported by four holders. In this way bending or distortion of the pipe can be minimized. Using four M12 adjustment bolts, allows for an accurate adjustment of the pipe in the holder, see figure 5.7. The bolts have plastic caps made of Multilene MRG, a hard ultrahigh molecular-weight polythene, which prohibits scratching and provides a low friction coefficient. The latter is needed to accommodate thermal expansion of the measurement pipe. For the alignment of the pipe, a HeNe-laser was used to give a horizontal laser beam over the entire length of the facility. We used a level tube for the horizontal adjustment of the laser beam, with an estimated maximum error of 0.2mm over 36 m. By placing a disk having a circular grid in the end of the pipe sections, we can align each pipe section within 0.2 mm of the laser beam position.

The support beams carry the H-beams, but they are also used for mounting the return pipe, the cable duct, and the traversing system support structure as is shown in figure 5.7. The return pipe is supported by strong brackets to carry the large weight when it is totally filled with water. The return pipe has a gradient of 1 in 100 to facilitate emptying of the facility. The traversing system support for the LDV- and DPIV-equipment consists of a horizontal stainless steel shaft mounted on an I-beam (HE-B 160, width=80 mm, height=160 mm) having a length of a little over 4 m. These I-beams are thus carried by three support beams and can be moved along the entire facility. Ball bushings are used to facilitate the movement of the traversing system of the LDV- and DPIV-equipment. For the alignment of the two shafts at each side of the facility, a stiff U-shaped arch could be placed over the pipe. The ends of the U-bend arch were machined in one fixture such to obtain perfectly parallel surfaces and the holes in the ends coincide with those of the LDV-traversing system.

5.7 Measurement pipe and components

5.7.1 Introduction

In this section, we will discuss the most important features of the measurement pipe. In particular, the connection of pipe sections is given much attention. In the measurement pipe, also a special LDV-section is used to eliminate refractive index effects. We have made two designs for this test section. Furthermore, special attention is paid to the connections of the flow meter and its support.

5.7.2 Measurement pipe

As we have discussed in section 5.2, most of the long pipe-flow facilities used for transition at high Reynolds numbers, consist of aluminum pipe sections, often honed to obtain a high precision of the inner diameter. However, as discussed in section 5.4 on the polymers, metals in general and zinc and aluminum in particular, should be avoided in the flow facility, due to degradation of the polymers. This basically leaves us with glass and plastic as construction

materials for the measurement pipe. The biggest problem with using plastic is the extremely large dimensional tolerances. Variations of 5 to 10% on wall thickness are standard and in general the measurement is specified on the *outer* diameter.

Glass can be manufactured with a much higher precision. Precision glass tubes manufactured by Schott Ruhrglas have a tolerance for a 40 mm internal diameter pipe of 0.01 mm with a maximum length of 1 m. These tubes can also be ground at the ends to have flanges for accurate concentric assembly. Unfortunately, these ground tubes can be supplied only having beveled edges of at least 0.2 mm, leading to V-shaped discontinuities in the inner diameter and would probably cause small air bubbles to gather in these grooves. This is quite unacceptable for a low disturbance pipe. Furthermore, glass is rather fragile and difficult to machine. Also, any machining can be done only in a specialized workshop, so no minor changes can be made by the experimenter.

All these disadvantages of glass as a construction material have forced us to use plastic. We have chosen Plexiglas since it is a transparent and widely used material. Transparency is needed for dye visualization experiments and convenient to check for any air bubbles (a horizontal one-phase flow makes one allergic to a two-phase system, particularly in extremely sensitive laminar flow facilities). The use of plastic implies that we have to take counter measures to compensate for the larger dimensional tolerances mentioned above. Instead of using standard extruded pipes, we used centrifugally moulded Plexiglas pipes, that were all manufactured in one batch. This ensures minimum dimensional variation between the pipe sections. Furthermore, centrifugal moulding reduces the ovalness of the pipe.

Nevertheless, small steps in diameter cannot be completely avoided. This is why we paid special attention to the connections of the pipe sections. In order to make the connections flush and the pipe sections interchangeable, the ends of the pipes are made slightly conical having a top angle between 2 and 3 degrees. It is vital that the centering of the pipe be done on the *inner* diameter. To ensure this, the pipe is fixed in a lathe and the end of the pipe is centered around a cone. In this way, the pipe is automatically centered on the inner diameter. The outer diameter of the pipe is then cut from the original 50 mm to 48 mm over a length of 60 mm. This surface is exactly centered with the inner diameter. Over this outer surface, a flange is shifted and glued to the pipe. The flange has an O-ring seal. Fixing the pipe at the flange centers the pipe at the inner diameter and permits the shaping of the end. The facing surfaces of the pipe sections are squared, and the slight cone is cut such that all pipe sections have the same diameter at their facing ends. This procedure resulted a pipe diameter at the facing ends of the pipe of 40.55 ± 0.02 mm. The inner diameter of the pipe outside the conical ends is 40.0 mm. A centering ring seals and centers two adjacent pipe ends and the two rings bolted together with threaded ends secure the connection as is shown in the top half of figure 5.8. For the O-ring we used a silicon rubber ring which is relatively soft and permits displacement of the centering ring by hand under most conditions. If, movement by hand is impossible, a split flange can be placed in front of the pipe flange and the centering ring can be positioned with the help of the threaded ends, as is shown in the bottom half of figure 5.8.

A big advantage of the connection design, is that in order to (re)place pipe section, no extra space is needed. In a previous pipe-flow facility, the pipes had threaded ends. This resulted in several undesirable effects. For instance, when a pipe section had to be replaced, all downstream sections not only need to be shifted, but in order to unscrew the connections, all these pipe

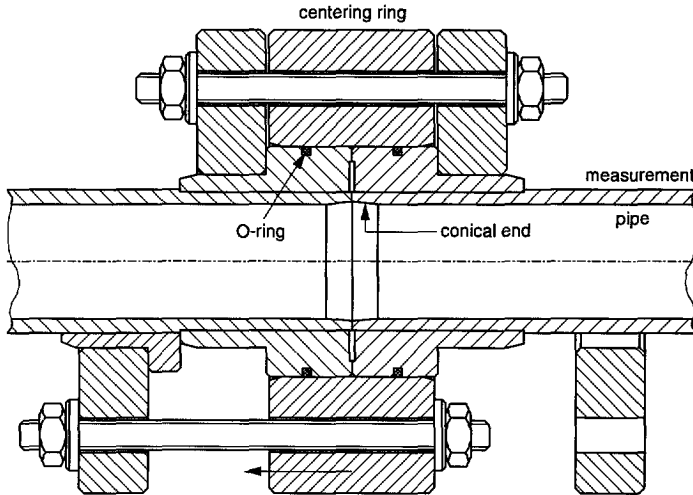


Figure 5.8: The design of the pipe connection which centers the two pipe ends at the inner diameter of the pipe and assures a flush connection and a good watertight sealing. The top half of the figure shows the connection under mounted conditions. In the bottom half the split flange is shown which allows movement of the centering ring with the use of the threaded ends.

sections had to be turned as well. This is a very tedious job which becomes much more difficult in a very long facility. Also, accurate alignment is impossible and the pipe surfaces easily scratch. All these disadvantages can be avoided by the design shown in figure 5.8.

5.7.3 Test sections

To measure the flow inside the pipe by means of LDV or DPIV, the curvature of the pipe poses problems for detailed measurements of the flow. Optical access is distorted or even impossible very close to the wall as a result of the differences in refractive index between air ($n=1.00$), water ($n=1.33$), and Plexiglas ($n=1.49$). To minimize this problem, we designed special test sections. These consist of a rectangular Plexiglas box, referred to as optical box, which is placed around the pipe. This box contains the same fluid (water) as in the pipe. This allows us to replace the pipe wall at several locations inside this optical box with a thin sheet of Teflon FEP (fluorized ethylene propylene) having a thickness of $190\ \mu\text{m}$, and which has been kindly provided by Du Pont de Nemours. This material has a refractive index of $n=1.344 \pm 0.003$, which is quite close to that of water. The combination of the optical box and the cylindrical thin sheet minimizes the refraction of the laser beams. This allows us to perform measurements till $0.2\ \text{mm}$ from the wall, as shown by Tahitu (1994). The suppression of refractive index effects is particularly useful for two-component LDV measurements in turbulent flows, since coincidence of the four laser beams is then guaranteed till very close to the wall. This is necessary for an accurate measurement of e.g. Reynolds stresses.

We have designed and constructed two versions of the test section, which have both been used during the stability measurements. Our first design was tailored to another short pipe-flow facility and has some interesting features that were not necessary in the new flow facility and

which are therefore not incorporated in the second design. Nevertheless, as the features may be interesting for other facilities, we discuss here both designs.

Test section 1

In the first test section was manufactured mainly to test the support of the thin sheet that replaces the pipe wall inside the optical box. This support is referred to as a sheet holder. This sheet holder simply consists of an Plexiglas cylinder with threaded ends. Its inner diameter is such that the sheet can be mounted flush with the inner pipe diameter, as shown in the top part of figure 5.9. The sheet has a rectangular shape with a width of 100.0 mm and a length of ≈ 127.5 mm. The length is equal to the circumference of the circularly bent sheet. The exact measure for the length is determined by trial and error until the thin sheet ends tightly fit to each other. To gain optical access, we milled a gap with a width of 60 mm, over approximately $5/6$ of the circumference. The resulting shape of the sheet holder is drawn as a 3-D object in figure 5.9. Thus, the thin sheet is supported over the entire circumference for 20 mm at each side and the seam is supported over the entire length. The tight fit of the seam secures the sheet and it can even sustain a reasonable excess pressure from the inside. For this reason, we always fill the measurement pipe first and then the optical box. The sheet holder performed very well and the same principle is used in the second test section, inside which the pipe wall is replaced with a thin sheet at three locations.

Therefore, the reason for describing the first test section is not the sheet holder but the way the sealing between the optical box and the pipe is achieved. The outside diameter of the sheet holder is 59.5 mm whereas that of the pipe is 50 mm. In order to be able to place the sheet holder inside the optical box, the opening in the side wall of the optical box is 60 mm which is larger than the pipe wall. This leaves a large gap which needs to be sealed. The method that we used can also be applied to cases where the optical box needs to be positioned over pipe connections with glued flanges.

To correctly position the optical box with respect to the pipe, we use the semicircular rings labeled 'A' in figure 5.9. Then the closed cell rubber ring is placed in the cavity. The use of closed cell rubber is imported to prevent creep of the rubber and to increase the compressibility of the rubber as compared with solid rubber. This rubber ring is compressed and thus seals the opening. For the compression we use the big hollow bolt labeled 'C'. This bolt also consists of two halves which are connected with two dowel pins. When manufacturing this bolt, the cutting in half and the placement of the dowel pins has to be done before the thread is cut in order to ensure a smooth thread. To decrease the torsion applied to the rubber ring by the bolt, the thin half rings labeled 'B' are inserted.

This construction functions quite well. However, if high pressures exist inside the measurement tube, this pressure must also be present inside the optical box since the thin sheet does not provide a watertight seal. As a result, above several meters of water pressure, this construction with the rubber ring is no longer completely watertight.

Test section 2

The second test section is specially designed for the long pipe-flow facility used for the transition study. As the sheet holder design used in the first test section performed well, we have concentrated only on improvement of the design of the optical box. First, easy access to the

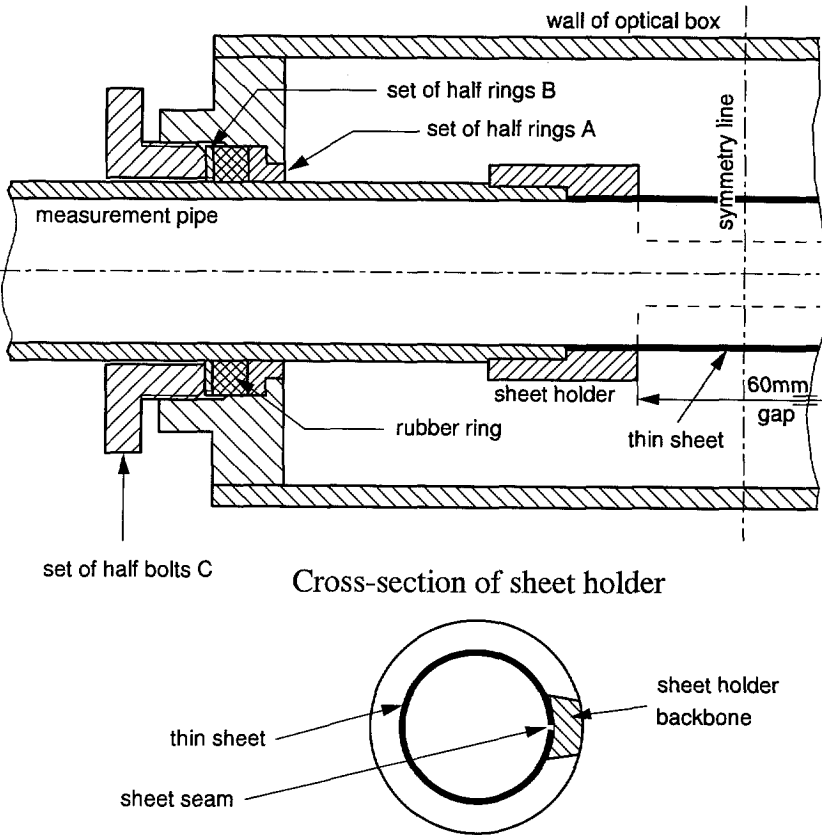


Figure 5.9: The design of the first test section. The top part shows the optical box with the special construction to seal the large gap between the pipe and the optical box, and the bottom part shows the sheet holder. Rings A and B and the hollow bolt labeled C all consist of two halves. The closed cell rubber ring may have one slanting cut if its elasticity is not large enough to pass large flanges that may be present. The cross section of the sheet holder is located at the symmetry line, looking to the left. Note that the gap at the location of the seam is drawn only for reasons of clarity, and in practice the two ends fit securely.

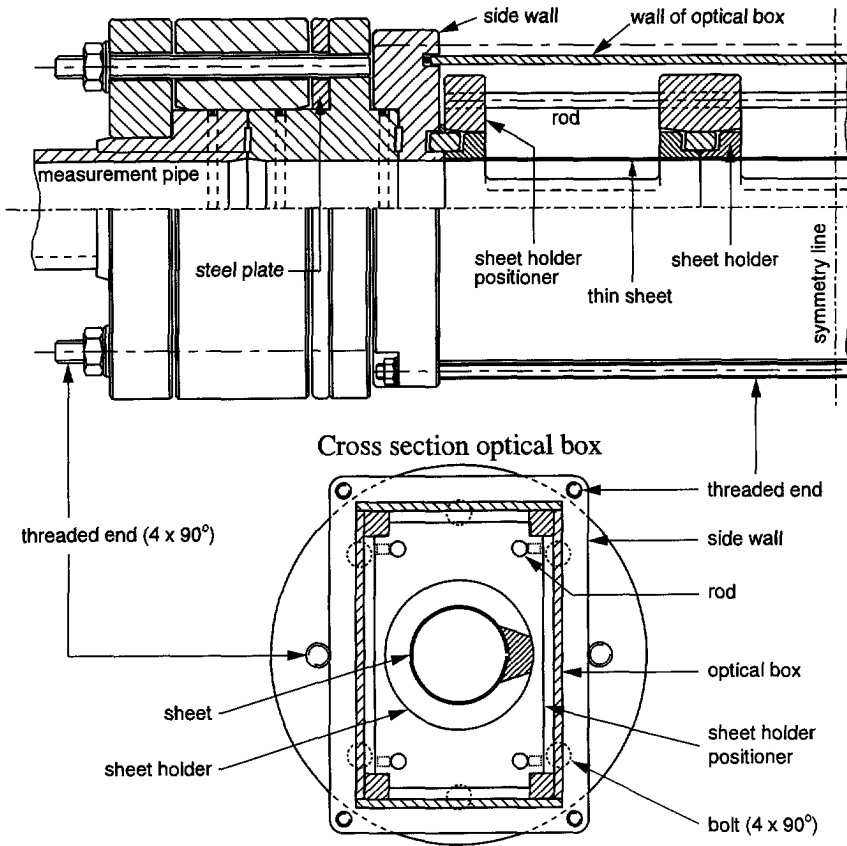


Figure 5.10: The second test section contains three sheet holders. Only half of the test section is drawn as it is completely symmetric. The top half is drawn as a cross section and the bottom half is an elevated view. The cross section of the optical box is located at the symmetry line, looking to the left. Note that the gap at the location of the seam is drawn only for reasons of clarity, and in practice the two ends touch.

inside of the optical box is required for cleaning purposes. Algae tend cause a deposit of dirt on the walls of the optical box. Second, a large part of the test section should be available for measurements, which is required for detailed studies of e.g. the spacial evolution of disturbances.

We realized these requirements by using a rectangular optical box which is fixed in between two side walls with the help of threaded ends. Inside the optical box, we placed three sheet holders which are kept in place by rectangular plates, called sheet holder positioner, that fit just inside the optical box, as is shown in figure 5.10. These plates are connected with rods to provide a stiff frame for the sheet holders. After the optical box is assembled, the flanges are fixed to the side wall using four bolts. The side walls also accommodate holes for filling the optical box and bleeding of air.

Disassembly of the pipe/test section connection becomes difficult, since it is hard to apply

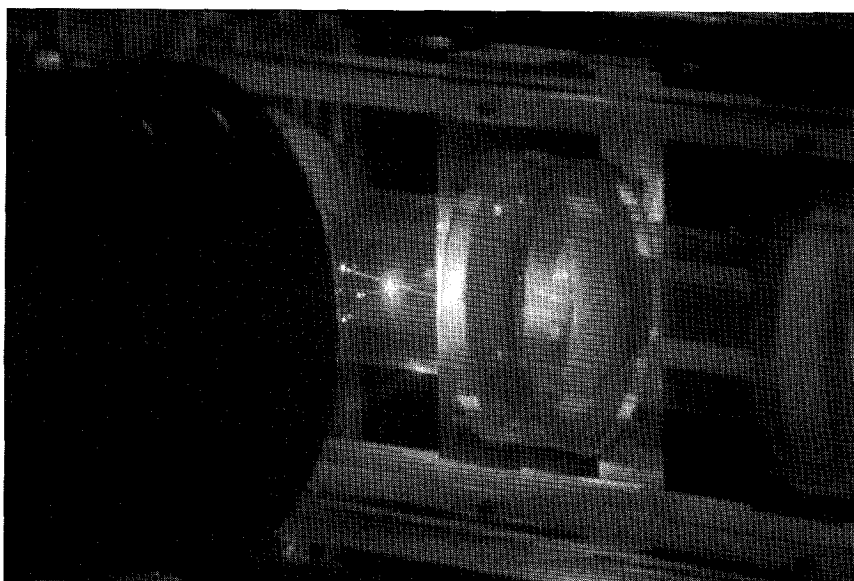


Figure 5.11: Close-up of the second test section. The black area to the left represents the LDV-probe. The four laser beams are clearly visible and the four bright spots which are close together represent the locations where the laser beams cross the thin sheet. In the center of the picture, we see the sheet-holder positioner. At the right-hand side of the picture, the backbone of the sheet holder which supports seam can be discerned. For an overview picture we refer to figure 6.2.

force to the centering ring. For this, a stainless steel plate is added containing 8 holes; four large holes and four threaded holes in alternating order. The large holes accommodate the threaded ends for the connection with the measurement pipe. For the disassembly, these threaded ends are screwed in the threaded holes of the stainless steel plate until they touch the four bolts in the flange. Now turning the threaded ends results in pushing the steel plate away from the flange and taking the centering ring of the connection with it.

The test section including the flanges is 0.5 m long. The measurement pipe sections have a length of 2.0 m. To be able to place the test section at any location in the pipe, we also need to have measurement pipe sections of lengths 0.5 m, 1.0 m, and 1.5 m.

Flow meter construction

A magnetic inductive flow meter (Krohne-Altometer, type M950/6 and control unit SC-100 AS) is mounted in the measurement pipe just in front of the discharge chamber. The two sensor elements are lens-shaped and protrude approximately 3 mm into the flow. As most of these flow meters are used in process industry applications, the indication DN-40 (suggesting an inner diameter of 40 mm) actually stands for 1.5 inch=38.1 mm. To avoid any metal contact, the flowmeter has a Teflon lining which has a rounded at the flanges. This radius may trap bubbles and disturb the flow. Also, this type of flow meter required grounding rings at each side of the flow meter.

The cavity in the stainless steel grounding rings was filled with epoxy resin which also filled

the gap caused by the radius of the lining. In this way, a smooth inner surfaces could be obtained. Plexiglas adaptor flanges were mounted at each side of the flow meter to provide a smooth expansion from the 38.1 mm inner diameter of the flow meter to the inner diameter of the measurement pipe. The total length of the flow meter including the adaptor flanges becomes 0.5 m.

The flow meter is quite heavy and its weight cannot be supported by the measurement pipe. On the other hand, due to the large difference in thermal expansion of the Plexiglas measurement pipe and the steel H-beam support structure, the flow meter cannot be fixed directly to the H-beam. The linear coefficient of thermal expansion for Plexiglas and steel are $\pm 85 \cdot 10^{-6} / ^\circ\text{C}$ and $12 \cdot 10^{-6} / ^\circ\text{C}$ respectively. For a temperature change of 10°C , which can be easily achieved between summer and winter. The coefficients of thermal expansion lead to a difference of 25 mm in expansion between the Plexiglas measurements pipe and the steel H-beams over the total length of the pipe (34 m). As we fixed the settling chamber to the H-beam, the entire expansion has to be accommodated for at the discharge chamber side of the pipe. The connection of the pipe to the discharge chamber is such, that the measurement pipe can slide. Also, we constructed a support in which the flow meter can slide. The flow meter connection flanges resulted in a laminar flow up to $Re \approx 20\,000$ after the flow passed the flow meter as opposed to $Re > 60\,000$ in the measurement pipe before the flow meter. This has been checked using dye injected in the settling chamber.

5.8 Settling Chamber

5.8.1 Introduction

In most wind and water tunnels a settling chamber is present to generate a smooth, low turbulence and uniform inflow. Honeycombs are used to eliminate possible swirl and screens are used to break down turbulence to scales where the turbulent energy is quickly dissipated. A contraction is a very powerful tool to reduce flow non-uniformities. This can be shown using Bernoulli's theorem for an inviscid fluid (Ward-Smith 1980, p. 358), where index (1) stands for the flow inside the settling chamber and (2) for the flow after the settling chamber, i.e. downstream of the contraction:

$$p_1 + \frac{1}{2}\rho(v_1 + v'_1)^2 = p_2 + \frac{1}{2}\rho(v_2 + v'_2)^2 \quad (5.5)$$

Here v_i is the mean flow velocity and the prime indicates a mean flow velocity disturbance. Subtracting the equation for the mean flow, i.e. $p_1 + \frac{1}{2}\rho v_1^2 = p_2 + \frac{1}{2}\rho v_2^2$ gives and keeping only first-order terms in v'_i gives:

$$v_1 v'_1 = v_2 v'_2 \quad (5.6)$$

With this we can obtain the following expression for v'_2/v_2 :

$$\frac{v'_2}{v_2} = \frac{v_1^2 v'_1}{v_2^2 v_1} = \frac{D_2^4 v'_1}{D_1^4 v_1} \quad (5.7)$$

From equation 5.7 we can see that the mean flow non-uniformity suppression efficiency of a contraction depends to the fourth power on the diameter ratio. For turbulent velocity fluctuations,

arguments based on vorticity filaments give the same reduction for axial velocity fluctuations (Ward-Smith 1980, p. 358, Hussain & Ramjee 1976).

Maintaining laminar flow in pipes at high Reynolds numbers can be realized only by suppressing disturbances at the inlet of a smooth pipe. A large contraction is beneficial in achieving this. Thus a large Plexiglas tube is used as the settling chamber with an inside diameter of 250 mm. With the 40 mm diameter pipe, the contraction ratio becomes: $CR = D_1^2 / D_2^2 = 39$. Equation 5.7 then shows that the axial velocity fluctuations in the settling chamber are reduced by a factor of more than 1 500. As the diameter ratio of the contraction is quite large and only a limited space is available for the length of the contraction, it is important to find a suitable form for the contraction.

Hussain & Ramjee (1976) compared several contraction shapes with respect to turbulence suppression and other characteristics. Compared to bell-mouth shaped contractions and a contraction where the inflection point is shifted towards the large diameter side, a contraction of which the contour is described by a third-order polynomial gives the most turbulence suppression. However, to avoid discontinuities in the pressure gradient, we used a fifth order polynomial, which is the lowest order to satisfy these conditions. In combination with the honeycombs and the screens in the settling chamber, the flow was found to be stable up to Reynolds numbers of over 30 000. On one occasion, a natural transition Reynolds number of $Re = 40\,000$ was reached. In this case, the experiments were conducted in November 1993 with fresh water. Although no temperatures were measured, the water had probably a temperature of 11 to 12°C whereas the ambient air temperature was most likely to be around 18°C. At that time the Plexiglas pipe was not yet insulated so effectively the wall was heated. As experiments by Barker and Gile (1981) show, wall heating stabilizes water boundary layers and therefore may delay transition. For this reason, a transition Reynolds number of around 32 000 is probably the correct value for the natural transition Reynolds number of our pipe flow. which is more than sufficient for our purpose.

Due to convection problems, we had to reduce the diameter of the settling chamber, which is explained in the next section.

5.8.2 Convection

The pipe-flow setup is a recirculatory system. Thus, if we neglect heat input from the pump and viscous dissipation, the temperature of the water will approach the temperature of the surrounding air. However, during the night the central heating in the lab shuts down and the air temperature drops by several degrees, and consequently the water cools. This is particularly the case during the winter months. Given the large heat capacity of water and the rapid increase of the air temperature in the morning, the water temperature is below that of the air. Typical temperature differences are 1.5 to 2.5°C and these temperature difference will influence the flow. Some of the measured velocity profiles which are influenced by convection flows are presented in Aanan (1995). Whenever temperature differences influence the flow, the Rayleigh number is the nondimensional parameter characterizing this convection flow:

$$Ra = \frac{g \alpha \Delta T D^3 Pr}{\nu^2} \quad \text{and} \quad Pr = \frac{\nu}{\kappa} \quad (5.8)$$

Where g : gravitational acceleration, α : thermal cubical expansion coefficient, ΔT : temperature difference, Pr : Prandtl number, κ : thermal diffusivity, and ν : kinematic viscosity. For water $Pr = 7.03$ & $\alpha = 0.21 \cdot 10^{-3} \text{K}^{-1}$ and for air $Pr = 0.713$ & $\alpha = 1/T \cong 3 \cdot 10^{-3} \text{K}^{-1}$. Note that for the same geometry, Ra is much larger for water than for air, which is mainly due to the kinematic viscosity ν that is 15 times larger for air than for water. Substitution of the values in for water equation 5.8 then gives:

$$Ra_{\text{pipe}} = 9.3 \cdot 10^5 \Delta T \quad (5.9)$$

$$Ra_{\text{settling chamber}} = 2.3 \cdot 10^8 \Delta T$$

Note that the Rayleigh number is much larger on the settling chamber, which is caused by the larger diameter, which increases the Rayleigh number according to D^3 . Generally, above Rayleigh numbers of the order 10^3 convection cells begin to form. Therefore, in order to avoid generation of convection cells in the pipe, the temperature difference between the water and the inner surface of the pipe should not exceed $\Delta T = 10^{-3} \text{°C}$. Heat-transfer calculations show that the temperature difference between inner surface of the pipe and the water is approximately 10% of the temperature difference between the water and the air. Thus, the temperature difference between the water and the ambient air should not exceed 10^{-2}°C . Measurements of such small temperature differences are barely possible, let alone controlling the air and water temperatures this accurately. So, insulation of both the pipe and the settling chamber is inevitable. Minimizing the temperature difference between the air and the water is vitally important. Increasing the viscosity decreases the Rayleigh number but we have not used this in our experiments. In water this could be done with glycerine-water mixtures or by adding most glucose syrup. A decrease in size is most effective, as this effects Ra to the third power. Since these improvement separately cannot reduce Ra to small enough values, we combined them which resulted in the following actions:

- We placed an array of three domestic aquarium heaters, 300 W each, in the reservoir. Thus we can increase the temperature of the 1.5 m^3 of water with approximately 1°C per hour. A temperature sensor is included in a control circuit and a target temperature could be set using a 1000-step potentiometer. After calibration of this circuit, the temperature of the water could be controlled within 0.1°C of the target temperature. As the temperature in the basement is relatively constant during the day-time and changes only slowly with the weather conditions, the temperature of the water can be maintained within 0.5°C of the day-time ambient air, and usually this temperature difference is smaller than 0.2°C . To prevent cooling during the night, we circulated the water 24 hours a day during measurement periods.
- The pipe is insulated with 30 mm thick insulation material (Climaflex by NMC-Kenmore). Also the pipe connection are completely enclosed by a 30 mm thick layer of the insulation material. In addition, a large wooden box was constructed, covered at the inside with insulation material, which encloses the settling chamber. As the insulation material is rather soft, we placed 2 mm thick cylindrical PVC plates around the insulation material at the places where the measurement pipe is supported to maintain a good alignment of

the pipe. Due to the 110 mm outer diameter of the insulation material, the Multilene plastic caps placed over the adjustment bolts (shown in figure 5.7) had to be removed because of space limitations.

- We placed a smaller diameter settling chamber inside the housing of the large settling chamber. The inside diameter of the small settling chamber is 121 mm thus resulting in a contraction ratio of $CR=9$, i.e. velocity fluctuations are suppressed by a factor of 81. This should still be sufficient provided that a reasonably smooth flow can be generated before the contraction. The space between the small settling chamber and the original large housing can be used to further reduce the heat flux by circulating water having the same temperature as the water in the pipe around the small settling chamber. A further advantage of the smaller settling chamber is the shorter residence time of the fluid and thus convection flow has less time to develop in the settling chamber.

Heat-transfer calculations show, that insulation reduces the temperature difference between the water and the inside wall of the pipe by a factor of five, i.e. the temperature difference between the water and the inner surface of the pipe is reduced till 2% of the temperature difference between the water and the ambient air. Assuming that the latter is $\pm 0.2^\circ\text{C}$ as a result of the heating elements, we now find Ra -values of:

$$Ra_{\text{pipe}} = 3.7 \cdot 10^3 \quad (5.10)$$

$$Ra_{\text{settling chamber}} = 1.0 \cdot 10^5$$

Although this means a significant improvement over the values in equation 5.9, this still does not entirely suppress the generation of convection cells especially in the settling chamber. As a result, some distortion of the velocity profiles is to be expected. The settling chamber has probably improved more than indicated by the change in Ra -values, since the velocity in the settling chamber increased by a factor of 4.3 and due to the circulation of the water around the small settling chamber, the temperature difference is probably much smaller.

To estimate the resulting vertical velocities in the convection cells, we simply use the analytical solution for the laminar free-convection flow between two vertical plates, with a temperature difference ΔT at a distance $2h$, given by (Bird *et al.* 1960, p. 300):

$$v(y) = \frac{g\alpha h^2 \Delta T}{12\nu} \left(\frac{y^3}{h} - \frac{y}{h} \right) \quad (5.11)$$

The maximum value of the third order polynomial is 0.385 for $y/h=0.58$. Substitution of the values for water and replacing $h=D/2$ gives for the maximum convection velocity:

$$v_{\text{convection, max}} \cong 0.069 \Delta T \quad (5.12)$$

When we estimate the maximum convection velocity, we use the temperature difference between the water and the inner surface of the pipe, as discussed in relation to equations 5.9 and 5.10. For a 1°C temperature difference between the water and the ambient air, the maximum convection velocity for the non-insulated pipe would become 0.007 m/s. This is in fair agreement

with LDV-measurements, which showed vertical velocities of 0.003 m/s. For the insulated pipe with temperature difference between the water and the ambient air of 0.2°C, the maximum convection velocity would become 0.0003 m/s, which we can no longer measure. This is a significant improvement, but even these small velocities may still distort the axial velocity profile. However, another problem becomes apparent, namely now that we have strongly reduced the convection flow, the Coriolis force due to the rotation of the earth. It turns out that this force is able to strongly distort the axial velocity profile. This will be shown in section 5.12 and discussed in detail in appendix C.

Given the sensitivity of the laminar pipe flow to temperature differences, a climate controlled room would be an optimal situation. Certainly, the placement in the basement of the building is a blessing, as temperatures stay here much more constant than on the main floor.

The reduction of the diameter of the settling chamber, reduces the suppression of velocity inhomogeneities by the contraction. Thus, even more attention should be paid to the design of the settling chamber. As the length–diameter ratio of the contraction is also more favorable, a better contraction can be designed. This will be discussed in the next section. The lay-out of the settling chamber is the subject of the section thereafter.

5.8.3 Contraction design

The construction of a smaller contraction permits a redesign. Since the same length is available for a smaller contraction ratio, a better optimization is permitted with respect to adverse pressure gradients and the growth of Görtler vortices. The latter are centrifugal instabilities that can occur in boundary layers along a concave wall (Drazin & Reid 1981, p. 116). To characterize these instabilities Saric (1994) defines the Görtler number as:

$$G = \left(\frac{W_\infty \delta_r}{\nu} \right) \left(\frac{\delta_r}{R} \right)^{\frac{1}{2}} \quad \text{with} \quad \delta_r = \sqrt{\frac{\nu s}{W_\infty}} \quad (5.13)$$

Here, R is the radius of curvature of the wall, s is the streamwise position from the beginning of the boundary layer, Drazin & Reid (1981, p. 118) use the momentum thickness instead of length scale δ_r . According to figure 3 of Saric (1994), Görtler vortices grow for $G \gtrsim 0.5$ although experiments give a higher limit of $G \approx 2$.

For a rough estimate, the free stream velocity W_∞ in our case can be calculated from the continuity equation by assuming a constant velocity at each z -position (axial position) in the contraction. The measure for the boundary layer thickness δ_r is used although the boundary layer thickness will be smaller due to the favorable pressure gradient in the contraction. Based on all these assumptions, the Görtler number can be calculated for fifth order contractions for the original and the small settling chamber (see figure 5.12). The large contraction has a length of 200 mm. Due to a different connection, the length of the small contraction could be extended to 237 mm.

Equation 5.13 can be reformulated to clarify the dependence of the Görtler number on its various components:

$$G = W_\infty^{1/4} s^{3/4} R^{-1/2} \nu^{-1/4} \quad (5.14)$$

Although the small contraction is longer which increases s and has a much larger W_∞ , the Görtler number is still smaller than for the large contraction due to much larger radius of

curvature. However, in both the large and the small contraction, the Görtler number exceeds the theoretical as well as the experimental threshold for growth. So, during a finite time the Görtler vortices will grow and they may possibly disturb the entrance flow.

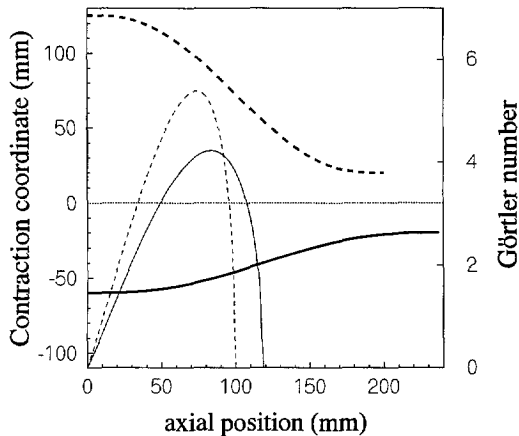


Figure 5.12: Contraction shapes (thick lines) and Görtler number (thin lines) for the fifth order polynomial contractions.

By changing the form of the contraction, the Görtler number can be reduced further. Furthermore, care has to be taken to avoid adverse pressure gradients at the in and outflow of the contraction which can cause separation. At high Reynolds numbers, with exception of the region in the immediate vicinity of the wall, the flow field in a contraction can be analyzed using inviscid potential calculations (Ward-Smith 1980, p. 363). Here, the method proposed by (Cohen & Ritchie 1962) is followed and extended. They use a stream function Ψ to describe an axisymmetric flow of an ideal fluid. Potential-flow theory for this case leads to the Stokes-Beltrami equation in Ψ :

$$\frac{\partial^2 \Psi}{\partial z^2} + \frac{\partial^2 \Psi}{\partial r^2} - \frac{1}{r} \frac{\partial \Psi}{\partial r} = 0 \quad (5.15)$$

With z the axial and r the radial position. Writing Ψ as a series solution

$$\Psi = \sum_1^{\infty} f_m(z) r^{2m} \quad (5.16)$$

they derive a recurrence relationship between higher order terms and the higher order derivatives of the lowest order term f_1 (see also appendix B). The velocity distribution at the axis of the contraction turns out to be $w(r=0) = 2f_1(z)$ and Cohen & Ritchie (1962) selected the following function:

$$w_{r=0} = A + B \cdot \tanh\left(\frac{z}{C}\right) + D \cdot e^{kz^2} \quad \text{with} \quad k \leq 0 \quad (5.17)$$

Values A and B are determined from the uniform velocities at $z=\pm\infty$. C determines the slenderness of the contraction. The term $D \cdot e^{kz^2}$ is added to shift the point of inflection

upstream to avoid adverse pressure gradients at the outlet of the contraction. This term can also be used to reduce the length of the concave section of the contraction, or to decrease the Görtler number. Each value for Ψ gives a streamline which might be used as a wall profile for the contraction (neglecting the displacement of the wall boundary layer).

For practical applications, a contraction of infinite length as assumed in equation 5.17 is not realistic. To overcome this problem, the calculated contraction was curtailed at both ends. Curtailing is also favorable with respect to adverse pressure gradients as the same space is now available for the contraction itself rather than the in- and outlet where the diameter hardly changes. (Kachhara *et al.* 1974) showed that curtailing of the contraction using a wall slope at D_1 of 3.5° and 2° at D_2 did not impair its performance. They also found that adverse pressure gradients in the small diameter section of the contraction as high as

$$\frac{1}{\frac{1}{2}\rho W_2^2} \frac{dp}{d(z/D_2)} = 0.38$$

do not cause separation. This adverse pressure gradient is comparable to a diffuser having a top-angle of 4.6° which would show no stall for diffuser lengths smaller than $20D$. In their contraction, the inflection point is rather close to the small diameter end of the contraction resulting in a relatively large adverse pressure gradient. This can be improved by choosing appropriate parameter combinations in equation 5.17 as will be shown later.

In the small contraction, a wall slope of 3° at D_1 was used and at D_2 a wall slope of 1° was chosen. The calculated pressure gradients shown in figures 5.13–5.16 are made dimensionless using the local velocity at the wall in the contraction diameter at that location.

The numerical procedure followed in the contraction calculations consists of several iteration steps:

1. Choose values for C , D , k , and the contraction ratio D_1/D_2 as well as the length L available for the contraction.
2. The values for A and B follow from:

$$W(r = 0, z = -\infty) \equiv A - B = 1 \quad \text{or} \quad B = A - 1 \quad (5.18)$$

$$W(r = 0, z = +\infty) \equiv A + B = \frac{D_1^2}{D_2^2} \quad (5.19)$$

3. Select a starting value for Ψ and determine the values for r from equation 5.16 with $m = 1 \dots 5$ for $-10 \leq z \leq 10$. This involves derivatives up to order eight of f_1 (listed in appendix B). The negative z -position where the wall slope equals 3° gives the begin location of the contraction and similarly, the positive z -position where the wall slope equals 1° locates the end of the contraction.
4. Rescaling of the radius at the 1° wall slope position to $D_2/2$ gives the inlet diameter D_1 and the contraction length L .
5. If the length L is larger than the available length, the value for Ψ has to be increased and vice versa. This iteration process is continued until the correct length has been found.

6. Due to the curtailing of the contraction, the contraction ratio does no longer match the values at infinity as was assumed in the choice for A and B . If the contraction ratio of the curtailed contraction is too large, then the value of A needs to be lowered or vice versa. The relationship $B = A - 1$ is still used. Steps 3 through 6 are repeated until the correct values for A and B are found.
7. The velocities are scaled such that the Reynolds number in the pipe equals 15 000. With the velocities at the wall and using Bernoulli's theorem, the value of the pressure gradient at the wall can be calculated. Using the velocity at the wall streamline as a free-stream velocity estimate W_∞ , and calculating the distance along the contraction wall gives us the information needed to calculate the Görtler number. The origin of the boundary layer is located at the beginning of the contraction as in our case a fine screen is placed right in front of the contraction.

Using this procedure, a large range of parameter values for C , D , and k were studied. Due to the large number of parameters, more than one combination (C, D, k) resulted in contractions showing no adverse pressure gradients and comparable values for the maximum Görtler number of approximately 3.3. This is smaller than that for a fifth order polynomial; $G_{\max} = 4.1$. Curtailing a fifth order polynomial in the same way as the contractions described above, reduces the maximum Görtler number to 2.9. In figure 5.13 the results are shown for a short contraction of $L = 140\text{mm}$. As a result of this short contraction, the adverse pressure gradient near the contraction entrance reaches a value as high as 0.57 which is much larger than 0.38 which was found to be the maximum above which separation can occur (Kachhara *et al.* 1974). Also, due to the large curvature, i.e. small radius of curvature, the Görtler number has a maximum of $G = 8.0$ at 29% of the contraction length. This is four times larger than the experimentally found threshold for growth of Görtler vortices. Therefore, the connection of the pipe to the settling chamber of the small contraction was constructed in such a way that the length available for the contraction was increased to $L=237\text{mm}$. As a result, adverse pressure gradients disappear and the maximum Görtler number is almost reduced by a factor of 2. By optimizing the design with respect to a small Görtler number in the absence of adverse pressure gradients, the maximum Görtler number can be reduced to 3.4 at 25% of the contraction length (see figure 5.14). In this figure, a second 'hump' in the Görtler number appears downstream of the contraction. Here, the curvature of the wall (streamline) is slightly negative reaching $-2.6 \cdot 10^{-6}\text{mm}^{-1}$. Due to the much larger boundary layer length at this location, the Görtler number reaches values above 0.5. The boundary-layer thickness measure δ , is overestimated in this region as the strongly favorable pressure gradient in the contraction will have a suppressing effect on the boundary layer thickness. The Görtler number can be further reduced to 2.8 at 27% of the contraction length as is shown in figure 5.15. However, small adverse pressure gradients are now present at both ends of the contraction. The inner diameter even shows a minimum at $z = 263\text{mm}$, resulting in a wall curvature as high as $-7 \cdot 10^{-5}\text{mm}^{-1}$. Although the boundary layer thickness may be overestimated, and with it the Görtler number, a contraction with these characteristics is highly undesirable. Also, the Görtler number exceeds the threshold for growth over a much longer length thus permitting Görtler vortices to grow during a longer period of time.

This problem can be somewhat alleviated by simply shifting the bell curve in the upstream

direction:

$$w_{r=0} = A + B \cdot \tanh\left(\frac{z}{C}\right) + D \cdot e^{k(z+s_h)^2} \quad (5.20)$$

The main effect is that the concave part of the contraction is shortened (see figure 5.16). Although the maximum in Görtler number remains 2.8, the length over which the experimental threshold value of 2 is exceeded is shortened considerably. In addition, the minimum in internal diameter just downstream of the contraction vanishes as well as the downstream adverse pressure gradient. The one near the contraction entrance is larger but it is with a value of 0.08 still much smaller than the critical value of 0.38. The contraction in figure 5.16 is the one which has been selected and manufactured. It sustains laminar flow up to Reynolds numbers as high as 63 000 which is also an indication of the quality of the contraction.

5.8.4 Settling chamber setup

To improve the flow condition even further, an array of honeycombs and screens is placed in the settling chamber. It is very important to use screens that have a porosity, i.e. ratio of open to total screen area, that exceeds a value of 0.57 to prevent coalescence of two adjacent 'jets' (Laws & Livesey 1978). We used stainless steel screens with a mesh size of 0.5 mm, denoted as 'fine' screens, and PVC screens having a mesh size of 2 mm, denoted as 'coarse' screens.

Let us follow the fluid on its voyage from the pump until the moment it enters the pipe, for this we refer also to figure 5.17. After the pump, three 90°-bends guide the fluid in a rubber hose which makes a large U-bend. The rubber U-bend is used to mechanically insulate the settling chamber from the pump. Then another 90°-bend directs the fluid to the settling chamber. Curvature induces secondary flows and also swirling flows when curvature is not confined to a plane. These flow disturbances have to be eliminated before entering the measurement pipe. To redistribute the skewed velocity profile generated by the bends, we placed two static mixer elements (Sulzer SMV-8, diameter=50 mm) between the settling chamber and the last 90°-bend. The second mixing element is rotated 90° compared to the first one. Then, before entering the diffuser, we used a honeycomb, mesh size 5 mm and 50 mm long, to suppress the swirl. The diffuser has a top angle of 25°. We placed a perforated plate (16 mm holes and 20 mm center-to-center distance) at end of the diffuser. This introduces extra resistance, which suppresses separation and enhances mixing of the flow. Then a tandem of again a 5 mm honeycomb and 20 mm long packet of drinking straws (poor man's honeycomb) is used to suppress any remaining swirl. Next, a fine screen was placed to filter any dirt. After this, another honeycomb is used with directly behind it a coarse screen. This is a combination which strongly suppresses turbulence (Loehrke & Nagib 1976). Finally, two other coarse screens and a fine screen just in front of the contraction complete the settling chamber. The distance between the last coarse screen and the fine screen is 40 mm, i.e. 20 times the mesh size. This is the minimum separation distance between two consecutive screens and coincides with the region of rapid decay of turbulence intensity (Groth & Johansson 1988).

A large problem is formed by air bubbles that stay trapped in the settling chamber, particularly near the contraction and inside the drinking straws. The housing of the large settling chamber contains an opening which gives access. Right under this opening, we have access to the small settling chamber to remove any air bubbles in the drinking straws. For this, we constructed a semi-cylindrically shaped part of the wall of the small settling chamber that can be removed.

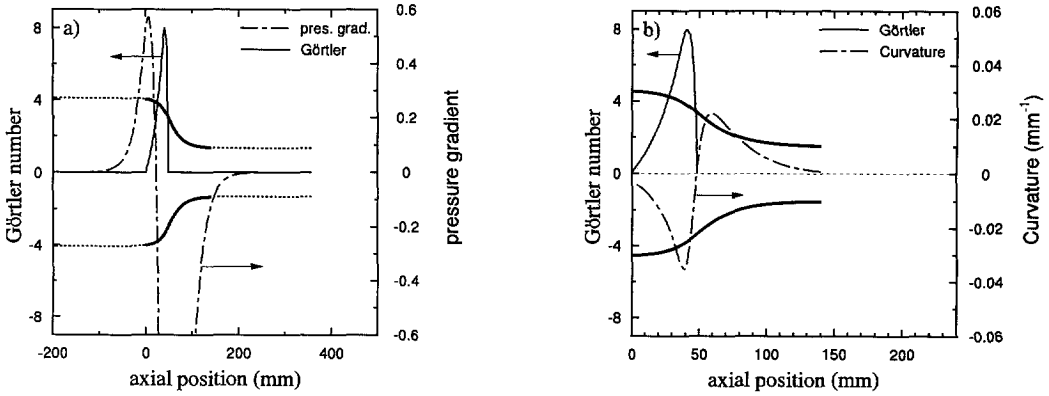


Figure 5.13: Görtler number a) & b), non-dimensionalized pressure gradient a), and curvature b) for a contraction length $L = 140\text{mm}$. Parameter values: $C = \sqrt{2}$, $D = 0$, $k = 0$, $s_h = 0$. The contraction contour is depicted in the thicker solid line. The thin dotted lines indicate the rest of the computational domain. The contraction shape in a) is compressed in the axial direction. In b) the contraction shape is scaled using the same factor in both directions and only the contraction itself is shown. Note the difference in scaling for the Görtler number and the curvature when compared to figures 5.14 to 5.16.

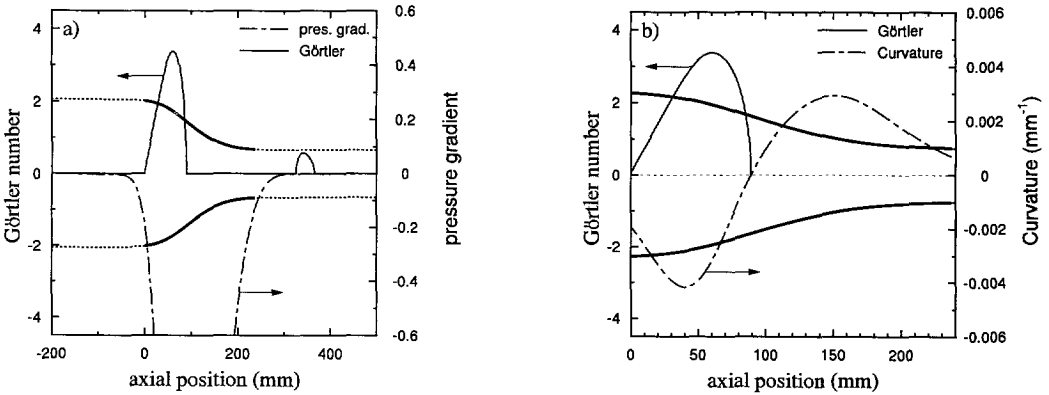


Figure 5.14: Görtler number a) & b), non-dimensionalized pressure gradient a), and curvature b) for a contraction length $L = 237\text{mm}$. Parameter values: $C = 1.30$, $D = 1.0$, $k = -0.3$, $s_h = 0$. The contraction contour is depicted in the thicker solid line. The thin dotted line indicate the rest of the computational domain. The contraction shape in a) is compressed in the axial direction. In b) the contraction shape is scaled using the same factor in both directions and only the contraction itself is shown.

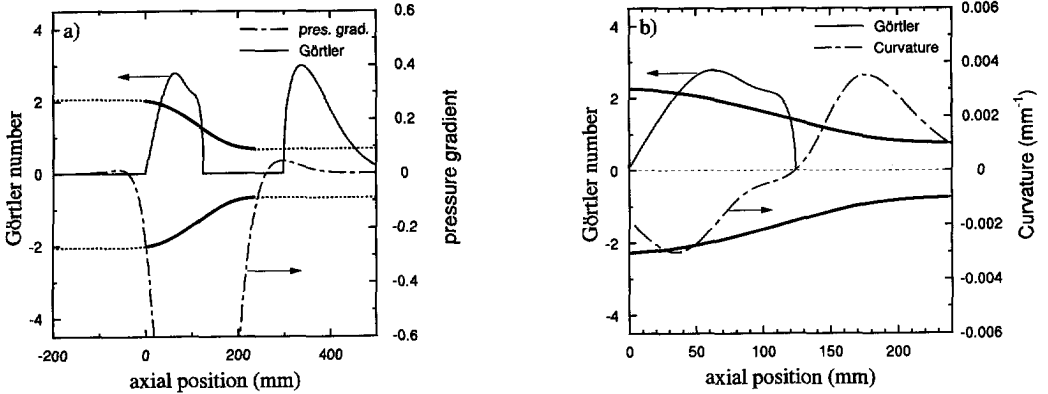


Figure 5.15: Görtler number a) & b), non-dimensionalized pressure gradient a), and curvature b) for a contraction length $L = 237\text{mm}$. Parameter values: $C = 1.3$, $D = 1.4$, $k = -0.27$, $s_h = 0$. The contraction contour is depicted in the thicker solid line. The thin dotted line indicate the rest of the computational domain. The contraction shape in a) is compressed in the axial direction. In b) the contraction shape is scaled in both directions and only the contraction itself is shown.

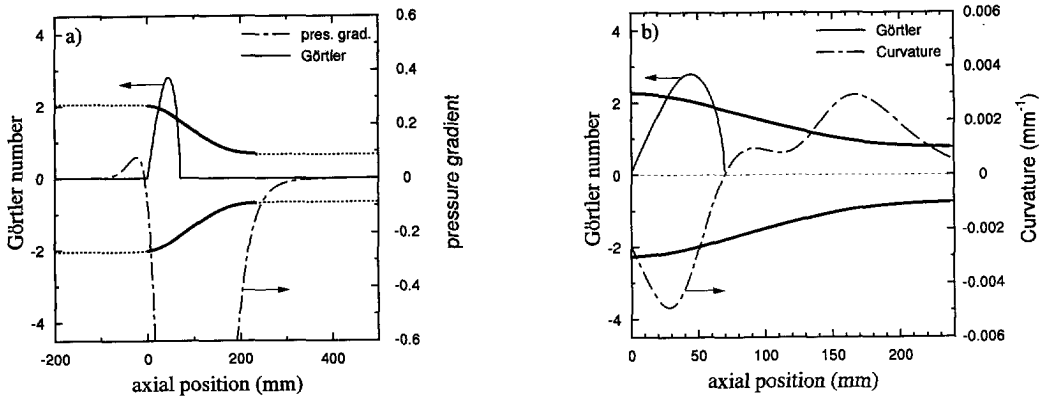


Figure 5.16: Görtler number a) & b), non-dimensionalized pressure gradient a), and curvature b) for a contraction length $L = 237\text{mm}$. Parameter values: $C = 1.30$, $D = 1.0$, $k = -0.3$, $s_h = 0.75$. The contraction contour is depicted in the thicker solid line. The thin dotted line indicate the rest of the computational domain. The contraction shape in a) is compressed in the axial direction. In b) the contraction shape is scaled in both directions and only the contraction itself is shown.

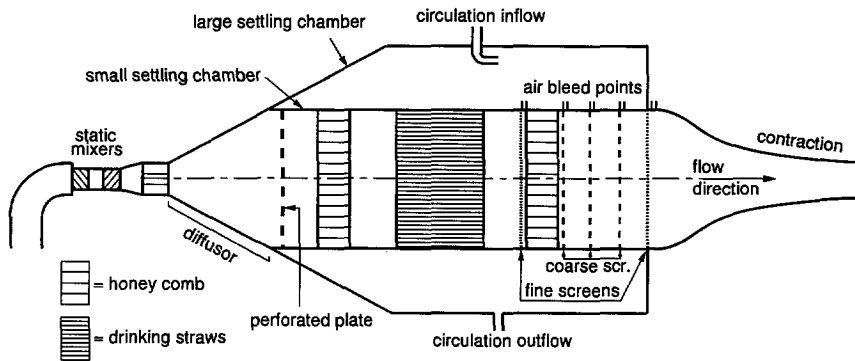


Figure 5.17: The composition of the various screens and honeycombs in the small settling chamber. The air bleed holes are connected to the outside of the large settling chamber. This allows removal of air bubbles during circulation.

This part is located between the drinking straws and the fine screen and is kept in position by two O-rings. To remove air bubbles, fluid is sucked through the drinking straws by a small centrifugal pump (Iwaki MD30R, maximum flow rate 321/min) and this fluid is discharged in the space surrounding the small settling chamber. In this way, all the air can be removed from the drinking straws and the honeycomb downstream. Also dirt can be removed from the fine screen. To remove air bubbles in between the screens, we made air bleed holes in the top of the small settling chamber. These are connected with the cover of the housing of the large settling chamber through small hoses (not drawn in figure 5.17). Any remaining air bubbles have a relatively small effect on the operating quality of the settling chamber. Moreover, after circulating the water for several days, these bubbles will dissolve in the water. The bubbles in the drinking straws do not dissolve as they block the flow through the straw.

The space between the small and the large settling chamber is employed as a kind of heat exchanger. A small centrifugal pump circulates the water in this space through a long hose which has a large number of loops that are placed in the reservoir. In this way, a closed circulation loop is created in which the water adopts a temperature very close to that of the water in the reservoir, i.e. the water in the measurement pipe. This helps to suppress convection. Creating an open loop, i.e. pumping water from the reservoir through the space between the large and the small settling chamber and back into the reservoir, results in high pressures inside the small settling chamber. This would result in lifting of the semi-cylindrical part and disturbing the flow in the settling chamber. By maintaining a closed system, this is impossible.

The small settling chamber performed very well as we will show in section 5.12. At first we found the same natural transition Reynolds number as for the large settling chamber. However, after some slight changes, the natural transition Reynolds number increased from approximately 30 000 to more than 60 000. One of these changes was cleaning the fine mesh which is located just in front of the contraction. A few of the openings close to the wall were blocked by dirt. The only other change in the settling chamber has been replacement of the honeycomb placed directly behind the static mixers and before the diffusor of the settling chamber (see figure 5.17). The old honeycomb was erroneously pushed into the conical adapter between the

static mixers having a diameter of 50 mm and the 80 mm entrance of the settling chamber. This resulted in deformation of the honeycomb which may have resulted in transitional stall in the diffuser. These small changes may have affected the transition Reynolds number. The transitional Reynolds number of more than 60 000 is found ever since after each of the various (dis)assemblies of the small settling chamber that we performed, and this can be considered a property of our pipe setup and not a single best achievement.

In the next section, we will discuss the discharge chamber and the return pipe.

5.9 Discharge chamber and return pipe

As already mentioned in section 5.7.3, we made a sliding connection between the measurement pipe and the discharge chamber to accommodate the difference in thermal expansion. This connection is mounted in a larger flange, which functions as an arms-hole for cleaning purposes. A second hole is provided in the walls at the other side. In this wall, we also have constructed a small opening in line with the measurement pipe axis. Through this opening, we can align the laser beam for alignment of the pipe sections or pull the wire of the device used to clean the measurement pipe (see below). The discharge chamber is in essence a box with measures: length=0.90 m, width=0.55 mm, and height=0.50 mm which results in a capacity of 0.25 m³. To facilitate emptying of the discharge chamber, we inclined its bottom as is indicated by the dotted line in figure 5.5. To let any air escape that enters the discharge chamber, we also inclined the roof of the discharge chamber so that the air can leave through a small riser pipe. The riser pipe has a length of 0.5 m and also functions as a pressure limiter for the discharge chamber. A 0.5 m water column applies a force of 2.4 kN. Much larger pressures and pressure pulses may lead to rupture of the discharge chamber. The riser pipe also smoothes any sudden increases in pressure.

The return pipe has an inner diameter of 150 mm and consists of six 6 mm sections which are bolted together because gluing would make the pipe extremely difficult to handle. With its length of 36 m it has a significant contribution to the system volume (its volume is larger than the capacity of one storage vessel), which leads to a reduction of mechanical degradation of the polymers because the circulation time of the fluid through the facility depends on the volume. We have seen in section 5.4 that degrading can be expressed in the number of passes of the fluid through the facility. Also, the larger diameter reduces the Reynolds number such that mechanical degradation caused by the turbulence is much less than in the measurement pipe. We placed the return pipe under a gradient of 1 in 100 with the lowest end directed toward the pump.

As algae or other material may cause the system to become dirty, we have incorporated a system to clean the pipe without needing to completely dismantle the facility. For this, the ends of the return pipe are provided with a T-piece having a screw cover. To these covers we fixed a plastic wire which is permanently present in the return pipe. With this wire, we can pull a cleaning device through the return pipe. The cleaning device consists of a circular shaped piece of foam rubber. A similar but smaller cleaning device is used for the measurement pipe. The thin sheets in the test sections can withstand any extra pressure exerted by the cleaning device so no special precaution is needed. As no wire can be present in the measurement pipe during normal operating conditions, we first place a small wire through the pipe which is pulled by the flow resistance of a plastic 35 mm-film-can. This small wire is then used to pull a larger

wire which is attached to the cleaning device.

Growth of algae can be suppressed by the addition of sodium hypochlorite. However, this method cannot be used in combination with polymer solutions as the hypochlorite chemically degrades the polymers. Covering most transparent parts of the flow facility with black agricultural plastic also suppresses the growth of algae as these need ultraviolet light (emitted by e.g. strip light) to grow. However, covering alone was found to be insufficient because temperatures may rise to 25°C in the basement during a hot "greenhouse-effect" summer and this provides an ideal environment for growth of algae.

5.10 Dispersing and storage vessels

Two large storage vessels are used and are indicated as reservoir (normally included in the flow loop) and as mixing vessel (mostly used to mix the dilute polymer solution). See figure 5.18 for a sketch of the setup. Both storage vessels have a semi-spherical bottom. This ensures that no fluid stays behind when the system is emptied. The vessels are made of glass-fiber reinforced polyester. The color is black, which in combination with the covers blocks all the light, which is useful for suppressing growth of algae. The manufacturer stated that, although difficult, the PVC-sockets for the piping systems could be bonded to the polyester. After delivery, the bonds were found to be not watertight but repair was possible with the use of a special elastic cement. The one-way valve in the pipe which connects the return pipe with the reservoir, as is shown in figure 5.18, prevents air from entering the pump when the solution in the return pipe is being pumped in one of the vessels. The level at which the pipe enters the reservoir, is approximately 5 cm higher than the roof of the discharge chamber. Thus, during circulation with the reservoir included (normal operating condition), the discharge chamber is always completely filled.

The dispersing vessel, which is used to prepare the concentrated (master) polymer solution, is placed next to the two storage vessels on top of the catwalk frame. To be able to study the mixing (dissolving) of the polymers, we used Plexiglas for the dispersing vessel. Four baffles block solid body rotation of the fluid and enhance mixing. We used a mixer (Lightnin LP25VH) with a continuously variable rotational speed between 36 and 185 rpm. We increase the rotational speed at the beginning of the dispersion phase. After a few minutes, the rotational speed is reduced to approximately 100 rpm, and the solution is gently stirred for another two hours. We used a three-bladed stainless steel impeller (Lightnin A-310, which at the time was not yet coated) with a diameter of 300 mm. The dispersing vessel is not coupled to the flow loop and the concentrated solution has to be poured by hand (using buckets) into the vessels (both the mixing vessel and the reservoir are now filled) to make a dilute polymer solution. To enhance mixing in these storage vessels, the fluid can be circulated in each of the vessels separately or between the two by means of the piping system discussed in relation to figure 5.6. Also, the mixer can be easily moved between the dispersing vessel and the two storage vessels and is used to speed up the mixing process.

The weight of the mixer is approximately 30 kg, which is quite heavy to handle. Therefore, a hoist was used for the lifting of the mixer. The hoist can move along a rail which is attached to the ceiling, as is shown in figure 5.18.

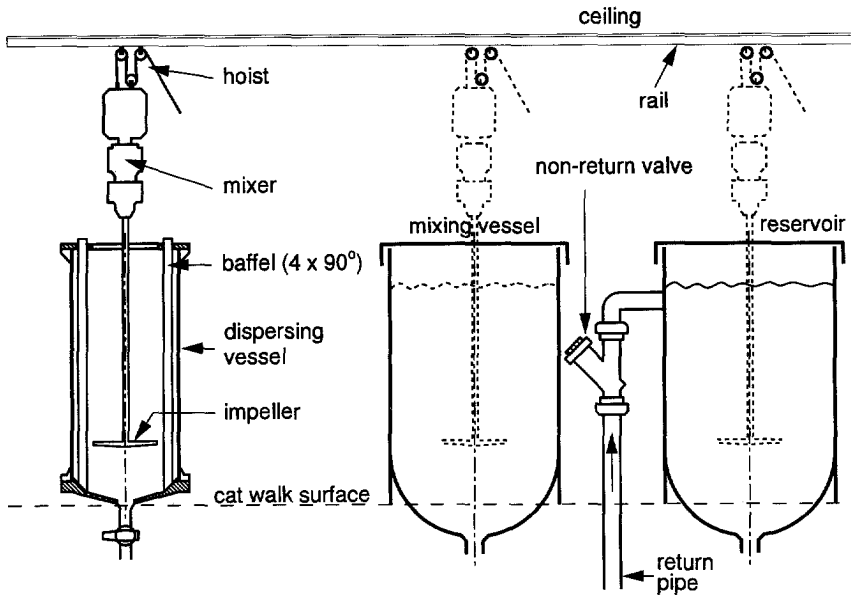


Figure 5.18: The two storage vessels and the dispersing vessel are located such that the impeller mixer can be easily changed between the vessels. With the help of the hoist, such an operation can be handled by one person within a few minutes. The pipe which includes the one-way valve is the only one drawn for simplification reasons.

5.11 Measurement equipment

5.11.1 Introduction

In this section, we will discuss the measurement equipment that we used in our experiments, together with some of the problems involved. We will start with a discussion on the pressure drop measurements, the flow meter, temperature recording, and LDV-equipment. At the end of the section, we will give a short discussion of Digital Particle Image Velocimetry (DPIV), which is a very promising technique to study transition. From the preliminary results, we feel that a discussion of this technique is justified, if only to highlight its potential.

5.11.2 Pressure drop transducer

In a 40 mm diameter pipe, the pressure drop over a 2 m pipe section in laminar flow is only 0.1 mm H₂O per $Re/1\,000$, i.e. for $Re=2\,000$ a pressure drop of 0.2 mm H₂O has to be measured accurately. This is impossible to do this with standard water manometer. A micro manometer is capable of measuring with an accuracy of 0.02 mm H₂O, but unfortunately, this type of manometer is suited only for gas pressure differences. Furthermore, it has to be read with the help of a magnification lens making it less suitable for data acquisition systems using PC's. Therefore, we have adopted another measuring method, which is a membrane differential pressure transducer (Validyne Engineering Corp., type DP15-20). This instrument measures the deflection of a thin stainless steel membrane, due to the pressure difference at both sides of the membrane, inductively. A membrane suited for 88 mm H₂O full scale was found to give a linear response with only a slight hysteresis, and able to indicate pressure differences as small as 0.03 mm H₂O. The differential pressure transducer is connected through small hoses to 1.0 mm pressure holes at the bottom of the pipe. We use a micro-manometer (Betz) to calibrate the membrane differential pressure transducer with air as fluidum.

The signal from the pressure transducer is very noisy but averaging over several seconds gives a very accurate value. As a result, we use during the stability measurements an average of all signals over 30 s. Also, a problem with this transducer is that the membrane for 88 mm H₂O full scale is rather thin. After measurement periods of many months, some corrosion of the stainless steel membrane can occur. Sometimes, also small holes are formed which make the membrane useless. Such behavior is easily noticed by erroneous signals and a slow response. Therefore, regularly cleaning and checking of the membrane is advisable. Another problem is zero drifting. Several times a day, the zero value should be checked. For this and to prevent overloading of the membrane, we connected the two hoses, that connect the two sides of the membrane to the pressure holes in the pipe, with a third hose containing a valve. All hoses are completely filled with water and any air bubbles distort the pressure measurement. Opening this valves, reduces the pressure over the membrane to almost zero. However, as the flow in the pipe causes a pressure difference between the pressure holes, a small flow will be generated through the pressure hoses. Thus, for an accurate measurement of the pressure transducer zero, these hoses should be blocked. We found that the flow through these hoses can trigger transition to turbulence in the pipe above Reynolds numbers of $Re \approx 20\,000$.

5.11.3 Flow meter

For an accurate recording of the flow rate, we employed a magnetic inductive flow meter (Krohne-Altometer, type M950/6 and control unit SC 100 AS). We tried to calibrate the flow meter by measuring the volume of the flow passed through the flow meter during a certain

time. The agreement between the volume-per-time method and the flow rate as indicated by the flow meter is very good. However, this method gives an accuracy approximately of only one percent, which is much larger than the assumed accuracy of the flow meter. The calibration certificate indicates standard error limits of 0.4% of the actual flow with a minimum of 0.1% of a bulk velocity of 1 m/s. The display gives a flow indication in discrete steps of 3 l/hr, i.e. steps of $7 \cdot 10^{-4}$ m/s in the bulk velocity. Summarizing, our method of calibration is not accurate enough to test the accuracy claimed by the manufacturer but we have no reason to doubt this alleged accuracy.

Fortunately, the flow meter also functioned in demineralized water, but due to the low conductivity, some problems were encountered. For a laminar flow, the signal is stable. However, for turbulent flow large fluctuations in the flow meter signal occurred. Averaged over half a minute, the signal still gives an accurate measurement which we could check by measuring a flow characteristic (Moody diagram) for demineralized water.

5.11.4 Thermometer

A mercury thermometer with a 0.1°C scale is used to measure the air temperature and calibrate the thermocouple elements (copper-constantan). The thermocouple elements are used to record the temperatures in the reservoir and in the pipe exit into the discharge chamber. For all measurements, the temperature in the discharge chamber is used to determine the density and the viscosity of the fluid. The thermocouples are connected to a temperature transducer (Monogram Omega) and the signal is directly fed to the measurement PC. As the copper-constantan wires function as an antenna for all signals present in the lab, the signal-to-noise ratio is rather small. Again averaging the signal gives reproducible recordings and calibration against the mercury thermometer ensured accurate readings. A large source for electro-magnetic interference is the frequency control unit for the pump. To improve signal-to-noise ratios of all measurement signals, an adequate electro-magnetic shielding for this frequency control unit is advisable but has not been used in our experiments.

5.11.5 Laser Doppler Velocimetry

Although Laser Doppler Velocimetry (LDV) is a well-established technique for flow measurement, a lot of problems are still encountered when using the equipment in an experiment, in particular in pipe-flow geometries. This is especially the case with the fiber-optics system that we used. The LDV equipment that we employed in our experiments, consists of a two-component full-backscatter system. Laser light from an argon-ion laser (Spectra Physics, type 2020) is split into green and blue light of 514.5 nm and 488 nm respectively. Each color is in its turn split into a frequency-shifted and unshifted laser beam. The pre-shifting of the laser beam is to avoid directional ambiguity of the measured velocity signal. The laser light is transmitted to the measuring probe (Dantec) by optical fibers. The focal length of the front lens of the measuring probe, used to focus the four beams on a measuring volume but also to receive the back-scattered light, is 80 mm. The backscattered light is transmitted by one optical fiber to a color separator and fed into two photo-multipliers which amplify the signal. The amplified signal is then transformed into a 2-D velocity signal by two Burst Spectrum Analyzers⁴ (Dantec,

⁴The Flow Velocity Analyzer (FVA, Dantec) that we used previously, has been replaced by these BSA's since the 8-bit output of the FVA turned out to be insufficient to do accurate turbulence measurements.

type Enhanced 57N20 and Enhanced slave 57N35).

As mentioned above, several problems were encountered. For instance, the alignment of the laser beams entering the optical fibers turned out to be extremely critical. Slight misalignment will result in burning of the fiber, thus strongly reducing the transmitting efficiency of the fiber as well as the quality of the LDV signal. Alignment of the laser beams depends on the location of the laser beam exiting the laser. As this changes with the temperature of the laser plasma tube, a warming up period is needed and this takes 1.5 hours (0.5 hour at low power, 1 hour at measurement power). The laser output is dependent on the alignment of the mirrors, and the best alignment of the mirrors of the laser is obtained after more than 6 hours. To obtain a good LDV signal, not only the optical coupling of the light into the fibers is important, but also very accurate (and tedious) alignment of the laser beams exiting the measuring probe is vital. For this, all four laser beams have to cross in one point which is also located at the optical axis of the measuring probe. This can be achieved by adjusting all laser beams such that they coincide at the same position. This can be done with the help of a $20\ \mu\text{m}$ pinhole, which is placed in the focal point of the measuring probe front lens. After adjustment, the dimension of the measurement volume is estimated to be $20 \times 20 \times 100\ \mu\text{m}^3$ in the stream-wise, normal and span-wise directions respectively.

The alignment procedure takes place in air, which gives no guarantee that the four laser beams will form one measurement volume inside the pipe. For instance, light refraction effects can cause problems, particularly close to the pipe wall. To minimize these problems, we constructed a LDV test section which consists of a rectangular optical box filled with water that is placed around the pipe and in which the pipe wall is locally replaced by a thin sheet having a refractive index close to that of water. For a detailed discussion we refer back to section 5.7.3.

The measuring probe is mounted on a traversing mechanism (Dantec - Isel). The BSA's and the traversing mechanism are controlled by a PC, thus making fully automated measurements possible. For this first the origin, i.e. the center of the pipe has to be determined. This is done by locating the position of the wall (thin sheet) in a vertical and horizontal traverse. When the measurement volume hits the wall, a strong increase in noise level of the Doppler signal is observed. The accuracy of the wall determination using this procedure and thus also of the pipe center, is estimated to be 0.1 mm.

5.11.6 Digital Particle Image Velocimetry

Digital Particle Image Velocimetry (DPIV) is a relatively new technique which yields instantaneous two-dimensional velocity fields in a planar cross section of the flow. The principle is estimating the displacement of small particles in the flow. The motion of these particles is recorded in a multiple exposed image using a 1000×1016 pixel CCD camera. In this multiple exposed picture, each particle appears several times, shifted by the flow. By measuring this distance, the velocity can be reconstructed. This is done by dividing the image into small sub-images, and for each sub-image we compute the auto-correlation. All particle-images that correspond to the motion of a single tracer particle contribute to an off-center peak in the correlation of the particle position. The displacement of the particle images is obtained from measuring the distance of this peak from the center peak. Given the image magnification and time delay between the exposures, we obtain the in-plane velocity. The cameras were operated at a frame rate of 10 Hz, thus giving a time series of velocity fields.

We used DPIV to study its possibilities in exploring transition to turbulence. These measurements were performed exactly one year before the stability measurements which are presented in chapter 6 and 7 (when experimental facilities are fully operational, August is a very good month for an intense measurement program). As we used a different disturbance mechanism at the time (injection through a 1 mm hole), we cannot compare the results of the DPIV measurements with the stability diagrams presented in this thesis. This, and the fact that only a fraction of the large data set is analyzed as of this writing, have caused us to decide not to incorporate the DPIV measurements. Nevertheless, since we believe that DPIV is a very powerful tool for studying laminar-turbulent transition, we will briefly discuss the main problems that we encountered and give an indication of the fascinating results that can be obtained using DPIV. For a more detailed discussion on the DPIV equipment and the preliminary results see Westerweel *et al.* (1994), Draad *et al.* (1995), and Draad & Westerweel (1996).

The three largest problems that we encountered when performing DPIV measurements in a transitional pipe flow are related to the seeding particles, reflections of the laser light into the camera, and aliasing due to the multiple exposed images. These will be briefly discussed below.

The flow was seeded with small tracer particles (Optimage) which have a density which is slightly larger than that of water. However, given the length of the pipe and the long residence time, particularly close to the wall, these particles tend to slowly settle. This results in low particle concentrations in the top part of the pipe, leading to a poor image quality in this region. This problem can be solved by triggering turbulent flow at the beginning of the pipe shortly before a 13 s time series is recorded. Turbulence mixes the particles and redistributes them over the entire cross section. After relaminarization of the flow, images can be recorded with a sufficient particle density throughout the cross section.

We used a sheet of laser light to illuminate the seeding particles. To reduce distortion of the image related to differences in index of refraction between the air, water and the Plexiglas, we used the test section that we have also used for the LDV measurements. However, strong reflections of laser light gave rise to bright horizontal lines in the recorded images and these lines totally destroyed a large part of the image for DPIV analysis. We found that these lines are the result of the laser light which is reflected from the location where the sheet of laser light crosses the walls of the optical box. Next, this light is reflected into the camera via the thin plastic sheet replacing the pipe wall. These reflections can easily be blocked when plastic plates are placed just above and below the pipe containing thin slits which let the sheet of laser light pass (see figure 1 in Draad *et al.* 1995).

We also found, that the velocity profiles measured with DPIV show large humps which were not found when using the LDV equipment. We found that these humps, further called shoulders, occur as a result of aliasing. As mentioned before, we determined the displacement of the particles in small interrogation areas of 32×32 pixels using auto-correlation techniques involving Fast Fourier Transforms (FFT). In a laminar flow, the multiple exposed images of the particles are aligned. When the displacement of a particle approaches an integer fraction of the size of the interrogation area, i.e. $32/2$, $32/3$, $32/4$, $32/5$, and so on, aliasing occurs and a strong bias to these values is found. The aliasing can be suppressed by applying zero-padding to the data, as is shown in figure 5.19. A detailed discussion on this subject can be found in Aanen (1995).

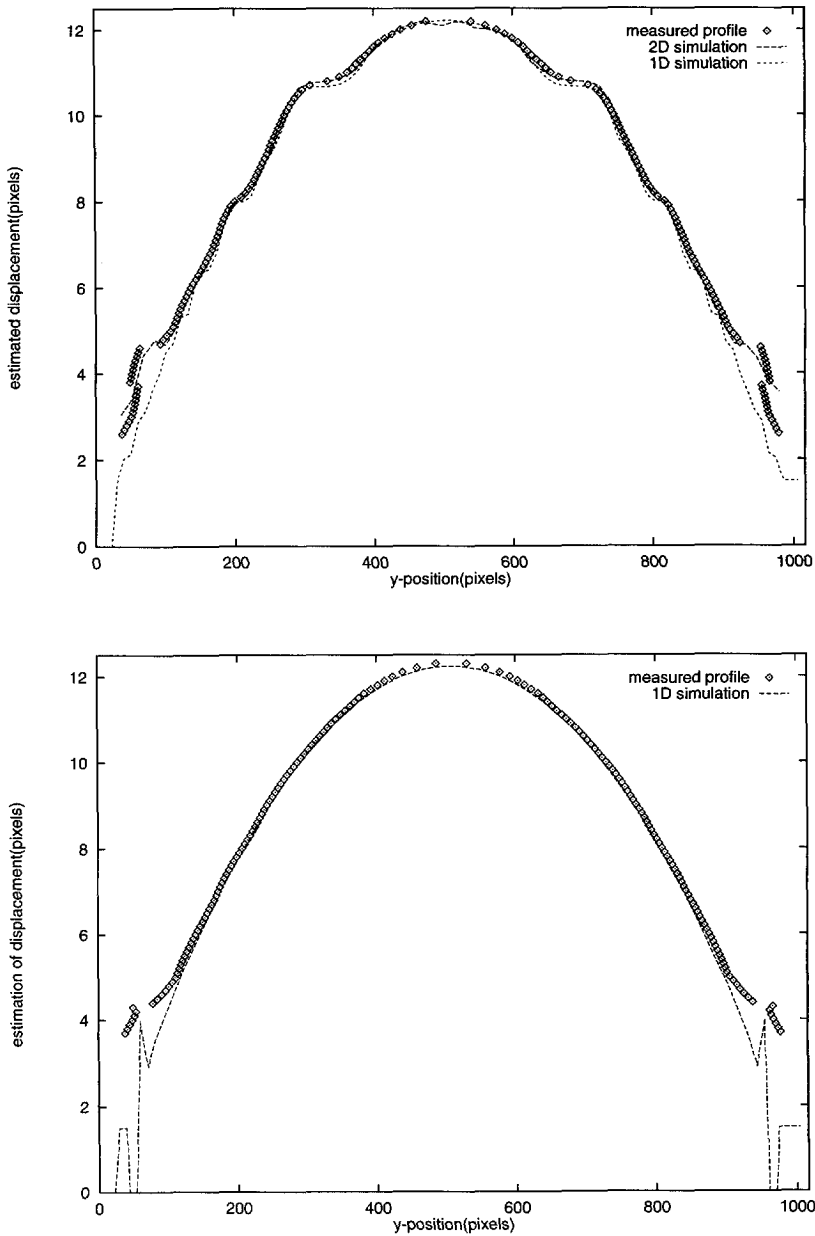


Figure 5.19: Comparison between the velocity profiles obtained by numerical calculations and the measured velocity profile using Digital Particle Image Velocimetry. Note that the measured velocity profile is symmetric and seems to have a gap near the center. This is caused by the horizontal averaging of the measured velocity profile to obtain a symmetric profile that can be compared with the simulations. From Aanen (1995).

To give an indication of the detailed flow structures in a transitional flow that can be captured, we show in figure 5.20 a disturbance velocity field which has been obtained by subtracting the average laminar velocity profile from the measured velocity field. We see a series of vortices close to the wall, at the side where the fluid is injected which disturbs the laminar flow, shortly before the flow became turbulent over the entire cross section. The preliminary results show that DPIV can be used to elucidate phenomena governing transition to turbulence that previously could not be studied quantitatively. Furthermore, the velocity fields that can be obtained using DPIV give a much more detailed view of the flow and are more easily interpreted than (time averaged) contourplots of disturbance velocities, which are commonly used. Therefore, further use of DPIV techniques in transition research is strongly recommended, which has also been pointed out recently by Darbyshire & Mullin (1995).

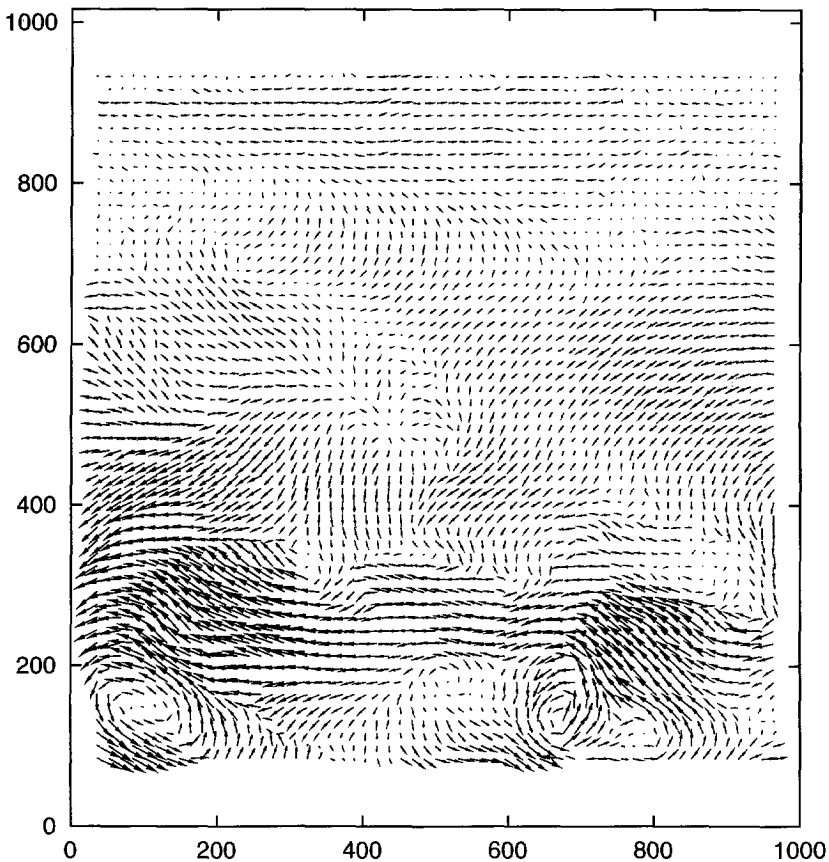


Figure 5.20: Instant relative velocity plot from one frame for $Re=5860$, showing the eddies close to the wall shortly before transition to turbulence occurs over the entire cross section of the pipe. From (Draad *et al.* 1995).

5.12 Flow quality

In this section, we will illustrate some of the gross flow characteristics of our pipe-flow facility. An appropriate method is the so-called Moody diagram. In a Moody diagram, the dimensionless pressure pressure gradient, i.e. the Moody⁵ friction factor f_M , is plotted as a function of the dimensionless flow rate in the form of the Reynolds number Re . Here, Re and f_M are defined as:

$$Re = \frac{\rho \bar{W} D}{\eta} = \frac{\bar{W} D}{\nu} \quad (5.21)$$

$$f_M = \frac{D}{L} \frac{\Delta p}{\frac{1}{2} \rho \bar{W}^2} \quad (5.22)$$

where ρ is the density, \bar{W} is the bulk velocity, D the pipe diameter, η the dynamic viscosity, and ν is the kinematic viscosity of the fluid.

For fully developed laminar pipe flow, i.e. Hagen–Poiseuille flow, the relationship between the pressure drop and the flow rate can be rewritten into the Moody friction factor form, with as result:

$$f_M = 64/Re \quad (5.23)$$

For turbulent flow, a different relationship is found. As the turbulent velocity profile can be fairly well described by a $\frac{1}{7}$ -power law in a Reynolds number range representative for our experiments, this may be recasted in the friction factor form to give the so-called Blasius law (Bird *et al.* 1960, p. 187):

$$f_M = 0.3164 Re^{-1/4} \quad 2.1 \cdot 10^3 < Re < 10^5 \quad (5.24)$$

Transition to turbulence can now be easily detected since the measurement points ‘jump’ from the laminar Hagen–Poiseuille line to the turbulent Blasius line. In figure 5.21 we show the Moody diagram for our facility. It is clear that we can maintain laminar flow up to Reynolds numbers past $Re=60\,000$. No measurements for turbulent flow are shown in this figure because the corresponding turbulent pressure drop values for these high Reynolds number are beyond the range of our pressure transducer. To be able to measure turbulent pressure drops up to high Reynolds numbers (needed for triggered transition experiments), we measured the pressure drop over a relative short pipe section which is only 2.5 m long. This results in very small laminar pressure drop values and a small error in the zero value has a large influence on the obtained pressure drop. To correct for a slight error in the zero value for the pressure drop, we linearly extrapolate the pressure drop vs. flow rate data to find the reading corresponding to zero flow rate. The pressure drop measurements are then corrected using this value. These correction always fall within 0.05 mm H₂O, which is well within the zero drift that has been observed. In figure 5.21, we also see that the measurements deviate from the Hagen–Poiseuille curve, well before $Re=14\,300$, i.e. the Reynolds number up to which fully developed flow should exist in our facility. However, the measurements follow up to about this point, the markers labeled

⁵Another commonly used definition of the friction factor is the so-called Fanning friction factor f_F , which is related to f_M : $f_M=4f_F$.

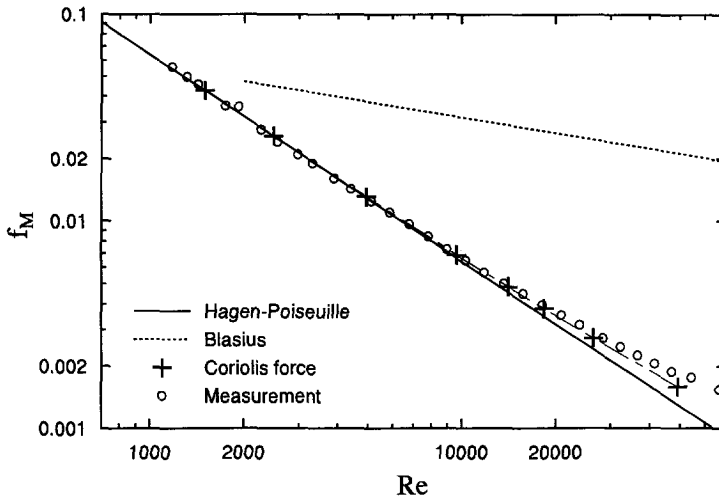


Figure 5.21: The Moody diagram for water in our new pipe-flow facility. The points labeled ‘Coriolis force’ are results from numerical calculations accounting for the influence of the earth’s rotation on fully developed laminar pipe flow.

‘Coriolis force’. These points labeled ‘Coriolis force’ are obtained from numerical simulations of fully developed laminar pipe flow under influence of the Coriolis force caused by the earth’s rotation. This is because, perhaps surprisingly, it turns out that the laminar flow in our pipe-flow facility, is strongly influenced by the Coriolis force. Although the Moody diagram does not suggest a drastic change in flow behavior, due to this effect the axial velocity profiles reveal a quite different picture, as is illustrated figure 5.22. Here the measured axial velocity profiles are compared to those obtained using numerical simulation, discussed in more detail in appendix C. We see that the agreement between the observations and the computations is excellent, which confirms that the distortion of the axial velocity profiles in our pipe-flow facility, are primarily caused by the rotation of the earth.

One may wonder why the Coriolis force, being very small, is still able to strongly distort the axial velocity profiles? To explain this, one should first realize that in a fully developed laminar pipe flow, the terms representing the inertia forces all vanish. This leaves the balance of the pressure gradient and the viscous force resulting in standard conditions in a parabolic velocity profile. Since in water, the viscous force is extremely small, due to the small kinematic viscosity, an extra force even when relatively small, may have a large influence. In our pipe, the magnitude of the Coriolis force is 19% of that of the viscous force. So, compared to the viscous force, which normally causes the parabolic velocity profile, the Coriolis force is large. However, as the ratio of the Coriolis force to the viscous force, represented by the ratio of the Reynolds number Re and the Rossby number Ro (see appendix C for a definition and a detailed discussion of the influence of the Coriolis force on laminar pipe flow), is constant, one may ask why does the distortion of the axial velocity profile become stronger with an increase in Reynolds number? This is due to the difference in scaling for the cross sectional secondary velocities and the axial disturbance velocity. According to linear theory, the cross sectional velocities of the secondary

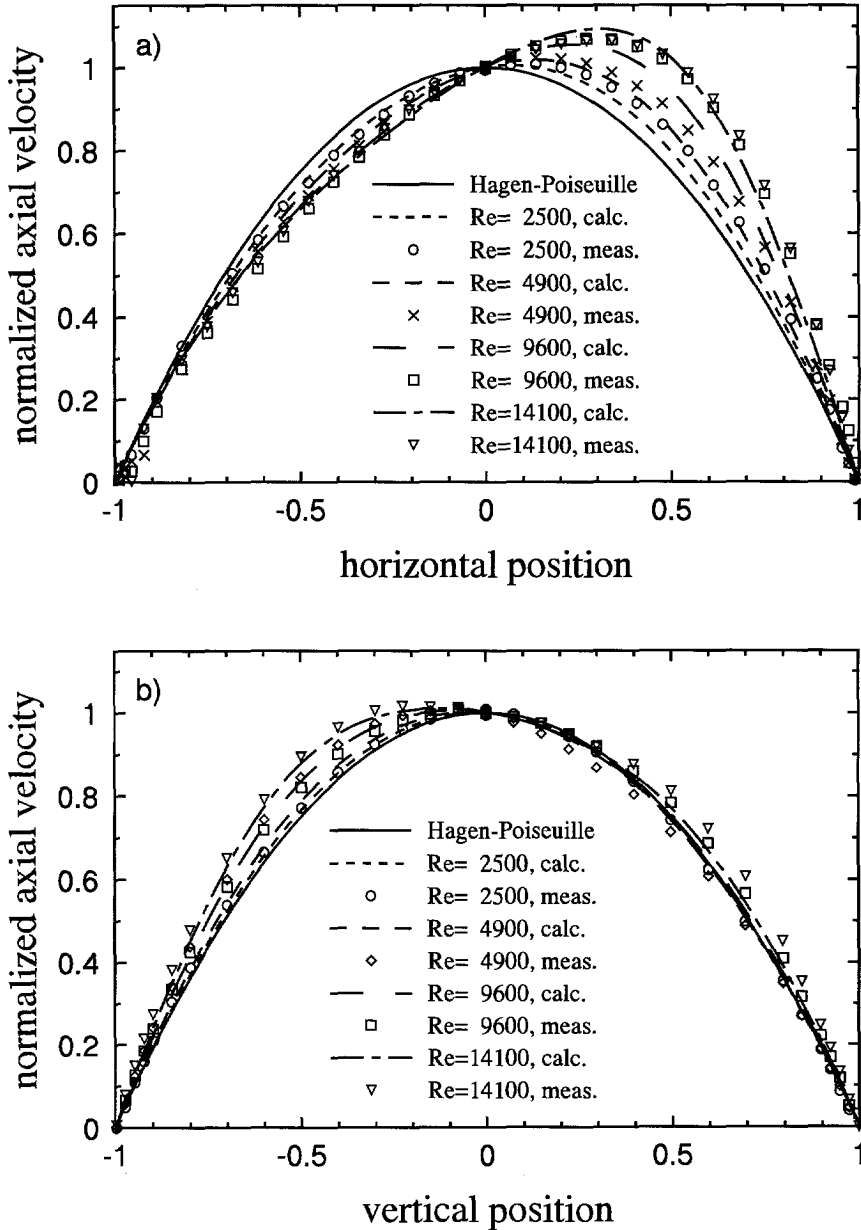


Figure 5.22: Comparison between calculated (lines) and measured (markers) axial disturbance velocity profiles in a) horizontal and b) vertical direction for various Reynolds numbers.

flow caused by the Coriolis force, scale according to Re/Ro and the axial disturbance velocity scales according to Re^2/Ro . The ratio Ro/Re is also known as the Ekman number (Drazin & Reid 1981, p. 365):

$$Ek = \frac{Ro}{Re} = \frac{\nu}{2\Omega D^2 \sin \alpha} \quad (5.25)$$

where Ω is the rotational speed of the earth and α is the angle between the pipe axis and the axis of rotation. For our case, $Ek=5.23$ as already mentioned above. In order to reduce the Coriolis force effects at a constant Reynolds number, we have to increase the Ekman number. This can be done by increasing the viscosity of the fluid, by orienting the pipe parallel to the axis of rotation, or by reducing the pipe diameter. Reduction of Ω , although extremely difficult, would also solve the problem of having too few hours in a single day.

That above $Re=14\,300$, the flow is no longer fully developed can also be observed in figure 5.23, where the axial velocity profiles are plotted for several Reynolds numbers. The axial velocity is here normalized with the bulk velocity and for a parabolic profile this would result in a maximum value of 2 at the centerline. Clearly, at the largest Reynolds number the velocity profile becomes flatter in the central part of the flow.

5.13 Disturbance mechanism

5.13.1 Introduction

In many investigations on triggered transition, the triggering mechanism that is used is a single jet (e.g. Klingmann 1992, Darbyshire & Mullin 1995, Wygnanski *et al.* 1975). This means for instance, that the disturbance is not divergence free, which may cause pressure disturbances at large distances from the injection point. In other words, the disturbance cannot be considered as localized. Nevertheless, we have also used this method. We injected fluid through a 1 mm hole in the pipe wall during 0.5 s and found that injection velocities up to 9 times the centerline velocity are needed for causing a transition at $Re=3\,000$ (Draad *et al.* 1995). With an oscillating jet the injection velocities necessary to trigger transition become much smaller (Aanen 1995). However, rather than using a point disturbance with its disadvantages as mentioned above, we wanted to use a disturbance that resembles more the functions used in non-linear theories by e.g. Smith & Bodonyi (1982). These authors suggest that disturbances which are not axisymmetric but having an azimuthal wave number of 1 or more may be the ones most likely to become unstable and trigger turbulence.

A disturbance with azimuthal wave number 1 can be constructed using four sets of double working syringes, each shifted 45° in phases as described by Aanen (1995). He showed, using stream functions, that injection at 8 points in a thin slit results in a reasonably smooth sinusoidal disturbance at the pipe wall. However, the construction of such a disturbance mechanism was found to be too time consuming and expensive. Therefore we constructed a somewhat simpler disturbance mechanism, with only 2 injection points connected to a single oscillating double working syringe. To study the stability of the flow, the amplitude of the disturbance, i.e. the displacement volume of the syringes, has to be adjustable, and also a continuously variable frequency is required. After examination of some possibilities (Boere 1995) we decided to use an eccentric mechanism to drive the syringes which is described in the next section.

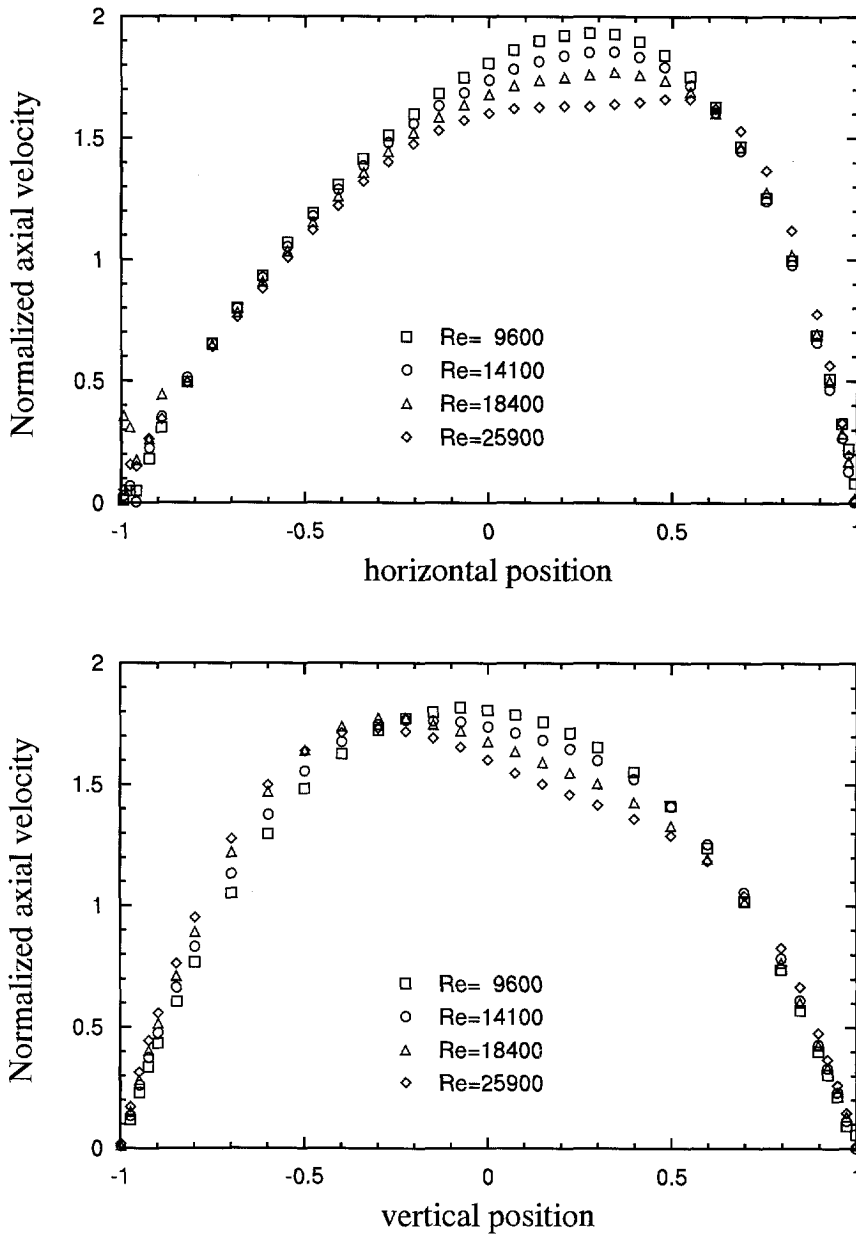


Figure 5.23: Axial velocity profiles in water normalized with the bulk velocity in the horizontal plane (top) and the vertical plane (bottom). The length of the pipe-flow facility permits fully developed flow up to Reynolds numbers of $Re=14\,300$.

5.13.2 Eccentric disturbance mechanism

The eccentric disturbance mechanism operates two syringes that are mounted in opposite direction, as is shown in figure 5.24. This means that when one syringe is injecting the other extract fluid. The amplitude of the oscillation can be continuously adjusted between 0 and 20 mm by sliding the eccentric point, which is fixed by four bolts. The eccentric mechanism is driven by a strong electric motor of which the rotational speed can be continuously varied between 0 and 40 Hz. The frequency is measured using a pulse counter which has a resolution of 0.02 Hz. The joints of the connecting rod are formed by ball bearing and ball bushings are used for the guiding of the rod that drives the syringes.

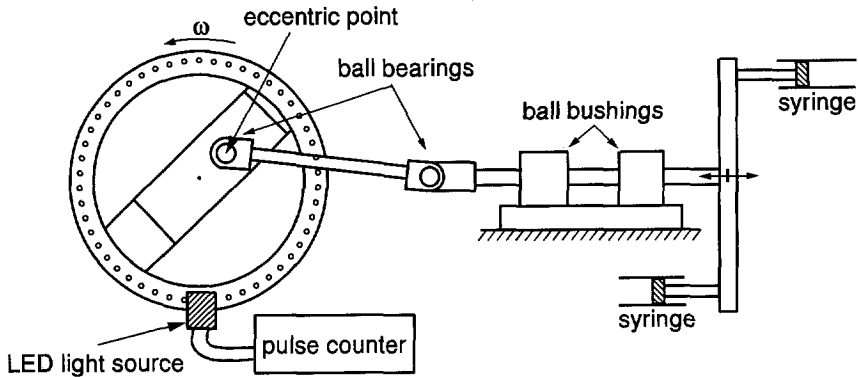


Figure 5.24: The eccentric disturbance mechanism which is used to trigger transition.

We used two sets of low cost commercially available syringes (BD Plastipak, 1 and 5 ml) having an internal diameter of 4.7 and 12.0 mm respectively. These plastic syringes provide a smooth transparent cylinder which can be replaced if wear occurs and which also allows for a visual inspection to detect any trapped air bubbles. The latter is important, since a compressible air bubble would destroy the relationship between the amplitude of the syringes and the injection velocity. The soft rubber pistons that come with these syringes display too much elastic deformation at high frequencies and no longer follow the displacement of the driving rod. Therefore, we replaced them with plastic pistons which have a groove to accommodate the quadrings (a special type of rubber ring with four-lobbed cross-section) which prevent leakage. Quadrings are much better suited for oscillating conditions and give less friction than e.g. O-rings. To provide a stiff wall, the syringes are placed in Plexiglas holders which can be mounted to the injection piping. This allows us to quickly change the syringes. The piping which connects the syringes with the forcing system, also called the injection flange, are made of transparent PVC. This gives visual access to detect bubbles but also provides a stiff wall that prohibits damping of the oscillating flow caused by the flexibility of the wall. The inner diameter was 13 mm to minimize flow resistance which could lead to cavitation in the injection flange (Boere 1995).

The geometry of the injection flange is shown in figure 5.25. The fluid is injected/extracted perpendicularly to the pipe wall through a thin slit. The construction is made so that the disturbance is spread as evenly as possible over the entire circumference. In this way, the disturbance is much more smooth compared to injection through holes in the pipe walls. Moreover,

as equal amounts of fluid are injected and extracted, the disturbance is divergence free and large pressure pulses are avoided which would disturb the pressure drop measurement. This effect is also found when air bubbles are trapped in the injection piping.

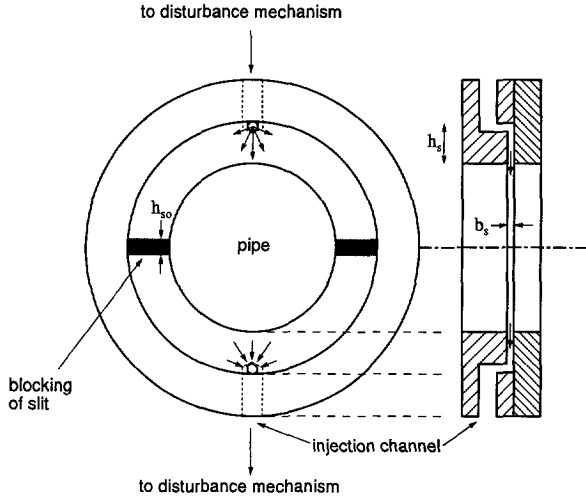


Figure 5.25: Illustration of the injection flange to excite the pipe flow with a non-axisymmetric disturbance in order to trigger transition to turbulence. $b_s=0.55$ mm, $h_s=15.0$ mm, and $h_{so}=3$ mm.

To characterize the disturbance, we use the disturbance velocity and the frequency. As we do not know the precise azimuthal distribution of the velocity, we defined the disturbance velocity as the average velocity through the injection slit in the pipe wall, i.e. over half the injection opening, whereas over the other half suction is applied, at the moment where the velocity of the syringes reaches its maximum, i.e. the maximum of the azimuthally averaged injection velocity. The total injection+extraction area (O_{ring}) measures:

$$O_{ring} = (\pi D - 2 \cdot h_{so}) b_s \quad (5.26)$$

Here, b_s is the width of the slit and h_{so} is the height of the areas blocking the slit (see figure 5.25). The relationship between the maximum piston velocity $v_{p,max}$ and the disturbance velocity v_i is then governed by the ratio of the surface of the piston to that of the injection area ($O_{ring}/2$):

$$v_i = \frac{\frac{\pi}{4} D_s^2}{\frac{1}{2} O_{ring}} v_{p,max} \quad (5.27)$$

where D_s is the inner diameter of the syringe. Since, $v_{p,max}=2\pi f A$, where f is the frequency and A is the amplitude of the oscillation of the piston, the disturbance velocity (in m/s) can now be expressed as:

$$v_i = 0.0001909 \cdot \frac{\pi}{4} \cdot D_s^2 \cdot A \cdot f = 0.0001909 \cdot \Delta V \cdot f \quad (5.28)$$

Here, ΔV is the displacement volume in mm^3 (D_s and A have to be substituted in mm's).

Note that the disturbance velocity depends on both ΔV and f . The frequency can be changed without stopping and modifying the disturbance mechanism to change the amplitude of the oscillation. That is why we used several discrete values of ΔV in our stability measurements, and varied f . The frequency f is recorded directly into the measurement computer together with quantities like pressure drop and flow rate.

We found that the reproducibility of the experiments is quite good and we feel that our disturbance mechanism operates satisfactorily. The results of the stability measurements obtained with the disturbance mechanism described in this section, will be presented in chapters 6 and 7 for Newtonian and non-Newtonian fluid respectively.

Chapter 6

Newtonian stability measurements

Abstract

In this chapter we present the stability measurements for a Newtonian fluid, i.e. water. The stability measurements can be divided into $Re \leq 2700$ where transition is characterized by the presence of puffs or $Re \geq 3000$ where transition is characterized by turbulent slugs.

In the puff- Re -range, the largest number of puffs per time-trace of 15 min are generated at an optimal frequency. This frequency is very close to the value at which turbulent slugs are generated around $Re = 3000$. The percentage of puffs that show so-called incursions in their trailing edge centerline velocity is much smaller than the 30% found by (Darbyshire & Mullin 1995).

In the slug- Re -range, the disturbance velocity that just triggers transition, i.e. the critical disturbance velocity, varies weakly with the nondimensional wave number α^ . Only for $\alpha^* \approx 1$, does the flow seem extra sensitive, particularly for $Re \geq 30000$. For $\alpha^* \leq 2$, the ratio of critical disturbance velocity to bulk velocity seems to vary according to $Re^{-2/3}$. For large α^* , $\alpha^* \geq 5$, the critical disturbance velocity is practically independent of Re and thus the ratio of critical disturbance velocity to bulk velocity seems to vary according to Re^{-1} .*

For $Re \geq 30000$ and $\alpha^ \geq 2$ multiple transition points are found. For such a case, increasing the disturbance velocity for constant α^* , the flow regime may change from laminar to turbulent, back to laminar and at even larger disturbance velocities the flow will become turbulent again.*

6.1 Introduction

In this chapter, the pipe-flow stability of a Newtonian fluid will be discussed. This in itself is an interesting topic as it is still one of the greatest unsolved fundamental problems in fluid mechanics. Considering the amount of work which has already been done on this topic, the main aim of this project cannot be to completely solve it. Apart from the small contribution we hope to make to Newtonian transition research on pipe flow, these stability measurements will also serve as a reference for the study of the effect of polymer addition on pipe-flow transition. These non-Newtonian stability measurements are presented in the next chapter.

To study laminar-turbulent transition of both Newtonian and non-Newtonian fluids, we constructed a experimental pipe-flow facility. Its design, construction and performance have been described in detail in chapter 5. The natural transition Reynolds number in our facility is $Re \gtrsim 60000$, whereas the lowest natural transition Reynolds number for pipe flow is $Re \approx 2300$ ¹. This gives us a wide range of Re where the flow can be triggered to become turbulent. This can be done using disturbances of which characteristics like amplitude and frequency can be

¹Many values circulate for the minimum transition Reynolds number. Darbyshire & Mullin (1995) find that below $Re = 1760$ no puffs can be sustained. However, Wygnanski *et al.* (1975), show that equilibrium puffs exist around $Re \approx 2200 - 2300$. Based on this, we prefer to use $Re = 2300$.

accurately adjusted. In this way, we can measure the disturbances that trigger transition and study the influence of various disturbance parameters.

Based on the theoretical work of e.g. Smith & Bodonyi (1982), our idea was to disturb the flow with disturbances which are not axisymmetric but have an azimuthal wave number of 1 or more. Nonlinear theories, suggest that such disturbances may be the most likely to become unstable and trigger turbulence. To generate such disturbance, we used the disturbance mechanism described in more detail in section 5.13. The frequency and the amplitude of the disturbance can be varied continuously between zero and a maximum value. We used this to measure which combinations of disturbance amplitude and frequency trigger transition. The Reynolds number for these measurements was in the range of $1800 \leq Re \leq 50\,000$. The disturbance that just triggers transition is referred to as *critical*.

The measurements can be grouped into those where a critical disturbance generates turbulent slugs or so-called puffs of which the characteristic were discussed in section 2.3.5. This corresponds to Reynolds numbers of $Re \geq 3\,000$ and $Re \leq 2\,700$ respectively. Owing to their nature, it is more difficult to detect puffs than turbulent slugs. The reason for this is explained in the next section where we discuss measurement methods together with some definitions of (non-)dimensional quantities that will be used to present the stability measurements. Then, in section 6.3, we will discuss the stability measurements performed in the slug- Re -range. These measurements are the basis for the choice of the parameter values for the stability measurements in the puff- Re -range. That is why the stability measurements for the high Reynolds numbers, i.e. slug- Re -range, are discussed before considering the puff- Re -range in section 6.4. Finally, a transition model is proposed that may give an explanation for measured pressured drops at high Reynolds numbers which sometimes become smaller than the laminar pressure drop or even negative.

6.2 Measurement method

6.2.1 Introduction

In a basic study of the stability of the flow, one of the basic needs is to discriminate between the various flow regimes. The laminar and the turbulent flow regime are separated not by a sudden transition but by a finite transition region. The flow structures which can be observed in this transition region, depend on the Reynolds number. This has an effect on the method of transition detection which will be elucidated in the next section. With a clear detection criterion for transition, we are able to study the variation of the disturbance magnitude and frequency which are just able to trigger transition for a given Re . In order to be able to compare our results with theory and other experimental observations, we need to normalize our results. How this is will be explained in section 6.2.5.

6.2.2 Transition detection

Before we can study transition, we have first to be able to detect it. Such detection must clearly depend on the flow characteristics in the transition region. The types of transitional flow depend on the Reynolds number (e.g. Wygnanski & Champagne 1973). For $Re \leq 2\,700$, so-called puffs are observed. To give a short description of a puff (for more details see section 2.3.5) we note that initially the velocity in the puff decreases slowly below the laminar value. At the end of a puff, the velocity increases rapidly again to reach the laminar value. The stream-wise

rms disturbance within a puff is observed to be strongest near the center of the pipe. The length of a puff is approximately $10\text{--}40D$. For larger Re , the puffs start merging and so-called turbulent slugs are formed for $Re \geq 3\,000$. The flow characteristics in the interior of a turbulent slug closely resemble turbulent pipe flow. Both leading and trailing edges of a slug are sharp so that the velocity changes quickly between the laminar and turbulent values. Turbulent slugs can have a length of the order of the pipe length. These two structures, i.e. puffs and slugs, have been found in both natural as well as in triggered transitional flows.

The difference in structure between puffs and slugs also affects the transition detection. In our case, two measurement techniques available to detect transition; Laser Doppler Velocimetry (LDV) and differential pressure drop measurements. For both techniques, it turned out that detection of transition in the puff- Re -range is more difficult than in the slug- Re -range.

Let us first look in somewhat more detail at the pressure drop measurement. As already mentioned, the undisturbed flow in our facility is laminar for $Re \leq 60\,000$. So the lowest pressure drop we have to be able to measure accurately is for laminar flow at $Re = 2\,000$ and the highest pressure drop is that for turbulent flow at $Re = 60\,000$. This results in a range of pressure drops we should be able to measure accurately of $0.25\text{ mm H}_2\text{O}$ to $117\text{ mm H}_2\text{O}$ ². Although a pressure gauge for this total range was not available, we have been able to obtain good results with a membrane differential pressure gauge which could be used up to $80\text{ mm H}_2\text{O}$ which is equivalent to a pressure drop over 2.5 m in turbulent flow at $Re \approx 50\,000$. With this device, we could also observe the laminar pressure drop for the puff- Re -range, i.e. $Re \leq 2\,700$, with sufficient accuracy. However, as the flow does not become fully turbulent, the increase in pressure drop due to the presence of puffs is too small to be accurately captured. Thus, the detection of transition with help of the pressure-drop measurement is restricted to $3\,000 \leq Re \leq 50\,000$.

Next we consider the Laser Doppler Velocimetry (LDV). In fact we used two LDV's; a HeNe-laser system in combination with a frequency tracker, and an argon-ion laser together with a two-component fiber-optic system by Dantec and a BSA to analyze the signal (for more details see section 5.11.5). The various (dis)advantages of the two systems are:

- The HeNe-system requires no safety protection other than a prevention of not looking directly into the laser beam. For the argon-system, safety precautions like wearing laser glasses and screens to block the (reflected) laser radiation are necessary.
- The HeNe-system can be used immediately after it is switched on. Due to the extremely accurate alignment which is required for the fiber optics, the argon-ion laser needs 1.5 hours of warm-up time before it is operational.
- The HeNe-LDV time-traces of the mean velocity and higher order moments are displayed on a computer screen. This is very helpful in detecting the type of flow. Unfortunately, the Burstware software by Dantec allows no such on-line time-trace information but gives only on-line the mean and the rms-velocity values plus a histogram of the velocities.
- Unfortunately, a low velocity tracker for the HeNe-LDV system was not available and the tracker that we used, could measure only the centerline velocity for $Re \geq 7\,500$. As the

²Here we used that the pressure drop is measured over a 2.5 m pipe section and the kinematic viscosity of the fluid is $\nu(24.4^\circ\text{C}) = 9 \cdot 10^{-7}\text{ m}^2/\text{s}$.

argon-LDV has no such problems, all measurements for $Re < 7500$ have been done using this system.

- An advantage of the argon-LDV system is that it is equipped with a computer controlled traversing mechanism. Thus all velocity *profiles* were measured using the argon-LDV.

Now, let us explain how we used the two LDV's for the detection of transition. During transition, the most pronounced changes in the velocity in both the puff- Re -range and the slug- Re -range can be observed at the centerline (Wynanski & Champagne 1973). Thus both LDV's measured the centerline velocity for the detection of transition.

In the slug- Re -range, i.e. $Re \geq 3000$, transition could be detected easily by this method. The on-line time-trace of the HeNe mean velocity (used above $Re = 7500$) clearly showed the presence of slugs. Also, the argon-system gives in this case two peaks in the velocity histogram, around the laminar and the turbulent centerline velocity. Furthermore, it gives in that case also rms-velocity fluctuations exceeding 10% of the average velocity.

In the puff- Re -range, i.e. $Re \leq 2700$, only the argon-LDV could be used and transition detection becomes much more difficult. This is in particular the case for measurement around $Re = 2000$. The problems are caused by the very nature of the centerline-velocity signal of a puff. This is because, the shape of a centerline-velocity time-trace of a puff resembles a saw-tooth; a slow decrease in velocity near the leading edge of the puff and a sharp rise at the trailing edge. As a result, no second peak will emerge in the velocity histogram but only a slight asymmetry appears towards the turbulent velocity value. The degree of asymmetry depends on the amount of puffs that are generated. Also, the average velocity decreases only slightly by about several percent and the rms-velocity is increased only a little, typically to 2.5-3% of the average velocity. With respect to the latter, we may mention that this increase of the rms is also hard to notice due to the rms-values of 1-2% caused by noise of the average velocity for the laminar flow. To minimize these difficulties, we measured in this case velocity time-traces during 15 minutes in which the puffs are easily noticed. As such measurements are rather time consuming, only a limited number of frequencies and amplitudes could be studied. The choice for the values for the disturbance frequency was based on the frequency for which transition was found at $Re = 3000$. This is why the results in the slug- Re -range are discussed before those in the puff- Re -range.

6.2.3 Measurement location

In the previous section, we discussed the method which we used to detect transition. However, the location of the 'detection system' relative to that of the disturbance mechanism also plays a role in the detection of the transition. The reason is that a disturbance needs time to grow before it reaches a magnitude at which triggers transition. During this time the disturbance moves downstream. So, suppose a disturbance is slightly above critical and will trigger turbulence at a certain location downstream. Then, depending on whether the transition detector is placed upstream or downstream of this location, it will detect a (disturbed) laminar or a turbulent flow respectively.

In figure 6.1, the configuration of the pipe segments, the disturbance mechanism, and the measurement locations are shown. The disturbance mechanism is located at 26.95 m (673.75 D) downstream of the contraction. The locations of the two pressure holes over which we record

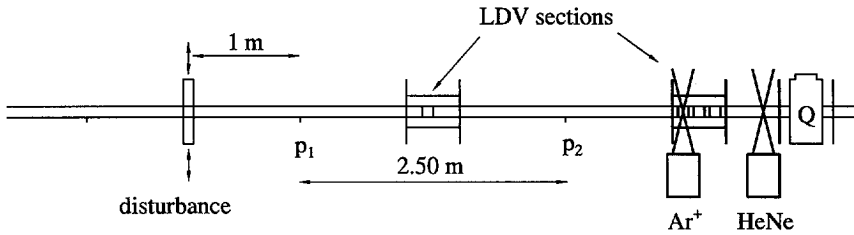


Figure 6.1: Configuration of the pipe segments and the measurement sections during the stability measurements. The squares inside the LDV-measurement sections having the size of the pipe diameter depict the location of the thin sheets replacing the Plexiglas pipe wall. p_1 and p_2 indicate the location of the pressure holes. The magnetic inductive flow meter is labeled "Q".

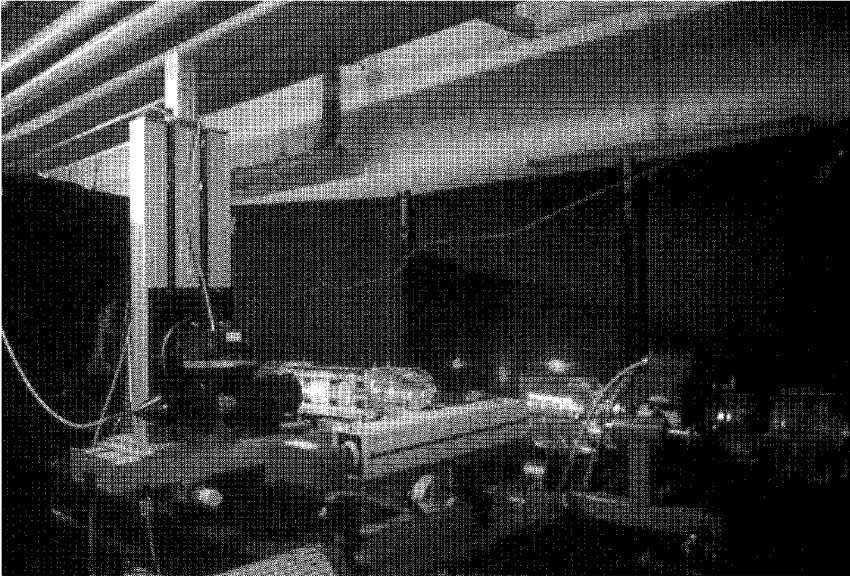


Figure 6.2: An overview of the two LDV's and the flow meter. The Argon-LDV together with the traversing mechanism is shown at the left. At the bottom-center, the white elongated 'box' represents the HeNe-laser. To the right, in the lower corner, we can see the flow meter with the sliding support. The black screens in the back are used to block laser light since for the Argon laser light, even reflected beams can be harmful.

the pressure drop and of the LDV position are given in table 6.1 relative to the position of the disturbance mechanism.

This configuration gives us four locations at which we can detect transition; the two LDV-locations and both pressure hole locations. So, what happens if the disturbance velocity v_i is raised above the critical value? Even though the disturbance will trigger transition somewhere downstream, v_i could be so close to the critical value that transition occurs downstream of the HeNe-LDV and the flow seems to remain laminar. When it is increased a little, the transition

Table 6.1: Locations of the various components in the stability measurements. The axial positions are relative to the position of the disturbance. Values are given in physical length as well as number of pipe diameters.

$z(p_1)$	$z(p_2)$	$z(\text{Ar}^+)$	$z(\text{HeNe})$
1.00 m	3.50 m	4.60 m	5.36 m
25 D	87.5 D	115 D	134 D

location could move upstream and transition may occur in between both LDV-systems or even upstream of the argon-LDV. Although the disturbance velocity can be adjusted very accurately, in most cases the transition was located either upstream or downstream of *both* LDV's and very rarely in between. This is an indication that this far downstream of the disturbance mechanism, the transition location is extremely sensitive to the value of v_i . However, in most cases it is possible to position the transition location in between the downstream pressure hole (p_2) and the argon-LDV by carefully adjusting v_i . As the distance between p_2 and the Argon-LDV is comparable to that between the two LDV's (27.5 D and 19 D respectively), we feel that for an accurate measurement of the critical disturbance velocity, the position of transition detection should be located at least 100 D downstream of the disturbance mechanism. Based on this result, we used the disturbance frequency at which the LDV's detected transition for the determination of the critical disturbance velocity rather than the first observation of an increase in pressure drop. However, it is found that the latter is only slightly larger than the value given by the LDV and can still be considered as a reasonable estimate for the critical value. Increasing the disturbance velocity further by only a few percent will move the transition location close to the upstream pressure hole, so that both the LDV's and the pressure detect turbulent flow.

Thus, given the observed sensitivity of the transition location on the disturbance velocity, particularly for distances more than 100 D downstream of the disturbance mechanism, the critical disturbance velocity v_i will be at most overestimated by less than one percent.

6.2.4 Measurement procedure

Next we consider the procedure that we followed to located the transition at various Reynolds numbers and disturbance frequencies. Since the procedure is directly related to the nature of the disturbance mechanism, discussed in detail in chapter 5, let us briefly recall its main features.

The disturbance is generated by two syringes which are mounted in opposite direction and which are oscillated by an eccentric mechanism of which the amplitude and the frequency are continuously variable between 0–20 mm and 0–40 Hz respectively. The flow from the syringes are distributed over two slits opposite of each other in the pipe wall. As we do not know the precise azimuthal distribution of the velocity in these slits, we defined the disturbance velocity as the average injection velocity over a slit surface at the moment where the velocity of the syringes reaches its maximum. In section 5.13.2, the following equation was derived giving the relationship between the disturbance velocity v_i in m/s, the frequency f in Hz, and the

displacement volume ΔV in mm^3 :

$$v_i = 0.0001909 \cdot \Delta V \cdot f \quad (6.1)$$

The ΔV is given by $\frac{\pi}{4}D_s^2A$, where D_s is the diameter of the syringe and A the amplitude of the oscillation. We have used syringes with two diameters to obtain a reasonable continuous range of ΔV values. These are given in table 6.2.

Table 6.2: Combinations of D_s and A that are used in the stability measurements and the corresponding displacement volume ΔV .

D_s (mm)	A (mm)	ΔV (mm^3)
4.7	1.00	17
4.7	2.00	35
4.7	4.99	87
4.7	10.01	174
12.0	3.01	339
12.0	4.99	565
12.0	10.01	1131

The procedure of the stability experiment which we follow is given by:

1. Mount one of the two sets of syringes.
2. Adjust A to one of the values of table 6.2.
3. change the Reynolds number to one of the values in the measuring range by adjusting the flow rate.
4. Roughly locate the transition frequency by increasing the frequency from close to zero up to a maximum in several large steps. This maximum is limited by the beginning of cavitation or mechanical stability of the disturbance mechanism. Meanwhile, check the flow regime using the pressure drop measurement and the LDV's. Once we roughly located the frequency at which transition occurred, we concentrated the measurements around this frequency to accurately localize the critical transition frequency. In these measurements we have taken into account that the flow needs some time to adjust itself to the new disturbance. This time is of the order of the time needed for the disturbance to move to the LDV location.
5. Repeat 3. and 4. for all Re to be studied.
6. Repeat 2. to 5. for all values of A that are used in combination with this set of syringes.
7. Change the syringes and repeat 2. to 6. .

This procedure gives information of the stability of the flow over a wide range of Re , f , and v_i . However, much care is involved in step 4. The main reason is the occurrence of the possible existence of multiple transition points which will be discussed in section 6.3.2. When the steps in frequency are too large³, one of the transition points may be missed. A good indication of multiple transition points is a sudden change in the transition frequency when the Reynolds number is increased. However, this is no guarantee and even now after our own careful experiment, it may be that some multiple transition points have not been discovered.

6.2.5 Dimensionless quantities

Now that we have defined criteria to detect transition, which allow accurate measurement of the critical disturbance velocity, let us consider the presentation of the stability measurements. The raw data gives us combinations of v_i and f for various Reynolds numbers which will just trigger transition, i.e. below these values the flow remains laminar. However, these critical values are meaningful only in our facility with our disturbance mechanism. In order to be able to compare our measurements with other experiments and theories, we need to recast these observations into appropriate dimensionless quantities. In stability theory, the disturbance magnitude is commonly expressed as a ratio of the amplitude of the disturbance velocity and the velocity scale used in the definition of the Reynolds number. Following this convention we define the quantity

$$v_i^* = v_i/\overline{W} \quad (6.2)$$

with $\overline{W}=4Q/\pi D^2$ the bulk velocity. The transformation of frequency into a dimensionless wave number as used in theory is more complicated. In linear stability theory, disturbances vary according to $\sin[\alpha(z - c_r t)]$. Here, α is made dimensionless with the length scale which is also used in the definition of Reynolds number, and the wave speed c_r is made dimensionless with the velocity scale. For pipe flow the scaling parameters are D and \overline{W} . At fixed axial z -position the disturbance then varies in time according to:

$$\sin(\alpha c_r t) = \sin(2\pi f t) \quad (6.3)$$

The wave speed c_r is unknown in our experiments. However, as c_r is commonly of the order of \overline{W} , we take $c_r=\overline{W}$ when we nondimensionalize the experimental results. Thus, the nondimensional wave number becomes:

$$\alpha^* = 2\pi f D/\overline{W} \quad (6.4)$$

In our stability measurements we want to study the disturbance velocities that just trigger transition. These so-called critical disturbances will be indicated by the index 'c', thus in nondimensional form: $v_{i,c}^*$. If we plot $v_{i,c}^*$ as a function of α^* at several Re , we will find that all data points for a constant ΔV lie on an imaginary line crossing the origin. This is caused by the fact that both the disturbance velocity v_i as well as the frequency f are nondimensionalized

³The magnitude of the step in frequency which is required to detect multiple transition points largely depends on the characteristics of the multiple transition area. Since this varies widely, as we will see later, no standard value for the magnitude of the steps in the frequency variation can be given.

using \overline{W} . Therefore, the linear relationship between v_i and f at constant ΔV (equation 6.1) transforms to a linear relationship between v_i^* and α^* .

Now that we have discussed all the tools we need for the stability measurements, we present the results. Those in the slug- Re -range will be discussed in the next section. As these are the basis for the measurements in the puff- Re -range, the latter will be presented in the section thereafter.

6.3 Slug- Re -range

6.3.1 Introduction

In this section, the stability measurements for $Re \geq 3000$ are presented. As this is the range of Reynolds numbers where only turbulent slugs exist, we call this the slug- Re -range. The tools that we will use for the detection of transition have been discussed in section 6.2. However, some of the implications for practical use will be commented in this section.

In section 6.3.2, the results of the stability measurements will be discussed. Most of the transitions are characterized by a single transition to turbulence. However, for certain combinations of the disturbance parameters v_i^* , f , and Reynolds numbers, multiple transition points have been found. To cast our results in a more general form, we will present them in nondimensionalized stability diagrams.

As some theories predict certain scaling rules for the dependence of the critical relative disturbance velocity $v_{i,c}^*$ on Re , we have extracted such information from the nondimensionalized stability diagrams and the results will be shown in section 6.3.3.

For high Reynolds numbers, we sometimes measure pressure drops below that for laminar flow when the transition is located around the downstream pressure hole. For very high Re these pressure drops may even become negative. A simple model for the transition process is presented in section 6.3.4 that could give a possible explanation for such sub-laminar and negative pressure drops.

6.3.2 Single and multiple transitions

In this section we present the stability results from a Newtonian pipe flow in the range $Re \geq 3000$, up to $Re = 50\,000$. The procedure for the determination of the critical values of the disturbance mechanism is described previously in section 6.2.4.

We found that the transition depends sensitively and also reproducibly on frequency. Although one may suspect that the transition from laminar to turbulent flow is determined primarily by the disturbance frequency, it turns out that the frequency is not the parameter on which the transition depends most, which we show later. One should note that our disturbance mechanism generates an oscillation with a fixed displacement volume. Thus, by increasing the disturbance frequency, the disturbance *velocity* is also increased as shown by equation 6.1. Therefore, in the figures where we show pressure drop as a function of frequency, the dependence on frequency should be interpreted in terms of disturbance velocity, where one can use equation 6.1 to transform the value of f into v_i . We have nevertheless chosen to present these figures as a function of f , because that is how we have performed the experiment, i.e. changing f at fixed ΔV and Re .

In figure 6.3 we show the result of a single measurement at $Re = 35\,000$ and $\Delta V = 35\text{ mm}^3$. We plot in this figure the measured pressure drop, over the 2.5 m section 1 m downstream of

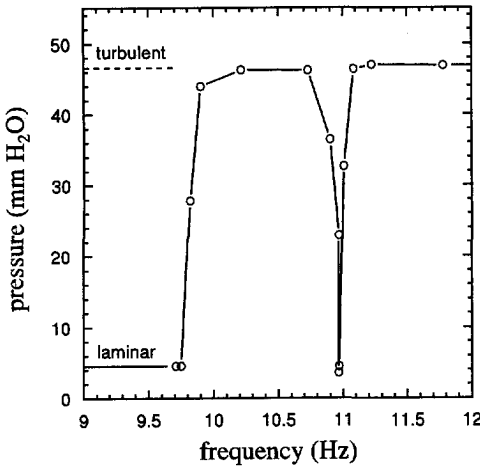


Figure 6.3: Measurement at $Re=35\,000$, Displacement volume $\Delta V=35\text{ mm}^3$. Dotted line indicates full turbulent pressure drop.

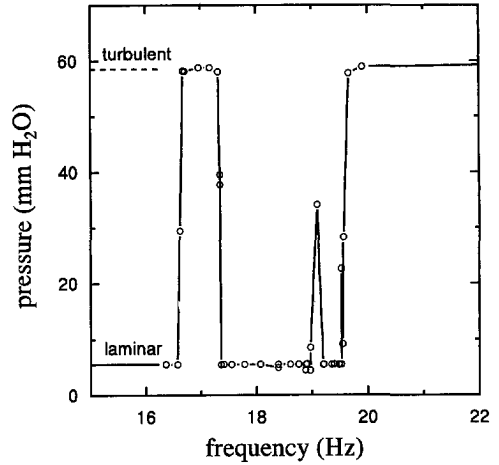


Figure 6.4: Measurement at $Re=40\,000$, Displacement volume $\Delta V=17\text{ mm}^3$. Dotted line indicates full turbulent pressure drop.

the injection location, as a function of the frequency. This measurement is a typical result except for the dip around 11 Hz. This result is typical because, as in most measurements, the pressure drop is equal to the laminar value until a critical frequency, i.e. critical disturbance *velocity*, is reached. Increasing the frequency further gives a transition which lies in between the two pressure holes. As a result, the measured pressure drop lies in between the laminar and turbulent one. Eventually, the disturbance frequency/velocity is so large that transition to turbulence occurs within 1m of the injection location resulting in a fully turbulent pressure drop. Figure 6.3 is peculiar in the sense that increasing the frequency results in relaminarization of the flow at $f \approx 11$ Hz.

However, such measurements as presented in figure 6.3 are certainly not unique. In figure 6.4 we present the data obtained at a Reynolds number of $Re=40\,000$ where three turbulent regions can be discerned, one of which does not seem to reach the full turbulent pressure drop.

The data taken at several displacement volumes, frequencies, and Reynolds numbers, have been reanalyzed in terms of the disturbance velocity as function of the Reynolds number. In figures 6.5a - 6.5f we have plotted the critical disturbance velocity as a function of Re for a fixed displacement volume. It is clear from figures 6.5a and b, that apart from the "standard" laminar-turbulent transition, also within the turbulent region several patches of laminar flow seem to exist. The extremely narrow laminar region around 11 Hz found in figure 6.3 represents the 'nose' of the triangular shaped laminar region in figure 6.5b, indicated by "C". Although figures 6.5a and 6.5b appear to be similar at first sight, the behavior at the smallest displacement volume, $\Delta V=17\text{ mm}^3$, shows a much more complicated transition behavior. For instance for Reynolds numbers around 30 000 and 40 000 a small relaminarization and transition region seem to exist indicated by "A" and "B" respectively. A much larger laminar area is formed for $Re > 32\,500$.

At a higher displacement volume, i.e. $\Delta V=87\text{ mm}^3$ which is shown in figure 6.5c, the stability

diagram shows another behavior, quite different from the results found in figure 6.5a and b at smaller ΔV values. At Reynolds numbers just over $Re=45\,720$ the critical disturbance velocity decreases drastically. This behavior has been checked by additional measurements. For these measurements the frequency and consequently the disturbance velocity is kept constant, and the flow rate, i.e. Reynolds number, is increased. The flow characteristics during these additional experiments are indicated in figure 6.5c by 'L' (laminar) and 'T' (turbulent). The results are in excellent agreement with the transition points found in the experiments at constant Re values in which the the disturbance frequency (disturbance velocity) is increased. This fact, namely that the same result can be reproduced by two measuring procedures, gives us confidence that our observations are not in some way an artefact of the measurement procedure.

For displacement volumes $\Delta V=173\text{ mm}^3$ and beyond, shown in figures 6.5d-f, no multiple transition points nor drastic changes in critical transition disturbance velocity have been found. For the three largest displacement volumes, shown in figure 6.5e-f, the transition lines practically coincide. In other words, for these large ΔV the dependence on frequency is negligible and only the disturbance magnitude itself matters.

In figures 6.5a-f, an increase in disturbance velocity is linked to an increase in frequency due to the nature of the disturbance mechanism. The effect of solely a change in frequency remains thus unrevealed. Hence, the data should be replotted to show this dependency. Therefore, we have plotted the dimensionless disturbance velocity v_i^* against wave number α^* as defined by equation 6.4 in section 6.2.5 for constant Re . The results are shown in figure 6.6 where figure 6.6b is an enlargement of the left-hand lower corner region of figure 6.6a. The first result which follows is that the critical relative disturbance velocity $v_{i,c}^*$ decreases with increasing Reynolds number. This can be interpreted as the somewhat obvious result that at higher Reynolds numbers the flow is less stable⁴. Note that the measurement points in figure 6.6 are all located on seven straight lines (not shown) radially originating from the origin and representing the seven displacement volumes used in this stability experiment. The linear dependence of the disturbance velocity on the disturbance frequency from equation 6.1 is reflected in this nondimensionalized representation since the bulk velocity is used in the denominator of both plotted variables.

Above a dimensionless wave number $\alpha^*=5$ the critical relative disturbance velocity $v_{i,c}^*$ is only weakly dependent on α^* . For very small α^* , $v_{i,c}^*$ seems to be also constant but with a smaller value than for large α^* . At intermediate values of α^* , $v_{i,c}^*$ depends both on α^* and Re . For low Re , the critical relative disturbance velocity increases rapidly when α^* exceeds approximately 1, to level out at a constant value which is only a function of Re . For $Re=20\,000$ and higher, the the values for $v_{i,c}^*$ at large α^* lie below those at small α^* . In addition, at these large Reynolds number, the flow seems to become extremely sensitive to disturbances with $\alpha^*\approx 1^5$, particularly at Reynolds numbers $Re\geq 40\,000$. The measurements with $\Delta V=87\text{ mm}^3$ are located precisely in this range. This explains the drastic fall in critical disturbance velocity found in figure 6.5c around $Re=45\,720$, which in effect shows the changeover at high Reynolds

⁴Usually, $v_{i,c}^*$ decreases with Re , but the *absolute* critical disturbance velocity $v_{i,c}$ may show different behavior and we found that $v_{i,c}$ increases with Re as shown in figure 6.5. Darbyshire & Mullin (1995) find a decrease of $v_{i,c}$ with Re . However, they used a single jet disturbance and in another experiment not discussed here, which employs such a single jet disturbance, we also found a decrease with Re (Draad *et al.* 1995).

⁵Although the measurements are not conclusive, and the large sensitivity to α^* is found in the range of approximately $0.6\leq\alpha^*\leq 1.4$, we will use $\alpha^*\approx 1$ to indicate this large sensitivity to α^* .

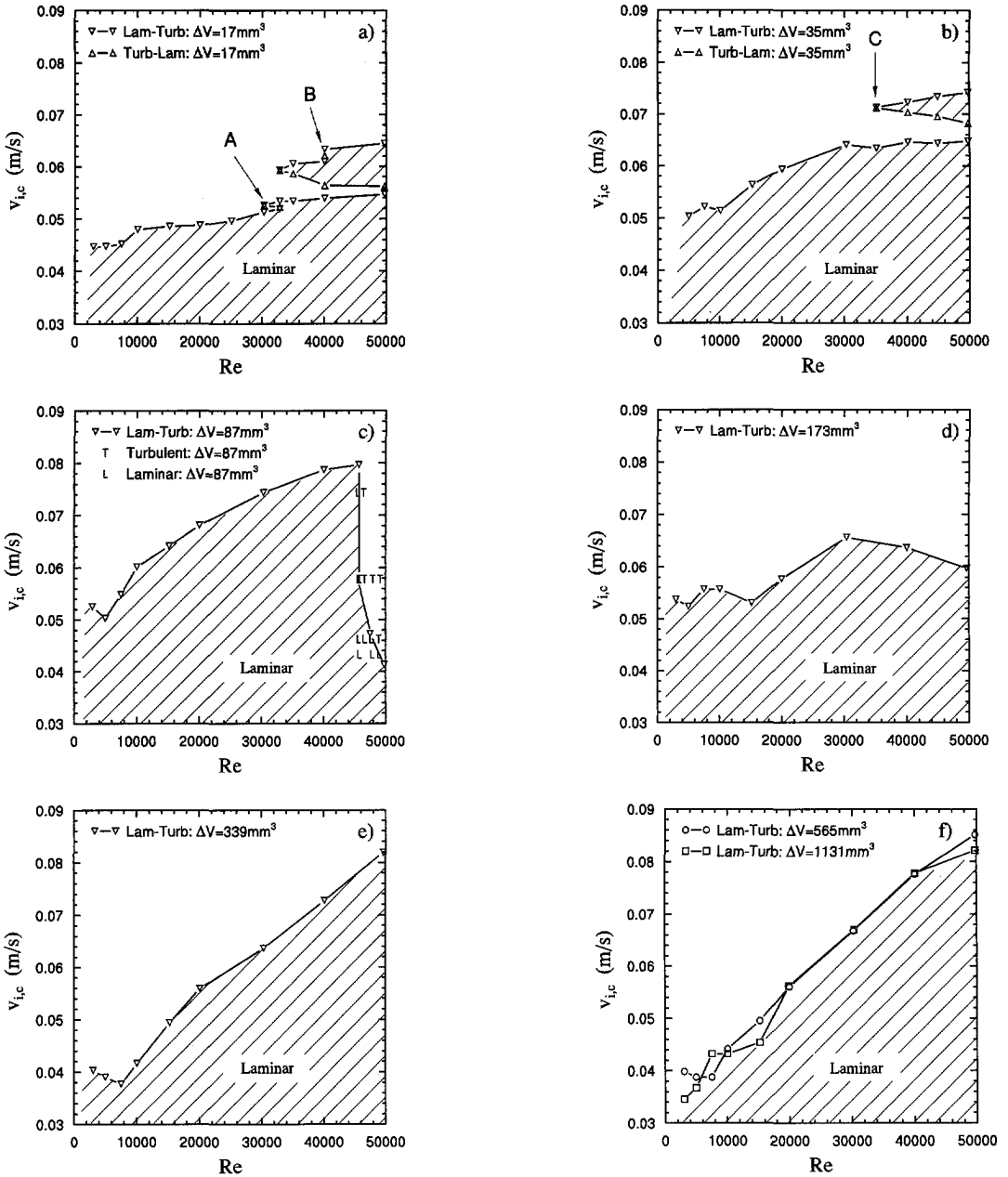


Figure 6.5: Critical disturbance velocity vs. Re for various displacement volumes.

number from the small $v_{i,c}^*$ around $\alpha^*=0.6$ to the multiple transition points for $\alpha^*>2$. More measurements around this area are needed to describe the changeover more accurately. In analogy to the measurements denoted by 'L' and 'T' in figure 6.5c, variation of $v_{i,c}$ as a function of Re rather than the frequency f may be necessary here as the sensitivity to the frequency is too large.

The multiple transition points found in figure 6.6b are located in the range $2 \leq \alpha^* \leq 6$ and are characterized by three transition lines; two laminar-turbulent transition lines depicted with open markers and one turbulent-laminar transition (relaminarization) line depicted with solid markers. The solid marker for $Re=30\,000$ coincides with the second laminar-turbulent transition and is the representation of the small multiple transition area denoted "A" in figure 6.5a. The relaminarization line and the upper laminar-turbulent transition line seem to approach each other when α^* is decreased thus bounding the extension of the multiple transition area. Similar trends can be discerned for the relaminarization line and the lower laminar-turbulent transition line with increasing α^* . More measurements are needed using intermediate values for ΔV to resolve the behavior in this α^* -range at high Re ⁶.

With respect to this high sensitivity of the flow for $Re \geq 40\,000$ and $\alpha^* \approx 1$, it is interesting to look again at the pressure drop as a function of frequency. In figure 6.7 we have plotted these variables at various values of Re for the case $\Delta V=87\text{ mm}^3$. Up to $Re=45\,720$ all curves exhibit a single sharp rise in pressure drop at a given value of f and beyond this value, the pressure drop changes from the constant laminar value at the left to the turbulent value at the right of figure 6.7. For $Re=47\,540$, we first notice a decrease of the pressure drop below the laminar value (the same behavior is also apparent for $Re=49\,800$). We will defer a discussion of this perhaps surprising effect to section 6.3.4. After this initial behavior, the pressure drop starts to rise above the laminar value at low frequencies, but does not reach the full turbulent pressure drop. Only at the transition frequency found for $Re=45\,720$, does a sharp rise in pressure drop occur to the full turbulent flow value. This behavior might suggest that for $Re=47\,540$ at approximately 3 Hz ($\alpha^*=0.7$) a second disturbance mode is excited which at this Reynolds number has a much smaller growth rate than the mode which triggers turbulence at $f=5$ Hz ($\alpha^*=1.2$) for $Re \leq 45\,720$. This latter then takes over again at $f=5$ Hz. At even larger Reynolds numbers, e.g. $Re=49\,800$, the growth rate of the second mode seems to be much larger and the measured pressure drop rises again quickly with increasing frequency to the full turbulent pressure drop. The extra sensitivity of the flow to disturbances with $\alpha^* \approx 1$ at $Re \geq 40\,000$ may thus be related to a competition between different instability modes. This fact and also, the existence of multiple transition points for $Re \geq 30\,000$ and $\alpha^* \geq 2$ shows that the transition to

⁶Multiple transition points have also been found by Boere (1995), who performed his experiments in the same experimental setup. At that time the natural transition Reynolds number was $Re \approx 30\,000$. After Boere finished his experiments, this natural transition Reynolds number was increased to more than 60 000 after some changes in the small settling chamber (see also chapter 5).

Boere found multiple transition points for $15\,000 \lesssim Re \lesssim 17\,000$ and $\alpha^* \approx 1.5$ using a displacement volume $\Delta V=87\text{ mm}^3$. Boere also found the high sensitivity of the flow to disturbances around $\alpha^* \approx 1$. This could suggest that the phenomena found by Boere and ourselves are related. Perhaps the change in transition behavior with an increase in α^* is linked to an interaction of small disturbances which are naturally present in the laminar flow and the artificial disturbances we added to the flow. Due to severe time constraints, no research in this direction could be done nor could the transition process be studied in detail using e.g. LDV or Particle Image Velocimetry (PIV) techniques. For a comparison of the measurements by Boere with our stability results, the reader is referred to appendix D.

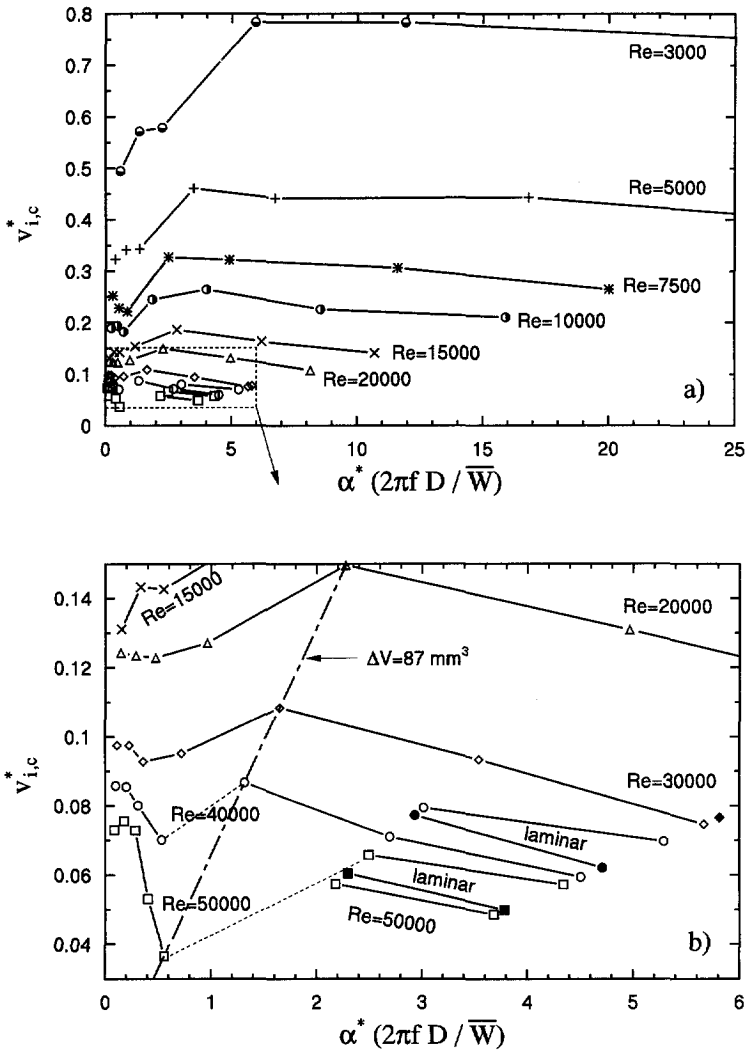


Figure 6.6: Critical relative disturbance velocity $v_{i,c}^*$ as a function of dimensionless wave number α^* for constant Reynolds number. Figure b) is an enlargement of figure a) indicated by dotted region. The solid markers indicate points where the flow relaminarizes if the disturbance velocity is increased at constant α^* . If above a solid marker no open marker is present, then the two practically coincide. The indication 'laminar' marks the multiple transition region in between the relaminarization and the second transition line. The lines for $Re \geq 40\,000$ for small α^* are not connected to those at large α^* due to the sensitivity of the flow around $\alpha^* \approx 1$.

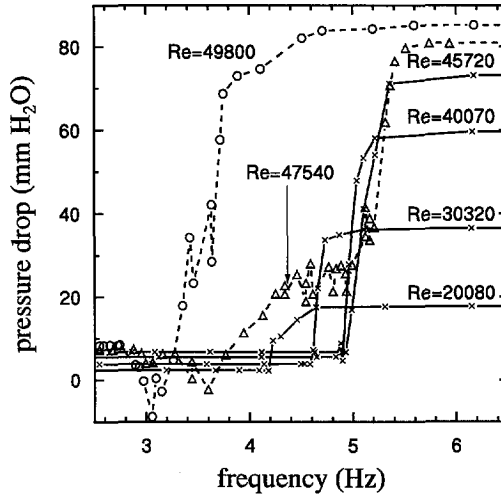


Figure 6.7: Pressure drop vs. frequency for various Reynolds numbers with $\Delta V = 87 \text{ mm}^3$.

turbulence in pipe flow is very complicated. Further research on this subject is needed to disclose the mechanics behind this behavior.

Because the transition behavior can apparently be quite complicated, it is worth while to plot the stability measurements in a different fashion; $v_{i,c}^*$ as a function of Re for various α^* which is carried out in the next section.

6.3.3 Scaling rules

The way in which the stability measurements were plotted in the previous section, i.e. $v_{i,c}^*$ vs. α^* at several Re , is well suited to show the high sensitivity of the flow to disturbances with $\alpha^* \approx 1$ and the location of the multiple transition points. Due to the linear relationship between $v_{i,c}^*$ and f at constant ΔV , the dependence of $v_{i,c}^*$ on the Reynolds number at constant values of α^* is not available directly from our experiments (for details see section 6.2.4). However, such information is very interesting as it would allow for a comparison with stability theories. For instance, some nonlinear theories, e.g. Davey & Nguyen (1971), Smith & Bodonyi (1982), and Sen *et al.* (1985) predict that $v_{i,c}^*$ at constant α^* scales with Re according to a certain power.

To extract this information from our stability measurements, we have to use the following procedure. For constant values of α^* in figure 6.6, we used a linear interpolation procedure to find the corresponding value for $v_{i,c}^*$ at a specific value for Re . As for most Re values, the change of $v_{i,c}^*$ with α^* is smooth, linear interpolation will not introduce significant errors. For $\alpha^* = 2$ and $\alpha^* = 5$, extrapolation was needed for $Re \geq 40\,000$ and these points should thus be considered with care. Since we have found that the flow for $Re \geq 40\,000$ is very sensitive around $\alpha^* \approx 1$, no interpolation is allowed in this region. The results are collected in figure 6.8.

A change in behavior can be observed for low ($\alpha^* \leq 2$) versus high wave numbers ($\alpha^* \geq 5$). For large α^* , i.e. 5 and 10, $v_{i,c}^*$ is practically independent of α^* and seems to vary according to Re^{-1} . This implies that the absolute critical disturbance velocity $v_{i,c}$ is independent of both α^* and \bar{W} . In other words, the Reynolds number $v_{i,c}^* D / \nu$ constant and approximately 3 000.

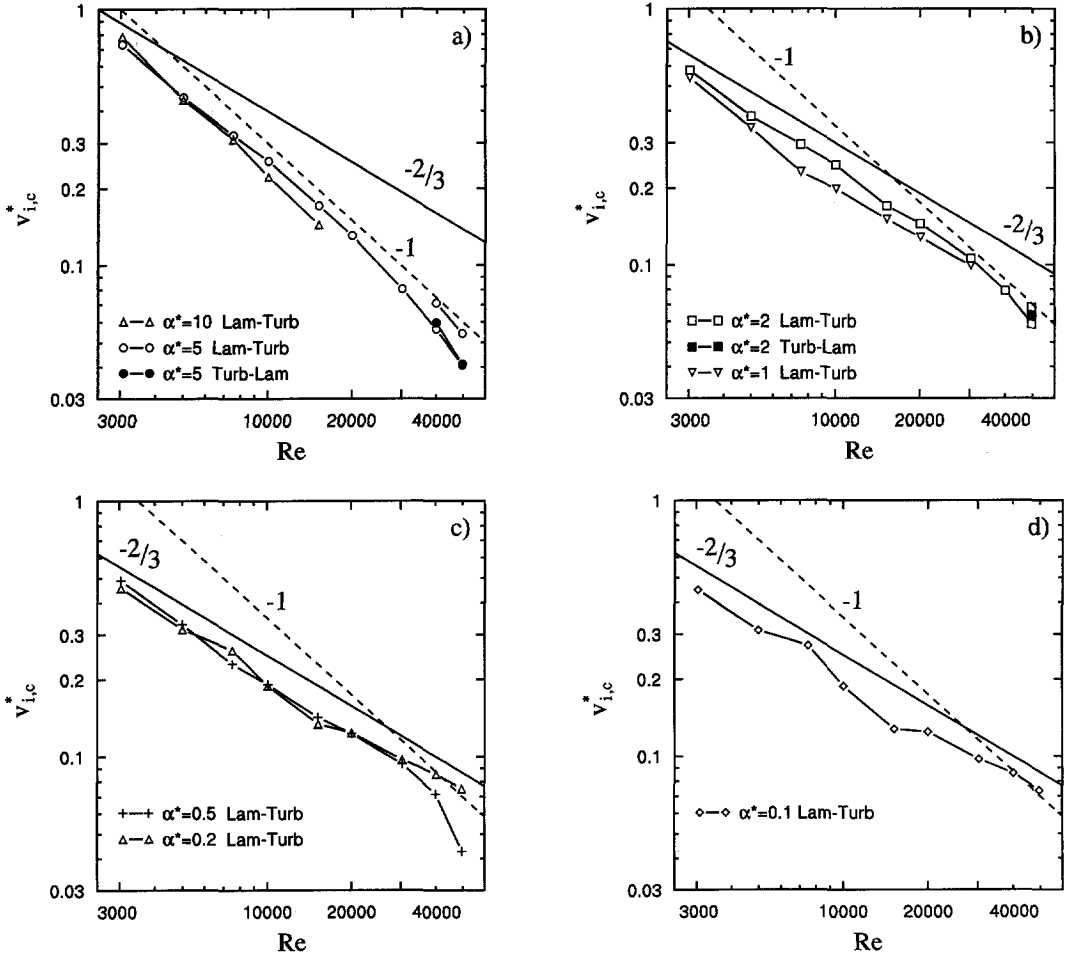


Figure 6.8: Critical relative disturbance velocity vs. Reynolds number for constant dimensionless wave numbers $\alpha^* = 10, 5, 2, 1, 0.5, 0.2,$ and 0.1 . Note that the lines with slopes -1 and $-2/3$ have different origins in all four figures.

For the very small wave numbers $\alpha^* \leq 0.5$, $v_{i,c}^*$ is again practically independent of α^* but now seems to vary according to $Re^{-2/3}$. This power is in agreement with the scaling rules found by (Davey & Nguyen 1971) for axisymmetric disturbances and Sen *et al.* (1985). In an appendix to paper of Davey & Nguyen, Gill shows that a $Re^{-2/3}$ scaling rule is obtained when in the center of the pipe the viscosity and the curvature of the velocity profile are used to construct a disturbance velocity scale. Davey & Nguyen also give a scaling rule for the length scale of the disturbance. Unfortunately, no such information is available from our experiments.

The scaling of the critical relative disturbance velocity is nowhere near $Re^{-1/3}$ as proposed by (Smith & Bodonyi 1982). This may be due to inapplicability of their theory or to the simple fact that the disturbance added to the flow is not representative for the disturbance proposed by Smith & Bodonyi. Their disturbance is sinusoidal in tangential direction. Although the exact circumferential shape of our disturbance is not known, it probably has no sinusoidal dependence. For this, more injection points in circumferential direction are needed.

Nevertheless, it is interesting to find that for small α^* the scaling of the critical disturbance velocity may have a link with theory and that for large α^* , the critical disturbance velocity is almost constant. This, together with the multiple transition points is more than sufficient reason to warrant further study.

6.3.4 Negative pressure drops

When discussing figure 6.7, we promised to comment on the occurrence of pressure drops found at high Re which are smaller than the laminar value or even negative, i.e. the downstream pressure is higher than the upstream pressure. It is striking that these negative pressure drops are measured for $Re=47\,540$ and $Re=49\,800$ only, and that sub-laminar pressure drops or even negative ones are almost nonexistent for lower Reynolds numbers. This suggests that these negative pressure drops are probably related to the second mode which becomes active near $f=3$ Hz instead of the first mode which grows for $f \approx 5$ Hz⁷. These sub-laminar pressure drops occur in the neighborhood of the transition frequency when the transition is located near the downstream pressure hole. In order for these low pressure drops to occur, the pressure at the downstream pressure hole has to increase with respect to its laminar value because at the upstream pressure hole the flow remains laminar and the pressure thus constant.

This phenomenon of sub-laminar pressure drops might be explained by the wall normal velocity resulting from the fluid redistribution from the pipe center towards the wall during a transition from laminar to turbulent flow is illustrated in figure 6.9. With a simple model, we can estimate the magnitude of the radial velocity needed to account for the increase in pressure at the downstream pressure hole.

Although the laminar flow in our pipe is not parabolic (see appendix C), we nevertheless use a parabolic profile to illustrate our point. The velocity is thus given by:

$$W_z = 2\bar{W} \left[1 - \left(\frac{r}{R} \right)^2 \right] \quad (6.5)$$

⁷Further evidence for this hypothesis is given by figures 5.10 and 5.11 in Boere (1995), where the measured pressure drop is plotted as a function of frequency at various Reynolds numbers for $\Delta V=87$ mm³. The measurements where multiple transition points are found (figure 5.10) all show sub-laminar pressure drops whereas those in the absence of multiple transition points (figure 5.11) show no sub-laminar pressure drops.

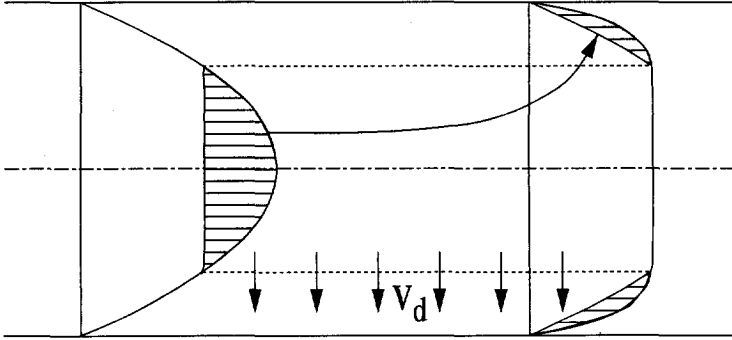


Figure 6.9: Schematic representation of velocity redistribution from center to wall in the transition phase resulting in a normal to wall velocity v_d .

For the turbulent velocity profile we use a power law model with power $n = 7$, (Hinze 1975, p. 273) which implies:

$$W_z = W_{cl,T} \left(1 - \frac{r}{R}\right)^{(1/n)} \quad (6.6)$$

Integration over the cross section gives the flow rate Q :

$$Q = \int_0^R W_z 2\pi r dr = \pi R^2 W_{cl,T} \frac{2n^2}{(n+1)(2n+1)} \quad (6.7)$$

With the flow rate Q equal to $\pi R^2 \bar{W}$, we find for the centerline velocity of the turbulent flow with $n = 7$:

$$W_{cl,T} = 1.22 \bar{W} \quad (6.8)$$

Equating 6.5 and 6.6 also gives the radius at which the velocity does not change when the flow changes from laminar to turbulent. This is:

$$r_e = 0.695R \quad W_e = 1.03 \bar{W} \quad (6.9)$$

The flow rate inside the cylinder with radius r_e is $0.733\pi R^2 \bar{W}$ and $0.538\pi R^2 \bar{W}$ for the laminar and turbulent profile respectively. The difference is to be redistributed during the transition process. Assume that this redistribution takes place through a cylindrical surface characterized by radius r_e and length L_{tr} , then the following must hold for the redistribution velocity v_d :

$$v_d = \frac{(0.733 - 0.538)\pi R^2 \bar{W}}{2\pi r_e L_{tr}} \quad (6.10)$$

The increase in pressure at the downstream pressure hole is now assumed to be the result of the additional stagnation point pressure resulting from v_d . From figure 6.7 we can see that the additional stagnation point pressure for $Re=49\,800$ can reach values as high as twice

the laminar pressure drop over the 2.5m section. Although the flow is instationary, we use Bernoulli's theorem in analogy to its application for a pitot tube to calculate the stagnation point pressure and equating this to twice the laminar pressure drop we can obtain an estimate for the transition length $L_{tr} = \xi R$:

$$\Delta p_d = \frac{1}{2} \rho v_d^2 = \frac{1}{2} \rho \left[\frac{(0.733 - 0.538) \pi R^2 \bar{W}}{2 \pi r_e \xi R} \right]^2 = 2 \frac{1}{2} \rho \bar{W}^2 \frac{L}{D} \frac{64}{Re} \quad (6.11)$$

With equation 6.9, $L=2.5$ m, $D=0.040$ m and $Re=49\,800$ we obtain $\xi = 0.349$ and with equation 6.10:

$$v_d = 0.4 \bar{W} \quad L_{tr} = 0.35 R \quad (6.12)$$

A transition length of $0.35R$ may seem very short and a radial velocity of 40% of the bulk velocity is large but transition to turbulence at these high Reynolds numbers is a violent and fast process which can also be seen from visualizations with dye. The pressure drop reduction measured by Boere (1995) at $Re=25\,000$ is 1/3 of the laminar pressure drop. Using the previous analysis, this leads to a transition length of $L_{tr}=0.61R$ and $v_d=0.231\bar{W}$. This implies an increase in transition length for lower Reynolds numbers, which is to be expected as disturbance-growth rates will become smaller when Re is decreased.

Radial velocities this large can indeed be found in transition flow as shown in figure 6.10 where we plot time-traces of the axial and radial velocities of naturally occurring turbulent slugs at $Re=27\,000$. At the leading edge of a slug the radial velocity is found to be as large as 0.14m/s with a bulk velocity of $\bar{W}=0.65$ m/s. Thus radial velocities can be as high as 22% of the bulk velocity at the leading edge for this Re and this agrees well with the estimate from our simple model. However, the two conditions are not completely comparable. Figure 6.10 shows developed slugs whereas the turbulent slugs in the pressure drop measurements are being generated at that location. Also, no multiple transition points (which seem to be related to the sub-laminar pressure drops) were found for the flow in figure 6.10 when the Reynolds number was lowered and transition was triggered with $\Delta V=87$ mm³. Furthermore, the velocity measurements are taken at the pipe axis and not at $r=0.695R$.

The model that has been presented in this section is rather crude and the actual transition process is certainly much more complicated. Nevertheless, the redistribution of velocity has to occur during transition and it is interesting whether or not the estimate given for the length in which such redistribution takes place can be confirmed by e.g. DPIV measurements of transition.

All stability results that have been discussed so far, are performed in the slug-*Re*-range. Some stability measurements in the puff-*Re*-range are presented in the next section and suggest a link with transition in the slug-*Re*-range.

6.4 Puff-*Re*-range

6.4.1 Introduction

In this section, we study the flow stability for Reynolds numbers in the puff-*Re*-range, i.e. $Re \leq 2\,700$. As we have discussed already in section 2.3.5, the transitional flow structure is different from a turbulent slug. For all details we refer to this subsection, however, let us here recollect the main differences between slugs and puffs. The interior of a slug resembles turbulent

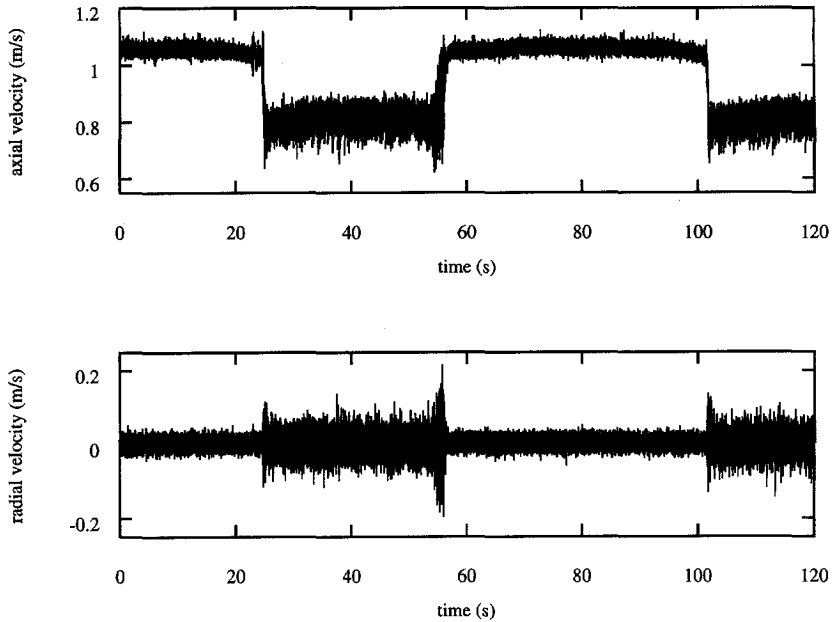


Figure 6.10: Time-traces of axial and radial velocity for naturally occurring slugs at $Re=27000$ measured at the pipe axis. $\bar{W}=0.65$ m/s.

pipe flow and the centerline velocity time-trace is characterized by sharp leading and trailing edges, i.e. the velocity changes quickly between the laminar and turbulent value. In contrast, for a puff the centerline velocity time-trace is more shaped like a saw-tooth. The front of a puff is characterized by a slow decrease in centerline velocity whereas the trailing interface is sharp.

The most important motive for studying the puff- Re -range is off course that this is the 'onset' of transition in pipe flow. Below $Re \approx 2200$ the puffs decay as they are convected downstream and the puffs grow for $Re \geq 2300$. So, a value for the minimum transition Reynolds number of $Re \approx 2300$ seems appropriate.

The detection of transition at these low Reynolds numbers is more difficult than in the slug- Re -range as already explained in section 6.2.2. However, given the significance of experiments in this Re -range, we studied its stability and found a link with those for the slug- Re -range⁸.

6.4.2 Velocity time-traces

As puffs are much more difficult to detect than turbulent slugs, we studied the stability at these low Reynolds numbers in a different way. We recorded 15 min time-traces of the centerline velocity at several Reynolds numbers and frequencies using two displacement volumes ($\Delta V=87 \text{ mm}^3$ and $\Delta V=173 \text{ mm}^3$). Since we want to study the 'onset' of transition we performed measurements for $Re=1800, 2000,$ and 2200 . Two time-traces were also recorded for

⁸These results have been measured by Boere (1995) as a part of his MSc-work which he performed in the context of this PhD-work and will be discussed in the next section.

$Re=2500$. In section 6.3.3 we showed that the disturbance velocity is relatively insensitive to Re over a wide range of wave numbers α^* . Extrapolating this result, we chose the frequencies for our stability measurements in the puff- Re -range such that one frequency was smaller than the critical value at $Re=3000$ i.e. (the lowest Reynolds number in the slug-range) and the other frequencies larger than this critical value. The combinations of frequency and displacement volumes that we used in the puff- Re -range are given in table 6.3 and some corresponding dimensionless quantities are shown in table 6.4.

Table 6.3: Disturbance frequencies (in Hz) in combination with the two displacement volumes used in the stability measurements for several Reynolds numbers ($Re=1800$, 2000 , and 2200).

$\Delta V=87 \text{ mm}^3$	$\Delta V=173 \text{ mm}^3$
3 Hz	1 Hz
3.5	1.5
4	2
6	4
8	10
10	20

Table 6.4: Relative disturbance velocity v^* and dimensionless wave number α^* at frequencies near the transition point of $Re=3000$ for the combinations of Re and displacement volume used in the low Reynolds number stability experiments.

Settings	v_i^*	α^*
$Re=1800$ 3.5 Hz $\Delta V=87 \text{ mm}^3$	1.36	20.7
$Re=2000$ 3.5 Hz $\Delta V=87 \text{ mm}^3$	1.22	18.6
$Re=2200$ 3.5 Hz $\Delta V=87 \text{ mm}^3$	1.11	16.9
$Re=1800$ 1.5 Hz $\Delta V=173 \text{ mm}^3$	1.17	8.9
$Re=2000$ 1.5 Hz $\Delta V=173 \text{ mm}^3$	1.05	8.0
$Re=2200$ 1.5 Hz $\Delta V=173 \text{ mm}^3$	0.96	7.3
$Re=2500$ 1.5 Hz $\Delta V=173 \text{ mm}^3$	0.84	6.4
$Re=2500$ 2.0 Hz $\Delta V=173 \text{ mm}^3$	1.12	8.5

The time-traces show that the flow was laminar for $Re=1800$ for all frequencies applied except for $\Delta V=87 \text{ mm}^3$ and $f = 3.5 \text{ Hz}$ where the time-trace exhibited one puff during the 15 minutes observation time. For $Re=2000$ and $Re=2200$ the turbulence activity is larger. Figures 6.11 – 6.14 show the complete series for both displacement volumes⁹. Several general trends are apparent:

⁹These time-traces have been measured by Boere (1995) and he presents a smaller selection of the data in his figures 5.16 and 5.17 than we show here.

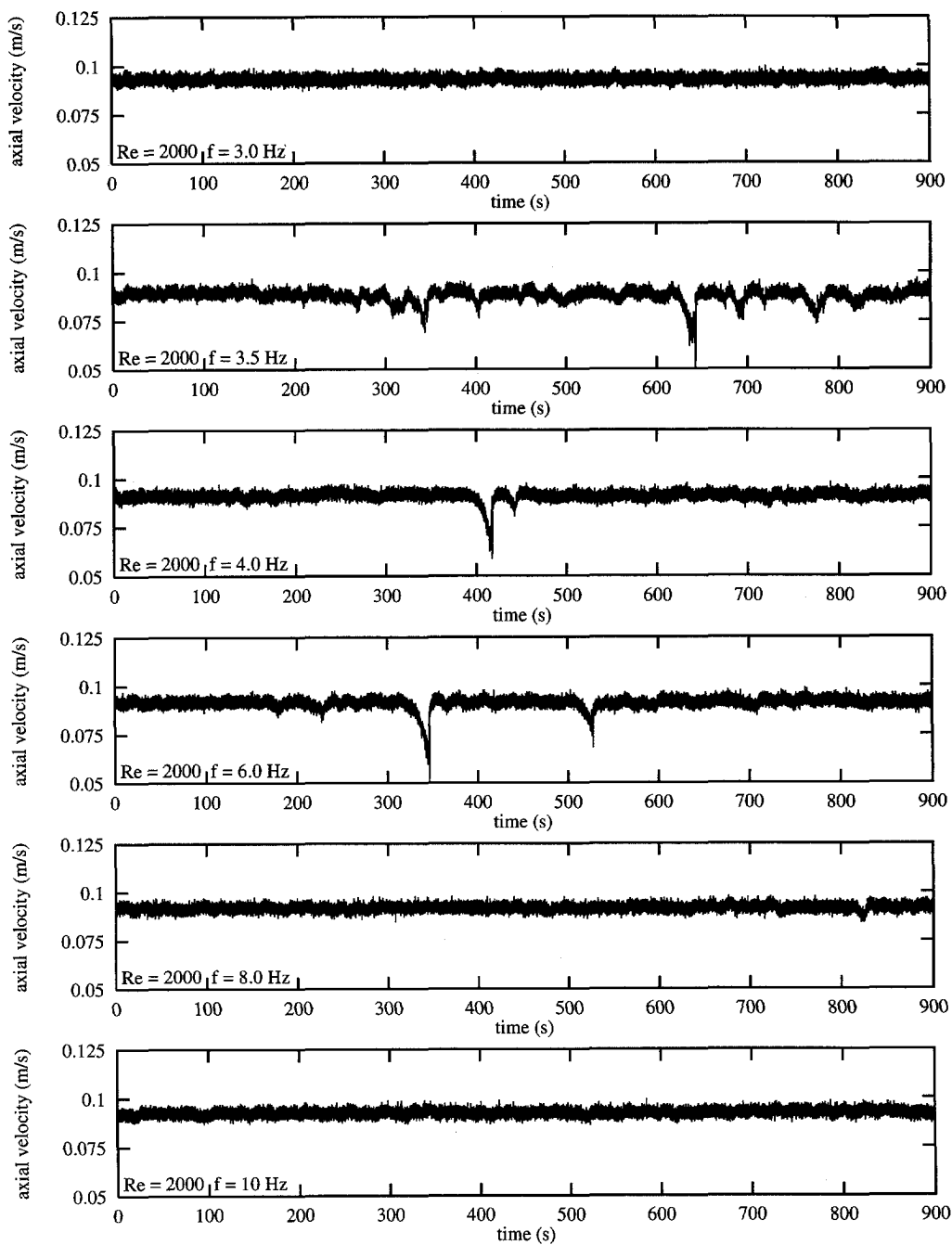
1. For the frequencies below the critical values for $Re=3000$ (i.e. measurements at 3 Hz and 1 Hz, for $\Delta V=87\text{ mm}^3$ and 173 mm^3 respectively) the flow remained laminar at all Reynolds numbers.
2. For $Re=2000$, figures 6.11 and 6.13, the flow is practically laminar at almost all frequencies. Typically not more than a few puffs can be observed in the whole time-trace. Only at frequencies close to the transition point for $Re=3000$, i.e. 3.5 Hz and 1.5 Hz for $\Delta V=87\text{ mm}^3$ and $\Delta V=173\text{ mm}^3$ respectively, can a strong increase in turbulent activity be seen, particularly for $\Delta V=173\text{ mm}^3$.
3. For $Re=2200$, the turbulent activity is much stronger compared with that at $Re=2000$. For $\Delta V=87\text{ mm}^3$, figure 6.12, again the turbulent activity is maximal at $f=3.5\text{ Hz}$. However, at larger frequencies, the turbulent activity is also large and only at $f=10\text{ Hz}$ does this activity become smaller.

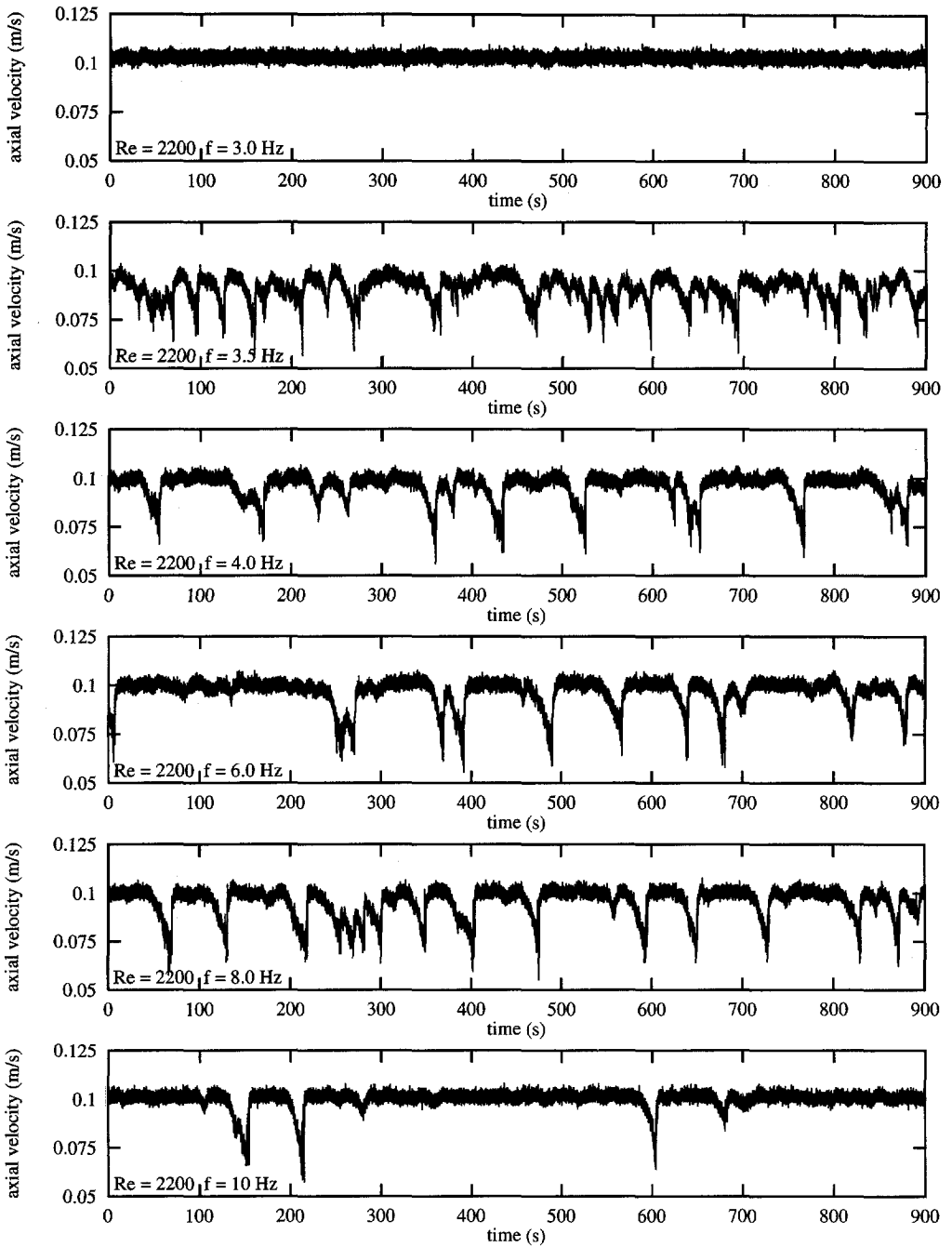
For $\Delta V=173\text{ mm}^3$, figure 6.14, only two puffs are present for $f=1.5\text{ Hz}$, i.e. the critical frequency for $Re=3000$. Apparently, the frequency to which the flow is most sensitive is slightly higher and indeed the number of puffs is much larger for $f=2.0\text{ Hz}$ and decreases for higher frequencies.

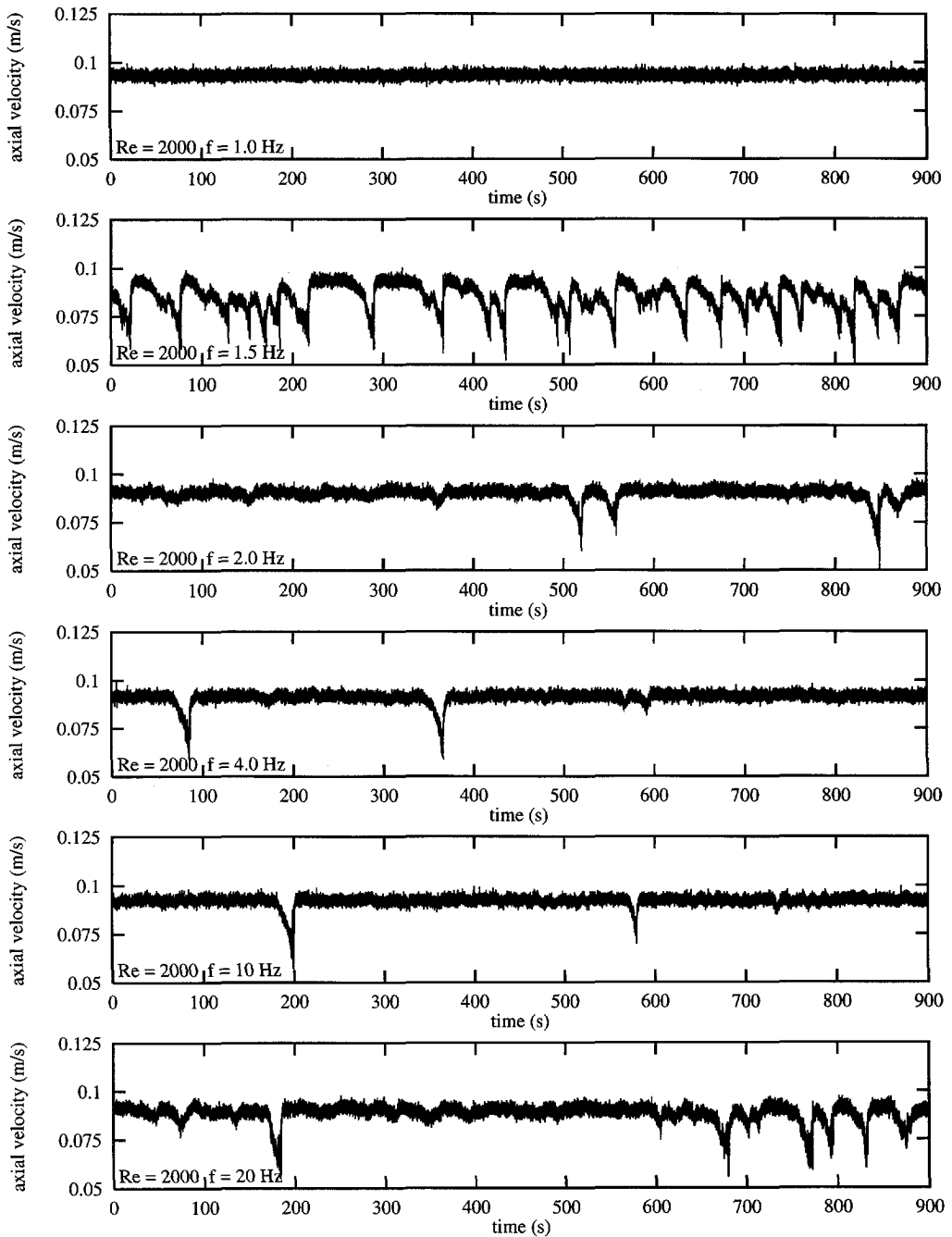
4. For $\Delta V=87\text{ mm}^3$, the number of puffs decreases from its maximum value at $f=3.5\text{ Hz}$ to smaller values when the frequency is increased to its maximum of $f=10\text{ Hz}$. When the frequency is increased to its maximum of $f=20\text{ Hz}$ for $\Delta V=173\text{ mm}^3$, this leads to an increase in the number of puffs, particularly for $Re=2200$. However, the injection velocity for $f=20\text{ Hz}$ and $\Delta V=173\text{ mm}^3$ is four times as high as for $f=10\text{ Hz}$ and $\Delta V=87\text{ mm}^3$. At $Re=2000$, $f=20\text{ Hz}$, and $\Delta V=173\text{ mm}^3$, the disturbance velocity v_i is 14 times the bulk velocity! For such very large disturbance velocities, the disturbance may need longer to decay and thus may appear in the LDV-signal.

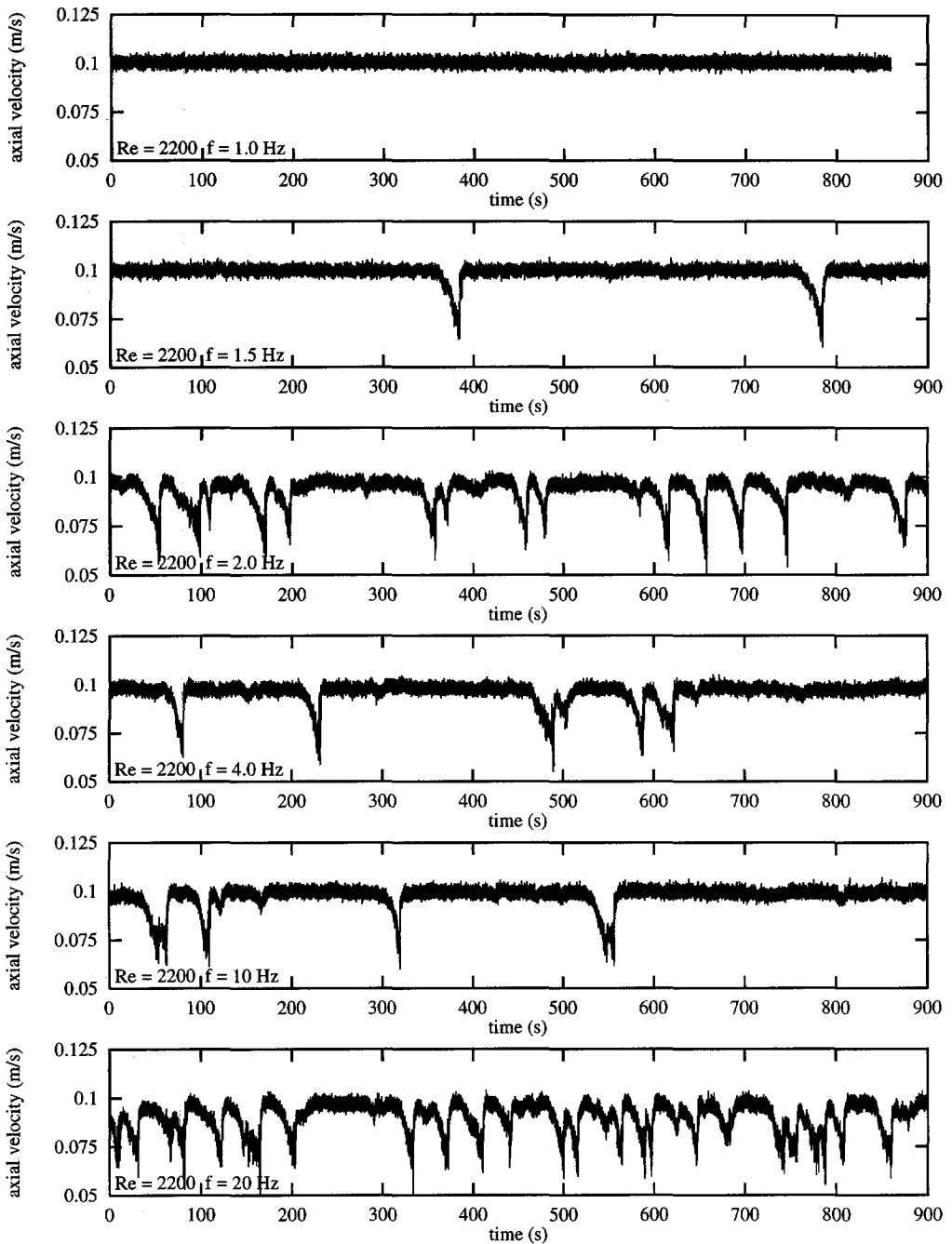
Wyganski *et al.* (1975) showed that near $Re=2200$, a so-called equilibrium puff exists, i.e. a puff which does not grow nor decay when moving downstream. The turbulent activity for $Re=2200$ is much larger than for $Re=2000$. This may indicate that puffs are decaying for $Re=2000$. This could be checked by performing measurements at different locations downstream.

For $Re \geq 2300$, the puffs grow and splitting occurs according to Wyganski *et al.* (1975). We performed measurements at $Re=2500$ for only two frequencies and the time-traces are shown together with the measurements at $Re=2000$ and $Re=2200$ in figure 6.15. It seems that, the critical frequency increases with Reynolds number. At $Re=2000$, the flow seems rather unstable at $f=1.5\text{ Hz}$, whereas at $Re=2500$ the flow stays laminar at this value. On the other hand, much turbulent activity is present for $f=2\text{ Hz}$ at $Re=2200$ and $Re=2500$. For $Re=2500$ and $f=2\text{ Hz}$, not many single puffs can be observed and the rest of this time-trace looks like an intermediate form between puffs and turbulent slugs. This is very similar to what Darbyshire & Mullin (1995) found. Note that the centerline velocity no longer reaches its laminar value (compare with the time-trace with $f=1.5\text{ Hz}$). Splitting of puffs as reported by Wyganski *et al.* (1975) is not clear for $Re=2500$ and $f=2\text{ Hz}$. This is most likely caused by the fact that Wyganski *et al.* (1975) studied single puffs whereas our disturbance mechanism continuously

Figure 6.11: Velocity time-traces for $\Delta V = 87 \text{ mm}^3$ at $Re = 2000$.

Figure 6.12: Velocity time-traces for $\Delta V = 87 \text{ mm}^3$ at $Re = 2200$.

Figure 6.13: Velocity time-traces for $\Delta V = 173 \text{ mm}^3$ at $Re = 2000$.

Figure 6.14: Velocity time-traces for $\Delta V = 173 \text{ mm}^3$ at $Re = 2200$.

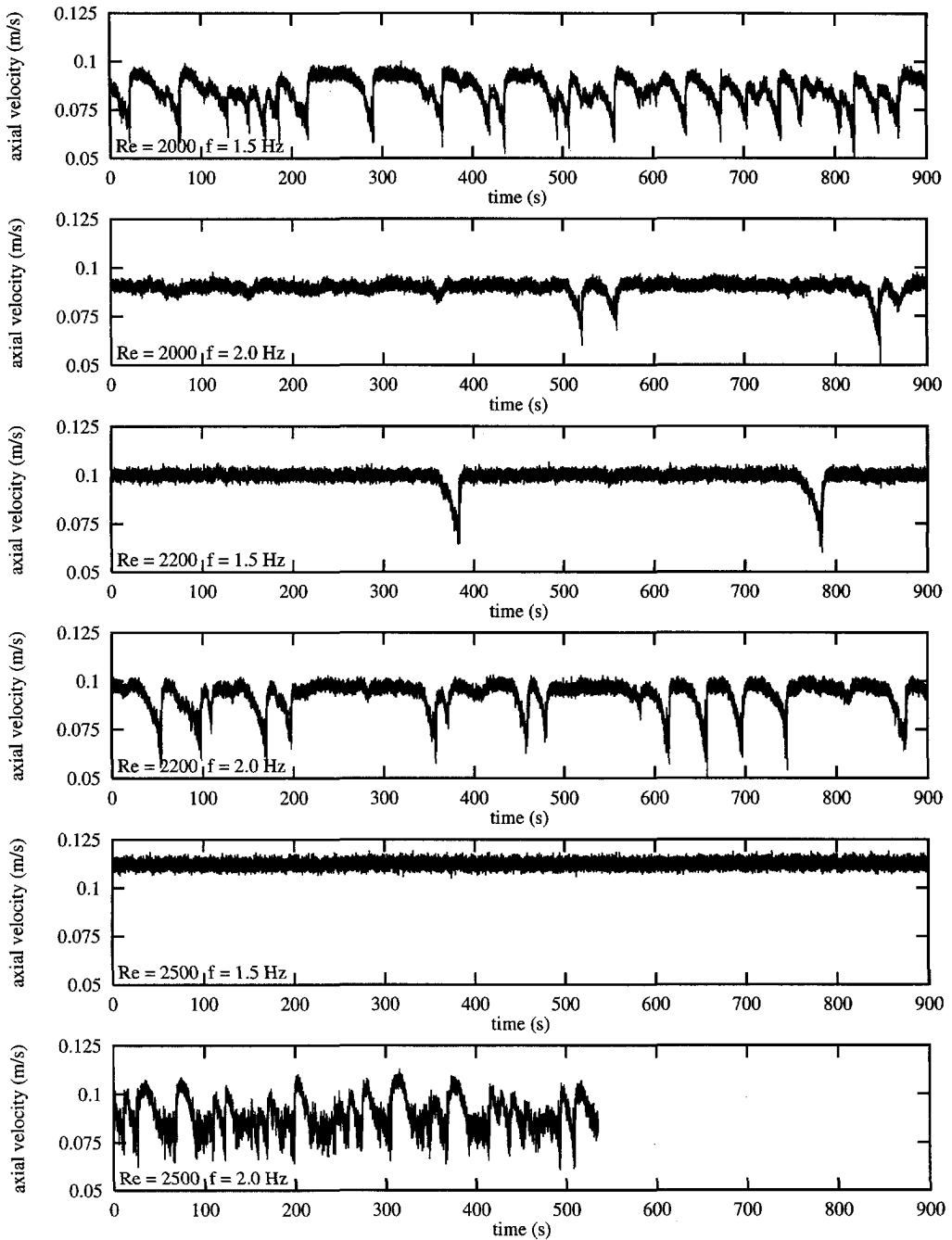


Figure 6.15: Velocity time-traces for $\Delta V = 173 \text{ mm}^3$ at $Re = 2000$, $Re = 2200$, and $Re = 2500$.

disturbs the flow and generates many puffs. Thus the merging of puffs, which form turbulent slugs at $Re=2800$ (Rubin *et al.* 1980), may generate the intermediate structures observed in figure 6.15 for $Re=2500$ and $f=2.0$.

Another aspect of puffs noted by Darbyshire & Mullin (1995), is the existence of so-called incursions at the trailing edge. An incursion is defined as a peak in the velocity trace where the velocity reaches the laminar value during only a very short time. Then it drops again and the flow further relaminarizes. An example of an incursion is shown in figure 6.16. Darbyshire & Mullin (1995) found these incursions in 20–30% of their puffs. Furthermore, they also found them in the trailing as well as in the leading edge of turbulent slugs at higher Reynolds numbers. In our time-series, incursions seem to be present in much less than 20% of the puffs but further research is needed to confirm this conclusion.

6.4.3 Discussion

The time-traces of the centerline velocity seem to suggest that the flow is very sensitive to a particular frequency at which many puffs are generated, whereas below this frequency laminar flow is sustained. For larger frequencies, puffs are also generated but their number is smaller. Such behavior was not found for the experiments in the slug- Re -range. These show that, particularly for the range of α^* studied in the puff- Re -range, the critical relative disturbance velocity $v_{i,c}^*$ varies only slightly with α^* . Although the behavior in the puff- Re -range and the slug- Re -range seems to be different, it is most likely similar behavior as we will explain below. Puffs are generated in large numbers for both displacement volumes for values of $v_i^* \approx 1$, but the corresponding values for α^* range from 8 to 20 (see table 6.4). Thus, interpreting the sensitivity to the frequency as a sensitivity to α^* is questionable.

Increasing the frequency also implies increasing the disturbance velocity. But for larger disturbance velocity one would expect an increase in the number of puffs generated instead of the decrease that we have found. However, another possibility is that the same or larger number of puffs are generated when v_i increases, but that due to the larger disturbance velocity, they are formed earlier upstream, i.e. closer to the disturbance mechanism. Thus, knowing that puffs decay for $Re=2000$ (Wyganski *et al.* 1975), we may conclude that before reaching the LDV, the puffs will have decayed during a longer time and as a consequence, less puffs can be seen. For equilibrium puffs no such behavior could exist. Although Wyganski *et al.* (1975) found equilibrium puffs for $Re \approx 2200$, our results could be an indication that puffs still decay at this Reynolds number. To confirm this hypothesis, similar puff experiments should be performed at slightly larger Reynolds numbers.

It is interesting to note here that similar arguments explain why turbulent slugs show up only in the LDV-signal if the disturbance is such that the transition to turbulence is located just upstream of the LDV. This is because, as the propagation speed of the slug interfaces is not equal, viz. the leading edge propagates at $1.5\overline{W}$ and the trailing edge with $0.5\overline{W}$, the slug will grow in length when moving downstream. Increasing the frequency, and with it the disturbance velocity, moves the transition location in the upstream direction. Hence, consecutive slugs can grow and merge resulting in a continuous turbulent flow before reaching the LDV location.

The values for v_i^* at which puffs and turbulent slugs occur are very close, suggesting a link between the generation of puffs and turbulent slugs. Rubin *et al.* (1980) showed that turbulent slugs are formed through the merging of puffs. This may perhaps suggest that all turbulent

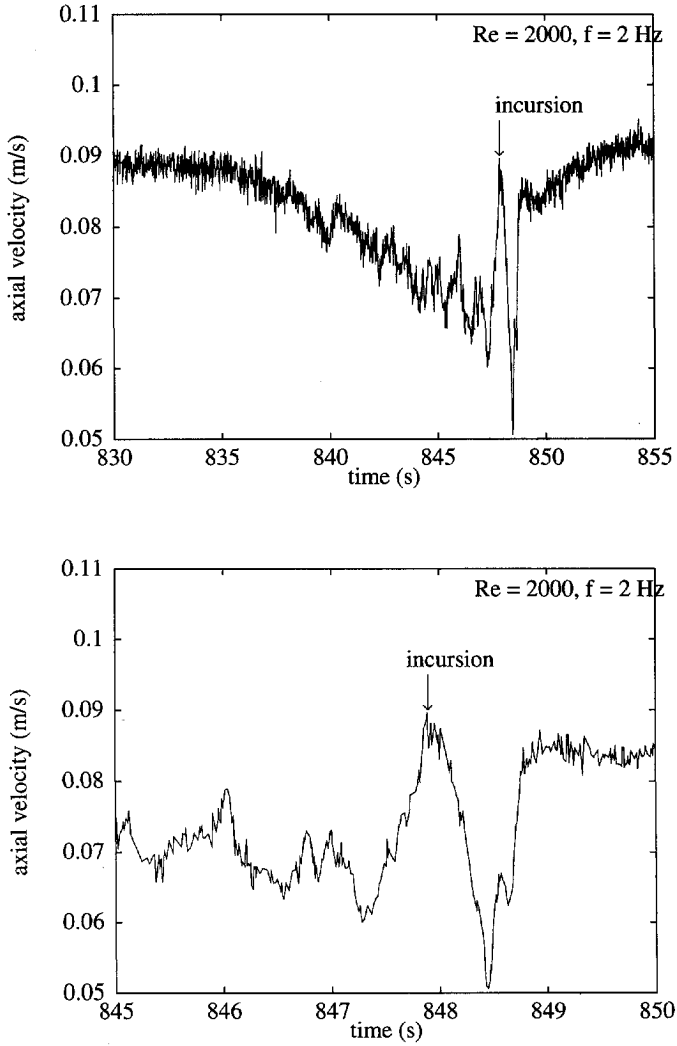


Figure 6.16: Puff with a clearly distinguishable incursion. In b) the time-scale is enlarged. From Boere (1995).

slugs are born as puffs but are very rapidly transformed into turbulent slugs provided that the Reynolds number is large enough to permit such transformation.

As we now have quantitative information on the stability of Newtonian pipe flow, we can study the stability of polymer solutions using the same equipment and compare the results with the Newtonian flow data. This is done in the next chapter.

Chapter 7

Non-Newtonian stability measurements

Abstract

In this chapter, the stability measurements for non-Newtonian fluids will be presented and compared to those for the Newtonian fluid presented in chapter 6. The non-Newtonian fluids that we used are solutions of a partially hydrolyzed polyacrylamide (PAMH) in water. The rheological properties of the PAMH-solutions depend, amongst others, on the concentration of the polymer (in our case varied between 20 and 40 ppm) and the concentration of salt in the solution. The latter turned out to be the key parameter in our measurements. In absence of salt, PAMH is forced to have, on the average, a stretched conformation, resulting in a strong increase in viscosity (2.5 to 15 times that of water depending on the shear rate) and also in shear thinning behavior. After addition of salt, the polymers coil up which leads to a much lower viscosity (less than twice that of water) and subsequently less shear thinning.

Since the effects of adding PAMH on the viscosity of the solution cannot be disregarded, we account for the shear-rate-dependent viscosity by using a Reynolds number definition in which the viscosity in the Newtonian case is replaced with the viscosity at the wall in the non-Newtonian case. This results in Moody diagrams (friction factor as function of Re) where the laminar measurements practically collapse onto the Hagen–Poiseuille line for Newtonian fluids. From the Moody diagrams it is obvious that the natural transition Reynolds number of our setup is reduced from $Re > 60\,000$ for water to $8\,000 \leq Re \leq 12\,000$ for fresh solutions. Chemical and mechanical degradation of the polymers increases the natural transition Reynolds number. In the presence of salt, a sudden increase in the measured pressure drop and thus in Moody friction factor is found when the flow becomes turbulent. In absence of salt, in which case the polymers are stretched, the laminar flow follows the Hagen–Poiseuille line for Newtonian fluids. When the flow becomes turbulent, the points in the Moody diagram just bend away from the laminar line and no jump in pressure drop appears.

The stability measurements for the polymer solutions are influenced by salt concentration and mechanical degradation. Increasing the concentration from 20 to 40 ppm has only a small effect. The polymer solutions containing salt show a stabilizing effect, i.e. the critical relative disturbance velocity $v_{i,c}^$ is increased compared to that of water. However, no delay in transition is present, viz. onset of turbulence still occurs at $Re = 3\,000$. For a 20 ppm solution in softened water (somewhat extended polymers), full turbulent flow was found for $Re = 2\,160$ whereas in Newtonian fluids at such low Reynolds numbers only decaying puffs exist. This could even be interpreted as an advancement of transition. In demineralized water, where the polymers are forced to have, on the average, a stretch conformation, the transition to turbulence is delayed to $Re \approx 4\,000$, i.e. below this Reynolds number the flow could not be triggered to undergo transition, not even at disturbance velocities as high as six times the bulk velocity. Mechanical degradation eliminated this delay in transition and only the stabilizing effect is found, i.e. increase in $v_{i,c}^*$.*

7.1 Introduction

In this chapter, we will present our measurements on the stability of non-Newtonian fluids in pipe flows. Instead of just mixing countless solutions of several concentrations of many polymers, we opted for a different approach. We studied the transition of a polymer solution at two low concentrations (20 and 40 ppm) and changed the salt concentration of the solvent water. This gives us the opportunity to change the polymer conformation between two extremes; fully coiled up and fully stretched.

The idea to concentrate our investigation on this aspect is based on several results presented in literature. Stability theory for plane Poiseuille flow shows that the critical Reynolds number, below which no linear disturbances grow, decreases when elasticity is introduced in the fluid in the form of the Maxwell model (Porteous & Denn 1972a). On the other hand, linear stability theory shows that the introduction of rods in the fluid increases the critical Reynolds number (Bark & Tinoco 1978). The Maxwell model and suspended rods can be regarded as models of a solution in which the polymers are coiled up and stretched respectively. Also, Virk & Wagger (1990) performed pressure drop vs. flow rate measurements and proposed two types of drag reduction behavior; type-A, related to coiled polymers, and type-B, found for stretched polymers. Unfortunately, they did not correct for the viscosity increase and thus seem to have overlooked a delay in transition for the fully stretched polymers (see also chapter 2). Thus by studying the influence of the coil-stretch transformation on the stability of pipe flow of polymer solutions, we hope to reveal the key parameter(s) that govern(s) the transition to turbulence.

To be able to study the influence of polymer addition on pipe-flow transition, a quantitative measure of the disturbance responsible for triggering transition is needed. The best way to obtain such information is to introduce a known disturbance into a laminar flow and measure for which combinations of disturbance features transition to turbulence occurs. We performed such measurements for the water and polymer solutions. Thus we can compare the stability measurements of the non-Newtonian fluids to that of the Newtonian fluid. This is the only way to study the effect of polymers on pipe-flow transition quantitatively, because the mechanisms of transition in pipe flow is still poorly understood.

When, at the same Reynolds number, a larger critical relative disturbance velocity $v_{i,c}^*$ (defined in equation 6.2) is found for the polymer solution than for water, we will speak of a *stabilizing* influence of the polymers. This is not necessarily linked to a *delay* in transition Reynolds number, i.e. the minimum Reynolds number below which no transition can be initiated is increased.

For a correct comparison between the stability measurements for the polymer solutions and water, we have to take into account non-Newtonian properties like a shear-rate-dependent viscosity. As these are strongly related to the polymer conformation, i.e. coiled or stretched, we will discuss in section 7.2 how this conformation can be changed by salt. Then the influence of the polymer conformation on the shear-rate-dependent viscosity and the pressure drop vs. flow rate measurements (Moody diagrams) will be touched upon in sections 7.3 and 7.4 respectively. Here, only the main results will be presented. A detailed discussion on the subject can be found in appendix E including some of the problems encountered. After correction for the shear-rate-dependent viscosity, the stability measurements for the polymer solutions will be compared to their Newtonian counterparts in section 7.5. Finally, a discussion is added including some ideas on practical implications as well as possible future research topics in this field.

Before entering into the non-Newtonian results, the peculiar notation for the concentration of some polymer solutions needs a clarification. For the polymer solutions in demineralized water, concentration descriptions like 20 + 10 ppm and 20 + 10 + 10 ppm are being used. This is to indicate that the 30 ppm solution is obtained by adding 10 ppm fresh polymer to an already used (and somewhat degraded) polymer solution of 20 ppm. After performing stability measurements on the 20 + 10 ppm solution, we added another 10 ppm of fresh polymer which results in a solution which is labeled 20 + 10 + 10 ppm. Although a totally fresh polymer solution of 40 ppm is to be preferred over a 20 + 10 + 10 ppm solution, this turned out to be impossible mainly due to time constraints. Not only does it take half a day to clean the entire setup (for an experienced worker), but it will also take half a day to make the demineralized water in situ. Furthermore, one or two additional days are needed to eliminate dissolved air, which generates small bubbles, in particular on the screens in the settling chamber and on the contraction wall. Nevertheless, we believe that the main conclusions of our stability experiments on stretched polymers are not strongly affected by the addition of fresh polymer to an already partly degraded solution.

7.2 The effect of salt

The polymer that we used in our experiments is a partially hydrolyzed polyacrylamide (PAMH), brand name Superfloc A-110 (Cytec Industries, formerly American Cyanamid). For more details on this polymer we refer to section 5.4. One of the most important arguments for our choice to use this polymer, is that its conformation can be manipulated through the change of the salt content in the solution. In absence of salt, the polymer is forced to have, on the average, a stretched conformation whereas in the presence of salt it coils up. The coiling up is stronger as more salt is dissolved. Also, this polymer is more sensitive to divalent salt (e.g. magnesium Mg^{2+} , calcium Ca^{2+}) than to monovalent salts (e.g. sodium Na^+ , potassium K^+) (Tam & Tiu 1990). The sensitivity to salt gives us the possibility to study the effect of the polymer conformation on the stability of the flow.

To get some feeling for the influence of polymer addition on pipe-flow stability, we first performed experiments using softened water. This was obtained by running tap water through an ion-exchanger which replaces divalent salts with monovalent sodium salt. The increase in viscosity as a result of the polymers is larger in softened water than in tapwater. In other words, the PAMH polymers are stretched more in softened than in tapwater.

Next, the stability of the flow was studied for solutions containing much less salt than the softened water case. Ideally, distilled water should be used in this case. However, the system volume of the flow loop is 1.5 m^3 . For these large quantities, it takes a very long time to make distilled water and it is costly as well. The Central Chemicals Depot of Delft University of Technology (CMC) can produce distilled water at a speed of 4l/h at a price of 1.5 guilders/l. Therefore, the best alternative is to use demineralized water, which contains only very small amounts of salt. Still, 1.5 m^3 of demineralized water costs approximately 300 guilders. With demineralized water as a solvent, we studied the stability behavior of the pipe flow for several concentrations of the polymer.

Finally, to study the effect of salt on the flow behavior in more detail, three different salt concentrations were used. After the experiments with the 20 + 10 + 10 ppm A-110 solution in demineralized water, sodium chloride was added in three stages; 90 g, 810 g, and 8100 g

Table 7.1: Concentrations in mg/l of monovalent and divalent salts in tap water, softened water, demineralized water, and demineralized water with added salt. For the measurement of magnesium and calcium the ICP-OES Perkin-Elmer Plasma 2000 was used. For the sodium and potassium the flame-AAS Perkin-Elmer 1100 was used. The listed values for demineralized water with 0.001 M NaCl are obtained by simply adding the 23.6 mg/l Na^+ corresponding to 0.001 M NaCl. Note that the softened water contains Na^+ concentrations in between that of 0.001 M and 0.01 M Na^+ .

Ion	tap water	softened water	demineralized water	demineralized water + 0.001M NaCl
calcium Ca^{2+}	48	0.75	0.21	0.21
magnesium Mg^{2+}	7.0	0.123	0.018	0.018
sodium Na^+	34	94.4	1.19	1.19+23.6
potassium K^+	5.0	0.6	2.8	2.8
total divalent	55.0	0.873	0.228	0.228
total monovalent	39.0	95.0	3.98	27.59

amounting to a total of 90 g, 900 g, and 9000 g respectively in 1.5 m³ of solution. The atomic weights for Na^+ and Cl^- are 23 g/mol and 35.5 g/mol respectively. Adding 90 g NaCl to 1.5 m³ of demineralized water thus gives an extra 23.6 mg/l Na^+ and a concentration of 0.001 M NaCl (1 M=1 mol/l). Since the concentration as well as the valency of the salts is important, fluid samples have been analyzed by the Laboratory for Material Science, section Atom-spectrometry. In table 7.1 the measured concentrations for the various solutions are given. The values for tap water as supplied by the water company are added for comparison. Assuming the sodium salt was pure (Broxo by Akzo-Nobel), the total salt distribution for the demineralized water solutions with extra salt can be obtained by just adding the extra sodium to the salt distribution in the demineralized water. As an example, the values for 0.001 M are also recorded in table 7.1.

From the data given in table 7.1, it appears that softening water reduces the amounts of Mg^{2+} and Ca^{2+} to less than 1 mg/l. In demineralized water even less divalent salt is present. For softened water the monovalent salt concentration is in between that of 0.001 M and 0.01 M NaCl. Therefore, the amount of coiling of the polymer will also be ranged in this way. It is interesting to check if properties like viscosity follow a similar trend. The dependence of viscosity on polymer concentration and salt contents will be discussed in the next section.

7.3 Non-Newtonian viscosity

7.3.1 Introduction

For dilute polymer solutions at 40 ppm and lower concentrations, any increase in viscosity and effects of shear thinning are commonly disregarded. The reason for this is mainly twofold. Firstly, many of the experiments with dilute polymer solutions are aimed at obtaining drag reduction. Only for laminar flow, does viscosity play a direct role whereas for turbulent flow a viscosity increase may be masked by drag reduction. Furthermore, many drag reducers are coiled polymers and show only a small increase in viscosity. Secondly, as the vast majority of viscometer measurements is performed for concentrated polymer solutions and polymer melts,

most viscometers cannot be used to accurately measure shear-rate-dependent viscosities close to that of water. Moreover, very few viscometers can measure the zero-shear-rate viscosities of these solutions.

However, by measuring the viscosity with a very accurate viscometer, we found that even for the dilute polymer solution of 40 ppm where the polymers were coiled up due to the presence of large amounts of salt, the viscosity is increased by 10%. Vlassopoulos and Schowalter (1994) found a zero-shear-rate viscosity increase for a 2 ppm polyacrylamide solution in distilled water (stretched polymers) of 60% above the solvent viscosity. In other words, viscosity effects cannot be disregarded for dilute polymer solutions, not even for coiled polymers.

In the next section, we will discuss the measurements of the shear-rate-dependent viscosity of the polymer solutions as well as the viscosity function used to describe them.

7.3.2 Viscosity function

In order to correct all non-Newtonian measurements for viscosity effects, the viscosity has been measured as a function of shear rate. For this we used a Contraves Low Shear LS-40 concentric cylinder viscometer. The Contraves LS-40 is an apparatus, one of the few that exist, which is suited for viscosity measurements of dilute polymer solutions in water. This is because, the viscosity of water is so low that most viscometers cannot measure it accurately over a wide range of shear rates. In particular, measurements at very low shear rates of the order of 10^{-2}s^{-1} are needed to find a zero-shear-rate viscosity plateau, i.e. η_0 , for these dilute solutions. At these low shear rates, the shear stress and coupled to it the torque is so small that very sensitive measuring equipment is needed to accurately determine the viscosity.

From the measured viscosity data a viscosity function is determined which will be used to correct the Moody diagram and also the stability measurements (to be discussed later). As only viscosity effects are regarded here, we are essentially modeling the polymer solutions with a generalized Newtonian fluid model. A widely used generalized Newtonian fluid model which captures a number of important parameters is the four parameter Carreau model which gives the non-Newtonian viscosity η as a function of the shear rate $\dot{\gamma}$ (Bird *et al.* 1987a, p. 171):

$$\frac{\eta - \eta_\infty}{\eta_0 - \eta_\infty} = [1 + (\lambda\dot{\gamma})^2]^{(n-1)/2} \quad (7.1)$$

where η_0 is the zero-shear-rate viscosity, η_∞ the infinite-shear-rate viscosity, n the power-law exponent, and λ time constant. The Carreau model describes the transition from the zero-shear-rate plateau to the power-law region described by exponent n . $n=1$ represents a Newtonian fluid and for shear thinning we find $n<1$. For many polymer melts and concentrated solutions a good fit can be obtained with $\eta_\infty=0$. For dilute polymer solutions, however, very often the power-law region of the shear-rate-dependent viscosity is limited in the higher shear rate range and seems to level off. If this is the case, the assumption $\eta_\infty = 0$ is no longer valid. However, our viscosity measurements do not extend far enough in the η_∞ -region, and an accurate estimation of η_∞ is almost impossible¹. For this reason, we have set the value of η_∞ to the solvent viscosity value which poses a lower bound to η_∞ . As temperatures varied only slightly during the non-Newtonian experiments, 24.25–24.45°C with a few excursions to 24.75°C, the infinite-shear-rate viscosity was taken $\eta_\infty(24.35^\circ\text{C})=0.904\text{mPa}\cdot\text{s}$ for all our viscosity measurements. Vlassopoulos

¹Kalashnikov (1994) used capillary viscometers and could obtain measurements in the η_∞ -range.

& Schowalter (1994) use $\eta_\infty=0$ and obtain good fits, however, their data show a higher viscosity than predicted by the Carreau model in the high shear rate tail of the viscosity measurement, thus indicating $\eta_\infty>0$. For determination of the other parameters in equation 7.1, software supplied with the book by Gordon & Shaw (1994) was used. As the Carreau model incorporated in their software assumed $\eta_\infty=0$, we fed the fit program with shear rate vs. $\eta-\eta_\infty$ data. The fit program then supplies $\eta_0-\eta_\infty$, λ , and n . Some of the parameter values for the Carreau model found in this way are listed in table 7.2.

Several of the most prominent effects found in our viscosity measurements are illustrated in figures 7.1 and 7.2, where we plot the measured shear-rate-dependent viscosities (markers) together with the fitted Carreau model viscosity functions (dotted lines).

- On average, the viscosity data seems to be represented fairly well by the Carreau model. A general result seems to be that the value of η_∞ is somewhat too small since for most fluids the measured viscosities for large shear rates is larger than the value predicted by the fitted Carreau model. A larger value would have resulted in a better fit. Nevertheless, for the purpose of transforming Moody and stability measurement data, the Carreau model representation using the solvent value for η_∞ is very well suited since the stability measurements are not located in the high shear rate range.
- Dissolving small amounts of polymer in demineralized water results in a spectacular increase in viscosity, as is shown in figure 7.1. The zero-shear-rate viscosity is more than 10 and 20 times as high as the solvent viscosity for the fresh 20 and 20+10+10 ppm respectively. The time constant increases to approximately $\lambda=5$ s and the shear thinning becomes much stronger when compared to softened water; $n=0.61$ (20 ppm) and $n=0.64$

Table 7.2: Carreau model parameters for some of the Superfloc A-110 polymer solutions used in the stability experiments. η_∞ is set to the solvent viscosity value, thus giving $\eta_\infty=0.904$ mPas.

Concentration (ppm)	Solvent (-)	Age (days)	η_0 (mPas)	λ (s)	n (-)
40	soft. water	1	1.94 ± 0.02	1.16 ± 0.27	0.862 ± 0.006
20	dem. water	1	9.58 ± 0.12	4.96 ± 0.03	0.612 ± 0.004
20	„	3	7.18 ± 0.07	2.81 ± 0.15	0.631 ± 0.004
20+10+10	„	1	$22.12^b\pm 0.38$	5.58 ± 0.54	0.643 ± 0.007
20+10+10	0.001M NaCl	1 ^a	$3.37^b\pm 0.02$	0.82 ± 0.08	0.772 ± 0.006
20+10+10	0.01M NaCl	1 ^a	$1.43^b\pm 0.01$	0.31 ± 0.09	0.877 ± 0.010
20+10+10	0.1M NaCl	1 ^a	1.02^b		1

^aViscosity measurements performed on 2 months old fluid samples.

^bMoody diagram measurements after viscosity correction indicate an incorrect viscosity. For some cases a different value has been used in the viscosity correction procedure. Please refer to appendix E for details and all measurement results.

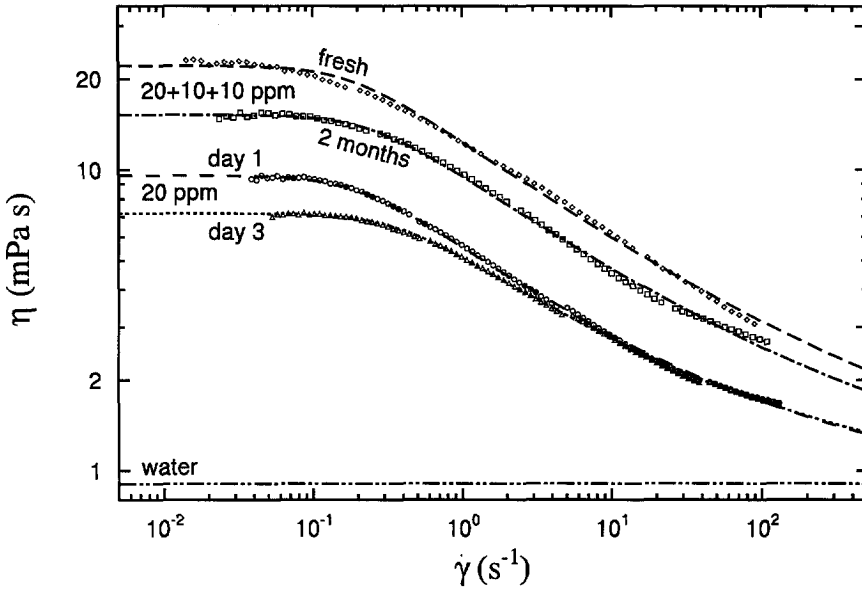


Figure 7.1: Non-Newtonian viscosity as a function of steady shear rate for several solutions of Superfloc A-110 in demineralized water. Measured using a Contraves Low-Shear LS-40.

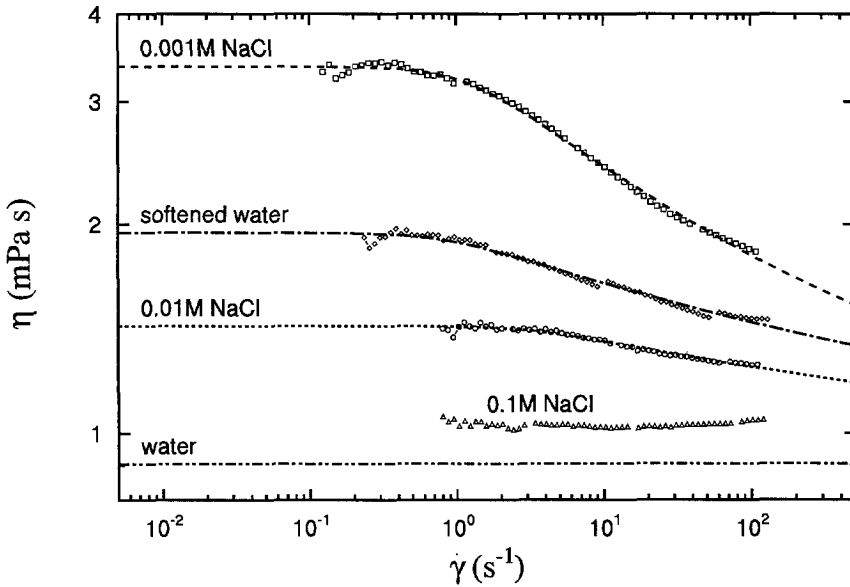


Figure 7.2: Non-Newtonian viscosity as a function of steady shear rate for 20+10+10 ppm solutions of Superfloc A-110 in demineralized water after addition of various amounts of salt. The measurement of the 40 ppm solution in softened water is added for comparison. Measured using a Contraves Low-Shear LS-40.

(20 + 10 + 10 ppm). This value is remarkably close to the value $n=2/3$ found for rigid dumbbells from kinetic theory (Bird *et al.* 1987b, p. 123). This could be an indication that the stretched polymers indeed show rod-like behavior.

- From the data shown in figure 7.1, we see that mechanical degradation of the 20 ppm A-110 solution in demineralized water does not affect the viscosity at high shear rates. However, η_0 is reduced to 75% of that of the fresh solution. The time constant is reduced even further to almost half of the value of the fresh solution.
- Also, chemical degradation with time (aging) occurs as is shown by the difference between the measurement of the fresh 20 + 10 + 10 ppm solution and that measured two months later. Thus, measurements of the shear-rate-dependent viscosity should be performed immediately after the Moody diagram and stability measurements.
- Adding a small amount of salt results in a dramatic fall in viscosity as shown in figure 7.2. The reason for this is the coiling up of the polymer caused by the presence of salt. Adding 0.001 M NaCl reduces η_0 to approximately $1/6^{\text{th}}$ of its value in demineralized water. The time constant becomes $\lambda=0.82$ s, even smaller than found with softened water as solvent but the uncertainty in the time constant is quite large. Adding ten times more sodium chloride reduces the viscosity to values smaller than those for softened water. This is in agreement with the salt content which is also ranged in this way (see table 7.1). For 0.1 M NaCl, the viscosity is reduced to a value only 10% above that of water and hardly any shear thinning is found.

For a discussion of all the solutions used in the stability measurements, we refer to appendix E. There, we also explain the jumps present in some of the viscosity data. Furthermore, the inconsistencies for several solutions between the data from the viscometer and those in the Moody diagram are discussed.

In the next section, the method that we used to correct the Moody diagram for the shear-rate-dependent viscosity, is discussed.

7.4 Non-Newtonian Moody diagram

7.4.1 Introduction

The Moody diagram for Newtonian fluids has already been discussed in chapter 5. However, let us briefly recall the most important relationships. The Moody diagram is in essence a plot of the nondimensionalized pressure drop, i.e. Moody friction factor f_M , as a function of the dimensionless flow rate, i.e. Reynolds number Re , where Re and f_M are defined as:

$$Re = \frac{\rho \bar{W} D}{\eta} = \frac{\bar{W} D}{\nu} \quad (7.2)$$

$$f_M = \frac{\Delta p D}{\frac{1}{2} \rho \bar{W}^2 L} \quad (7.3)$$

From equation 7.3 it is obvious that the friction factor, apart from geometrical constants like pipe diameter D and length L over which the pressure drop Δp is measured, depends only on

flow quantities Δp and the bulk velocity \bar{W} . Given the small amounts of polymer we used, the density will be assumed constant and equal to the solvent density.

For a Newtonian fluid, the viscosity is constant and this results in a relationship between f_M and Re that is valid for all Newtonian fluids. For laminar flow the friction factor follows the Hagen–Poiseuille relationship represented by $f_M=64/Re$ and for turbulent flow the Blasius law is found, i.e. $f_M=0.3164Re^{-1/4}$ ($Re\leq 100\,000$), see e.g. Bird *et al.* (1960, p. 187). Moody diagrams for Newtonian fluids (in a hydraulically smooth pipe) can differ only in the Reynolds number for which transition to turbulence occurs. Normally, the transition range extends from $2\,000\leq Re\leq 3\,000$. However, as we have seen in section 5.12, when a settling chamber is used to generate a low turbulence inflow, the transition Reynolds number can be increased to much higher values. For instance, in our facility it is larger than $Re=60\,000$.

From the viscosity measurements for dilute polymer solutions, in particular when the polymers have a stretched conformation, a large increase in viscosity relative to that of the solvent is found as well as shear thinning behavior. The shear rate is different at every radial location in the pipe and also dependent on the flow rate. So, one may ask which viscosity value should be used in the calculation of the Reynolds number? Using the solvent viscosity seems to give unsatisfactory results as is shown in figure 7.3.

Due to the large increase in viscosity, the data are shifted strongly to the right of and moreover are no longer parallel to the Hagen–Poiseuille line. To be able to compare the results for non-Newtonian fluids to those of Newtonian fluids, we have to account both for the increase in viscosity and also for the shear-rate-dependent viscosity.

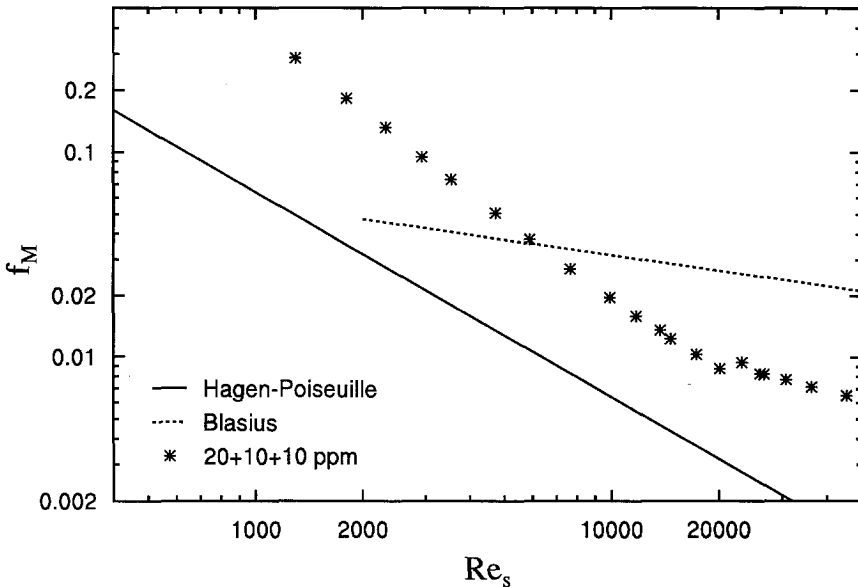


Figure 7.3: Moody diagram for a 20 + 10 + 10 ppm Superfloc A-110 solution in demineralized water. In the calculation for the Reynolds number the solvent viscosity has been used so no correction for the non-Newtonian viscosity is applied here.

In the next section, we discuss some theoretical arguments based on which a viscosity can be defined to be used in the Reynolds number. The corrected Moody diagrams are shown in the section thereafter.

7.4.2 Modified Reynolds number

In this section we will discuss the viscosity that we used to correct the Moody diagram and the stability measurements. For this, a Reynolds number for non-Newtonian fluids is introduced, which we call the modified Reynolds number.

To suggest a possible definition of a modified Reynolds number, we first study the power-law fluid. Although it does not describe the shear-rate-dependent viscosity as well as the Carreau model, we can obtain explicit relationships for the power-law model which are impossible to obtain with the Carreau model. Furthermore, the power-law model is able to capture well the important power-law region of the viscosity function that is also present in the Carreau model.

The empirical power-law model describes the non-Newtonian viscosity as a function of shear rate (Bird *et al.* 1987a, p. 173) according to:

$$\eta = K \cdot \dot{\gamma}^{n-1} \quad (7.4)$$

where K is the so-called consistency index and n the power-law exponent. Bird *et al.* (1987a, p. 177) derive for this viscosity function the equations for the velocity profile and the relationship between the flow rate and the pressure drop, for a pipe flow. Their results can be expressed as follows:

$$W = W_{cl} \left[1 - \left(\frac{2r}{D} \right)^{(1/n+1)} \right] \quad (7.5)$$

$$W_{cl} = \bar{W} \frac{3n+1}{n+1} \quad (7.6)$$

Taking the derivative of equation 7.5 and substitution of $r=D/2$ gives the shear rate at the wall:

$$\dot{\gamma}_w = 2 \frac{\bar{W}}{D} \frac{3n+1}{n} \quad (7.7)$$

From the relationship between Δp and the wall shear stress τ_w (given by $\tau_w = \Delta p D / 4L$), and applying the definition of the viscosity, i.e. $\tau = \eta \cdot \dot{\gamma}$, at the wall, we find using equation 7.7:

$$\Delta p = \frac{4L}{D} \tau_w = \frac{4L}{D} \eta_w \dot{\gamma}_w = \frac{8L}{D} \eta_w \frac{\bar{W}}{D} \frac{3n+1}{n} \quad (7.8)$$

Thus the friction factor for a power-law fluid can be written as:

$$f_M = \frac{\Delta p D}{\frac{1}{2} \rho \bar{W}^2} = \frac{64 \eta_w}{\rho \bar{W} D} \frac{3n+1}{4n} = \frac{64}{Re_n} \quad (7.9)$$

Here, Re_n is the modified Reynolds number (Metzner & Reed 1955) which is defined as:

$$Re_n = \frac{\rho \bar{W}^{2-n} D^n 2^{3-n}}{K (3 + 1/n)^n} \quad (7.10)$$

The use of Re_n gives us a Hagen–Poiseuille relationship between the friction factor and Re_n that we know for Newtonian fluids. Equation 7.9 also allows another definition for the Reynolds number. In this Reynolds number the viscosity is taken to be equal to the value at the wall. The relationship between this Reynolds number, denoted as Re_w , and Re_n then becomes:

$$Re_w \equiv \frac{\rho \bar{W} D}{\eta_w} = \frac{3n+1}{4n} Re_n \quad (7.11)$$

Working with Re_w requires the viscosity at the wall, the determination of which will be discussed later. The use of Re_w rather than Re_n in the Moody diagram will result in an overestimation of the Reynolds number with a factor $1/4 \cdot (3 + 1/n)$. Note that the factor depends only on n and is constant for a given fluid. In the Moody diagram (log-log-plot), this will show up as a shift to the right of the Hagen–Poiseuille line. We calculated the deviation in Reynolds number for various values of n and show them in table 7.3. Thus, the deviation in the Reynolds number becomes only large for very small n (which does not apply to our results).

Table 7.3: The Reynolds number in the Moody diagram is overestimated by a factor $1/4 \cdot (3 + 1/n)$ when using Re_w instead of Re_n . It is calculated for various values of n based on equation 7.11.

n	$\frac{3n+1}{4n}$
1	1.000
0.9	1.028
0.8	1.063
0.7	1.107
2/3	1.125
0.6	1.167
0.4	1.375
0.2	2.000

The advantage of using Re_w instead of Re_n , lies in the fact that it can be used for any viscosity model. Actual fluids do not follow the power-law model over the entire shear rate range, but have η_0 and η_∞ plateau's. Here, shear thinning is absent (or $n=1$ and the error introduced by the use of Re_w is zero. Since in our measurements the power-law constant in the Carreau model is minimum for the fresh 20 ppm A-110 solution, for which $n=0.612$, the maximum error introduced by Re_w is 16%. In order to calculate the friction factor as a function of Re_w for the Carreau model, we have to numerically calculate the velocity profile for a number of pressure drop values. This gives a maximum error of 11% at $Re_w \approx 80$. For $Re_w \geq 2000$, the error is smaller than 8%. This seems quite acceptable and given all the practical advantages, we decided to use Re_w in all our plots, both for the Moody diagram as well as the stability measurement plots.

In the calculation of Re_w , the following procedure is used to determine η_w :

1. The Carreau model parameters for the fluid are determined from the viscometer measurements.

2. The measured pressure drop was transformed into a wall shear stress using $\tau_w = \Delta p D / (4L)$.
3. The shear stress in a fully developed pipe flow varies linearly with the radial position with a maximum τ_w at the wall. The relation between the shear stress τ and the shear rate $\dot{\gamma} = \partial w / \partial r$ is given by $\tau \equiv \eta(\dot{\gamma}) \dot{\gamma}$. So, for a given τ , the values for η and $\dot{\gamma}$ can be determined by iteration. Integration over the pipe radius then gives the flow rate. With this the friction factor and the Re_w can be calculated.
4. 2. and 3. are repeated for all data points.

Using this procedure for the fresh 20 ppm A-110 polymer solution, we obtain figure 7.4. The Hagen-Poiseuille line as well as the theoretical line for a power-law fluid with $n=0.612$ are plotted for comparison. Surprisingly enough, the measurement collapses onto the Hagen-Poiseuille line and do not follow the calculations for the Carreau model. This seems to be the general trend for most of our solutions. We cannot explain why the viscosity-corrected data follows the Newtonian curve rather than the calculated line for the Carreau model. It may be related to the way in which the fluid samples have been obtained such that the fluid sample is not fully representative of the fluid in the pipe. For a discussion see appendix E.

In the next section, we will present Moody diagrams of some of the polymer solutions that we have used and discuss the most important features.

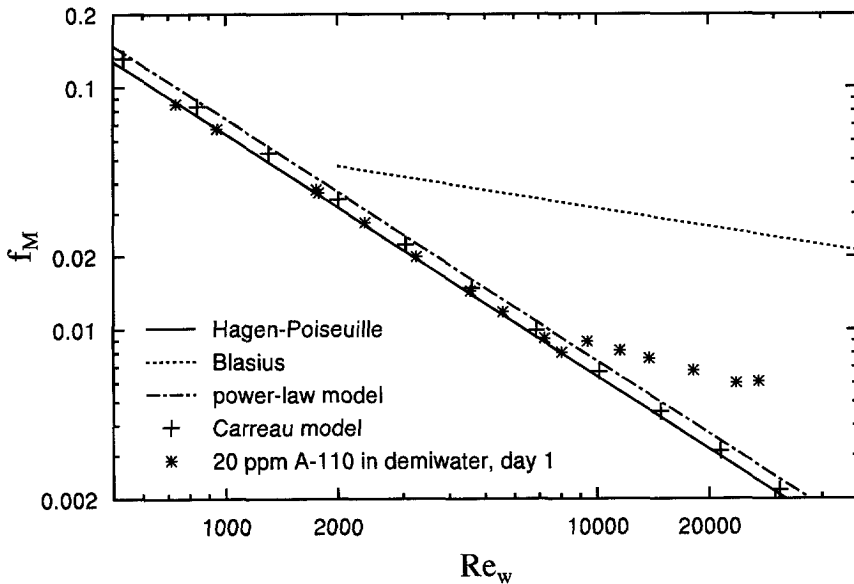


Figure 7.4: Moody diagram using the Reynolds number based on the viscosity at the wall, Re_w . The measurement for the fresh 20 ppm Superfloc A-110 solution in demineralized water is compared to the theoretical relationships for the power-law model and the Carreau model.

7.4.3 Moody diagram measurements

Here, we will discuss the main results obtained from the measurements of the non-Newtonian Moody diagrams. In all figures, the Reynolds number is calculated using the viscosity at the wall, i.e. Re_w , following the procedure discussed in the previous section. An overview of all measured Moody diagrams is given in appendix E together with a discussion of some of the inconsistencies and problems encountered.

The Moody diagrams, shown in figures 7.5 to 7.8, lead to several interesting results:

- Almost all laminar data practically coincide with the Hagen–Poiseuille line. As the viscosity functions of the various polymer solutions are quite different, we feel that our choice for the use of Re_w is supported by this result. In contrast, the measurements for 0.01 M and 0.1 M NaCl, shown in figure 7.7, exhibit a deviation from the Hagen–Poiseuille line, particularly for the lower Re_w . For a discussion of these and some other discrepancies, not shown here, we refer to appendix E.
- All Moody diagrams show a strongly different behavior with respect to natural transition when compared to that of non-Newtonian fluids. Whereas the natural transition Reynolds number for Newtonian fluids has been found to be larger than $Re=60\,000$, the non-Newtonian polymer solutions have a natural transition Reynolds numbers in the range of $8\,000 \leq Re \leq 30\,000$. Natural transition Reynolds numbers of $Re \approx 8\,000$ are shown figures 7.5 and 7.6 for polymer solutions of Superfloc A-110 in demineralized water, where the polymers have a stretched conformation. Natural transition Reynolds numbers of $Re \approx 30\,000$ are found for the 20 + 10 + 10 ppm polymer solution in the presence of the highest salt concentration that we studied, i.e. 0.1 M NaCl, as is shown in figure 7.7. For a discussion on the origin of the change in natural transition Reynolds number we refer to section 7.6.
- All polymer solutions show drag reduction, i.e. the turbulent f_M curve lies below the Blasius line. This means that for turbulent flow, at the same Reynolds number, the friction factor is smaller for the polymer solutions than for water. Whether or not this is also the case when dimensional quantities like pressure drop as a function of flow rate are compared, is checked in section 7.6.
- As mentioned before, in demineralized water the polymers are forced to have, on the average, a stretched conformation. This results in type-B drag reduction (see Virk & Waggener 1990) in which case the turbulent data starts deviating from the laminar line by just bending away, as shown in figure 7.6. The characteristic jump in friction factor, normally associated with transition of Newtonian fluid and also with a type-A drag reduction fluid, related to coiled polymers, has vanished.
- When the fluids are recirculated longer, the natural transition Reynolds number increases and the amount of drag reduction becomes smaller, as follows from figure 7.5. This decrease in drag reduction with circulation time is commonly attributed to mechanical degradation, i.e. the breaking of polymer molecules due to mechanical forces. For mechanically degraded polymer solutions in demineralized water, the jump in friction factor when going through transition to turbulence, which was almost absent for fresh polymer solutions, appears again.

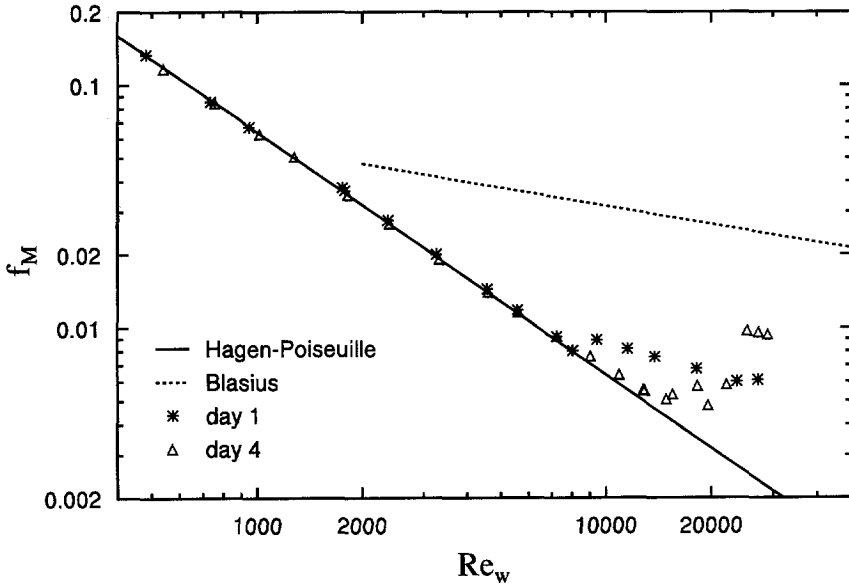


Figure 7.5: Moody diagram for 20 ppm Superfloc A-110 solutions in demineralized water water measured for the fresh solution and after for days of circulation in the pipe flow facility.

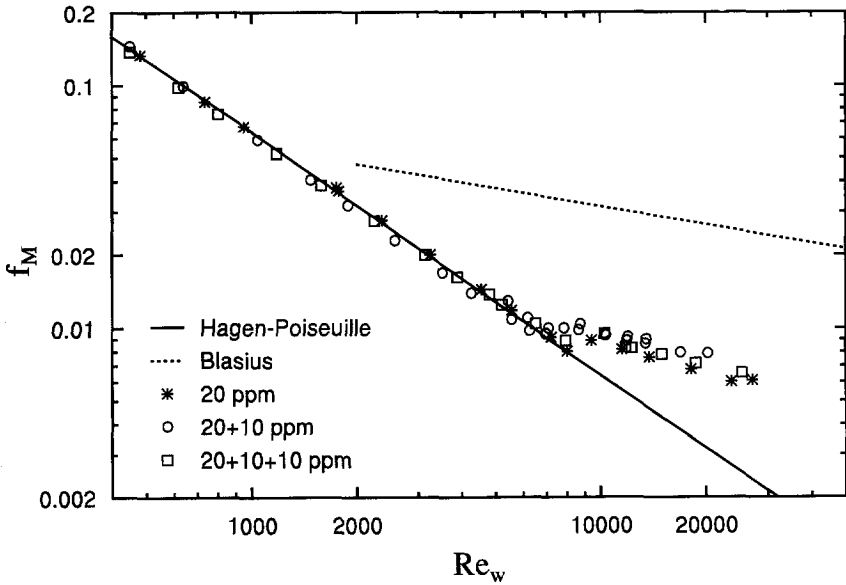


Figure 7.6: Moody diagram of fresh Superfloc A-110 solutions in demineralized water for various concentrations. As explained in section 7.1, the concentrations indicated by 20+10 ppm and 20+10+10 ppm have been obtained by adding another 10 ppm of fresh polymer to a degraded solution.

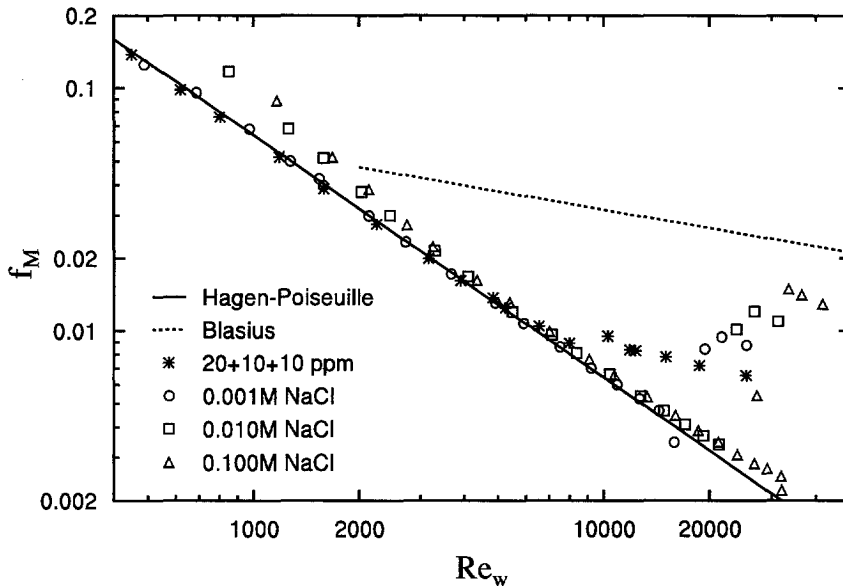


Figure 7.7: Moody diagram of 20 + 10 + 10 ppm Superfloc A-110 solutions in demineralized water with various concentrations of added sodium chloride salt. Note that the symbols indicate the same solution in the various Moody diagrams.

- By adding 10 ppm of fresh polymer to the degraded 20 ppm solution in demineralized water after 5 days, we obtain the 20 + 10 ppm solution. From figure 7.6 it is clear that adding fresh polymer practically restores the turbulent flow behavior to that of the fresh 20 ppm polymer solution. The viscosity is increased but this is concealed in the use of Re_w . The 20 + 10 + 10 ppm solution is obtained by adding 10 ppm of fresh polymer to a slightly degraded 20 + 10 ppm solution.
- A spectacular change in flow behavior can be seen after the addition of sodium hypochlorite to the fluid as illustrated in figure 7.8. Sodium hypochlorite is used to suppress the growth of algae which would clog the fine screens in the settling chamber leading to a strong fall in natural transition Reynolds number. However, adding sodium hypochlorite to a polymer solution of Superfloc A-110 results in the restoration of the Newtonian flow behavior. A natural transition Reynolds number of 60 000 is obtained and the viscosity is only 5% above that of water. Presumably, the polymers are *chemically* degraded. Therefore, no sodium hypochlorite can be added to the water resulting in a limited measuring time of less than one week, particularly at the high water temperatures that we encountered during our experiments, caused by a very hot summer month.

From the Moody diagram results discussed above, it is clear that non-Newtonian flow behavior is rather complicated and susceptible to various influences. Although we can make a fair prediction of the qualitative effect on the flow behavior of some of the most important parameters, a quantitative prediction is still impossible and remains one of the most important challenges in

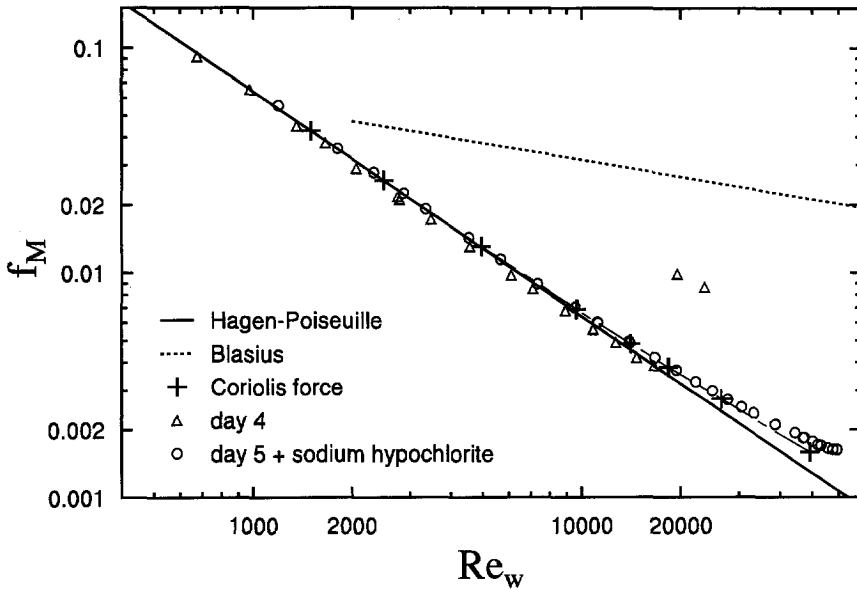


Figure 7.8: Moody diagram for a 40 ppm Superfloc A-110 solution in softened water after addition of sodium hypochlorite. Newtonian like flow behavior is restored with a viscosity only 5% above that of water.

non-Newtonian fluid mechanics.

As most of the turbulent data in Moody diagrams fall on straight lines, it is tempting to extrapolate these lines. Doing this for Newtonian fluids, we would get an intersection of the Blasius law with the Hagen-Poiseuille line for $Re=1187^2$. This is almost half of the minimum transition Reynolds number for Newtonian fluids. Linearly extrapolating the turbulent flow data of the fresh 20 ppm polymer solution, illustrated in figure 7.5, in the direction of the laminar line gives an intersection at $Re \approx 5500$. It would seem that no turbulence can be supported below this Reynolds number since that would imply a lower resistance to turbulent flow than to laminar flow. As we will see from the stability experiments, this estimate gives a reasonable indication of the transition Reynolds number.

In the next section, the results of the stability experiments for polymer solutions are presented.

7.5 Stability Measurements

7.5.1 Introduction

In this section, we will discuss the results of the stability experiments for the non-Newtonian fluids discussed in the previous sections and compare them to the results obtained for Newtonian fluids of section 6.3. However, we should remember that the viscosity is shear-rate dependent.

²This value is fairly close to the value above which Prengle & Rothfus (1955) find a deviation from laminar flow where an irregular wave is sustained. Between $1500 \leq Re \leq 2100$, they report a strong tendency towards a spiral wave, and above $Re=2100$ they find the occasional disturbance eddy (possibly what we now call a puff).

The stability diagrams, in which the critical relative disturbance velocity $v_{i,c}^*$ is plotted as a function of dimensionless wave number α^* , are however, unaffected by the viscosity. The viscosity correction appears only in the Reynolds number Re_w , which for a given flow rate can be different for each fluid.

We performed stability measurements for certain flow rates only corresponding to rounded values for Re for Newtonian fluids, e.g. $Re=3\,000$, $5\,000$, $7\,500$, $10\,000$, etc. In the calculation of Re_w , the viscosity at the wall is used, following the procedure discussed in section 7.4.2. This results in Re_w values that are different for each solution. For example, the flow rate corresponding to $Re=7\,500$ for water, gives $Re_w=4\,400$ and $Re_w=2\,600$ for the 40 ppm solution in softened water and for the 20 + 10 ppm solution in demineralized water respectively. This complicates the comparison but rather than interpolating the data to lines for the same Re_w for all fluids, the stability data is presented without such data manipulation. Nevertheless, some interesting conclusions can be drawn from these 'raw' the stability measurements.

Before discussing the stability measurements, particularly those of fresh polymer solutions in demineralized water, some further discussion on the background of these measurements is needed. As discussed in section 6.2.2, for all stability measurements, transition was detected by pressure drop measurements over a pipe section of 2.5 m starting 1 m downstream of the disturbance and also by using Laser Doppler Velocimetry (LDV) techniques. As mentioned before, both the Ar-ion and the HeNe LDV are located further downstream than the pressure drop measurement. Therefore, the LDV equipments could detect transition slightly earlier than the pressure drop measurement. For Newtonian fluids, a strong increase in pressure drop and strong fall in centerline velocity are clear indicators of transition. These characteristics could also be found in the polymer solutions made from softened water and the degraded polymer solutions in demineralized water. However, for fresh polymer solutions in demineralized water no jump in pressure drop occurs when going through transition as is shown in figure 7.6. This effectively eliminates the pressure drop value as a flow regime indicator and leaves us LDV measurements only. However, the fresh polymer solutions in demineralized water did also not show a clear drop in centerline velocity which would indicate turbulence. Although shear thinning fluids have a laminar velocity profile which is somewhat blunter than a parabola, the shear thinning effect for the fluids used here ($n \leq 0.61$) is not strong enough to explain the absence of the drop in centerline velocity. Thus, it is likely that also the entire velocity profiles changes slowly from the laminar to the turbulent profile for these fresh demineralized water solutions. This is not unreasonable. The velocity gradient near the wall is coupled to the wall shear stress in the viscous sublayer and the wall shear stress is linearly related to the pressure drop. Therefore, the only reliable indication for transition which is left for these fresh polymer solutions in demineralized water, is the turbulence intensity.

As we will see later, a delay in transition can be found. In combination with the low natural transition Reynolds number, this leaves us only a small Re -range in which the transition can be triggered. From Newtonian stability experiments, we know that just above the lowest possible transition Reynolds number so called turbulent puffs appear (see section 2.3.5). Puffs, in particular when their number is small, results in only a small decrease in average velocity. The turbulence intensity, however, increases from the laminar value of 1-2% to typically 2.5-3%. This in combination with a slight decrease in the average centerline velocity are a clear indication that turbulent structures are present. This is very similar to what we found for transition with

the fresh polymer solutions in demineralized water, but more study, e.g. measuring time-traces, is required.

Let us now look at the stability diagrams for the polymer solutions that are presented in the next section.

7.5.2 Stability measurements

In the stability diagrams we plot the critical relative disturbance velocity $v_{i,c}^*$ as a function of dimensionless wave number α^* for various Re_w values where these parameters are defined in section sec:normaliz. The diagrams have been measured for the 20 ppm and 40 ppm solutions in softened water, and the mechanically degraded 20 ppm as well as the 20 + 10 ppm solution in demineralized water. For all other solutions, we studied the the stability using one or two displacement volumes ΔV only. The reasons for this are related to time constraints as well as mechanical degradation.

Let us first discuss the $v_{i,c}^*$ vs. α^* stability diagrams for each solution separately. Then, we will compare the stability of several solutions for the case that the measurements were performed for only one or two displacement volumes.

Solutions in softened water

When comparing the stability measurements for softened water solutions of Superfloc A-110, figures 7.9 and 7.10, we see that over the entire α^* -range $v_{i,c}^*$ is higher than that of water at the same Re . The strongest stabilizing effect occurs for α^* in the range of 10 to 20. Also, stabilization is much stronger at low Reynolds numbers which may be an effect of the polymers. However, we could also speculate the it is related to the much lower natural transition Reynolds number for the polymer solutions. This is because, the disturbances that trigger natural transition and are present in the flow when the disturbance mechanism location is reached, may interact with the artificially added disturbance. Thus, the amplitude of the artificial disturbance can be lower than when no 'natural' disturbances would have existed.

Also for non-Newtonian fluids we find multiple transition points (relaminarization points are indicated by solid markers). However, the size of such areas seem to be much smaller than those found for water at higher Reynolds numbers. For Newtonian fluids, the multiple transition points at $Re \geq 30\,000$ were found for $2 \leq \alpha^* \leq 6$. For the 20 ppm solution, multiple transition points are found for $\alpha^* \approx 14$ and $\alpha^* \approx 20$ at $Re_w = 11\,600$ and $Re_w = 3\,650$ respectively. For the 40 ppm solution, however, the multiple transition points are found at $\alpha^* \approx 3.5$ for $Re_w = 9\,300$, comparable to those for Newtonian fluids. Possibly, the instability mode for the 20 ppm solution responsible for the multiple transition points is different from that for the Newtonian fluids and the 40 ppm solution.

For the second largest displacement volume, $\Delta V = 339 \text{ mm}^3$, measurements of day 1 and 2 are included and indicated with 'A' in figure 7.9b. For $Re_w = 5\,500$ and $Re_w = 7\,400$, the $v_{i,c}^*$ values measured on the second day are smaller than those for day 1, resulting in a 'zig-zag' in the curves. For smaller Re_w , the $v_{i,c}^*$ for day 2 are larger. The differences are of the order of 10%. This is larger than the reproducibility for the Newtonian stability measurements, which was of the order of 3 to 5%. Thus, mechanical degradation could play a role here. However, $v_{i,c}^*$ is rather sensitive to α^* in this area and the points of day 2 are still fairly close to the rest of the curve.

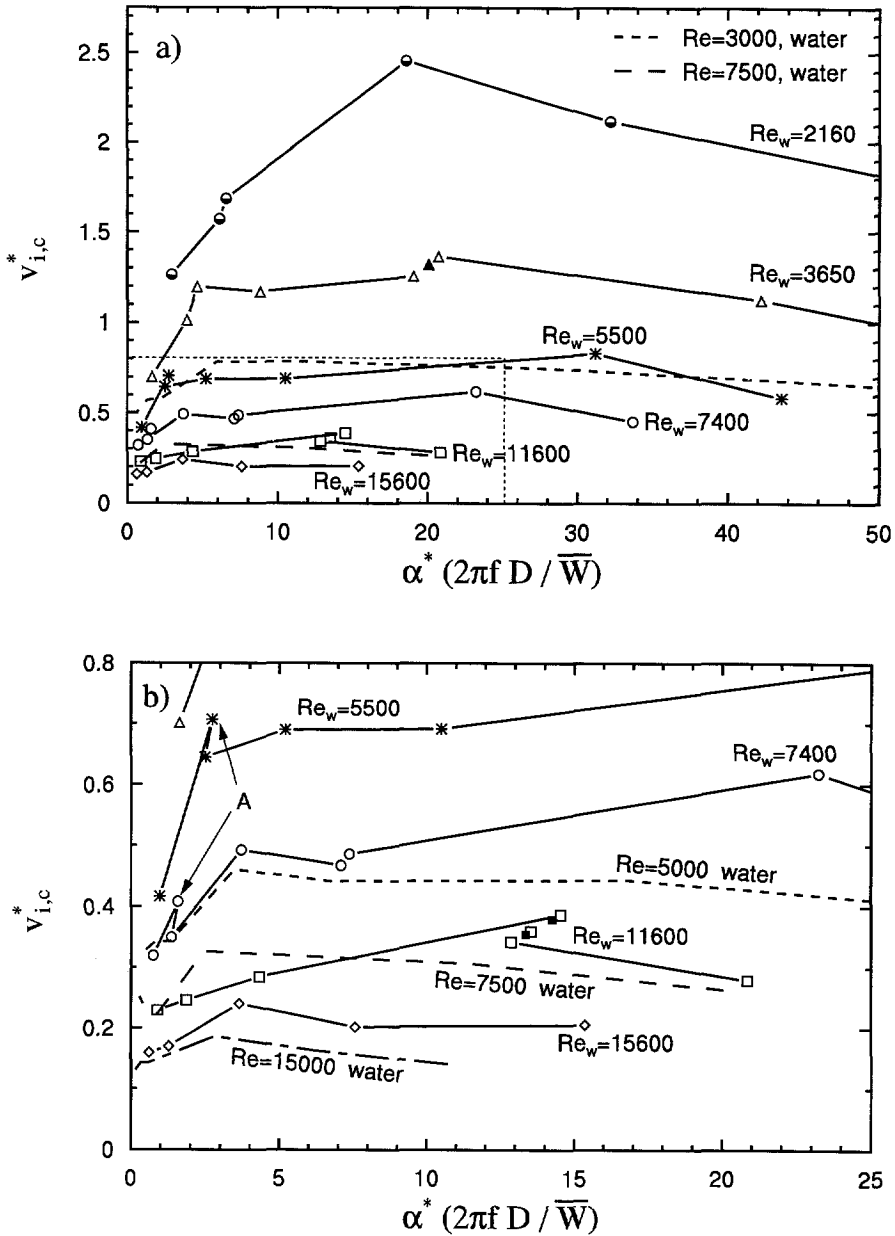


Figure 7.9: Critical relative disturbance velocity $v_{i,c}^*$ as a function of dimensionless wave number α^* for various Reynolds numbers for a 20ppm Superfloc A-110 solution in softened water. Figure b) is an enlargement of figure a). The solid markers indicate points where the flow relaminarizes if $v_{i,c}^*$ is increased. For reasons of comparison, the results for water are plotted using dotted lines.

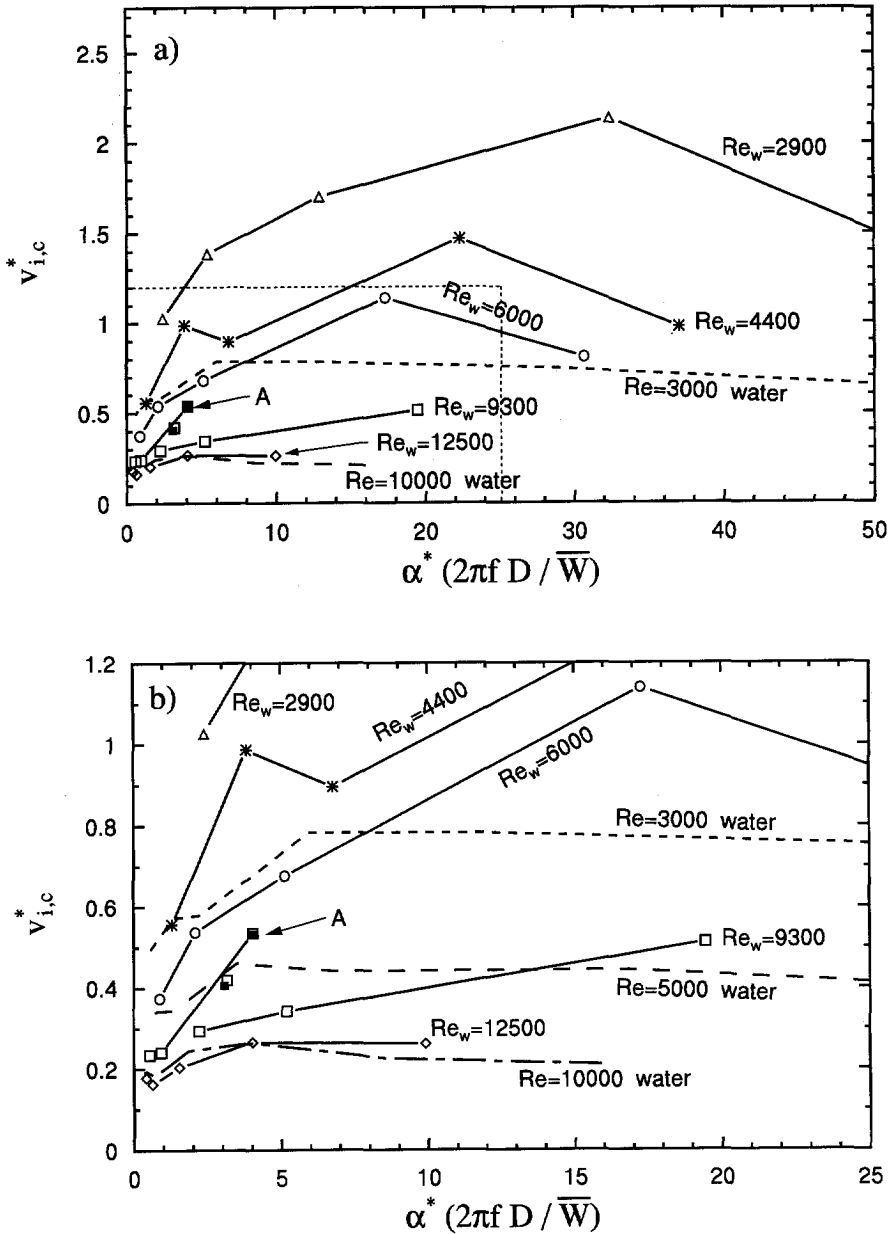


Figure 7.10: Critical relative disturbance velocity $v_{i,c}^*$ as a function of dimensionless wave number α^* for various Reynolds numbers for a 40ppm Superfloc A-110 solution in softened water. Figure b) is an enlargement of figure a). The solid markers indicate points where the flow relaminarizes if $v_{i,c}^*$ is increased. If above a solid marker no open marker is present, then the two practically coincide, as is the case with the points labeled 'A'. For reasons of comparisons, the results for water are plotted using dotted lines.

Mechanically degraded solutions in demineralized water

Due to the problems with the turbulence indicators described in section 7.5.1, only one displacement volume could be studied for the 20 ppm solution in demineralized water, the results of which will be shown later in figure 7.14. By the time this problem was recognized, the solution had degraded so much that no longer a delay in transition could be found. Before adding an extra 10 ppm of fresh polymer, the stability diagram of the degraded 20 ppm solution was measured during the 4th and 5th day and this is shown in figure 7.11.

For this mechanically degraded 20 ppm solution in demineralized water, we find a largest stabilizing effect, i.e. increased values of $v_{i,c}^*$ when compared to the Newtonian fluid, around α^* values from 10 to 20. This is comparable to the results with the polymer solutions in softened water. Above and below these values the critical relative disturbance velocities fall sharply and approach those for water. For $Re_w \approx 10\,000$ and at $\alpha^* \approx 1.5$, the polymer solution is even slightly less stable than water. Again, multiple transition points appear and they are located around the same $v_{i,c}^*$ and α^* values as for the 40 ppm solution in softened water. Also, for $Re_w = 7\,700$ and $Re_w = 10\,700$, an enhanced sensitivity of the flow at $\alpha^* \approx 1$ seems to emerge similar to what we found for Newtonian fluids for $Re \geq 30\,000$.

Based on the results given so far, we may conclude that for polymer solutions of Superfloc A-110 in softened water and in a mechanical degraded solution, larger $v_{i,c}^*$ values are found than in water, i.e. we have **stabilization**. However, it should be emphasized, that despite this stabilizing effect, the flow can still be triggered to undergo transition to turbulence. Therefore, no **delay** in transition has been found for these solutions, i.e. the minimum transition Reynolds number has not changed with respect to the Newtonian value.

Fresh solution in demineralized water

Adding 10 ppm fresh polymer solution to a degraded 20 ppm solution in demineralized water (denoted by 20 + 10 ppm) restores the smooth natural transition region as found for the fresh 20 ppm polymer solution (figure 7.6). The resulting stability diagram in dimensionless form is shown in figure 7.12. The two thick irregular lines indicate the maximum disturbances velocity that could be achieved for the present disturbance mechanism at which the flow remained nevertheless laminar. The maximum α^* that could be obtained was given by the maximum frequency of $f = 39$ Hz. This gives a maximum α^* value of 57 and 39 for $Re_w = 2\,600$ and $Re_w = 3\,600$ respectively. For smaller α^* , the thick lines roughly indicate settings where cavitation was initiated in the injection flange or where severe mechanical oscillations arose due to a large out-of-balance weight for eccentric positions of 5 mm. Even for these maximum disturbance velocities, no turbulent flow could be triggered. Only at $Re_w = 4\,100$ and larger, can the flow be triggered to undergo transition.

In other words, we have found a delay in transition for the 20 + 10 ppm solution in demineralized water till $Re \approx 4\,000$. This value is fairly close to Re at the intersection of the extrapolated turbulent line with the laminar line as we discussed in connection with figure 7.6. At Reynolds numbers for which turbulent flow can be triggered, the polymers still strongly stabilize the flow. Critical relative disturbance velocities are more than twice as large as those for water. However, for $\alpha^* < 5$ the stabilizing effect seems to decrease strongly as the Reynolds number is increased. For $Re > 6\,000$ natural transition sets in thereby limiting a triggered transition to the

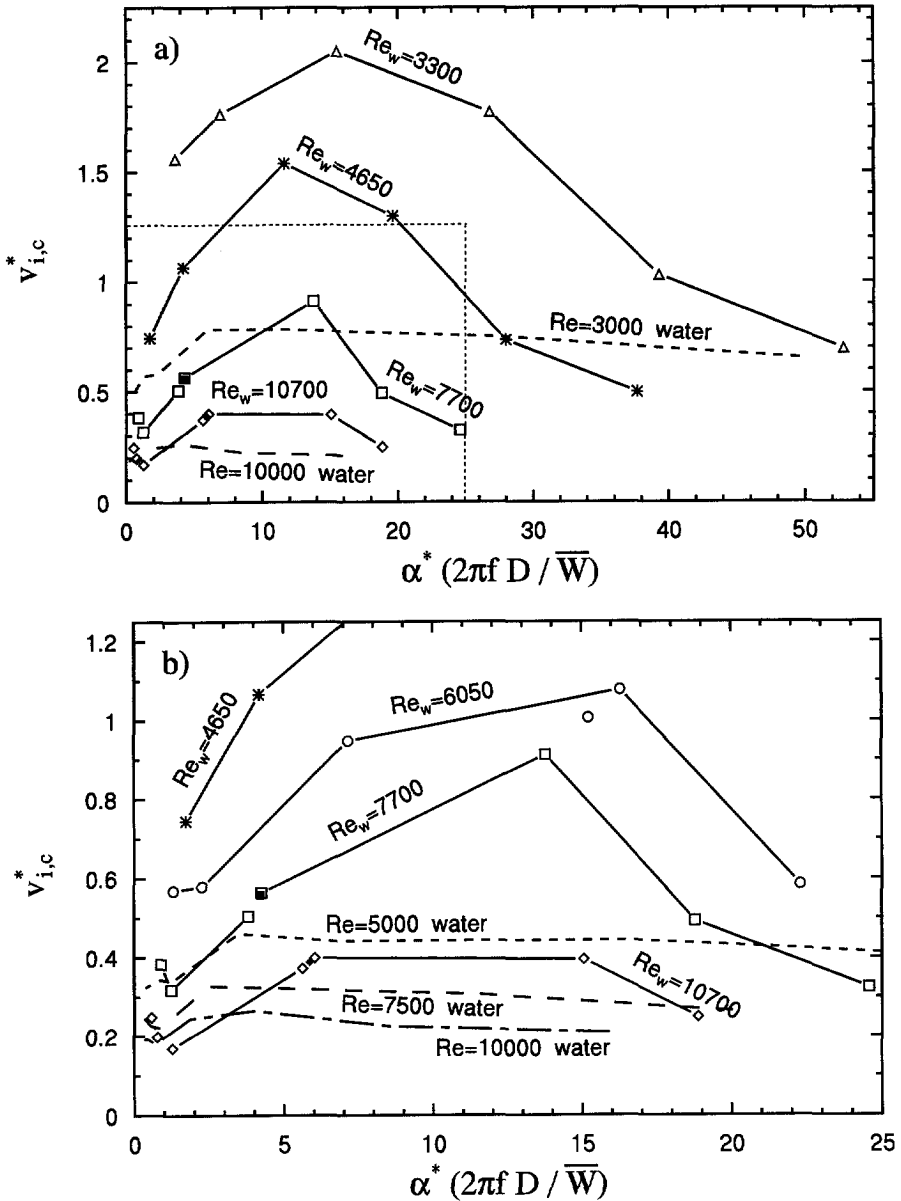


Figure 7.11: Critical relative disturbance velocity $v_{i,c}^*$ as a function of dimensionless wave number α^* for various Reynolds numbers for a 20 ppm Superfloc A-110 solution in demineralized water after circulation for 4 to 5 days. Figure b) is an enlargement of figure a). The solid markers indicate points where the flow relaminarizes if $v_{i,c}^*$ is increased. For reasons of comparison, the results for water are plotted using dotted lines.

range $4000 \lesssim Re \lesssim 6000$.

The stability diagram for the 20 + 10 ppm solution in demineralized water, in particular the measurement for $Re=4750$, shows that the Reynolds number below which no transition to turbulence could be found, is increased to a value of $Re_w \approx 4000$. This value seems to be independent of α^* , i.e. the Reynolds number to which the transition is delayed can be determined without measuring a large range of frequencies. Thus, if this is generally true, we can determine the Reynolds number below which no turbulence can be triggered, by performing a stability measurement for only one ΔV . If we are interested only in finding the minimum transition Reynolds number, performing measurement for only one ΔV saves huge amounts of time and reduces the problem of mechanical degradation.

Stability for constant ΔV

With this last remark in mind, we decided to perform the stability measurements for the 20 + 10 + 10 ppm solution in demineralized water for only two displacement volumes, i.e. $\Delta V=565 \text{ mm}^3$ and $\Delta V=174 \text{ mm}^3$. For the 20 + 10 + 10 ppm solutions with added salt, we performed stability measurements for $\Delta V=565 \text{ mm}^3$ only. The choice for these large displacement volumes is based on the observation that we can achieve the largest $v_{i,c}^*$ values in this ranges (see figure 7.12, where for a line with constant Re_w the point with the largest ΔV is the point to the left with the smallest α^*). Precisely for these small α^* values, the small $v_{i,c}^*$ values are found. This combination of a small $v_{i,c}^*$ needed to trigger transition to turbulence and the capability of disturbing the flow with very large v_i^* is advantageous. It ensures that, if transition can be triggered, we are also likely to be able to introduce a disturbance of sufficient magnitude such that transition occurs. We show the stability measurements for $\Delta V=565 \text{ mm}^3$ and $\Delta V=174 \text{ mm}^3$ in figures 7.13 and 7.14 respectively.

Comparing figures 7.13a and 7.14a, we see that the stability measurements of the 20 ppm and 40 ppm solutions in softened water almost coincide, except in the multiple transition area found in figure 7.14a. For $Re_w=10700$, we find from figure 7.13a that the mechanically degraded 20 ppm solution in demineralized water is less stable than water flows. On the other hand, for low Re_w this solution shows a strong stabilizing effect, but no delay in transition is found. However, the measurements should have been extended to lower Re_w in order to allow for an accurate estimate for the minimum transition Reynolds number. Particularly the measurements for the 20 ppm solution in softened water show no large increase in $v_{i,c}^*$ when Re_w is reduced to $Re_w=2100$. Such an increase for Re close to the minimum transition Reynolds number in Newtonian fluids has been reported by Darbyshire & Mullin (1995). This could even suggest that for the polymer solutions in softened water, the minimum transition Reynolds number is smaller than that for water, i.e. a transition enhancement. Further research is needed to disclose such possible behavior.

Figures 7.13b and 7.14b make clear that the fresh polymer solutions in demineralized water lead to a *delay* in transition. Particularly, the 20 + 10 + 10 ppm solution shows a delay in transition to $Re_w \approx 5000$. This is very close to the intersection of the turbulent data with the Hagen–Poiseuille line shown in figure 7.6. Thus, it seems that this intersection is a good estimate of the minimum critical Reynolds number for solutions in which the polymers have a stretched conformation. Above the minimum transition Reynolds number the fresh 20 + 10 ppm and 20 + 10 + 10 ppm solutions in figure 7.13b display lower $v_{i,c}^*$ values than the mechanically

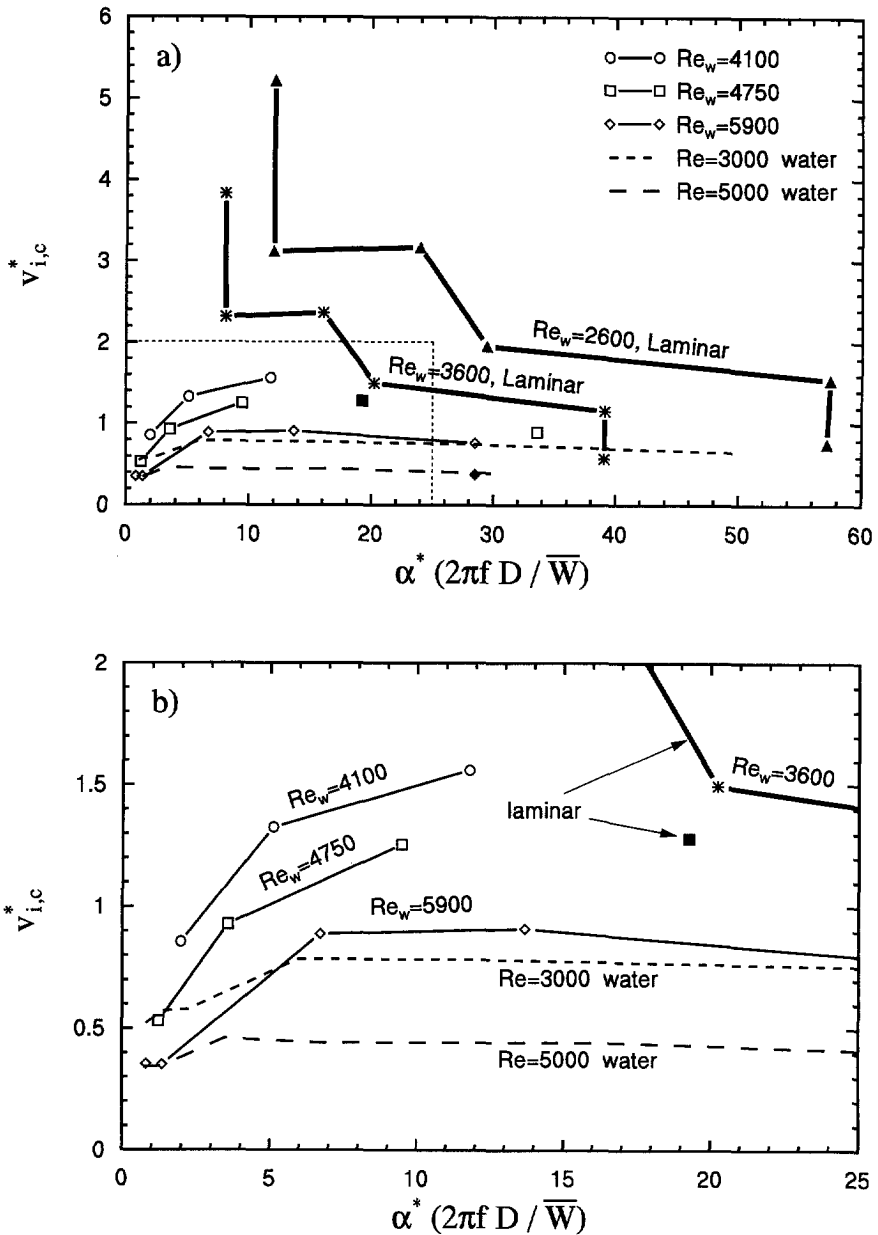


Figure 7.12: Critical relative disturbance velocity $v_{i,c}^*$ as a function of dimensionless wave number α^* for various Reynolds numbers for a 20 + 10ppm Superfloc A-110 solution in demineralized water. Figure b) is an enlargement of figure a). No multiple transition points are present and here the solid markers indicate points where the flow could not be trigger to undergo transtion due to limitations in $v_{i,c}^*$. For reasons of comparison, the results for water are plotted using dotted lines.

degraded 20 ppm solution. This could be related to the lower natural transition Reynolds number for fresh polymer solutions.

The values of $v_{i,c}^*$ for the fresh polymer solutions for which no transition could be triggered are very close to the $v_{i,c}^*$ values of the mechanically degraded solution in the measurements for $\Delta V=174 \text{ mm}^3$, as shown in figure 7.14c. For $\Delta V=565 \text{ mm}^3$, figure 7.13b, this difference is much larger, which gives more confidence in the observed delay in transition.

The stability measurements for the 20 + 10 + 10 ppm solutions with added sodium salt in figure 7.13c and d show that for the 0.001 M no transition could be triggered for $Re_w=2300$. For $Re_w \leq 7500$, the 0.001 M solution is more stable than the two other solutions containing more salt. The 0.1 M solution contains more salt than softened tap water and its stability behavior is very close to that of water, so that the polymers are apparently strongly coiled and have no stabilizing effect. For $Re_w \geq 7000$, the 0.1 M solution is more stable than water and the stabilization increases with the Reynolds number. Perhaps, the much higher shear rates at these high Reynolds numbers cause the polymers to partly stretch and slightly stabilize the fluid. Surprisingly, the 0.001 M solution (in which the polymers are certainly stretched to some extent) is less stable than the 0.01 M solution at high Reynolds numbers. This may be a result of the lower natural transition Reynolds number for 0.001 M. In this respect, it is also interesting to see that the 40 ppm solution in softened water, which has a salt content in between that of the 0.001 M and the 0.01 M solution, indeed shows stabilizing behavior in between these two added salt solution for low Reynolds numbers, as follows from in figure 7.13d.

7.6 Discussion

7.6.1 Introduction

In this chapter, we found that dissolving high-molecular-weight polymers in water, has several significant effects on its flow behavior: In particular the following points can be noted:

- The viscosity is increased for all polymer solutions of 20 and 40 ppm, even in the presence of large quantities of salt. If the polymers are stretched due to the absence of salt, we find shear thinning behavior and a zero-shear-rate viscosity of more than 15 times the viscosity of water for a 40 ppm solution in demineralized water.
- In the Moody diagram, i.e. dimensionless pressure gradient as a function of Reynolds number, the laminar data can be collapsed onto the Hagen–Poiseuille line by using the viscosity at the wall when calculating a modified Reynolds number Re_w .
- The natural transition Reynolds number is strongly reduced from more than 60 000 for water a value ranging from 8 000 to 30 000, depending on the concentration and the state of degradation of the polymer solutions. The natural transition Reynolds number is lowest for the fresh solutions in demineralized water and increases when salt is added or when the polymer solution is degraded.
- For coiled polymer solutions and degraded solutions of stretched polymers, the dimensionless disturbance velocity needed to trigger transition is larger than that found for water. We call this a *stabilizing* effect. Some indications are found, that the solutions for coiled polymers may sustain turbulent flow at Reynolds numbers lower than the minimum

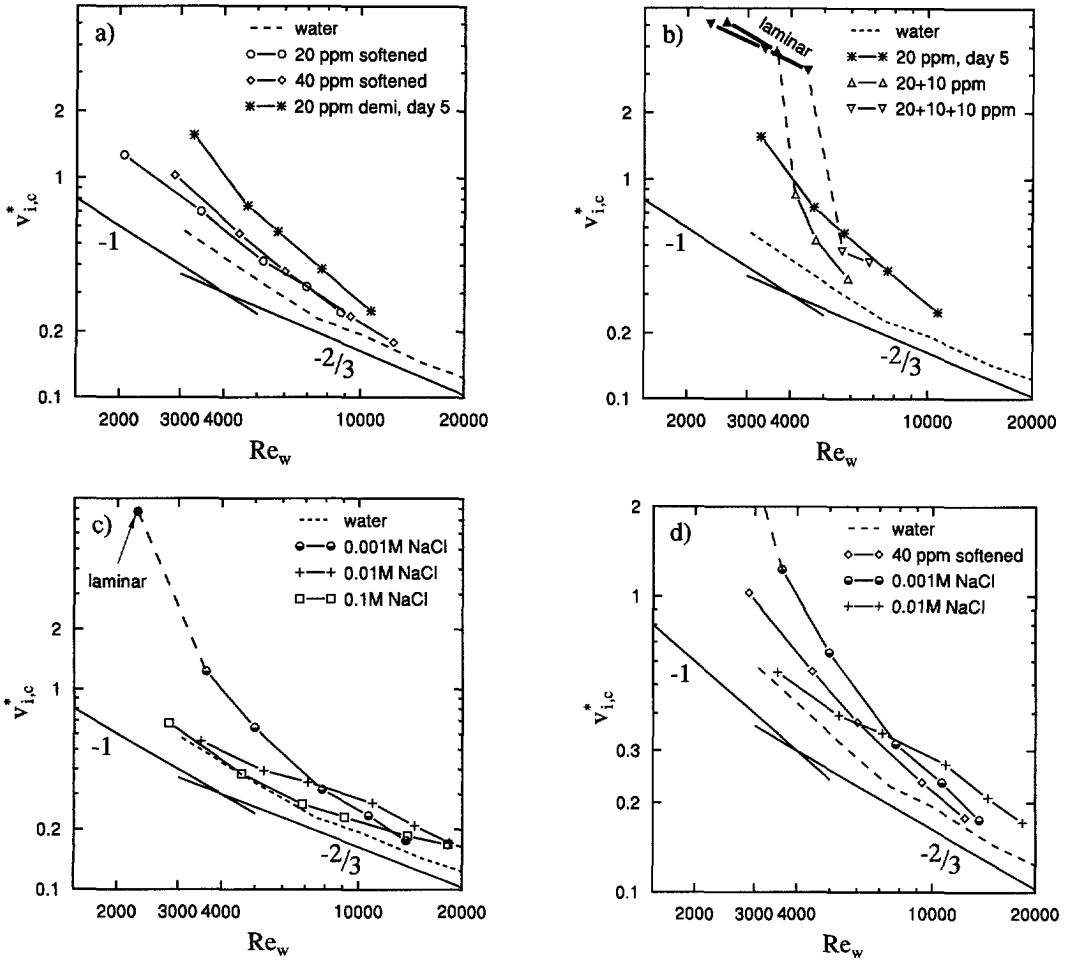


Figure 7.13: Critical relative disturbance velocity vs. Reynolds number for Superfloc A-110 solutions in various solvents for displacement volume $\Delta V=565\text{mm}^3$. No multiple transition points are present and all solid markers indicate points where no transition could be triggered at the maximum disturbance velocity available, and are labeled 'laminar'.

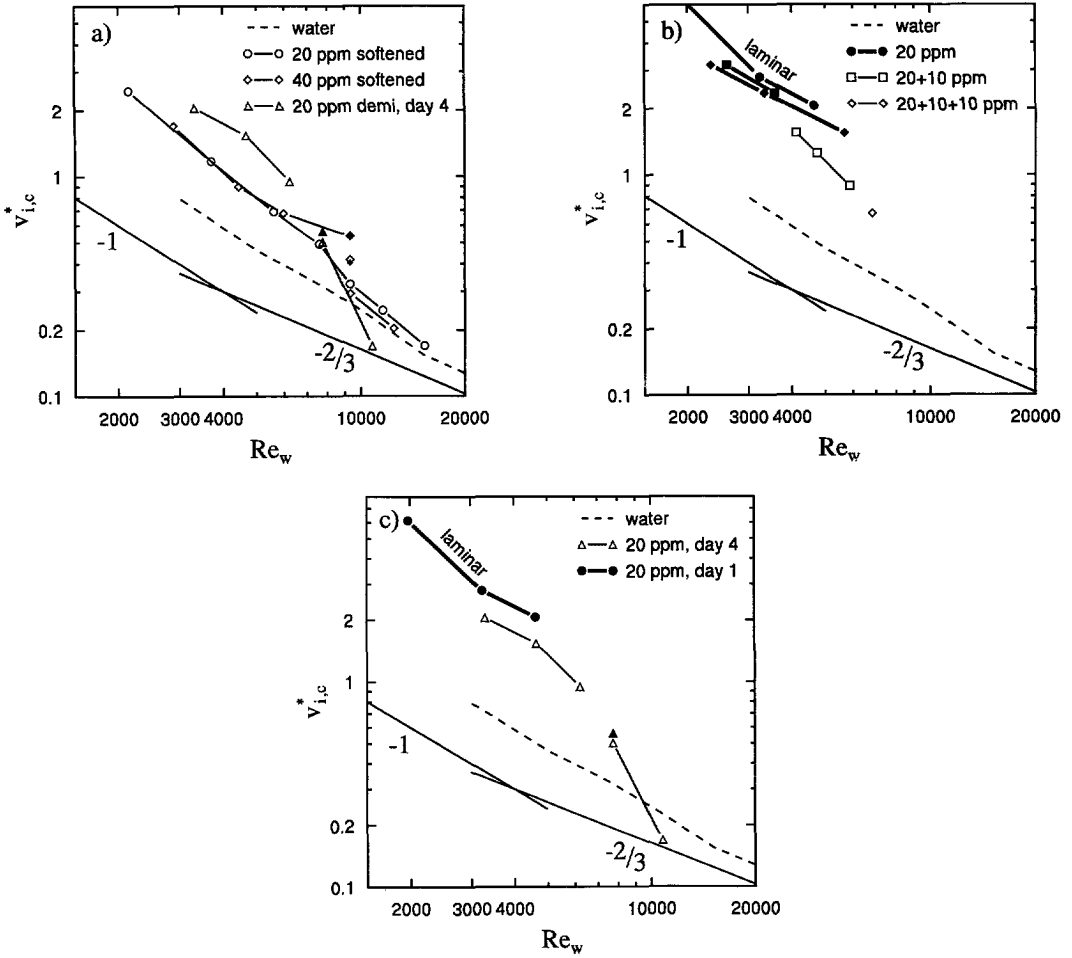


Figure 7.14: Critical relative disturbance velocity vs. Reynolds number for Superfloc A-110 solutions in various solvents for displacement volume $\Delta V=174\text{mm}^3$. Here, all solid markers labeled 'laminar' indicate points where no transition could be triggered at the maximum disturbance velocity available, and are part of a line. Any unlabeled solid markers indicate points where the flow relaminarizes if $v_{i,c}^*$ is increased in a multiple transition region.

transition Reynolds number for water. This would be a transition enhancement and more research is required to resolve such possible behavior, which would be in accordance with stability calculations of Porteous & Denn (1972b) (see also chapter 4).

For fresh solutions of stretched polymers, we find a *delay* in transition, i.e. no transition can be triggered below Reynolds numbers of approximately twice the minimum transition Reynolds number for water.

In the next section, we will discuss some possible causes for the decrease in natural transition Reynolds number. In section 7.6.3, the Moody diagrams with the points of triggered turbulence will be discussed together with some ideas on transition prediction. Finally, the consequences for practical applications are reviewed.

7.6.2 Natural transition Reynolds number

We find that polymers have a stabilizing influence on the pipe-flow stability, i.e. they can cause a delay in transition, but simultaneously cause the natural transition Reynolds number (for our experimental facility) to decrease compared to that for water. This may seem contradicting behavior, however, this is not necessarily the case. The stability of the flow is measured by adding disturbances to a fully developed pipe flow, and the result is found to be more stable than for water. The natural transition, however, is generated in the entry region of the pipe or in the settling chamber. This is the case for both the water experiments as well as the polymer experiments. This can be inferred from the behavior of the pump, because once natural transition occurs, the pressure drop in the system is increased and in order to maintain a constant flow rate, the rotational speed of the pump is increased. At the measurement location at the end of the pipe, however, the flow remains laminar for quite some time after natural transition is initiated. In other words, transition occurs near the beginning of the pipe and requires some time to be advect along our measurement section.

What could cause this decrease in natural transition Reynolds number for polymer solutions? Perhaps, the shape of the contraction is not optimal for these solutions. In abrupt contractions, flows of concentrated polymer solutions and melts form a much larger recirculation vortex than Newtonian fluids. If a small recirculation vortex is present in the polymer solutions, this could lead to a disturbed entry flow which in turn can result in an early natural transition.

Another possibility would be that the boundary layer in the entry region is less stable for polymer solutions than for water. The entry flow for water is linearly unstable above $Re \geq 9\,600$ (Tatsumi 1952). Linear and non-linear stability calculations of plane Poiseuille flow, show that adding elasticity to the fluid in the form of for example a Maxwell model, results in a destabilization of the flow (Porteous & Denn 1972a,b). In chapter 4, we showed that saturated two-dimensional nonlinear disturbances in plane Poiseuille flow exist till lower Reynolds numbers if the elasticity number of the flow is increased. All this points to a destabilization caused by elasticity. Thus, coiled polymers may lead to an earlier destabilizing behavior in the entry flow.

However, the stretched polymer solutions show an even lower natural transition Reynolds number whereas linear stability theory for rods predicts an increase in critical Reynolds number (Bark & Tinoco 1978). An explanation may be sought here in the orientation of the stretched polymers. The steady-shear viscosity measurements show that the largest time scale in the solution (associated with polymer orientation) is of the order of 5 s. Thus, the polymers may

not yet have adopted an orientation parallel to the pipe axis, unabling them to exert their stabilizing effect.

Summarizing, we conclude that the source for the decrease in natural transition number is not clear and more research is needed to clarify this topic. However, this would probably require a much better understanding of the way in which the polymers cause a (de)stabilizing effect.

7.6.3 Triggered transition in Moody diagram

Plotting the measured points for triggered turbulence in the Moody diagram together with the data for obtained without adding disturbances gives several interesting results. When studying these results, we should first recall that the key property of drag reduction is hypothesized to be the purely viscous anisotropic stress introduced by the extended polymers and that elasticity is counter productive in this stage (Toonder 1995). Thus, the so-called 'onset' of drag reduction found for coiled polymers, i.e. the value for the wall shear stress above which drag reduction begins, is likely to be related to the turbulence becoming strong enough to stretch the polymers, as is suggested by Virk & Wagger (1990). Then, above this onset point, the increase in drag reduction with an increase in Reynolds number can be explained as a greater proportion of the polymers being stretched by the turbulent flow, thus becoming effective as drag reducers. Toonder (1995)

In figure 7.15a we show the results for several 20 ppm solutions. When comparing the degraded and the fresh demineralized water solution, we can see that the turbulent data have practically the same slope. At Reynolds numbers larger than 25 000, the slope seems to decrease which may be due to mechanical degradation.

Comparing the degraded solution in demineralized water to the solution in softened water, shows that the demineralized water solution displays slightly more drag reduction for $Re \leq 10\,000$ whereas the reverse is true above these Reynolds numbers. This result may be explained as follows. In softened water, the polymers are much less extended than in demineralized water. For low Reynolds numbers, the turbulence is not strong enough to stretch the polymers in the softened water solution, thus resulting in less drag reduction than the degraded demineralized water solution. When, at higher Reynolds numbers the turbulence is strong enough to stretch the polymers, the undegraded solution in softened water shows more drag reduction since its polymers are longer than those in the degraded demineralized water solution. In figure 7.15b, we show the influence of adding salt, thus the coiling of the polymers. Clearly, the 0.1 M solution shows a higher onset-Reynolds number than the 0.01 M solution, whereas the 0.001 solution displays no onset behavior but drag reduction as soon as the flow becomes turbulent. This is in accordance with the coil-stretch transformation hypothesis.

For the fresh polymer solutions in demineralized water shown in figure 7.16, the triggered points show a quite different behavior. The measured friction factors for the triggered transition (solid markers) are much higher than what is expected from extrapolation of the turbulent data obtained without any added disturbances (open symbols). The triggered transition points represent the maximum pressure drop that was found for a ΔV - Re -combination as a function of disturbance frequency. For the degraded and salty solutions, we did find a plateau-region in the turbulent pressure drop for large disturbance frequencies. For the fresh demineralized water solutions, this was not the case. The measured pressure drop increases with increasing frequency

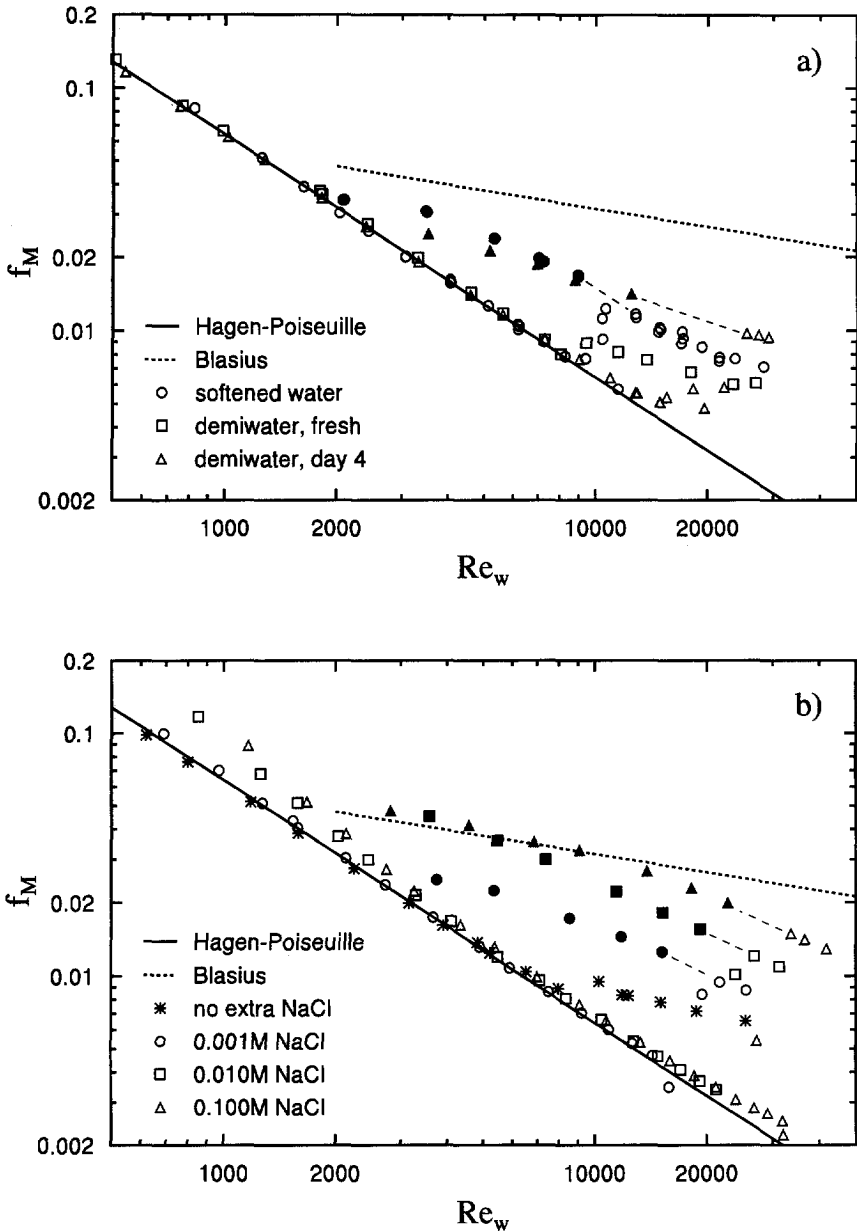


Figure 7.15: Moody diagram for several solutions of Superfloc A-110. The solid markers represent the measurements were transition is triggered by adding a disturbance and the open symbols denote measurements without any artificial disturbance added. Figure a) shows several 20 ppm solutions and figure b) shows the influence of salt on the flow behavior of the 20 + 10 + 10 ppm solution in demineralized water. The dashed lines are to guide the eye and connect the adjacent points with and without an added disturbance.

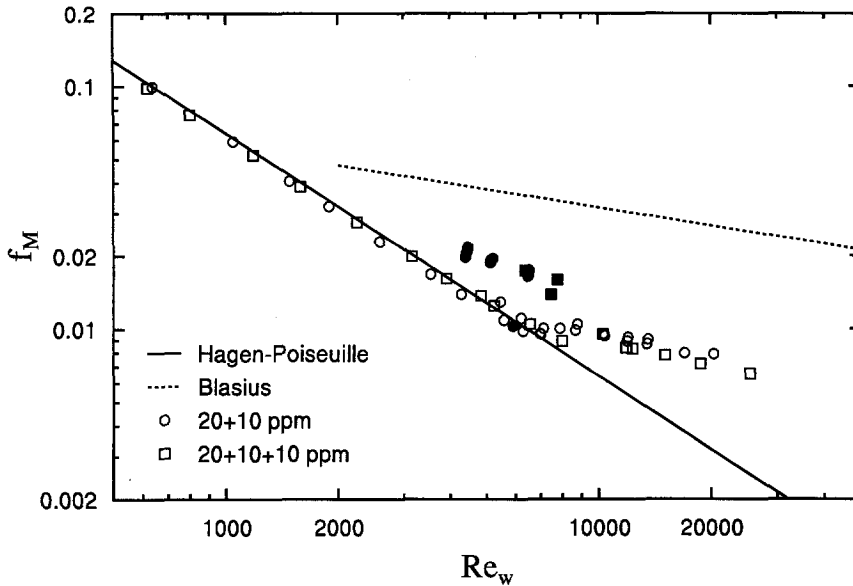


Figure 7.16: Moody diagram for two fresh Superfloc A-110 solutions in demineralized water. The solid markers indicate points where transition is triggered by adding a disturbance and the open symbols denote measurements without any artificial disturbance added.

(and thus increasing disturbance velocity). Very often, it reaches a maximum and decreases again after the frequency is increased further, in particular, for Reynolds numbers close to the minimum transition Reynolds number. All this may indicate that the flow is still developing and may even decay to a laminar flow when given enough time. That developing lengths can be increased for non-Newtonian fluids in comparison with Newtonian fluids is reported by Bewersdorff (1991). He used surfactant solutions forming rod-like micelles and found that as much as 280 diameters are needed to generate a fully developed turbulent pipe flow for these fluids, which is much larger than the $40\text{--}100D$ recommended for Newtonian fluids.

Thus, if the triggered transition points (solid markers) in figures 7.13 and 7.14 indeed represent turbulent flows which are still decaying, we underestimated the minimum transition Reynolds numbers for these cases, possibly bringing the minimum transition Reynolds number closer to that of the intersection between the laminar and the turbulent lines. Further research is necessary to establish this.

If this intersection is indeed a good estimator for the minimum transition Reynolds number, it would be interesting to find out if, for fully stretched polymers, the turbulent data follow the slope of the Blasius line and how we can predict the amount of the drag reduction in relation to the polymer properties. This would then enable us to predict the non-Newtonian transition point for stretched polymer solutions. In this respect, the work of Wang (1972) is worth noting. He used a two-parameter empirical formula to correlate drag-reduction data and he then related these two parameters to the rheological properties of the polymer solution through a molecular argument.

7.6.4 Applications

We have shown that stretched polymers lead to a delay in transition whereas coiled polymers give only a stabilizing effect. Mechanical degradation eliminates the delay in transition, indicating the importance of a high molecular weight of the polymers. When in practical applications, transition has to be avoided, it is important to use polymers that are stretched. However, in practice, very often mechanical degradation is severe and many other chemicals are present. For example, when drilling for oil or gas, a layer of salt may be present. When the salt dissolves, the PAMH polymers that we used would coil up which would destroy the delay in transition. Therefore, high-molecular weight polymers should be developed which are relative insensitive to mechanical degradation and chemicals which can be expected to be present in the flow of a particular application.

When drilling for oil, high pressure drops have to be avoided in the annulus between the drill pipe and the wall of the drilled hole. For such an application, it is important to also look at the relationship between the pressure drop and the flow rate. Considering only the friction factor as a function of a modified Reynolds number is not sufficient, since the stretching of the polymers results in a large increase in viscosity, which would lead to a corresponding increase in pressure drop. The pressure drop as a function of flow rate is shown in figure 7.17 for several concentrations of salt. For low flow rates, and thus laminar flow, figure 7.17b shows that the solution in demineralized water with no added salt gives the largest pressure drop due to its high viscosity. However, the triggered turbulence lines for the 0.01 M and 0.1 M show larger pressure drops than the solution without added salt for $Q \geq 5501/h$, and similarly for the 0.001 M solution for $Q \geq 8501/h$. The solution without added salt, is laminar for $Q \lesssim 20001/h$ and changes smoothly to a turbulent pressure drops.

Therefore, if only the pressure drop is important, the solution with no added salt is the best choice for large flow rates, despite the higher viscosity. Also, in drilling fluids, viscosifiers are added so that an increase in viscosity caused by the stretched polymers can be compensated by adding less viscosifiers.

It is remarkable, that the 0.001 M as well as the 0.01 M solution have their natural transition point at $Q=30001/h$. Surprisingly, at the same Reynolds number, the 0.1 M solution, shows one point during which one short turbulent slug was recorded. The actual natural transition point for this solution is however located at $Q=36001/h$. This suggests that around $Q=30001/h$, the flow is extra sensitive to some unknown cause. Furthermore, for a long time, the natural transition Reynolds number for water was also located near the same flow rate. Thus, the reduction in natural transition Reynolds number after adding polymers to the water, may very well be related to an interaction between an artifact of the experimental facility and the polymer solution flow. Again, more interesting work can be done in this direction.

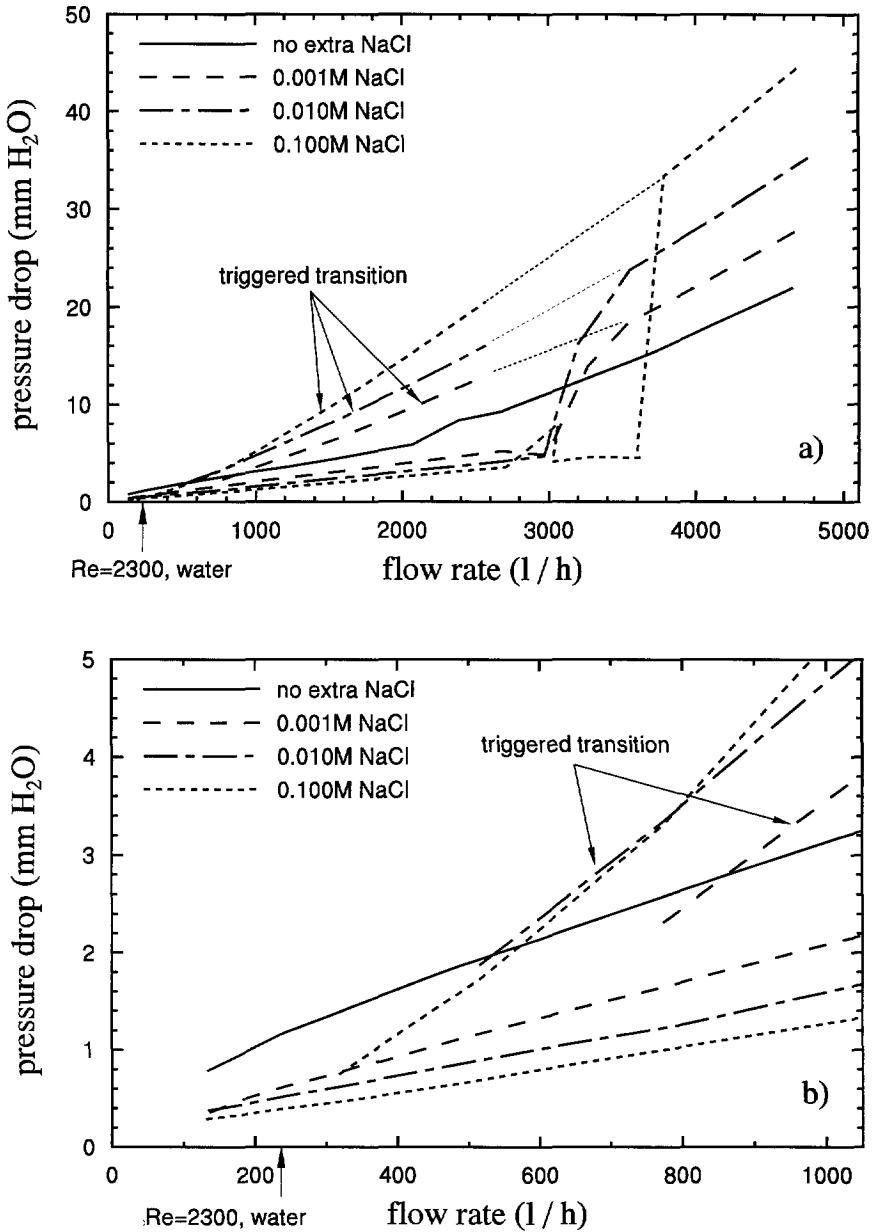


Figure 7.17: Measured pressure drop as a function of flow rate for the 20+10+10 ppm solution in demineralized water with various concentrations of sodium salt. Figure b) is an enlargement of figure a) in the low flow rate region.

Chapter 8

Main conclusions and discussion

The results presented in this thesis constitute, as far as we are aware, the most extensive comparison between the transition of laminar pipe flow for Newtonian and non-Newtonian fluids. By adding a controlled periodic disturbance to a laminar flow, we have determined the magnitude and frequency of the disturbance that is needed to trigger transition for a wide range of Reynolds numbers. This has given us information on the instability scenario at various Reynolds numbers in a Newtonian fluid. At low Reynolds numbers, our results are consistent with earlier measurements, e.g. those of Wygnanski & Champagne (1973) and Darbyshire & Mullin (1995). At higher Reynolds numbers, for which only few results are known, we have found surprising and also new phenomena. For a non-Newtonian fluid we have studied the influence on transition of the polymer conformation, which we varied between randomly coiled (on the average) and extended (on the average).

In this final chapter, we recapitulate the most important conclusions and discuss them in the context of the existing literature on transition. We also suggest several possible directions for future research in this fascinating field of fluid mechanics.

With respect to the main area of application discussed in the introduction, i.e. the use of non-Newtonian drilling fluids in oil exploration, our main conclusion is that polymers in the fluid need to have an extended conformation in order to be able to delay laminar-turbulent transition to higher Reynolds numbers.

For a more detailed review of the results that we have obtained in this study, we organize the conclusions in the same way this thesis is structured. Before discussing the results, we should first give a definition of the terms 'stabilization' and 'delay' that we use when comparing the results for Newtonian and non-Newtonian fluids. When comparing stability calculations, we use the term stabilization to indicate that in non-Newtonian fluids the disturbance has a smaller growth rate at the same Reynolds number or to indicate that an instability mode exists at lower Reynolds numbers for the Newtonian fluid than for the non-Newtonian fluid. When we discuss transition experiments, we say that the polymers have a stabilizing effect when at identical Reynolds numbers, a larger disturbance is needed to trigger transition to turbulence. The polymers are said to cause a delay in transition, when the Reynolds number above which the flow can become turbulent is larger for the polymer solution than for the Newtonian solvent.

Nonlinear stability of plane Poiseuille flow

Linear stability calculations for the simplest visco-elastic fluid, the i.e. Upper Convected Maxwell (UCM) model in a plane Poiseuille flow, show that the critical Reynolds number above which linear disturbances can grow decreases strongly with elasticity. In contrast, Porteous & Denn (1972b) have speculated by extrapolating the results of their weakly nonlinear stability calcula-

tions, that for larger disturbances, elasticity has a stabilizing effect. Our stability calculations of very large saturated 2-D disturbances show that this is not the case, at least not for the amount of elasticity studied by Porteous and Denn. The influence of elasticity can be quantified by the Weissenberg number, We , which is defined as the ratio of the relaxation time of the fluid and the flow time scale. So in terms of the Weissenberg number our results show initially destabilization as a function of We . When the elasticity is further increased till the Weissenberg number approaches unity, the critical Reynolds number for which saturated nonlinear disturbances exist, continues to decrease. However, for $We \geq 1.0$ the critical Reynolds number begins to increase again, which can be interpreted as a stabilizing effect of strong elasticity. Nevertheless, the critical Reynolds number for all our computations ($E \leq 10^{-3}$ or $We \leq 2.15$) remains smaller than the corresponding value for Newtonian fluids. Similar behavior of the critical Reynolds number as a function of We has been found for linear disturbances (Sureshkumar & Beris 1995b) but their minimum is located at much higher Weissenberg numbers ($We \approx 4$). Although the existence of saturated 2-D disturbances for UCM fluid flow has been demonstrated previously and although 3-D numerical simulations of UCM fluids have been attempted (Maulik 1989, Sureshkumar & Beris 1995a), this is, as far as we know, the first time that the range of Reynolds number – wave number combinations for which these 2-D nonlinear disturbances exist has been investigated systematically.

The computations show that in the range where the critical Reynolds number increases with We , i.e. $We \geq 1$, large elastic stretching in the direction of the flow occurs in the wall region. When translated to polymer behavior, this indicates that polymers are stretched near the wall which results in a stabilizing effect. That polymers can stretch in laminar flows is supported by numerical simulations of a FENE-bead spring polymer model in uniaxial, shear flows, and in the viscous sublayer of a turbulent flow. These calculations show that the polymers are stretched if the time constant of the polymer is large enough compared to the rate of shear at the wall (Massah *et al.* 1993).

Experimental pipe-flow facility

In an early phase of our investigation, it became clear that it was necessary to build an experimental pipe-flow facility, especially suited for our transition studies. We have chosen for a recirculatory pipe-flow facility with water as working fluid. All of the large-scale pipe-flow facilities that have been built up to now to investigate laminar-turbulent transition are of the non-recirculatory type. Our facility allows laminar flow up to $Re > 60\,000$ even in a recirculatory facility. The study of transition requires that the flow be free of natural disturbances. This requires a very careful design of the pipe and the in particular of the settling chamber and entrance conditions. However, there are also other sources of disturbances.

Just as many other investigators before us, we found that the flow is very sensitive to temperature differences between the water and the ambient air. A combination of temperature control, insulation, and a special design of the settling chamber greatly reduced this problem. In addition, we found, perhaps somewhat surprisingly, that in our pipe setup the rotation of the earth distorts the laminar (theoretically parabolic) velocity profile beyond recognition for a Reynolds number larger than $\pm 5\,000$. The physical background is that in a fully developed pipe flow, the Coriolis force should be balanced by the viscous force. Although the Coriolis

force of the earth's rotation is small, the viscosity of water is also small so that the result is non-negligible. A method to weaken the influence of the Coriolis force would be by increasing the viscosity. Whether or not the Coriolis force has any effect on the stability remains unclear¹ at this stage. However, the stability measurements do not show a change in behavior when the velocity profile is strongly deformed by the Coriolis force at high Reynolds numbers. Also, no obviously different behavior can be discerned when the pipe is too short for the flow to become fully developed, i.e. $Re \geq 14\,300$, which is in agreement with finding by Darbyshire & Mullin (1995). This could suggest that the most important factor is a laminar base flow with a roughly convex shape rather than a parabolic velocity profile. It would nevertheless be a good idea to study this insensitivity of transition to the profile shape in more detail. This could be done by increasing the viscosity of the water, e.g. by adding glucose or glycerine for example. Alternatively, air can be used which has a kinematic viscosity which is 15 times higher than that for water. In our facility, this could be done by placing disconnecting the fluid pump and placing a blower in front of the settling chamber.

Newtonian pipe-flow stability

With the experimental setup discussed above, we have studied the stability of pipe flow to non-axisymmetric periodic disturbances for a large range of disturbance magnitudes, for $1\,800 \leq Re \leq 50\,000$, and for $0 \leq f \leq 40$ Hz. Here, Re is the Reynolds number based on bulk velocity and pipe diameter and f is the frequency of the disturbance. For $Re \lesssim 20\,000$, the flow has been found to be almost insensitive to the disturbance frequency or alternatively to the dimensionless wavenumber α^* . Only for $\alpha^* \lesssim 5$, do we find a decrease in the dimensionless disturbance velocity $v_{i,c}^*$, an effect which is stronger for at Re . For $Re > 20\,000$, we find an increased sensitivity to disturbances with $\alpha^* \lesssim 1$, an effect that becomes more pronounced at higher Reynolds numbers. There are indications that this different behavior is related to a second instability mode but no detailed measurements could be done to confirm this. For $Re \geq 30\,000$ and α^* varying from 2 to 6, we have found multiple transition points: This means that, when at constant α^* we increase $v_{i,c}^*$, we find a transition to turbulence at the lower critical value $v_{i,c}^*$, relaminarization at a larger $v_{i,c}^*$ and a second transition occurs at the upper critical value, above which the flow remains turbulent. A possible explanation of this effect is that it may be related to an interaction between the artificially imposed disturbance and the very small natural disturbances that are present in the flow and which trigger natural transition at $Re > 60\,000$. A possible way to confirm such an explanation would be to introduce another disturbance upstream of the present one and study the interaction of both disturbances. However, in our opinion other influences also play a role. Therefore, we would suggest to carry out detailed measurements of the flow using Laser Doppler Velocimetry (LDV) techniques. These may reveal the nature of the multiple transition points and the increased sensitivity around $\alpha^* \lesssim 1$. However, a disadvantage of LDV is that it gives only velocity information at one point in the flow, while transition to turbulence is governed by very dynamical processes with a complicated spatial structure. Particle Image Velocimetry (PIV) is therefore potentially a very valuable technique for transition research as it provides velocity information in a plane or even a volume of the flow as a function of time (Westerweel

¹Some preliminary DNS calculations for linear center-mode disturbances show that the decay rate increases under influence of the Coriolis force, i.e. the flow becomes more stable to linear disturbances. (Private communication H. Shan 1996).

1993, Draad *et al.* 1995). Furthermore, PIV permits direct comparison between experimental results and those obtained by direct numerical simulation (DNS). In our opinion observation of spatial flow patterns would be a first step towards new theoretical developments and a better understanding of the mechanisms governing transition.

For $\alpha^* \geq 5$, we found that the critical disturbance velocity $v_{i,c}$ is practically independent of the Reynolds number, i.e. $v_{i,c}^*$ varies according to Re^{-1} . For $\alpha^* \leq 2$, however, the disturbance velocity $v_{i,c}^*$ depends on the Reynolds number according to $Re^{-2/3}$. This latter result is in agreement with theoretical studies (Davey & Nguyen 1971, Sen *et al.* 1985). The neutrally stable 3-D nonlinear disturbance introduced by Smith & Bodonyi (1982) obeys a scaling of $Re^{-1/3}$ and is not in agreement with our findings but it should be mentioned that the shape of their helical wave disturbance is quite different from the one we have applied. Development of a mechanism that generates a disturbance with the proper azimuthal wave number dependence, rather than the oscillating non-axisymmetric disturbance that we used in the present investigation, may help to check whether the disturbance proposed by Smith & Bodonyi exists. Such an experiment would also be closer to the instabilities investigated by Davey & Nguyen (1971) and Sen *et al.* (1985)².

Comparison of the critical parameters for the generation of puffs ($Re \lesssim 2700$) and turbulent slugs at low Reynolds number values ($Re \approx 3000$) reveals that these are practically identical. This could suggest that puffs and turbulent slugs ($Re \gtrsim 3000$) are produced through a similar mechanism. This agrees with findings by Rubin *et al.* (1980) who show that merging of puffs leads to the formation of turbulent slugs. It would be interesting to see whether or not every turbulent slug originates from puffs. A method to study this would be by using PIV at several locations downstream of the disturbance injection location.

In this present study, we have concentrated on the determination of the parameter combinations for which laminar-turbulent transition occurs and to estimate the scaling of the critical disturbance with the Reynolds number. With this information now available, we are in an excellent position to proceed to make a contribution to the theory of transition to turbulence. The largest problem obstructing theoretical progress, is the fact that until now all linear stability modes have been found to be stable. However, numerical simulations have shown recently that linearly stable disturbances can grow four to five orders in magnitude before decay sets in (O'Sullivan & Breuer 1994a). This is caused by a mechanism known as transient growth. At this stage it is not clear whether transient growth can explain the large gap between stability theory and experiments on pipe-flow transition, but nevertheless it would be a promising route to explore. Transient growth theory and simulations show that the largest growth occurs for wave numbers approaching zero. This agrees with our experiments, where we find that the flow is indeed most unstable to disturbances having a small wave number. Also, the relative insensitivity of the dimensionless disturbance velocity $v_{i,c}^*$ to α^* for $\alpha^* \gtrsim 5$ could be related to pseudo-resonance, i.e. large transient growth can occur even when the wave number is far from the value for optimal growth (Trefethen *et al.* 1993). Experimental investigation of transient growth is needed to verify the predictions from the numerical simulations. Our pipe-flow facility seems well equipped for such studies.

²Suggestions with respect to the construction of such a mechanism can be found in Aanen (1995).

Non-Newtonian pipe-flow stability

Dissolving minute amounts of high molecular partially hydrolyzed polyacrylamide (PAMH) in water has a huge effect on the flow behavior. In demineralized water, water without dissolved salts, PAMH is forced to have, on the average, an extended conformation and the viscosity for low shear rates can be increased more than ten times for a 40 ppm solution. Also at these concentrations shear thinning is significant. Adding a small amount of salt causes the polymer to coil up. This results in a large decrease in viscosity and the shear thinning more or less disappears. Nevertheless, the change in viscosity, with respect to demineralized water, is still considerable and cannot be disregarded. To account for the changing shear viscosity of the polymer solution, we use in the definition of the Reynolds number the viscosity at the wall. This gives very satisfactory results, viz. the laminar flow data collapses to the Hagen-Poiseuille line for water. Another advantage of the use of the wall viscosity is that it can be applied in both laminar and turbulent flows.

In addition to the change in viscosity, the polymers also strongly reduce the natural transition Reynolds number from $Re > 60\,000$ for water to approximately 8 000 for a fresh polymer solution with an extended conformation and to 30 000 for degraded as well as coiled polymer solutions. Similar effects have been reported by Paterson & Abernathy (1972). It is assumed that the natural transition originates from disturbances introduced in the entry section of the pipe or at the contraction. However, the cause for the reduction in natural transition Reynolds number by the polymers is unsolved. One could speculate that the polymers change the flow in the contraction or have a destabilizing effect on the developing boundary layer in the entrance region of the pipe, perhaps similar to the destabilizing effect which elasticity has in a plane Poiseuille flow of the UCM fluid, that we discussed above. Further research is needed and for instance measurements of the velocity fields in the entry section of the pipe may bring to light what causes for the reduction in natural transition Reynolds number.

Although the polymers reduce the natural transition Reynolds number, our forced stability experiments show that larger disturbances are needed to trigger the transition to turbulence. This means that the polymers have a *stabilizing* effect on *developed* pipe flow. The stabilizing effect decreases with the concentration of salt in the water. In other words, the more the polymers are forced to have, on the average, a coiled conformation the smaller their stabilizing influence becomes.

However, for randomly coiled polymers no *delay* in transition is found. In order to delay the transition, the polymers have to be forced to have, on the average, an extended conformation. This is consistent with findings by Virk & Wagger (1990) but they do not seem to have noticed the delay in transition as they concentrated on the effect of drag reduction. Our experiments suggest that the delay is mainly caused by the longest polymer molecules. This was inferred from the observation that once the polymers have degraded, the delay in transition disappeared. This is in agreement with White & McEligot (1970), who find that the delay in transition is dominated by the higher molecular weight polymer in a mixture of polymers.

Transition prediction?

Given the experimental data collected in this study and of which the results have been summarized in the previous sections, one may ask whether it is possible to explain to results that have been reported in the literature. Previously, a delay in transition for polymer solutions has

been mainly reported in small diameter pipes, usually smaller than 1 cm (e.g. Castro & Squire 1967, Chung & Graebel 1972, Rochefort & Middleman 1985, and Bewersdorff & Singh 1988). These results were found both for extended as well as coiled polymers, which seems surprising in the light of our own experiments. An explanation can be given using scaling concepts. We have already introduced the Weissenberg number (We) as the ratio of the relaxation time of the polymer to the time-scale of the flow:

$$We = \frac{U\lambda}{D} = Re \cdot E = Re \cdot \frac{\eta_0\lambda}{\rho D^2}$$

From this equation it is clear that when for a given fluid and Reynolds number the pipe diameter is decreased, the Weissenberg number will rapidly increase. Moreover, from our strongly nonlinear stability calculations for a UCM fluid in 2-D plane Poiseuille flow we found that the influence of polymers is stabilizing beyond $We \approx 1$. Let us use this criterion also for a delay in transition, we then find that a delay in transition occurs only when $We=1$ occurs before the lowest transition Reynolds number $Re \approx 2300$. Thus, in small diameter pipes the polymers are likely to be stretched sufficiently by the laminar shear flow to lead to a delay in transition. Recently, a numerical simulation using a FENE-bead spring polymer model has shown that stretching of a coiled polymer in shear flows can indeed occur when the time scale related to the shear rate at the wall is smaller than the relaxation time of the polymer (Massah *et al.* 1993).

Extending these arguments to the large body of available literature on drag reduction gives also an explanation why in most of these experiments, no change in transition Reynolds number is reported. The vast majority of drag reduction experiments have been carried out in relatively large pipe diameters in which the shear rate at the wall is insufficient to uncoil the polymers. The transition to turbulence then occurs at the same value as for Newtonian fluids. Once the turbulence becomes 'strong' enough so that it can stretch the polymers, drag reduction begins. This occurs at a so-called onset Reynolds number. The importance of stretched polymers for drag reduction has also been shown demonstrated by den Toonder (1995). The importance of extended polymers for a delay in the transition Reynolds number is also supported by linear stability theory and experiments with long fibers. It appears from the results of linear stability theory that fibers have a stabilizing effect on plane Poiseuille flow (Landahl 1973, Bark & Tinoco 1978). This is confirmed by experiments (Vaseleski & Metzner 1974), who show a delay in transition to $Re > 16\,000^3$ for a 5 000 ppm solution of asbestos fibers. We should note here that this stabilizing effect of fibers is opposite to the destabilizing effect of elasticity, as discussed in section 3.2.3.

However, the results discussed above do not seem to be the total picture. We find a delay in transition in our (large diameter) pipe only when the polymers are extended and fresh, i.e. undegraded (viz. having a very large molecular weight). In such cases, the characteristic jump in friction factor normally present during transition is practically absent. Despite the smooth contraction and our careful pipe construction, the flow cannot be kept laminar above this transition point. In this case, the minimum transition Reynolds number is thus equal to the

³Their data show a delay to $Re > 2 \cdot 10^5$ but they did not correct the data for the increase in viscosity. Estimating the viscosity from the shift in the Moody diagram gives a viscosity increase by a factor of 12 compared to the solvent.

maximum transition Reynolds number which is in sharp contrast with the results for Newtonian pipe flow and to a lesser extent for coiled and degraded polymer solutions. Somehow, the extended polymers seem to delay transition but at the same time generate their own instabilities. The transition Reynolds number for such behavior is denoted as $Re_{\min/\max}$. If such behavior were to scale with the Weissenberg number, then we could shift $Re_{\min/\max}$ to lower values by using very small pipe diameters or by increasing the viscosity. This is precisely what has been found by e.g. Forame *et al.* (1972) and Zakin *et al.* (1977) and is known as 'early turbulence'. Forame *et al.* show that the onset wall shear stress for early turbulence varies slightly with the polymer concentration and depends almost linearly on the viscosity, i.e. the shear rate at the wall is constant whereas the critical Reynolds number varies between 600 and nearly 2000. This suggests that a delay in transition for extended high molecular weight polymers can only be found in large pipe diameters. Further research is required to confirm the suggested scaling.

To try to formulate scaling rules for fiber suspensions based on a ratio of time scales is rather difficult. As can be seen from the equation 3.4 (40), the equation describing the stresses in fiber suspensions is fully viscous and contains no characteristic time constant such as for the UCM fluid. The parameter B describing the stability behavior of fibers (equation 3.5) contains only the aspect ratio of the fiber and the volume fraction occupied by the fibers. Thus, although fiber suspensions and extended polymers show similar behavior with respect to drag reduction and transition to turbulence, the difference in the equation for the stresses points to a fundamental difference which is likely to be important when searching for scaling rules describing transition to turbulence.

Applications

Although the results that have been obtained so far are rather fundamental in nature, several useful implications for practical applications can be deduced. Since this project has been started to predict the pressure drop in the flow of drilling fluids, we will somewhat tailor our remarks to this area.

We have seen that a delay in transition to higher Reynolds numbers can be achieved only by using high molecular weight polymers that have an extended conformation. Also, these polymers are highly effective as drag reducing agents in turbulent flow and the jump in pressure drop related to laminar-turbulent transition of Newtonian fluids is virtually absent. As a result, the pressure drop is relatively small in both laminar as well as turbulent flow and this reduces the need to maintain laminar flow in those situations where small pressure losses are required. However, chemical and mechanical degradation will quickly reduce the delay in transition and also the drag reduction capability of the polymer solutions. Thus, for practical applications, a careful choice of the polymer type is essential and depends on for example the amount of salt dissolved in the fluid (drilling through salt formations, formate muds!, i.e. muds containing very high concentrations of formate salts as weighing material to increase the fluid density). Development of high molecular weight long-chain polymers that are relatively insensitive to chemical and mechanical degradation is an interesting option to pursue. Another interesting alternative would be to use surfactants (surface active agents) that form rod-like micelles (Sabadell 1988, Bewersdorff 1990). These micelles are also subject to mechanical degradation but they can recuperate when given time, e.g. in the reservoir. However, the fact that some of the surfactants are toxic limits their use for practical applications. Also,

discharging may lead to the forming of huge amounts of foam, which can be unacceptable. Thus the choice for the type of surfactant to be used should be taken with great care.

With respect to the drilling process, it should be noted that the cooling capacity of polymer solutions is much smaller due to the large reduction in heat transfer (Matthys 1987).

Despite the advances that we have made in our study, we must confess that an accurate prediction of the transition Reynolds number and the amount of drag reduction is still lacking. The principle problem is that there is no adequate theory describing the process of transition in a pipe flow, for either Newtonian or non-Newtonian fluids. Scaling rules are likely to be the only candidates for some time to come that can bring order into the limitless number of combinations of polymer type, pipe diameter, concentration, salt content, and so on. Since for both transition and drag reduction, the stretching of the polymers is the key parameter, future research in this field of fluid dynamics should be directed to elucidate the scaling rules that are applicable to this phenomenon.

Appendix A

Disturbance energy

Abstract

In this appendix, the relationship between the averaged root-mean-square disturbance amplitude A_{rms} and the disturbance energy used by Herbert (1976) is derived.

To check the saturation amplitude of nonlinear subcritical disturbances, calculations are performed under constant pressure gradient and constant flow rate conditions. The analysis by Herbert (1976) considered nonlinear disturbances consisting of the base disturbance and several higher harmonics which are steady in a Galilean time frame moving with the wave speed. For his calculations, Herbert considered a flow driven by a constant pressure drop. The constant pressure drop condition necessarily leads to a decrease in flow rate if disturbance amplitudes increase. As a result, the time scale for the flow to reach a constant disturbance amplitude value is much larger than that for the reaction time under the constant flow rate condition. Also, since for the constant flow rate case the laminar parabolic profile is fixed, rescaling of the disturbances is relatively easy. For the constant pressure gradient case, the flow rate varies continuously and rescaling of the disturbance is much more difficult.

In order to be able to compare the amplitude of the disturbance with that by Herbert, the various definitions of disturbance amplitude and energy have to be compared. In the formulation by Herbert (1976) the flow is described by the stream function:

$$\Psi(x, y, t) = \Psi^*(y) + \sum_{-\infty}^{\infty} f_n(y) e^{in\alpha(x-ct)} \quad (\text{A.1})$$

where Ψ^* represents the basic flow (parabolic profile). f_n is complex and f_0 is the mean flow distortion. In order to obtain a real solution f_{-n} must equal the complex conjugate of f_n ; $f_{-n} = \bar{f}_n$. The velocity components in mean flow direction and wall normal direction, x and y direction respectively, are given by:

$$u_n = \frac{df_n}{dy} \quad , \quad v_n = in\alpha f_n \quad (\text{A.2})$$

and thus with f_n ; $f_{-n} = \bar{f}_n$:

$$u_{-n} = \bar{u}_n \quad , \quad v_{-n} = \bar{v}_n \quad (\text{A.3})$$

So, the disturbance velocity field is actually decomposed in pairs of complex conjugate eigen-

functions u_n and v_n and we can write:

$$\begin{aligned}
 u &= \sum_{\substack{n=-\infty \\ n \neq 0}}^{\infty} u_n e^{in\alpha(x-ct)} = \sum_{n=1}^{\infty} \left[u_n e^{in\alpha(x-ct)} + \overline{u_n e^{in\alpha(x-ct)}} \right] \\
 &= \sum_{n=1}^{\infty} 2\text{Re} \left[u_n e^{in\alpha(x-ct)} \right] \\
 &= \sum_{n=1}^{\infty} 2 \{ \text{Re}(u_n) \cos n\alpha(x-ct) - \text{Im}(u_n) \sin n\alpha(x-ct) \} \quad (\text{A.4})
 \end{aligned}$$

Similar relationships hold for v .

Our code uses the following definition of disturbance amplitude, which is the rms total (averaged over the entire computational domain) velocity fluctuation A_{rms} :

$$A_{\text{rms}} = \left[\frac{1}{\Omega} \int_{\Omega} |\underline{U} - \underline{U}_{\text{ref}}|^2 d\Omega \right]^{\frac{1}{2}} \quad (\text{A.5})$$

where Ω is the domain, \underline{U} is the total velocity vector and $\underline{U}_{\text{ref}}$ is the reference velocity. The reference velocity is, in accordance to Herbert, taken to be the average velocity i.e. not a parabolic profile since the disturbances distort the parabolic profile by several percent (see also figure 4.14). Comparing equations A.1 and A.5 reveals that the reference velocity is therefore the parabolic profile plus the $n = 0$ term. Then $|\underline{U} - \underline{U}_{\text{ref}}|^2$ becomes:

$$\begin{aligned}
 |\underline{U} - \underline{U}_{\text{ref}}|^2 &= u^2 + v^2 \\
 &= \left[\sum_{n=1}^{\infty} 2 \{ \text{Re}(u_n) \cos n\alpha(x-ct) - \text{Im}(u_n) \sin n\alpha(x-ct) \} \right]^2 \\
 &\quad + \left[\sum_{n=1}^{\infty} 2 \{ \text{Re}(v_n) \cos n\alpha(x-ct) - \text{Im}(v_n) \sin n\alpha(x-ct) \} \right]^2 \quad (\text{A.6})
 \end{aligned}$$

Expanding this gives quadratic terms $\cos^2 n\alpha(x-ct)$ and $\sin^2 n\alpha(x-ct)$ and mixed terms $\cos k\alpha(x-ct) \cos l\alpha(x-ct)$ and $\sin k\alpha(x-ct) \sin l\alpha(x-ct)$ with $k \neq l$ and $\cos k\alpha(x-ct) \sin l\alpha(x-ct)$. Given the domain Ω : $0 \leq x \leq \frac{2\pi}{\alpha}$ and $-1 \leq y \leq 1$, integration of the sine and cosine terms over x gives:

$$\begin{aligned}
 \int_0^{\frac{2\pi}{\alpha}} \cos(k\alpha x) \cos(l\alpha x) dx &= \int_0^{\frac{2\pi}{\alpha}} \sin(k\alpha x) \sin(l\alpha x) dx = \frac{\pi}{\alpha} \delta_{kl} \quad k \leq 1, l \leq 1 \\
 \int_0^{\frac{2\pi}{\alpha}} \cos(k\alpha x) \sin(l\alpha x) dx &= 0
 \end{aligned}$$

Substituting these results in the equation A.5 yields:

$$\begin{aligned}
 A_{\text{rms}} &= \left[\frac{\alpha}{4\pi} \int_{-1}^1 \sum_{n=1}^{\infty} \frac{\pi}{\alpha} 4 \{ \text{Re}^2(u_n) + \text{Im}^2(u_n) + \text{Re}^2(v_n) + \text{Im}^2(v_n) \} dy \right]^{\frac{1}{2}} \\
 &= \left[\sum_{n=1}^{\infty} \int_{-1}^1 \{ |u_n|^2 + |v_n|^2 \} dy \right]^{\frac{1}{2}}
 \end{aligned} \tag{A.7}$$

Equation A.7 shows that the definition (A.5) for the rms velocity fluctuations is identical to the one used by Herbert (1976). Herbert uses in his plots the energy of the disturbance, E_{Herbert} , which is defined as:

$$E_{\text{Herbert}} = \frac{15}{8} \sum_{n=1}^{\infty} \int_{-1}^1 \{ |u_n|^2 + |v_n|^2 \} dy \frac{15}{8} A_{\text{rms}}^2 \tag{A.8}$$

This definition of the energy normalizes the energy of the parabolic profile, $\underline{U}_p(y) = 1 - y^2$:

$$E_p = \frac{15}{8} \int_{-1}^1 \frac{1}{2} U_p^2(y) dy = 1$$

Appendix B

Contraction design

Abstract

In this appendix, the mathematical background of the stream function method following the work of Cohen & Ritchie (1962), is given, which we used in section 5.8.3 to optimize design of the contraction of the settling chamber. General equations are given for the higher order derivatives that are needed in the calculation.

The design of the contraction in the settling chamber is based upon a method by Cohen and Ritchie (1962). They prescribe the velocity distribution at the axis of the contraction and use potential flow theory to calculate streamlines which are then taken to be possible wall coordinates for the contraction. In this appendix, the functions they use in their series expansion are given in general form to allow for a parametric study to determine an optimal form of the contraction.

Cohen & Ritchie (1962) use a stream function Ψ to describe an axi-symmetric flow of an ideal fluid. Potential-flow theory for this case leads to the Stokes-Beltrami equation in Ψ :

$$\frac{\partial^2 \Psi}{\partial z^2} + \frac{\partial^2 \Psi}{\partial r^2} - \frac{1}{r} \frac{\partial \Psi}{\partial r} = 0 \quad (\text{B.1})$$

Writing Ψ as a series solution,

$$\Psi = \sum_1^{\infty} f_m(z) r^{2m}$$

and substitution in equation B.1 gives a recurrence relationship between higher order terms and the higher order derivatives:

$$f_{m+1}(z) = -\frac{f_m''(z)}{2m(2m+2)} \quad (\text{B.2})$$

where the function $f_1(z)$ is arbitrary. With this results Ψ can be written as a series solution in $f_1(z)$ and its derivatives:

$$\Psi = \sum_1^{\infty} \frac{(-1)^{n-1} f_1^{2n-2}(z) r^{2n}}{2^{2n-2} n \{(n-1)!\}^2} \quad (\text{B.3})$$

The axial and radial velocity distribution can be expressed in f_1 as well. Keeping only derivatives up to eight order gives:

$$w(z, r) = \frac{1}{r} \frac{\partial \Psi}{\partial r} = 2f_1(z) - \frac{2f_1''(z)r^2}{4} + \frac{2f_1''''(z)r^4}{64} - \frac{2f_1''''''(z)r^6}{2304} + \frac{2f_1''''''''(z)r^8}{147456} \quad (\text{B.4})$$

$$v(z, r) = \frac{1}{r} \frac{\partial \Psi}{\partial z} = -\frac{2f_1'(z)r}{2} + \frac{2f_1'''(z)r^3}{16} - \frac{2f_1''''(z)r^5}{384} + \frac{2f_1''''''(z)r^7}{18432} \quad (\text{B.5})$$

The velocity distribution at the axis of the contraction turns out to be $w(r=0) = 2f_1(z)$ and Cohen & Ritchie (1962) selected for this the following function:

$$w(r=0) = A + B \cdot \tanh\left(\frac{z}{C}\right) + D \cdot e^{kz^2} \quad (\text{B.6})$$

This function ensures a smooth increase of the centerline velocity. The term $D \cdot e^{kz^2}$ is added to create an asymmetric centerline velocity function, which is helpful in suppressing adverse pressure gradients. Also, this function is mathematically relatively simple, viz. calculating higher order derivatives is simple. This argument is no longer appropriate given the large computer power we have available now.

For the calculation of the stream function and the velocities, derivatives up to order eight are required:

$$\begin{aligned} h(z) &= A + BT \quad \text{and} \quad T = \tanh\left(\frac{z}{C}\right) \\ h'(z) &= \frac{B}{C} (1 - T^2) \\ h''(z) &= -\frac{2B}{C^2} (1 - T^2) T \\ h'''(z) &= -\frac{2B}{C^3} [1 - 4T^2 + 3T^4] \\ h''''(z) &= \frac{8B}{C^4} [2T - 3T^3] (1 - T^2) \\ h'''''(z) &= -\frac{8B}{C^5} [-2 + 17T^2 - 30T^4 + 15T^6] \\ h''''''(z) &= -\frac{8B}{C^6} [34T - 120T^3 + 90T^5] (1 - T^2) \\ h'''''''(z) &= -\frac{8B}{C^7} [34 - 496T^2 + 1512T^4 - 1680T^6 + 630T^8] \\ h''''''''(z) &= \frac{128B}{C^8} [62T - 378T^3 + 630T^5 - 315T^7] (1 - T^2) \end{aligned} \quad (\text{B.7})$$

$$\begin{aligned}
g(z) &= D \cdot e^{kz^2} \\
g'(z) &= g(z) \cdot 2kz \\
g''(z) &= g(z) \cdot [2k + (2kz)^2] \\
g'''(z) &= g(z) \cdot [3(2k)(2kz) + (2kz)^3] \\
g^{(4)}(z) &= g(z) \cdot [3(2k)^2 + 12k(2kz)^2 + (2kz)^4] \\
g^{(5)}(z) &= g(z) \cdot [15(2k)^2 2kz + 20k(2kz)^3 + (2kz)^5] \\
g^{(6)}(z) &= g(z) \cdot [15(2k)^3 + 45(2k)^2(2kz)^2 + 15(2k)(2kz)^4 + (2kz)^6] \\
g^{(7)}(z) &= g(z) \cdot [105(2k)^3 2kz + 105(2k)^2(2kz)^3 + 21(2k)(2kz)^5 + (2kz)^7] \\
g^{(8)}(z) &= g(z) \cdot [105(2k)^4 + 420(2k)^3(2kz)^2 \\
&\quad + 210(2k)^2(2kz)^4 + 28(2k)(2kz)^6 + (2kz)^8]
\end{aligned} \tag{B.8}$$

In order to further optimize the design, we shifted $g(z)$ to the large diameter side of the contraction by an amount s_h . All derivatives can be obtained by simply substituting $(z + s_h)$ for z in equation B.8. The results of the contraction calculations are presented in section 5.8.3. The contraction that we selected and used in our experiments is shown in figure B.1.

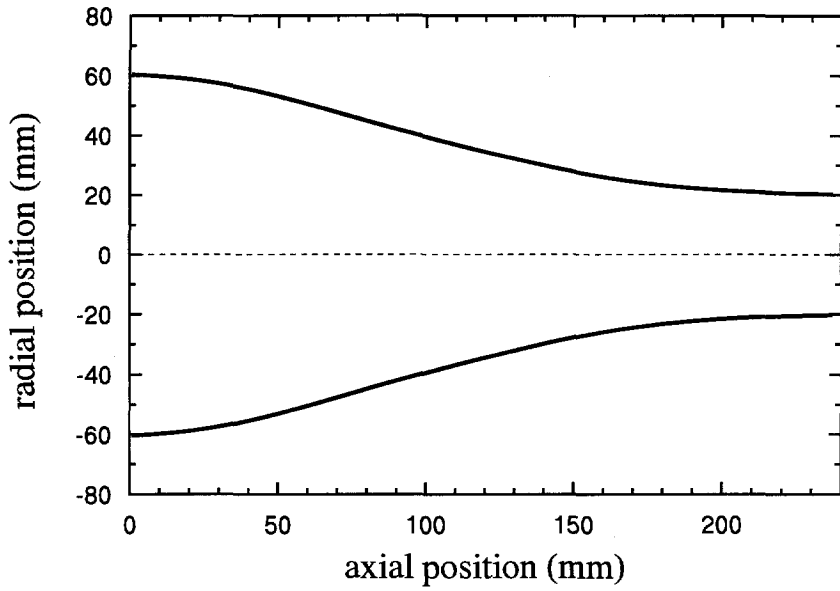


Figure B.1: The optimized contraction contour that we used in our experiments.

Appendix C

Coriolis force

Abstract

In our experiments, we have a strong vertical as well as a horizontal asymmetry in the axial velocity profile. After minimizing causes such as natural convection, we suspected the earth's rotation to be the cause, which proved to be correct. Therefore, we analyze in this appendix the influence of the earth's rotation on laminar flow in pipes. A complicating factor hereby is, that due to the orientation of the pipe relative to the earth rotation axis, the Coriolis force has components in both the horizontal and the vertical direction.

A first approach to estimate the effect of Coriolis force on pipe flow employs a linear perturbation analysis. This approach was first performed by Benton (1956) and it is discussed here in detail. It is shown that application of the linear theory is no longer permitted above $Re=2800$. To overcome this problem, the full equations of motion including the Coriolis force are solved numerically. These results show a good agreement with the velocity profiles and the pressure gradient that we observed in our facility. Therefore, it can be concluded that the asymmetry in the velocity profiles, in absence of buoyancy forces (see chapter 5), is in the first place due to the earth's rotation. It is found that at high Reynolds numbers the distortion of the parabolic profile in water is very large compared to the effects in air for which the kinematic viscosity is higher.

Finally, the effect of curvature of the pipe on the flow and its applicability to counteract the Coriolis force effects is discussed. According to linear theory, the disturbance shapes due to curvature and Coriolis force are practically identical but scale differently with Reynolds number. Therefore, the curvature required to counteract the effects of the Coriolis force needs to vary with the Reynolds number.

C.1 Historical background

By the end of 1993, our experimental facility was completed up to the point that water could be circulated through it and velocity profiles could be measured using Laser Doppler Velocimetry (LDV). Initially, we found that the flow could be maintained laminar up to $Re=32000$. However, our measurements plotted in terms of a Moody diagram (friction factor vs. Reynolds number) showed a significant deviation from the standard Hagen-Poiseuille flow for $Re \gtrsim 5000$. The length of the pipe has been estimated to be sufficiently long to obtain fully developed flow up to $Re=14300$. Therefore, another source for this unexpected behavior had to be found. In addition to these friction factor measurements, LDV measurements revealed a strong asymmetry in the axial velocity profile, both in the vertical as well as in the horizontal direction, particularly at high Re .

An explanation that immediately came to mind was natural convection due to a temperature

difference between the air in the laboratory and the water in the facility. During the night, the water temperature in the facility falls and during the day the central heating system warms up the air temperature very quickly. Typically, the water would be 2°C colder than the surrounding air. Some preliminary experiments in which we added hot water so that the water temperature increased to 2°C above that of the air, showed that buoyancy forces can strongly distort the vertical velocity profile (see chapter 5). However, after carefully insulating the facility and thermostatically matching the water temperature to that of the air, the vertical asymmetry decreased but the horizontal asymmetry remained very large.

In our search for other causes, we noticed that the horizontal axial velocity profile was always skewed towards the direction of the Coriolis force, which is on the Northern hemisphere to right looking downstream. However, the exact direction of the Coriolis force depends on the orientation of the pipe facility relative to rotation axis of the earth. This will be discussed in the section C.2.

Knowing the exact orientation of the Coriolis force, a linear perturbation analysis can be applied, first performed by Benton (1956). This analysis is discussed in detail in section C.3. However, it appears that the linear theory is valid in our pipe facility only up to $Re \approx 2800$. As we aim to study the flow stability at much higher Re and as we have estimated the length of the pipe to be sufficient for fully developed flow for $Re \lesssim 14300$, we need to study the Coriolis force effect beyond the applicability of linear theory. For this, we performed numerical computations using a finite volume, time dependent, pipe code. In section C.4, this code and the accuracy of the computational results is discussed. The comparison with the measured velocity profiles will also be presented there.

Finally, as the secondary flow resulting from the Coriolis force (Benton 1956) seems to be very similar to that generated by a curved pipe (Dean 1927, 1928), the possibility of counteracting Coriolis force effects by introducing curvature is discussed.

C.2 Direction of the Coriolis force

To study the effect of the earth's Coriolis force on laminar pipe flow, we first need to know its magnitude and direction. The Coriolis force takes the form of $-2\Omega \times \underline{u}$ with Ω the angular velocity of the earth's rotation and \underline{u} the fluid velocity (Batchelor 1967, p. 555). To determine the direction of this force, we define a Cartesian coordinate system with the x -axis normal to and the y, z -plane parallel to the surface of the earth at the location of the facility. The z -direction is taken as the pipe axis and the flow is in the positive z -direction (see figure C.1). The orientation of $\underline{\Omega}$ with respect to the laboratory frame of reference is now depicted in figure C.1.

Thus the x, y, z -components of $\underline{\Omega}$ are

$$\underline{\Omega} = \begin{pmatrix} \Omega \sin \alpha_L \\ \Omega \cos \alpha_L \sin \alpha_N \\ \Omega \cos \alpha_L \cos \alpha_N \end{pmatrix} \quad (\text{C.1})$$

where α_L is the degree of latitude and α_N the angle of the pipe axis with the direction of the true north. With this definition, the Coriolis force for cylindrical Poiseuille flow becomes:

$$-2 \begin{pmatrix} \Omega \sin \alpha_L \\ \Omega \cos \alpha_L \sin \alpha_N \\ \Omega \cos \alpha_L \cos \alpha_N \end{pmatrix} \times \begin{pmatrix} 0 \\ 0 \\ U(r) \end{pmatrix} = -2\Omega U(r) \begin{pmatrix} \cos \alpha_L \sin \alpha_N \\ -\sin \alpha_L \\ 0 \end{pmatrix} \quad (\text{C.2})$$

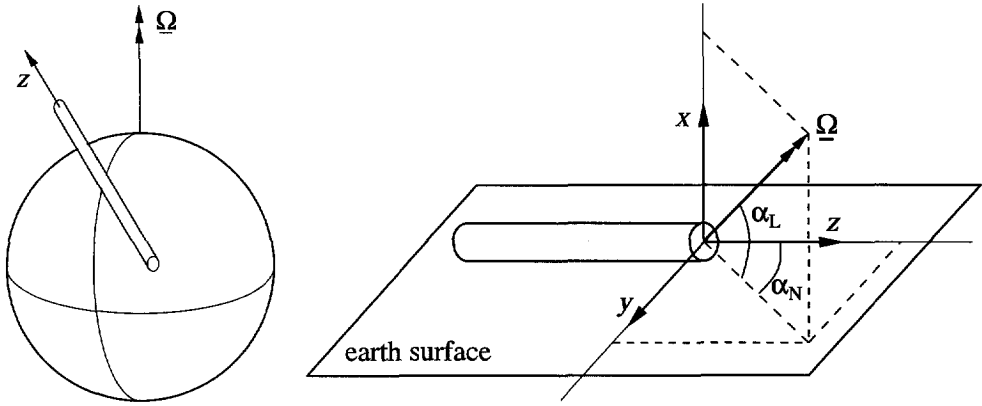


Figure C.1: Cartesian coordinate system with the orientation the rotation vector of the earth.

So, no Coriolis force is present when $\alpha_L=0$ and $\alpha_N=0$ which means that the pipe is located at the equator and oriented in the north-south direction. When $\alpha_N=\pi/2$, i.e. the pipe is oriented in the east-west direction, the magnitude of the Coriolis force does not vary with the degree of latitude. Except when the pipe is oriented in the north-south direction, the Coriolis force will have a component in the vertical plane, i.e. along the x -axis. So if Coriolis effects are to be avoided and the pipe cannot be located at the equator, orientation in north-south direction is still required, but in addition the pipe needs to be tilted to make an angle α_L with the surface of the earth.

For our pipe-flow facility we find for the angles α_L and α_N ¹:

$$\alpha_N = 22^\circ \text{ west} \quad \alpha_L = 52^\circ \text{ north} \tag{C.3}$$

With values for α_L and α_N the Coriolis force for cylindrical Poiseuille flow becomes:

$$-2\Omega U(r) \begin{pmatrix} \cos \alpha_L \sin \alpha_N \\ -\sin \alpha_L \\ 0 \end{pmatrix} = -2\Omega U(r) \begin{pmatrix} 0.23063 \\ -0.78801 \\ 0 \end{pmatrix} \tag{C.4}$$

where $\Omega=2\pi/(24 \cdot 3600)=7.272 \cdot 10^{-5} \text{ s}^{-1}$ is the magnitude of $\underline{\Omega}$. The Coriolis force has a positive component in y -direction, i.e. to the right looking downstream as already mentioned in the previous section. Furthermore, we find a negative component in x -direction which is 29% of

¹The magnetic north pole, as measured with a compass, does not coincide with the true north pole. In addition there is a difference between the north of the map and the true north and is called the meridian convention correction. For Delft, the true north lies $0^\circ 48'$ east of the north of the map and the magnetic north pole lies $2^\circ 0'$ west of the north direction on the map on January 1 1990 and moves $8'$ to the east every year. So for the period of measurements, i.e. mid 1994 till mid 1995, the magnetic north pole is approximately 2° west of the true north pole. In figure C.2 all the angles are indicated.

Measuring the angle between the magnetic north pole and the pipe axis is rather complicated due to the presence of abundant amounts of steel around the pipe, which influence the reading of the compass. Therefore the orientation of the building wall was measured to which the pipe is parallel. The building was found to be oriented 20° west of the magnetic north pole.

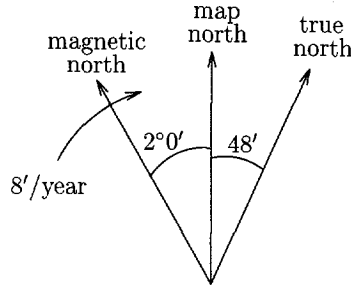


Figure C.2: Relative orientation of map north pole, magnetic north pole and true north

the magnitude of the y -component. The vertical (x -direction) contribution may be enhanced or reduced/reversed by other forces present like buoyancy due to temperature differences between the water and the surrounding air (see section 5.8.2).

C.3 Linear theory

C.3.1 Introduction

The effect of the earth's rotation on laminar pipe flow has been already studied by Benton (1956). His analysis shows that for water, the effect of the earth's rotation can very well be significant. His laboratory experiments were in qualitative agreement with his theory but the measured effect did amount only to 1/3 of the theoretically predicted effect. Benton also suggested that the effect of the Coriolis force may be of importance in the breakdown of laminar flow into turbulence at high Reynolds numbers.

In this section, the linear analysis by Benton (1956) will be reproduced and discussed in detail. The basic equations will be derived and the solution for the disturbance velocities will be applied for the conditions in our facility.

C.3.2 Basic equations

We start with the steady-state equations of motion for an incompressible fluid in laminar flow relative to a coordinate system rotating at a constant angular velocity $\underline{\Omega}$ (see e.g. Batchelor 1967, pp. 555 & 140):

$$\underline{u} \cdot \nabla \underline{u} = -2\underline{\Omega} \times \underline{u} - \nabla \Phi + \nu \nabla^2 \underline{u} \quad (\text{C.5})$$

where

$$\Phi = \frac{p}{\rho} + \varphi + \frac{\Omega^2 a^2}{2} \quad (\text{C.6})$$

Here \underline{u} is the velocity; p is the pressure and ρ is the density; φ is the gravitational geopotential; a is the distance from the axis of rotation; and ν is the kinematic viscosity. $\nabla \varphi$ is the acceleration of gravity and $\nabla(\Omega^2 a^2/2)$ is the centrifugal force. When the coordinate system is fixed to the surface of the earth, $\underline{\Omega}$ becomes the angular velocity of the earth's rotation.

Whether or not the Coriolis terms ($-2\Omega \times \underline{u}$) is significant can be estimated. It is common practice to compare all forces in the equations of motion to the inertia force $\underline{u} \cdot \nabla \underline{u}$. The ratio of the inertia to the viscous force is well known as the Reynolds number

$$Re = \frac{\overline{W}D}{\nu}$$

where \overline{W} is a characteristic velocity and D a characteristic length scale of the flow under consideration; for our pipe flow, these scales are the bulk velocity and the pipe diameter, respectively. ν is the kinematic viscosity of the fluid. The ratio of the inertia force to the Coriolis force is known as the Rossby number and is important when studying rotating flow such as occurring in meteorological processes. The Rossby number is usually written as:

$$Ro = \frac{\overline{W}}{2\Omega \sin \alpha D} \quad (C.7)$$

where α is the angle between the axis of the earth's rotation and the direction of motion. From vector calculus follows the following identity:

$$|\Omega \times \underline{u}| = |\Omega| \cdot |\underline{u}| \cdot \sin \alpha \quad (C.8)$$

Combining equations (C.2) and (C.8) the value of α can be determined:

$$\sin \alpha = \sqrt{\cos^2 \alpha_L \sin^2 \alpha_N + \sin^2 \alpha_L} = 0.821 \quad \Rightarrow \quad \alpha = 55.2^\circ \quad (C.9)$$

For our pipe flow with Reynolds number of 10 000 ($\overline{W}=0.25\text{m/s}$ and $D=40\text{mm}$), the Rossby number becomes $Ro=52\,336$. Thus, the Coriolis force seems to be much smaller than the inertia force and this could tempt one to conclude that the Coriolis force is not important for the pipe flow under consideration. However, this argument is solely based on a comparison of rotation to inertia forces, which is not an appropriate ratio to consider in this case. This is because for fully developed Hagen–Poiseuille flow, the equations of motion in radial as well as in tangential direction vanish and in the direction of the pipe axis the equation of motion reduces to:

$$0 = \nu \frac{1}{r} \frac{\partial}{\partial r} \left(r \frac{\partial U(r)}{\partial r} \right) - \frac{1}{\rho} \frac{\partial p}{\partial z} \quad (C.10)$$

Thus, for Hagen–Poiseuille flow *no inertia force exists* and the pressure gradient is balanced by the viscous force. For this flow the Reynolds number as ratio of inertia to viscous force loses its importance. A similar argument is valid for the Rossby number. In the absence of the inertia force, the shape of the velocity profile in cylindrical Poiseuille flow is determined by the viscous forces only. In order to assess the influence of the Coriolis force, the ratio of the viscous to the Coriolis force is a more relevant parameter. This ratio is called the Ekman number (Drazin & Reid 1981, p. 365) and it is equal to $Ek=Ro/Re$. The Ekman number is independent of the fluid velocity scale and for our pipe filled with water of 20°C it becomes:

$$Ek = \frac{\nu}{2\Omega D^2 \sin \alpha} = 5.23 \quad (C.11)$$

This value suggests that the presence of the Coriolis force, which in magnitude is almost 20% of the viscous force may significantly distort the parabolic profile.

In his analysis of the effect of the Coriolis force on the laminar flow in pipes, Benton (1956) starts with equation (C.5). As we are considering steady-state fully developed laminar pipe flow, none of the terms with exception of Φ varies in the direction of the pipe axis, i.e. they are independent of z . As a result, Φ can vary only linearly with z . In cylindrical coordinates the velocity \underline{u} can be decomposed into the components \underline{U} and \underline{u}' :

$$\underline{u}(r, \theta) = \underline{U}(r) + \underline{u}'(r, \theta) \quad (\text{C.12})$$

where $\underline{U}(r) = (0, 0, W(r))$ is the solution in absence of the Coriolis force, i.e. a parabolic profile. $\underline{u}'(r, \theta)$ represents the small perturbation or secondary flow due to the effect of the Coriolis force which may have components in all three directions. Similarly, Φ can be separated into:

$$\Phi(r, \theta, z) = \bar{\Phi}(z) + \Phi'(r, \theta) \quad (\text{C.13})$$

where $\bar{\Phi}$ is a linear function in z which drives the U -profile and Φ' is due to the perturbation. Subtracting the equations of motion for a inertial coordinate system, $\nu \nabla^2 \underline{U} = \nabla \bar{\Phi}$, the equations of motion of the secondary flow become:

$$\underline{u}' \cdot \nabla (\underline{U} + \underline{u}') = -2\Omega \times (\underline{U} + \underline{u}') - \nabla \Phi' + \nu \nabla^2 \underline{u}' \quad (\text{C.14})$$

Linearizing these equations, subject to the condition $\underline{u}' \ll \underline{U}$ gives the equations of motion which Benton studied to determine the effect of the Coriolis force on laminar pipe flow:

$$\underline{u}' \cdot \nabla \underline{U} = -2\Omega \times \underline{U} - \nabla \Phi' + \nu \nabla^2 \underline{u}' \quad (\text{C.15})$$

Equation (C.15) together with the continuity equation $\nabla \cdot \underline{u}' = 0$ forms the set of equations to be solved. It is convenient to first study the left hand side of equation (C.15). Remembering that $\underline{U}(r)$ has only components in z -direction shows us that $\underline{u}' \cdot \nabla \underline{U}$ solely contributes in z -direction. Using table A.7-2 of Bird *et al.* (1987a, p. 588) the component of the advective term in z -direction in cylindrical coordinates reduces to:

$$\underline{u}' \cdot \nabla \underline{U} = u'_r \frac{\partial U_z}{\partial r} \underline{e}_z \quad (\text{C.16})$$

As we have defined the perturbation velocity to be a function of r and θ only, we can separate the solution of equation (C.15) in the secondary flow of the pipe cross section and in the axial direction. Because of the independence of all components of the axial coordinate, we can integrate the continuity equation by means of a stream function Ψ which describes the flow in the pipe cross section, i.e. the r, θ -plane, the total perturbation velocity vector can be written as:

$$\underline{u}' = \underline{e}_z w - \nabla \times \underline{\Psi} \quad (\underline{\Psi} = \underline{e}_z \Psi) \quad (\text{C.17})$$

where \underline{e}_z is the unit vector in the direction of the pipe axis. Substitution in the equations of motion (C.15) and taking the curl gives:

$$\begin{aligned} \nabla \times [\underline{u}' \cdot \nabla \underline{U}] &= -2\nabla \times \Omega \times \underline{U}(r) - \nabla \times \nabla \Phi'(r, \theta) \\ &+ \nu \nabla \times \nabla^2 [w(r, \theta) \underline{e}_z - \nabla \times (\Psi(r, \theta) \underline{e}_z)] \end{aligned} \quad (\text{C.18})$$

On closer inspection we see that many of these terms vanish. Taking the curl of a vector in z -direction gives only components in the r, θ -plane. As a result, the term on the left hand side has no contributions in the direction of the pipe axis. The Coriolis term can be rewritten using the following mathematical identity:

$$\nabla \times [\underline{\Omega} \times \underline{U}] = \underline{\Omega} (\nabla \cdot \underline{U}) - \underline{U} (\nabla \cdot \underline{\Omega}) + (\underline{U} \cdot \nabla) \underline{\Omega} - (\underline{\Omega} \cdot \nabla) \underline{U} \tag{C.19}$$

The first term on the right hand side is equal to zero as a result of the continuity equation, the second and third terms vanish as $\underline{\Omega}$ is constant. The rightmost term has a component only in z -direction.

As the curl of the gradient of a scalar field equals zero, the second term on the right hand side of equation (C.18) disappears. Since $\nabla \times \nabla^2 (w(r, \theta) \underline{e}_z)$ denotes taking the curl of a vector in z -direction, this term contributes only in the r, θ -plane. The other viscous term can be transformed with the use of the identity:

$$\nabla \times (\nabla \times \underline{f}) = \nabla (\nabla \cdot \underline{f}) - \nabla^2 \underline{f} \tag{C.20}$$

With this and remembering that $\nabla \cdot \nabla \times \Psi(r, \theta) \underline{e}_z = 0$ we can write:

$$\nabla \times \nabla^2 (\nabla \times (\Psi(r, \theta) \underline{e}_z)) = -\nabla \times (\nabla \times (\nabla \times (\nabla \times (\Psi(r, \theta) \underline{e}_z)))) \tag{C.21}$$

With repeated application of equation (C.20) and using $\nabla \cdot \underline{e}_z = \frac{\partial}{\partial z}$ we can write equation (C.21) as:

$$\nabla \times \nabla^2 (\nabla \times (\Psi(r, \theta) \underline{e}_z)) = -\nabla^4 (\Psi(r, \theta) \underline{e}_z) \tag{C.22}$$

Thus, the component in the z -direction of equation (C.18) reduces to the simple equation for the stream function

$$\nabla^4 \Psi(r, \theta) \underline{e}_z = -\frac{2(\underline{\Omega} \cdot \nabla) \underline{U}(r)}{\nu} \tag{C.23}$$

In order to be able to solve this equation, we need to express $(\underline{\Omega} \cdot \nabla) \underline{U}$ in cylindrical coordinates. The coordinate system is assumed to be aligned in such a way that the positive z -direction coincides with the axial flow direction, and $\theta=0$ is the direction of $\underline{\Omega}_{r,\theta} = \Omega \sin \alpha$ where $\underline{\Omega}_{r,\theta}$ is the component of $\underline{\Omega}$ in the r, θ -plane, Ω the magnitude of $\underline{\Omega}$ and α is the angle between $\underline{\Omega}$ and the pipe axis. The coordinate system is shown in figure C.3. In this coordinate system the components of $\underline{\Omega}$ become:

$$\underline{\Omega} = (\Omega \sin \alpha \cos \theta, -\Omega \sin \alpha \sin \theta, \Omega \cos \alpha) \tag{C.24}$$

With this $(\underline{\Omega} \cdot \nabla) \underline{U}(r)$ can be rewritten as:

$$(\underline{\Omega} \cdot \nabla) \underline{U}(r) = \Omega \sin \alpha \cos \theta \frac{\partial W(r)}{\partial r} \underline{e}_z \tag{C.25}$$

Here $W(r) = 2\overline{W}(1 - r^2)$ is the parabolic velocity profile in the inertial frame. Substitution of equation (C.25) in equation (C.23) and recasting in nondimensional form using pipe diameter D

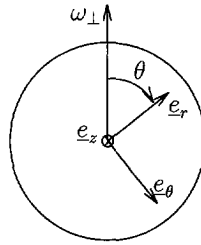


Figure C.3: The coordinate system for the Coriolis force.

and bulk velocity \overline{W} gives the equation for the nondimensional stream function ($\Psi^* = 2\Psi/\overline{W}D$) in terms of the nondimensional coordinates ϱ, θ ($\varrho = 2r/D$):

$$\nabla^4 \Psi^* = \frac{Re}{Ro} \varrho \cos \theta = \frac{\varrho \cos \theta}{Ek} \tag{C.26}$$

Equation (C.26) essentially represents a balance between the viscous and the Coriolis force. It is therefore not surprising to find that the stream function and the disturbance velocities u'_r and u'_θ scale with Ek^{-1} since the Ekman number is the ratio of viscous to Coriolis force.

Although equation (C.26) looks extremely simple, the nabla operator in cylindrical coordinates complicates matters:

$$\begin{aligned} \nabla^2 &= \frac{\partial^2}{\partial r^2} + \frac{1}{r} \frac{\partial}{\partial r} + \frac{1}{r^2} \frac{\partial^2}{\partial \phi^2} + \frac{\partial^2}{\partial z^2} \\ \nabla^4 &= \frac{\partial^4}{\partial r^4} + \frac{2}{r} \frac{\partial^3}{\partial r^3} - \frac{1}{r^2} \frac{\partial^2}{\partial r^2} + \frac{1}{r^3} \frac{\partial}{\partial r} + \frac{2}{r^2} \frac{\partial^4}{\partial r^2 \partial \phi^2} - \frac{2}{r^3} \frac{\partial^3}{\partial r \partial \phi^2} \\ &\quad + \frac{4}{r^4} \frac{\partial^2}{\partial \phi^2} + 2 \frac{\partial^4}{\partial r^2 \partial z^2} + \frac{2}{r} \frac{\partial^3}{\partial r \partial z^2} + \frac{1}{r^4} \frac{\partial^4}{\partial \phi^4} + \frac{2}{r^2} \frac{\partial^4}{\partial \phi^2 \partial z^2} + \frac{\partial^4}{\partial z^2} \end{aligned}$$

With boundary conditions $\Psi^*=0$ and $\partial\Psi^*/\partial\varrho=0$ at $\varrho=1$ the solution to equation (C.26) is given by Benton:

$$\Psi^* = \frac{1}{192Ek} \varrho (1 - \varrho^2)^2 \cos \theta \tag{C.27}$$

As Ψ is the stream function of the radial and tangential disturbance velocities due to the presence of the Coriolis force, u'_r and u'_θ respectively, these disturbance velocities can now be calculated from Ψ using

$$u'_r = -\frac{1}{r} \frac{\partial \Psi}{\partial \theta} \quad \text{and} \quad u'_\theta = \frac{\partial \Psi}{\partial r} \tag{C.28}$$

This leads to the following expressions for the radial and tangential velocities:

$$\frac{u'_r}{\overline{W}} = \frac{1}{192Ek} (1 - \varrho^2)^2 \sin \theta \tag{C.29}$$

$$\frac{u'_\theta}{\overline{W}} = \frac{1}{192Ek} (1 - \varrho^2) (1 - 5\varrho^2) \cos \theta \tag{C.30}$$

The secondary flow in the r, θ -plane takes the form of a pair of counter-rotating vortices (as will be shown later, e.g. in figure C.8). The maximum velocity in the r, θ -plane occurs at $\varrho=0$, where the flow is in the $\theta=\pi/2$ direction with relative magnitude:

$$\frac{\sqrt{u_r'^2 + u_\theta'^2}}{\overline{W}} = \frac{1}{192Ek} \tag{C.31}$$

Thus, the maximum disturbance velocity in the r, θ -plane solely depends on the bulk velocity \overline{W} as Ek is constant. In our pipe the maximum disturbance velocity in the r, θ -plane equals

$$\sqrt{u_r'^2 + u_\theta'^2}_{\max} = 0.000996 \overline{W} \tag{C.32}$$

In figure C.4 the relative disturbance velocities in the r, θ -plane are shown for the Ekman number representative for our experimental facility. Although these velocities are extremely small, they distort the axial velocity profile severely. To understand why, we reconsider the linearized equations of motion (equation (C.15)). If we restrict ourselves to only the z -component of this equation, we may eliminate contributions of $-2\Omega \times \underline{U}$, $\nabla\Phi'$ and $-\nu\nabla^2 \nabla \times \Psi e_z$ since they have only components in the r, θ -plane. Thus with the help of equation (C.16) we find

$$u_r' \frac{\partial W(r)}{\partial r} = \nu \nabla^2 w \tag{C.33}$$

As we can see, here indeed there is a balance between the inertia force and the viscous force. Since u_r' scales according to $u_r' \sim \overline{W}/Ek$, the axial velocity disturbance must scale according to $w/\overline{W} \sim \frac{1}{Ek} \frac{\overline{W}D}{\nu} = \frac{Re}{Ek}$. Substitution of the solution for u_r' and writing the results in nondimensional form gives the equation for w :

$$\nabla^2 \left(\frac{w}{\overline{W}} \right) = -\frac{1}{96} \frac{Re}{Ek} \varrho (1 - \varrho^2)^2 \sin \theta \tag{C.34}$$

This has the following solution for w :

$$\frac{w}{\overline{W}} = \frac{Re}{2^9 3^2 Ek} \varrho (1 - \varrho^2) (3 - 3\varrho^2 + \varrho^4) \sin \theta \tag{C.35}$$

Since Ek is constant, w/\overline{W} increases linearly with Re which implies that the disturbance of the axial velocity profile due to the Coriolis force scales as $w \sim \overline{W}^2$. It is precisely this quadratic increase of the axial disturbance velocity which is the source of the large deformation of the axial velocity profile. The maximum value of w occurs at $\theta=\pi/2$, $\varrho=2r/D=0.462$. At this point

$$w_{\max} = 1.897 \cdot 10^{-4} \frac{Re \overline{W}}{Ek} \tag{C.36}$$

In figure C.4, we show the radial and tangential disturbance velocity profiles according to equations (C.29) and (C.30) respectively. The relative axial disturbance velocity profiles according to equation (C.35) for $\theta=0$ are shown in figure C.5 for several Reynolds numbers for water in our 40 mm pipe.

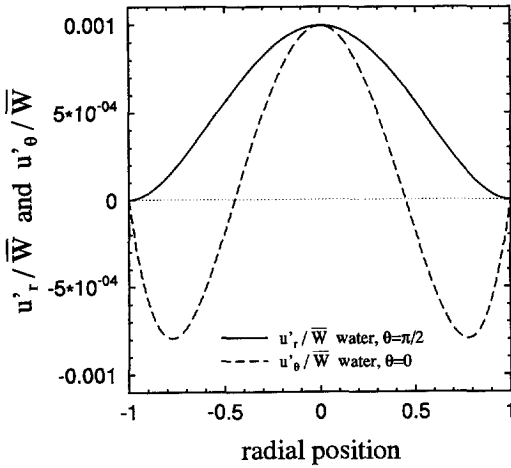


Figure C.4: Relative radial and tangential disturbance velocities according to Benton (1956) for water; $D=40$ mm and $\alpha=55.2^\circ$.

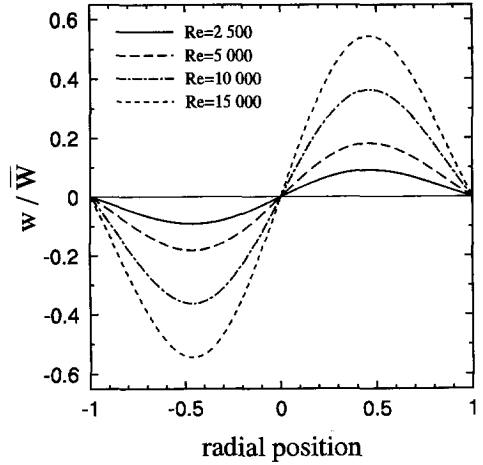


Figure C.5: Relative axial disturbance velocities according to Benton (1956) for water; $D=40$ mm and $\alpha=55.2^\circ$.

For a Reynolds number of only $Re=2\,000$, the axial disturbance velocity maximum is 7% of the bulk velocity and at $Re=5\,000$ this is already 18%. So for $Re=5\,000$ the linear analysis is no longer valid as the linearization used to obtain these results fails. For the Ekman number representative for our facility, substitution in equation (C.36) gives an axial disturbance velocity at $Re=15\,000$ of 54% of the bulk velocity. Moreover, the velocity profile is not anywhere near parabolic (see also figure C.6). This result shows that the presence of Coriolis force is one of the major sources for distortion of the parabolic velocity profile.

The question arises why this effect is not widely known and recognized. Previous experiments have been performed for laminar pipe flow at high Reynolds numbers but the vast majority of these experiments were conducted using air as a medium rather than water. It can be directly shown that for air the Ekman number $Ek = \nu / (2\Omega D^2 \sin \alpha)$ becomes larger by a factor of 15, i.e. the kinematic viscosity of air is 15 times larger than that of water. Therefore, the influence of the Coriolis forces becomes negligible for most of such pipe flows² Some of the pipe flow experiments which were also performed with water did not show this effect, most likely because the pipe length was too short to allow for fully developed flow to occur. Then, the Rossby number becomes the relevant parameter and we have shown above that this number is very large.

In figures C.6 and C.7 the axial velocity profiles are shown for water and air respectively. For water the velocity profiles for $Re=5\,000$ and higher are strongly distorted and even have a velocity profile with an inflection point, as shown in figure C.6.

As we have seen for our pipe flow, the disturbance velocities exceed values of 10% of the bulk velocities and it is clear that the linear theory can no longer be valid. For air, however, the distortion of the axial velocity profile is rather small and very accurate measurements are nec-

²In table 5.1 an overview is given of some pipe-flow facilities in which laminar flow at high Reynolds numbers was studied, mostly for transition studies.

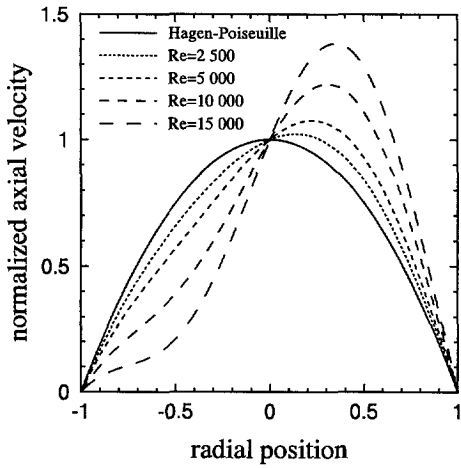


Figure C.6: Axial velocity profiles according to Benton (1956) for water at several Reynolds numbers; $D=40$ mm and $\alpha=55.2^\circ$, $\theta=\pi/2$.

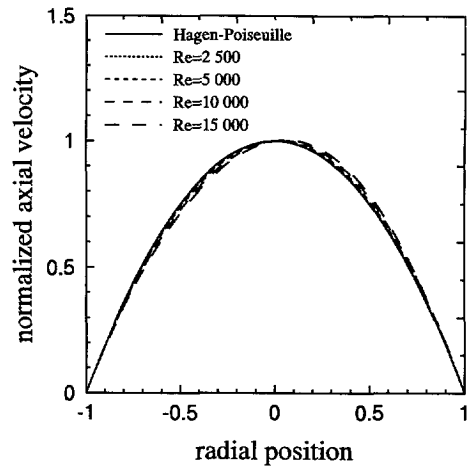


Figure C.7: Axial velocity profiles according to Benton (1956) for air at several Reynolds numbers; $D=40$ mm and $\alpha=55.2^\circ$, $\theta=\pi/2$.

essary to detect a deviation from the parabolic profile for Reynolds numbers below $Re=10\,000$.

In conclusion we may summarize our main results. We have seen that linear disturbance theory for Coriolis force effects shows that although the radial and tangential disturbances are very small, the axial velocity profile can be strongly distorted. The effect for air is 15 times smaller than for water due to the difference in kinematic viscosity. Thus, increasing the viscosity of water by adding viscosifiers like glycerol or glucose syrup can suppress Coriolis force effects and is also favorable for suppressing convection effects. But, when keeping the Reynolds number constant, this means that the velocity must also be increased.

For pure water, however, we have found that at high Reynolds numbers the linear theory by Benton is no longer valid and for a reliable comparison with the measured velocity profiles, numerical computations of the full equations of motion are necessary. This will be discussed in the next section.

C.4 Numerical computations

C.4.1 Introduction

From the analysis presented in the previous section it is clear that in our laminar pipe flow with water as fluid, the velocity profile becomes strongly distorted at high Reynolds numbers due to the presence of the Coriolis force. The linear analysis of the previous section is based on the assumption that the disturbance velocities are small compared to the undisturbed velocity profile. It is clear that this can no longer be valid for the Reynolds numbers at which measurements are performed in our pipe. Let us take an axial disturbance velocity of 10% of the bulk velocity to be the criterion below which the linear analysis is still valid. This implies for our 40 mm pipe that the linear solution is applicable only up to $Re=2\,760$ for water and up to

$Re=41\,400$ for air. Numerical computations of the full equations should be performed to obtain the solutions for a pipe flow at high Reynolds numbers. In the next sections, the accuracy of the pipe code for several meshes is discussed. Comparisons are made with the linear solution and with measurements.

C.4.2 Numerical techniques

For our numerical computations of the effect of the Coriolis force, we modified a pipe code that was developed in our laboratory by Eggels (1994) and Pourquié (1994) by incorporating the Coriolis force. The code, as is discussed in Eggels (1994) and Pourquié (1994), has an explicit time solver with second order accuracy in and a second order finite volume discretization in space. The code was developed for turbulent flows where stability of an explicit time scheme is mostly dictated by the nonlinear convection terms rather than by the viscous terms. However, for laminar pipe flow the time step in explicit schemes is dictated by viscosity which requires very small time steps for fine meshes. As the problem under consideration is the study of disturbance velocities due to the presence of the Coriolis force, fine meshes are needed to resolve the effects of the Coriolis force at lower Reynolds numbers, particularly when testing the code against the solution of a linear perturbation analysis. As the viscosity and the grid cell size near the pipe axis determine the time step, the grid size near the pipe axis was enlarged. The 9 radial points closest to the pipe axis were taken equidistant and mesh refinement was applied towards the wall in order to ensure a good resolution near the wall where the no-slip condition is imposed. The time step was further increased by removing the radial grid point closest to the pipe center. In radial direction, the number of grid points was varied between 20 and 60. In pipe axis direction, 3 elements were used with periodic boundary conditions. In circumferential direction, the grid was taken to be equidistant and the number of grid points used varied between 60 and 120.

In the first few runs at small Reynolds numbers, the initial velocity field was taken to be parabolic and the computations converged to the linear solution of the previous section. Therefore, in all later calculations the linear solution was taken as a starting point. The computation was then allowed to run till the solution reaches a steady state. One calculation typically takes 80–160 cpu hours on a Convex-3840 with a 60×120 grid, the finest grid used.

In the next section, the results of the code are checked against the linear solution.

C.4.3 Comparison with the linear solution

Before performing calculations at high Reynolds numbers, where the parabolic flow becomes strongly, the pipe code is first checked against the linear solution discussed in section C.3. For this we performed numerical computations at low Reynolds numbers at which only a relatively small deviation from Hagen–Poiseuille flow is to be expected.

A contour plot of the disturbance stream function and the value of the axial velocity along $\theta=\pi/2$ for a pipe flow of water at $Re=2\,500$ using the actual orientation of our pipe are shown in figures C.8 and C.9. The maximum values for the contour levels of Ψ are $\pm 2.140 \cdot 10^{-4}$ which should be compared to the theoretical values of $\pm 2.206 \cdot 10^{-4}$. In the contour plot of the stream function a slight irregularity around the pipe axis can be observed. This is probably due to the distribution of the radial grid points near the pipe center. In the numerical computations, the pipe axis itself is a singular point due to the r^{-1} -terms in the equations of motion and thus no grid points are located there. In addition, the coarse grid near the pipe

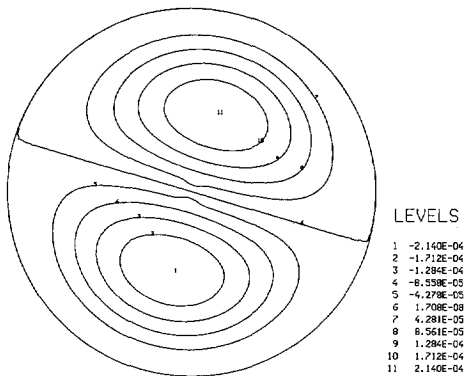


Figure C.8: Contour plot of disturbance stream function at $Re=2500$. The flow is directed into the paper.

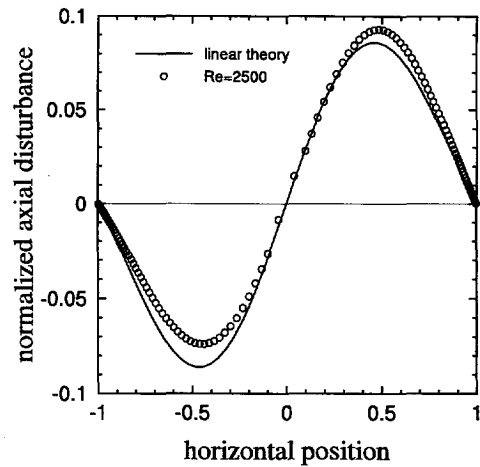


Figure C.9: Axial disturbance velocity at $Re=2500$ and $\theta=\pi/2$ normalized with half the centerline velocity (for a parabolic velocity profile this would be the bulk velocity).

axis, needed to enlarge the small time step, introduces an extra error. As at all other points the solution is smooth, this anomaly near the pipe axis is unlikely to be of real concern. A striking feature of the axial disturbance velocity is the asymmetry, clearly present in figure C.9. The maximum disturbance in the axial velocity at positive and negative radial positions is not equal in magnitude in contrast to the linear solution. This could be related to the method of extracting the disturbance velocities from the total velocity field or to a deviation from linear theory.

With the calculations we solve the total velocity from the complete equations of motion. In order to obtain the disturbance velocity, a parabolic velocity profile has to be subtracted. In the calculations a constant pressure gradient is imposed. If the magnitude of the disturbance increases the flow rate will decrease due to a raise in drag. In the linear analysis, this effect is not taken into account. Therefore, we cannot use the initial parabolic profile or the bulk velocity for the determination of the disturbances. Benton (1956) deals with linear theory and his axial velocity profiles all cross the pipe axis at the centerline velocity of the *undisturbed* flow. When comparing our solution to obtained from the linear theory, we determined the centerline velocity and subtracted a parabola having the same centerline velocity from the velocity field. This then gives the disturbance velocity field. Determination of the centerline velocity was done by fitting a high order polynomial to the axial velocity profile for $\theta=\pi/2$. The the axial disturbance according to Benton is of order 7 in r but a polynomial of order 11 was required to accurately fit the numerical profiles, especially for the larger Reynolds numbers. The two points closest to the pipe axis were excluded from the fit as they clearly deviate from the rest of the axial velocity profile. Although this procedure of determining the centerline velocity introduces some asymmetry in the axial disturbance velocity profiles it cannot explain the large asymmetry found in figure C.9.

This is illustrated somewhat more in figure C.10, where axial disturbance velocities are compared to Benton's solution for three different meshes at $Re=1500$. Note that the Reynolds number has been decreased, but also the rotational speed has been reduced which leads to an increase in the Ekman number from $Ek=5.23$ to $Ek=15.4$. This was done so that the linear theory was approached more closely. Refining the grid decreases the asymmetry. The agreement for the 60×120 grid at $Re=1500$ and $Ek=15.4$ is much better than at $Re=2500$ and $Ek=5.23$. This shows that fine meshes are needed to accurately capture the Coriolis force effect on laminar pipe flow and that deviations from linear theory occur already at low Reynolds numbers.

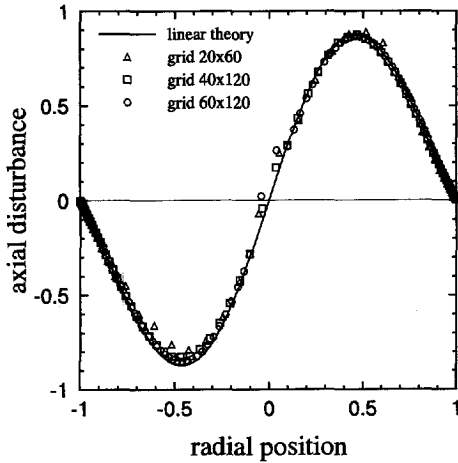


Figure C.10: Normalized axial disturbance velocity profiles at $Re=1500$ for several meshes. $Ek=15.4$.

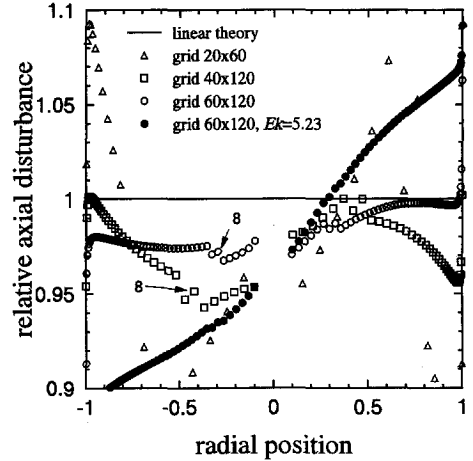


Figure C.11: Ratio of calculated axial disturbance velocities to that of the linear solution at $Re=1500$. $Ek=15.4$.

In figure C.11 the disturbance velocities for several meshes are plotted as a ratio to the linear solution. Clearly, the grid 20×60 is too coarse. Also the grid points closest to the pipe axis show large erroneous velocities and plotted as a ratio to linear solution they fall outside the scale of figure C.11. From figure C.11 we can conclude that the differences between the disturbance velocity and the linear solution is approximately 10% for a 20×60 grid, 5% for 40×120 , and 2.5% for 60×120 . As the maximum disturbance velocity for this case is approximately 1% of the centerline velocity, the inaccuracy of the numerical computation is 0.025% of the centerline velocity for the finest grid, which seems sufficient for our purpose.

The irregularities around the 8th grid point from the center as shown in figure C.11 (labeled with '8'; the innermost points fall outside the scale of the graph) are due to the change from the equidistant grid in the center to the refined grid near the wall. For comparison, the disturbance for the conditions in our pipe, i.e. $Ek=5.23$, is included. The axial disturbance velocities are then no longer accurately represented by the linear solution at this Reynolds number for this smaller Ekman number.

Figure C.11 clearly shows that our fit procedure slightly overestimates the centerline velocity since the disturbance velocities near the center do not approach zero. This introduces an asymmetry in disturbance velocities. However, this effect is much smaller than the asymmetry

introduced by non-linear effects. Thus, the linear solution is not applicable at higher Reynolds numbers. For $Re=1\,500$ and $Ek=15.4$ the inaccuracy is approximately 0.025% of the centerline velocity and it is therefore believed that the use of a 60×120 grid is sufficient to accurately capture the effects of the Coriolis force in the range of the Reynolds numbers studied. Now that we have established the performance of the numerical code, we can compare our measurements of the axial velocity profiles with those predicted by the numerical computations.

C.4.4 Comparison with measurements

Due to the constant impressed pressure gradient, the flow rate decreases when a secondary flow as a result of the Coriolis force develops. Consequently, the Reynolds number for a specific run of the numerical computations can be determined only after the flow has reached the fully developed state. It also takes a long time for the calculation to reach a steady flow rate. Although a constant impressed pressure gradient may be convenient for stationary turbulent flows, for developing and transitional flows a constant flow rate driven system is to be preferred and such an option should be included in numerical codes.

The calculations have been performed for several pressure gradients. The Reynolds numbers were defined with the bulk velocity, e.g. $Re=14\,100$ corresponds to a pressure gradient for $Re=15\,000$ in absence of Coriolis force effects. We measured the axial velocity profiles in vertical and horizontal direction at the bulk velocity values obtained from our computations, and we compare the velocity profiles in figure C.12. The lines represent the calculated profiles whereas the markers indicate measured velocities. All velocities are normalized with the centerline velocity. The agreement between the calculations and the measurements is good. Although, quantitatively the agreement is far from perfect, the qualitative agreement is excellent. It is clear that the asymmetry increases with the Reynolds number. Also, for both the horizontal and vertical profiles the shape of the measured profiles are in excellent agreement with those obtained from the calculations. Even a subtle detail like the behavior at positive vertical positions is reproduced. To show this more clearly, we plot in figure C.13 the difference between the vertical velocity profile and the parabola normalized with the centerline velocity. For positive values of the vertical coordinate, the measured velocities are smaller than for the parabolic profile at $Re=2\,500$ and $Re=4\,900$ whereas they are larger at $Re=9\,600$ and $Re=14\,100$. This was also predicted by the numerical computations, although the effect in the measurements is stronger. Note that linear theory does not predict such behavior.

Despite the fact that the air temperature exceeded the water temperature by 0.2°C the agreement between the measurements and the calculations is nevertheless quite good. Even very weak convection cells or swirl could displace or rotate the secondary flow induced by the Coriolis force. Keeping this sensitivity in mind, we feel that the comparison between the measured and the calculated axial velocity profiles presents strong proof that the asymmetry in the velocity profiles, under closely matched temperature conditions, is for the largest part due to the rotation of the earth.

If figure C.12 is compared to figure C.6 it is clear that at large Reynolds numbers, the linear solution by Benton is no longer valid and the nonlinear effects strongly limit the magnitude of the disturbance in comparison with the linear theory. In figures C.14 and C.15 the disturbance stream functions are given for $Re=2\,500$ and $Re=26\,500$. Although both plots are very similar, at high Reynolds numbers it can be seen that the cells are no longer symmetric but shifted to

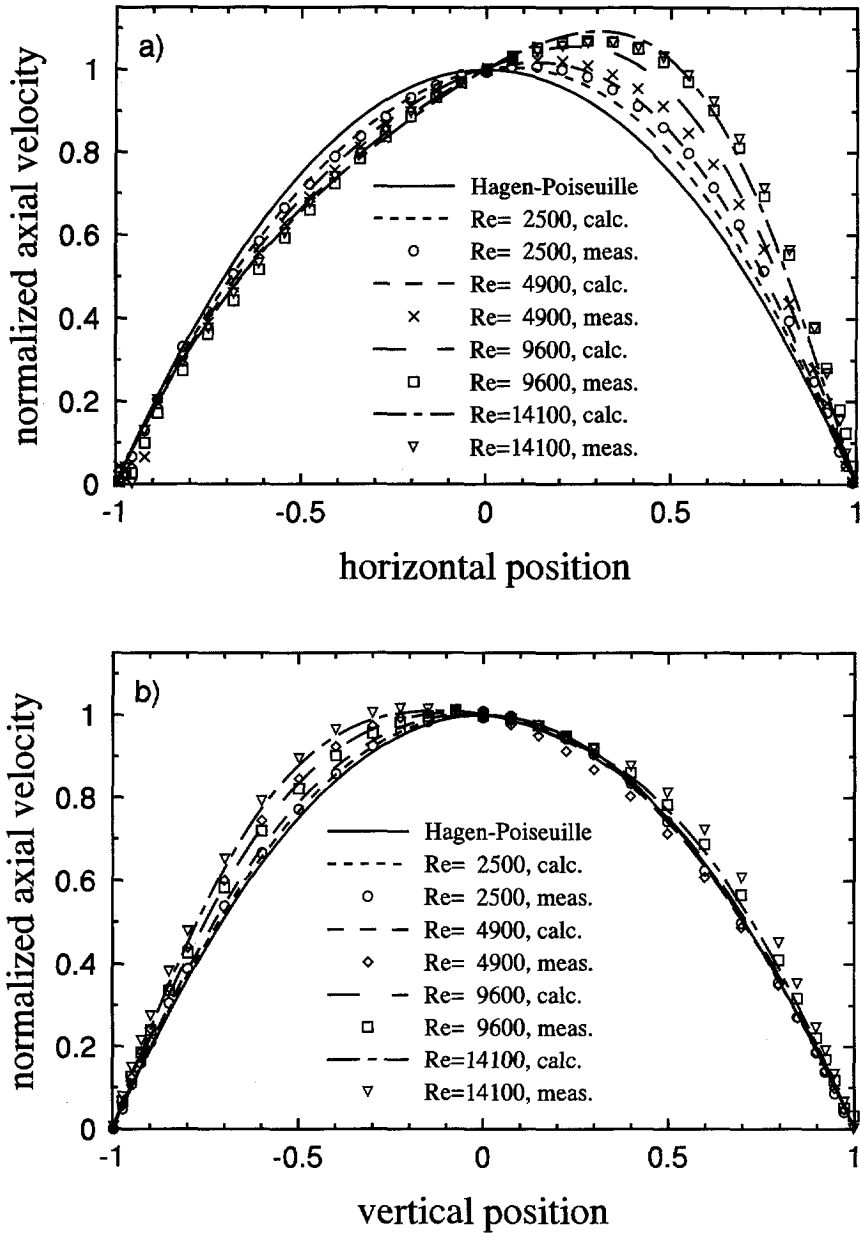


Figure C.12: Comparison between calculated (lines) and measured (markers) axial disturbance velocity profiles in a) horizontal and b) vertical direction for various Reynolds numbers.

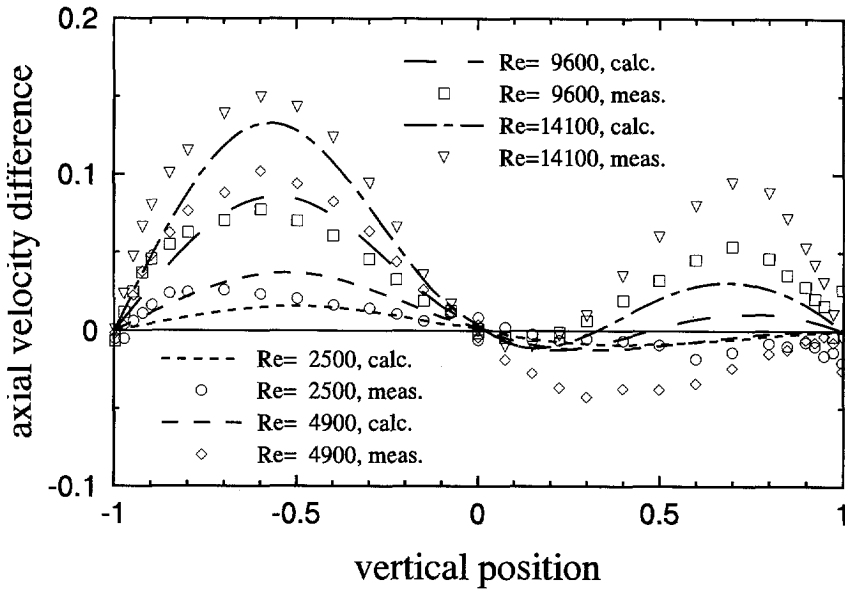


Figure C.13: Comparison between calculated (lines) and measured (markers) difference between the axial disturbance velocity profiles in vertical direction and the parabola for various Reynolds numbers. The results are normalized with the centerline velocity.

the right in the direction of the Coriolis force. The corresponding axial velocity contours are shown in figures C.16 and C.17. At $Re=26\,500$ the axial velocity profile is strongly asymmetric and the isolines are no longer circular in shape.

The Coriolis force not only distorts the axial velocity profile but it also increases the frictional drag in comparison with that for Hagen–Poiseuille flow. The common way to plot the frictional

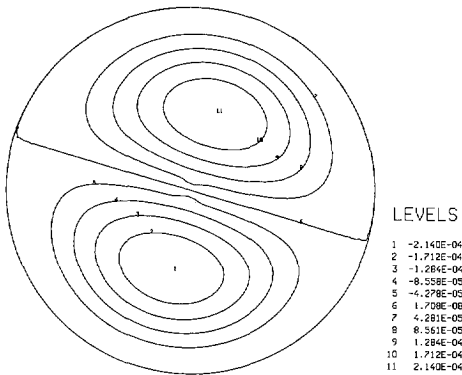


Figure C.14: Disturbance stream function at $Re=2\,500$ based on bulk velocity.

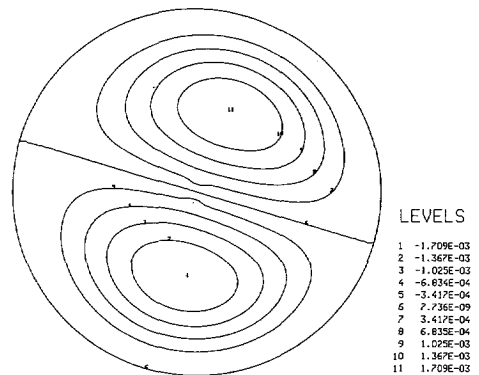


Figure C.15: Disturbance stream function at $Re=26\,500$ based on bulk velocity.

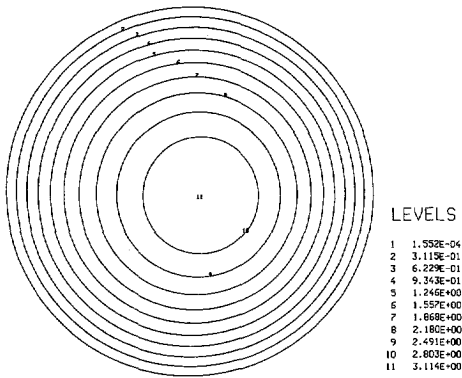


Figure C.16: Axial velocity contours at $Re=2500$ based on bulk velocity.

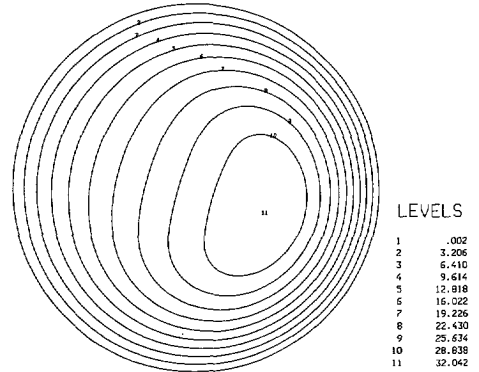


Figure C.17: Axial velocity contours at $Re=26500$ based on bulk velocity.

drag is in terms of a so-called Moody-diagram; friction factor vs. Reynolds number where the friction factor f_M is calculated in the following way:

$$f_M = \frac{D \Delta p}{\frac{1}{2} \rho \bar{W}^2 L} \tag{C.37}$$

with Δp the measured pressure drop over a pipe length L . For a Hagen-Poiseuille flow the relationship between f_M and Re is $f_M=64/Re$. If the length of the pipe is not sufficient to allow for a fully developed flow at the measurement position, this also results in a higher frictional drag compared with the fully developed flow. By plotting the measurements of the friction factor together with the calculated results of the fully developed pipe flow subject to Coriolis force (see figure C.18), one can assess the contribution of the Coriolis force in the deviation from the theoretical line for the Hagen-Poiseuille flow as opposed to the contribution to f_M as a result of the finite length of the pipe. At higher Reynolds numbers the length of the pipe is clearly insufficient to allow the flow to become fully developed. The entry length formula for pipe flow (see equation (5.1) at page (5.1)) based on the 99% developed center line velocity criterion, gives for a pipe our 32 m length a maximum Reynolds number of fully developed flow of $Re=14\,300$. This is in excellent agreement with the point at which our measurements begin to deviate from the calculation results. Coriolis force. We can also see that even at very high Reynolds numbers such as $Re=40\,000$, the Coriolis force is mainly responsible for the deviation in frictional drag from the Hagen-Poiseuille line.

C.5 Curved pipe

The Coriolis force leads to a secondary flow in the form of two cells similar to the circulation known in a pipe flow after a bend. Inasmuch it is preferable not to stop the rotation of the earth, it might be possible to counteract the effects of the Coriolis force by giving a slight curvature to the pipe. In this section, we investigate this option somewhat further.

The flow problem in slightly curved pipes was already solved by Dean (1927, 1928). He

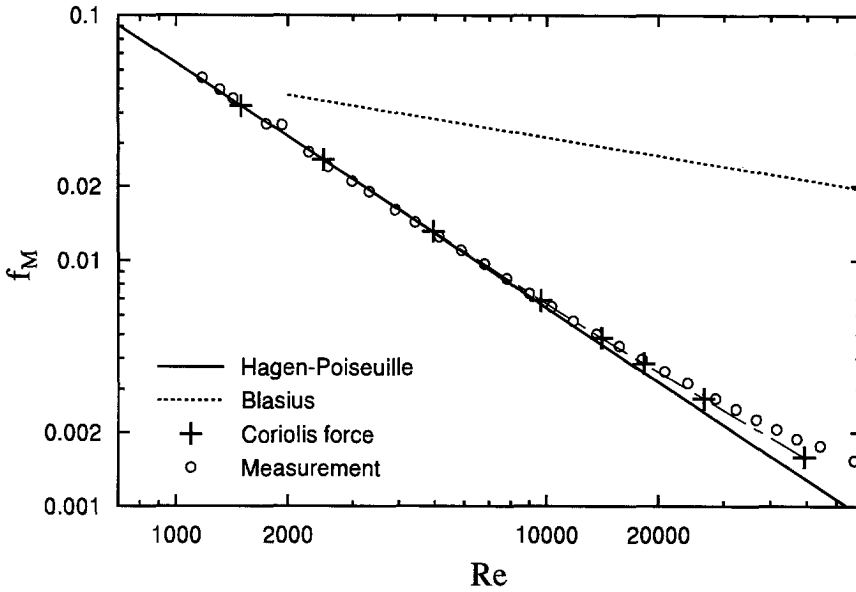


Figure C.18: Moody-diagram, friction factor f vs. Reynolds number Re , for the experimental setup and the numerical results including the Coriolis force.

solved the equations of motion linearized for small values of the curvature ratio $D/2R$ where R is the radius of curvature of the pipe with diameter D . The equations of motion in the cross-sectional plane used by Dean (1927) are essentially a balance between the centrifugal force and the viscous force; this is similar to the case of the Coriolis force where we had a balance between the viscous and Coriolis force. The ratio of the centrifugal force, scaling as $\frac{\bar{W}^2}{R}$, to the viscous force, scaling as $\nu \frac{\bar{W}}{D^2}$, leads to the characteristic number³:

$$\frac{\frac{\bar{W}^2}{R}}{\nu \frac{\bar{W}}{D^2}} = \frac{\bar{W} D D}{\nu R} = Re \cdot \frac{D}{R} \tag{C.38}$$

i.e. the Reynolds number times twice the curvature ratio. Dean's (1927) solution of the disturbance velocity field is:

$$\frac{u'_r}{\bar{W}} = \frac{Re D}{288 R} \sin \theta (1 - \varrho^2)^2 (4 - \varrho^2) \tag{C.39}$$

$$\frac{u'_\theta}{\bar{W}} = \frac{Re D}{288 R} \cos \theta (1 - \varrho^2) (4 - 23\varrho^2 + 7\varrho^4) \tag{C.40}$$

$$\frac{u'_z}{\bar{W}} = (1 - \varrho^2) \left[-\frac{3D\varrho \sin \theta}{4R} + \frac{Re^2 D \varrho \sin \theta}{11520 R} (19 - 21\varrho^2 + 9\varrho^4 - \varrho^6) \right] \tag{C.41}$$

³This dimensionless group is not equal to the Dean number (Dean 1928): $De = Re^2 D/R$. Sometimes the Dean number is defined as $(2De)^{1/2}$ (e.g. Berger *et al.* 1983).

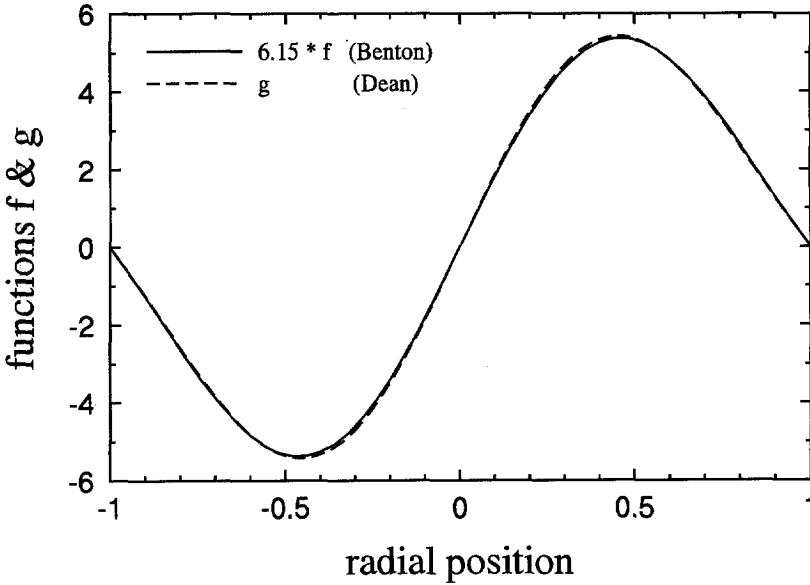


Figure C.19: Comparison of functions $f(\varrho)$ and $g(\varrho)$.

The term $-(1 - \varrho^2) \frac{3Dg \sin \theta}{4R}$ is present only in the exact solution of the linearized equations and is absent in the series solution proposed by Dean (1928). For the flows studied here, i.e. large Reynolds number flows, this term can be safely disregarded compared to the second term which depends on Re^2 .

If we would employ curvature to cancel Coriolis force effects, the axial disturbances described by equations (C.41) and (C.35) would have to counterbalance, which leads to:

$$\frac{Re^2 D}{11520R} g(\varrho) \sin \theta = \frac{Re}{2^9 3^2 Ek} f(\varrho) \sin \theta \tag{C.42}$$

$$\begin{aligned} \text{where } f(\varrho) &= \varrho (1 - \varrho^2) [3 - 3\varrho^2 + \varrho^4] \\ g(\varrho) &= \varrho (1 - \varrho^2) [19 - 21\varrho^2 + 9\varrho^4 - \varrho^6] \end{aligned}$$

First we investigate the form both the disturbance profiles. Figure C.19 shows functions $f(\varrho)$ and $g(\varrho)$. The disturbances are practically identical in shape when we multiply $f(\varrho)$ by the factor 6.15; $g(\varrho) \approx 6.15f(\varrho)$. Since the Ekman number is constant, equation (C.42) immediately shows that the curvature would have to be adjusted for each Reynolds number.

As an example, we compute the curvature needed to counteract the Coriolis force effects for $Re=10\,000$. Note that this computation is meant just to give an idea of the amount of curvature needed since the linear approximation is no longer valid for $Re=10\,000$. Using the similarity between $f(\varrho)$ and $g(\varrho)$ and using $Ek=5.23$ (see equation (C.11)) gives the equation

for the radius of curvature for our pipe:

$$R = \frac{2^9 3^2 Re \cdot D \cdot 6.15 \cdot 5.23}{11520} = 12.879 Re \cdot D \quad (\text{C.43})$$

For $Re=10\,000$ the radius of curvature then becomes $R=5151.6$ m. With a length of the pipe of $L=32$ m the maximum deviation from a straight line, Δ , would be:

$$\Delta \approx \frac{1}{2}R \left\{ 1 - \cos\left(\frac{L}{2R}\right) \right\} = 0.012\text{m} \quad (\text{C.44})$$

As the construction of the pipe supports allow for displacements this size, it should be possible to correct for the Coriolis force effects by using pipe curvature.

To present here an other example of the important influence that these small disturbance sources such as curvature or Coriolis force can have a large effect, we refer to Reshotko (1958), who performed stability experiments in a 5 cm diameter pipe up to $Re=16\,000$ using air and also found asymmetric velocity profiles. The asymmetry was more pronounced at higher Re and varied during the day. Reshotko attributed the asymmetry to lateral deflections of the pipe, either due to accidental misalignment or to constrained thermal expansion of the pipe which would lead to buckling. He found that misalignments as little as 0.25 mm can cause asymmetries of the order of 5%. However, as we have seen previously, the Coriolis force effects for these high Re flows can also not be neglected. Reshotko's facility is located in Pasadena, USA (latitude 34° north). If oriented in the most favorable direction, i.e. north-south, we would get, according to equation (C.11), for air in a 50.8 mm pipe: $Ek=71.5$. Substitution in equation (C.36) gives that the maximum axial velocity disturbance according to linear theory is 4% of the bulk velocity. So, Reshotko had a combined Coriolis force and curvature effect disturbing the flow that to a certain extend was able to (partly) cancel out these two effects. He states that "by careful alignment a pipe flow was established whose velocities were symmetric to within 5% of the local values". He does not claim that he can always adjust the alignment such that the velocity profiles will be symmetric.

As we have seen in this section, the curvature needed to counteract the effects of the Coriolis force has to vary with the Reynolds number which makes this method rather impractical. Given the rotational speed of the earth, suppression of Coriolis force effects can be obtained by building a pipe-flow facility at the equator (in the north-south direction) or tilting the one in Delft to 52° . Both possibilities have not yet been seriously studied. For our pipe facility in Delft, an alternative would be to reduce the pipe diameter, but this makes studying details of the flow more difficult. Increasing the viscosity of the fluid, e.g. by adding glucose, is a useful option which would also be beneficial for the suppression of buoyancy driven secondary flows.

Appendix D

Multiple transition points

Abstract

In this appendix we present several common features that can be found in the Newtonian stability measurements in this thesis and those by Boere (1995). These suggest that the multiple transition points in both studies, although found at different Reynolds numbers, are caused by a common mechanism.

D.1 Introduction

The occurrence of multiple transition points, which we have observed in our experiments discussed in section 6.3.2 is very interesting but not understood. It is not obvious that increasing the disturbance velocity can cause relaminarization of the flow. An indication that these multiple transition points are indeed a real phenomenon and not an artefact of our particular experimental setup is the fact that in the same facility, but with a slightly different settling chamber and another configuration of the test sections, Boere (1995) also found multiple transition points but at much lower Reynolds numbers. For this facility, the maximum Reynolds number for which the undisturbed flow remains laminar, i.e. the natural transition Reynolds number, was found to be much smaller, i.e. 30 000, than in the almost identical facility discussed in chapter 5 for which the flow was laminar up to $Re > 60\,000$.

Comparison of the stability measurements by Boere (1995) and our stability measurements may give some indication of the origin of the multiple transition points and at the same time may reveal some common features. This is discussed in the next section. Our stability measurements will be labeled “Draad” when shown together with Boere’s results.

D.2 Stability measurements

Boere (1995) performed measurements in the same experimental setup but at that time the natural transition Reynolds number was found to be in the range of $Re = 27\,000 - 32\,000$. The reason for this smaller natural transition Reynolds number remains unclear, but a possible cause may have been minute amounts of dirt blocking the fine screen mounted just in front of the contraction in the settling chamber, in particular close to the wall. For a more detailed discussion on the natural transition Reynolds number see section 5.8.4.

Boere also found multiple transition points in his measurements. The results of Boere should be divided into series A¹ and B according to the experimental setup used (as shown in figure D.1). The major change between A and B was the movement of the injection position 2m upstream. The multiple transition points were observed only in series-A and after this change,

¹Measurements for $\Delta V = 87\text{mm}^3$ of series Boere-A are not incorporated in figures 5.12 till 5.15 of Boere ².

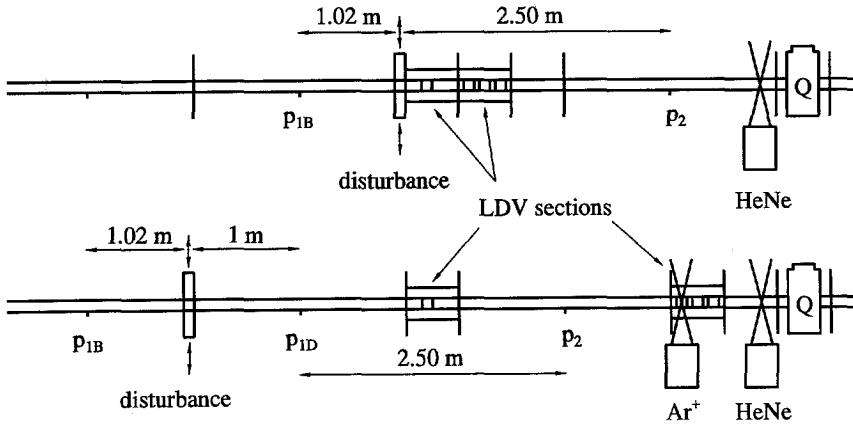


Figure D.1: Configurations of the pipe segments and the measurement sections during measurement series Boere-A (top) & B (bottom). The configuration for the experiments by Draad is identical to that of Boere-B with the exception of the location of the upstream pressure hole. Boere-B measured the pressure drop using pressure holes p_{1B} and p_2 whereas Draad used p_{1D} and p_2 .

the multiple transition points disappeared.

Furthermore, Boere found only multiple transition points for $\Delta V = 87\text{mm}^3$. In figure D.2a these measurements are compared with the measurements of series B and our measurements. Boere-A shows a drastic fall in critical disturbance velocity similar to Draad with the exception of the multiple transition points which were not present in measurements by Draad, where they were found only for $\Delta V=17$ and 35mm^3 . However, the fall in critical disturbance velocity is found at much smaller Re in Boere-A than in Draad. The Boere-B data show no sharp fall in critical disturbance velocity $v_{i,c}$.

The three measurements for the absolute critical velocity do not seem to coincide but this can be explained by the rise in water temperature as the summer progressed. For Boere-A, Boere-B, and Draad the average water temperature was 20.0°C , 21.8°C , and 24.4°C respectively. At constant Re , an increase in temperature results in a decrease in viscosity and therefore in bulk velocity. Correction for this effect by normalizing the critical disturbance velocity with the bulk velocity giving the critical relative disturbance velocity $v_{i,c}^*$ shows that the three measurements do coincide as shown in figure D.2b. This stresses the importance of scaling the results³. The fact that the measurements coincide, at least in one region, gives us more confidence in our experimental results.

The measurements by Boere together with our measurements are shown in figure D.3 where we use dimensionless parameters $v_{i,c}^*$ and α^* (defined in section 6.2.5). A problem with the measurements by Boere is that at the time we were unaware of the location and the extent of multiple transition points so that series A and B are both incomplete and complementary. The only overlapping measurement is at $\Delta V = 87\text{mm}^3$, which is unfortunately located in a very sensitive zone in the instability diagram as will be shown below. All measurements for $\Delta V \leq 87\text{mm}^3$

³The absolute disturbance velocities shown in figure 5.14 of Boere (1995) are 4 times too large. Relative disturbance velocities shown in other figures are correct.

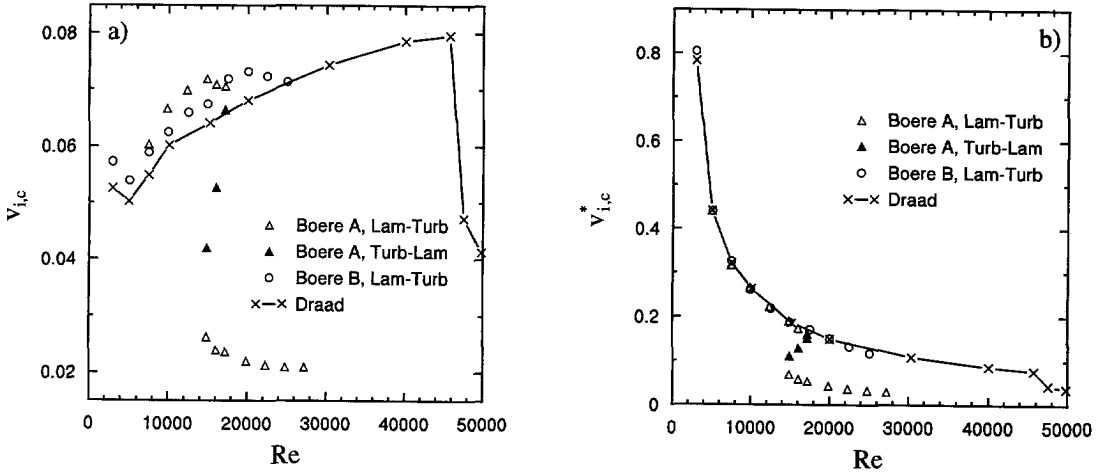


Figure D.2: Comparison of absolute and critical relative disturbance velocity vs. Re for $\Delta V=87\text{mm}^3$ between measurements series by Boere and Draad.

are located on the right hand side of the line $\Delta V=87\text{mm}^3$ and represent series-B. Measurements with $\Delta V \geq 87\text{mm}^3$ are located at the left hand side of this line and represent series Boere-A. The combinations of D_s and A used in the three experiments are listed in table D.1⁴.

The measurements series Boere-B is carried out using the same configuration as the measurements by Draad (i.e. all other measurements in chapter 6) and these results show a quite reasonable agreement with those of Draad as follows from figure D.3. For very large α^* , exceeding 25, Boere-B shows slightly larger critical relative disturbance velocities than Draad. On the other hand, the Boere-A experiment shows radically different behavior than found in Draad's experiment. At very small α^* , i.e. till approximately 0.2, both measurements are in reasonable agreement, but with increasing α^* , the critical relative disturbance velocities in the measurements Boere-A decrease strongly, approaching a minimum near $\alpha^* \approx 1$ whereas the measurements by Draad show at most a small decrease or mostly even a slight increase. The behavior shown by Boere-A in figure D.3b is very similar to that found by Draad above $Re=40\,000$. This is because, the multiple transition points at $Re=15\,000$ are located at α^* values near those of the multiple transition points of $Re=40\,000$ and $50\,000$ found by Draad. To facilitate comparison, the measurements for $Re=50\,000$ have been included in figure D.3b.

A possible explanation for this behavior is an interaction between the added disturbances and small natural disturbances present in the laminar flow as the natural transition point is approached. However, this explanation is not very convincing because for both series A and B performed by Boere, the natural transition Reynolds number varied between 27 000 and 32 000 and we did not observe the multiple transition points in series-B. The main difference between Boere series A and B is the movement of the injection flange 2 m upstream. Perhaps the injection flange for both series was mounted in a slightly different different way resulting in a

⁴In his pressure measurements, the upstream pressure hole was located $25.5D$ upstream of the disturbance and not $13D$ as indicated in Boere (1995)

Table D.1: Configurations for the three measurement series Boere-A & B and Draad. The axial positions are relative to the disturbance. Negative numbers indicate a position upstream of the disturbance. Values are given in physical length as well as number of pipe diameters.

Series	D_s (mm)	A (mm)	ΔV (mm ³)	$z(p_1)$	$z(p_2)$	$z(\text{Ar}^+)$	$z(\text{HeNe})$
Boere-A	4.7	4.99	87				
	4.7	9.82	170				
	12	1.7	192	-1.02 m	2.50 m		3.36 m
	12	3.01	340	-25.5 D	62.5 D		86 D
	12	4.51	510				
	12	10.28	1163				
Boere-B	4.7	1.00	17	-1.02 m	3.50 m	4.6 m	5.36 m
	4.7	1.99	35	-25.5 D	87.5 D	115 D	134 D
	4.7	4.99	87				
Draad	4.7	1.00	17				
	4.7	2.00	35				
	4.7	4.99	87				
	4.7	10.01	174	1.00 m	3.50 m	4.6 m	5.36 m
	12	3.01	339	25 D	87.5 D	134 D	115 D
	12	4.99	565				
	12	10.01	1131				

tiny change in disturbance shape. Another possibility is that in series-B, the LDV measurement section was placed at a larger distance downstream of the disturbance than in series-A, i.e. at 260 mm in series-A to 2260 mm in series-B (these values indicate the position of the thin sheet relative to the injection location). Possibly, an interaction between the disturbance and the thin sheet replacing the pipe wall in the measurement section may lead to a different transition behavior. Both these changes, the (dis)mounting of the injection flanges, the displacement of the test section may have altered the interaction between the flow and the added disturbance. This is in essence a receptivity problem, one of the most complex subjects in transition studies. The famous butterfly of Lorenz, known from chaos theory, might have done its trick also in our pipe.

Further research is needed on this subject and one experiment could be placing the LDV measurement sections even further downstream and check if the stability behavior of the flow changes or remove all test sections and place the HeNe-LDV directly in front of the pipe to track the centerline velocity. Alternatively, the interaction of a second, very small disturbance introduced further upstream, with the disturbance as used by Boere and Draad could be studied to disclose the source of the multiple transition points.

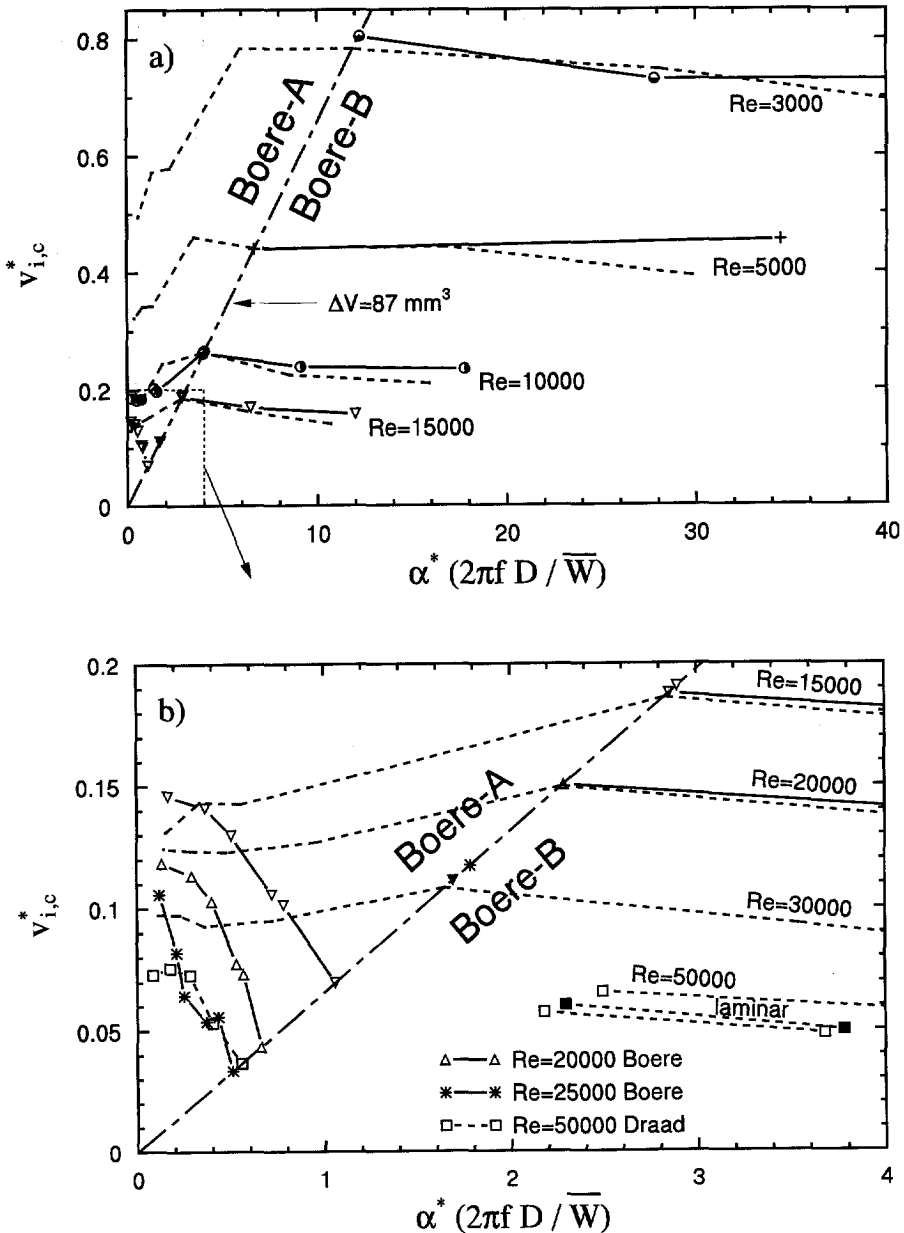


Figure D.3: Comparison of the critical relative disturbance velocity vs. dimensionless wavenumber between measurements by Boere (markers connected with solid lines) and Draad (dashed lines). The chain-dotted line represents the line for $\Delta V=87\text{mm}^3$ which marks the boundary between measurement series Boere-A and B. Solid markers indicate relaminarization with an increase in v_i^* . b) is an enlargement of a part of a) and the Boere-B measurements at $Re=20\,000$ and $30\,000$ as well as the Draad measurements for $Re=50\,000$ are included. The indication 'laminar' marks the part of the multiple transition region in between the relaminarization and the second transition line.

Appendix E

Non-Newtonian Moody diagram

Abstract

In this appendix we will discuss some of the inconsistencies found between the viscosity measurements and the shear-rate-dependent viscosity corrected Moody diagrams. Also, all measured viscosity curves and Moody diagrams are included in this appendix.

For most of the polymer solutions, the use of Re_w , based on the viscosity at the wall, results in a collapse of the laminar data onto the Hagen–Poiseuille line. However, for the 20 + 10 + 10 ppm as well as the 0.001 M NaCl solution, the data lie to the left of the Hagen–Poiseuille line, i.e. the measured viscosity seems to be too high. Since for most of the solutions, no such problem is found and the use of Re_w gives satisfactory results, we suspect that the sample of the fluid for which the viscosity is measured is probably not representative of the fluid in the pipe. Viscosity measurements of the demineralized water solutions with added sodium salt have been measured two months after the experiments. The Moody diagrams for the 0.01 M and the 0.1 M NaCl solution show a deviation to the right of the Hagen–Poiseuille line, especially for low Re_w values. This could be a result of aging.

E.1 Introduction

In chapter 7, we have discussed the most important results concerning the measured viscosity curves and the Moody diagrams for the polymer solutions. However, not all of the material was included there. To give a complete overview, all results are included in this appendix, including those already shown in chapter 7. We will not repeat our findings presented in chapter 7, but we concentrate on some of the inconsistencies found between the measured viscosity curves and the Moody diagrams that are corrected for the shear-rate-dependent viscosity using Re_w .

In the next section, we present all the measured viscosity curves. In the section thereafter, the Moody diagrams are discussed and the inconsistencies highlighted.

E.2 Viscosity curves

All measurements of the shear-rate-dependent viscosity have been performed using a concentric cylinder viscometer; the Contraves Low Shear LS-40. This is one of the few (concentric) viscometers that can measure the viscosity of dilute polymer solutions close to that of water at such low shear rates that even a η_0 (zero-shear-rate viscosity) value can be captured. In concentric cylinder viscometers, the fluid is sheared between two coaxial cylinders, see figure E.1. Usually, the outer cylinder, also known as 'cup', rotates. The inner cylinder, known as 'bob', is suspended from a torsional spring and the rotation of this spring is proportional to the shear stress. The torsion as a function of the rotational speed of the cup can be transformed into shear stress vs. shear rate data (see e.g. Collyer & Clegg 1988).

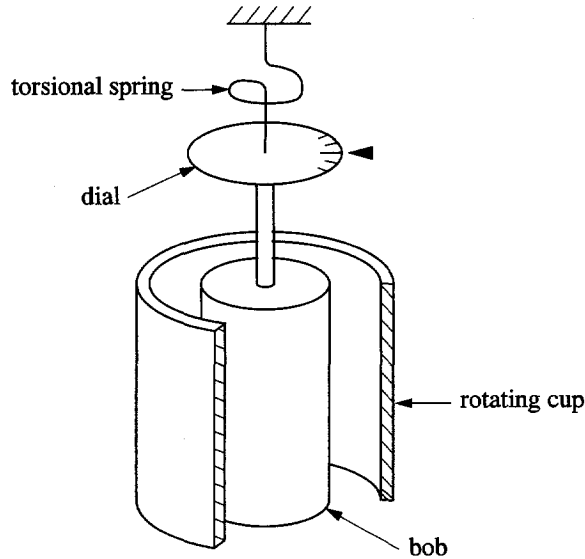


Figure E.1: Sketch of a concentric cylinder viscometer.

Fitting the Carreau model (equation 7.1) to the viscometer data in the way that we discussed in section 7.3.2 gives the parameter values listed in table E.1. The viscosity measurements are plotted together with the corresponding Carreau model in figures E.2 – E.8. Let us look at some of the results that have not been mentioned in chapter 7:

- The solutions in softened water shown in figure E.2 indicate a clear increase in viscosity when compared to water. In addition shear thinning behavior can be seen. Particularly the measurements for 40 ppm seem to show a zero-shear-rate plateau. The time constant is approximately 1 s and the power-law exponent slightly decreases from 0.90 to 0.86 after doubling the concentration. After circulating the 20 ppm solution for one additional day, the viscosity has decreased over the entire shear rate range by a factor of approximately 0.9.
- For very small shear rates we can see some scatter in the viscosity data in figure E.2. The scatter is already reduced by excluding all measurements where the torque is below 10% of its full range. Nevertheless, measurements within 10–20% of the range still show significant scatter. During a measurement, the LS-40 switches between ranges as the torque increases. The switch to a higher range is made when the torque has reached 20% of the next higher range. This explains the discontinuities in the data. During the measurement period, the LS-40 has been adjusted and the discontinuities have disappeared. Measurements taken with the adjusted instrument are labeled ‘b’ in table E.1.
- At shear rates of approximately 200s^{-1} and higher, the inner cylinder is no longer stably centered and oscillations were observed. Therefore, no measurements above these shear rates could be taken.

Table E.1: Carreau model parameters for the Superfloc A-110 polymer solutions used in the stability experiments. η_∞ is set to the solvent viscosity value, thus giving $\eta_\infty=0.904$ mPa.s.

Concentration (ppm)	Solvent (-)	Age (days)	η_0 (mPa.s)	λ (s)	n (-)
0	water		0.904	0	1
20	soft. water	1	1.47±0.05	1.02±0.87	0.901±0.010
20	„	2	1.33±0.02	1.13±0.99	0.913±0.010
40	„	1	1.94±0.02	1.16±0.27	0.862±0.006
20	dem. water	1	9.58±0.12	4.96±0.03	0.612±0.004
20	„	3	7.18±0.07	2.81±0.15	0.631±0.004
20+10+10	„	1	22.12±0.38	5.58±0.54	0.643±0.007
20+10	„	1 ^b	6.77±0.14	3.10±0.49	0.735±0.006
20+10+10	dem. water	1 ^b	15.21±0.29	4.05±0.35	0.641±0.006
20+10+10	dem. water	1	15.97 ^a	4.96 ^a	0.612 ^a
20+10+10	0.001M NaCl	1 ^b	3.37 ^c ±0.02	0.82±0.08	0.772±0.006
20+10+10	0.01M NaCl	1 ^b	1.43 ^{d,e} ±0.01	0.31±0.09	0.877±0.010
20+10+10	0.1M NaCl	1 ^b	0.995 ^d		1

^aCarreau parameters extrapolated from 20 ppm solution.

These are the values that have been used in the calculation of Re_w for the 20 + 10 + 10 ppm solution.

^bViscosity measurements performed on 2 months old fluid samples.

^cMoody diagram measurements after viscosity correction indicate a too high viscosity.

Thus in the calculation of Re_w , η_0 was reduced to 90% of the value listed in this table.

^dMoody diagram measurements after viscosity correction indicate a too low viscosity.

Despite the shortcomings, these values have been used.

^eThis value has been obtained after a correction procedure, see text for further explanation.

- As shown in figure E.5, measuring the same fluid sample of the 20 + 10 + 10 ppm solution in demineralized water two months later, results in a decrease in η_0 and λ of approximately 30% while the exponent n remains unchanged. Thus, aging is severe and viscosity measurements should be performed immediately after a sample has been taken. The solid line in figure E.5 indicates the Carreau model function that has been used to correct the Moody diagram for this solution, will be explained later in relation to equation E.2. Vlassopoulos & Schowalter (1994) mention that formaldehyde prevents aging and other antimicrobial agents also seem to have this effect. This is interesting but it should be checked to see if such a solution is allowed to be disposed of into the public sewer system. Disposal as chemical waste is rather expensive for nonflammable substances.
- In figure E.4 we show that the 20 + 10 ppm solution of Superfloc A-110 in demineralized water, measured two months later, shows quite different behavior from the 20 ppm and the 20 + 10 + 10 ppm solutions. Shear thinning is less and η_0 is even smaller than the 20 ppm solution on day 3. This unexpected behavior is most likely related to chemical degradation that seems to affect the low shear rate range much stronger than the high shear rate range. This is similar to the mechanical degradation of the 20 ppm solution in demineralized water.
- For the 0.1 M NaCl solution, the measurements are compared to the viscosity measurements for distilled water (see figure E.7). Both solutions show very similar behavior and for both two measurement runs are shown. As the viscosity of distilled water is constant and for this temperature equal to 0.898 mPa s, the measurement seems to overestimate the viscosity by 2.5%. For the small shear rates, the scatter is fairly large and the deviation between the two runs is obvious. For higher shear rates, a shear thickening behavior is measured for both water as well as the polymer solution. Since this is very unusual, particularly for water, this is likely to be an error in calibration of the LS-40 rather than a physical phenomenon. Thus, we corrected the polymer solution measurement using the water measurement as follows. Averaging the results of both runs and normalizing the viscosity of the 0.1 M NaCl solution with the measurements of distilled water according to

$$\hat{\eta} = \frac{\eta(0.1 \text{ M NaCl})}{\eta_{\text{measured}}(\text{water})} 0.898 \quad (\text{E.1})$$

where $\eta_{\text{water}}(26.4^\circ\text{C}) = 0.898 \text{ mPa s}$, gives the viscosity curve shown in figure E.8. Hardly any shear thinning is apparent and given the way this figure has been obtained, the viscosity for this solution can be assumed to be constant at a value of $\eta = 0.995 \text{ mPa s}$.

E.3 Viscosity corrected Moody diagram

In this section the Moody diagram measurements for the polymer solutions are reviewed. We plot the friction factor as a function of Re_w , the Reynolds number based on the viscosity at the wall (for an explanation we refer to section 7.4.2). Rather than repeating our findings of chapter 7, we concentrate on those measurements for which the laminar data do not collapse

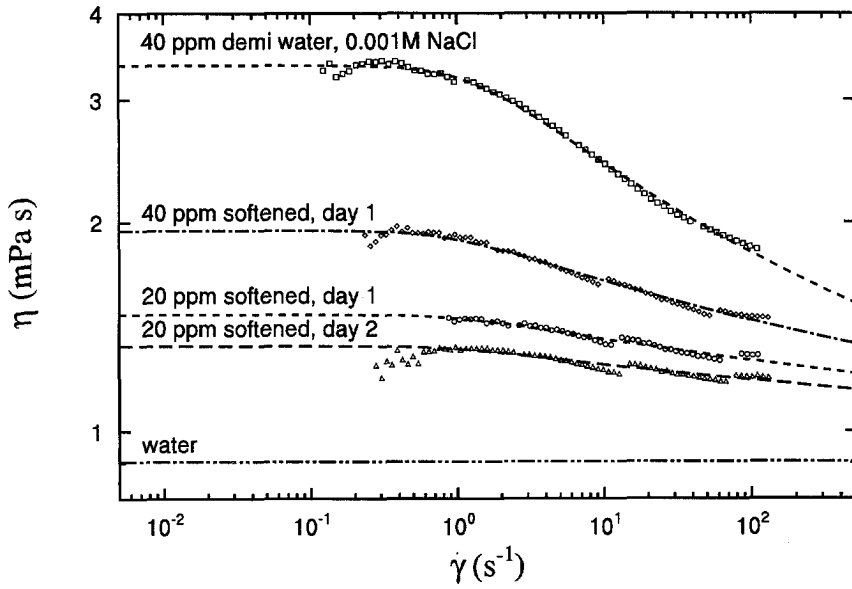


Figure E.2: Viscosity as a function of steady shear rate for several solutions of Superfloc A-110 in softened water. For comparison, a 20 + 10 + 10 ppm solution in demineralized water with addition of 0.001 M sodium chloride is shown.

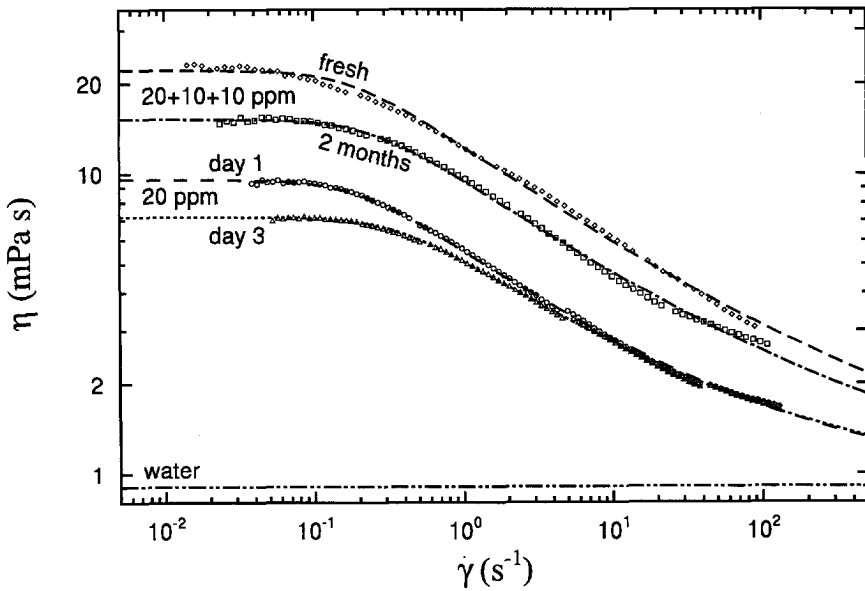


Figure E.3: Viscosity as a function of steady shear rate for several solutions of Superfloc A-110 in demineralized water. Note the mechanical degradation for the 20 ppm solution as well as the aging for the 20 + 10 + 10 ppm solution.

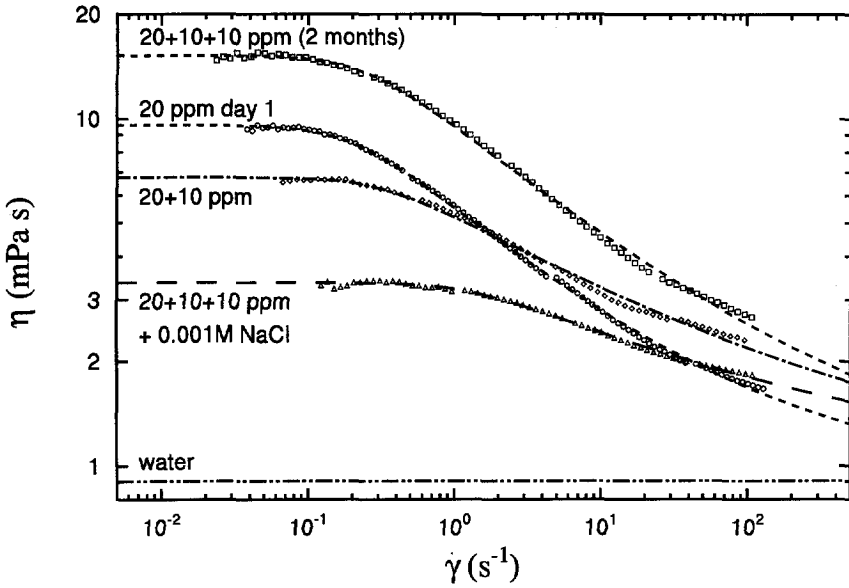


Figure E.4: Viscosity as a function of steady shear rate for several solutions of Superfloc A-110 in demineralized water. Note the unexpected behavior of the 20+10 ppm solution (also measured 2 months after the experiments) compared to the 20 ppm and the 20 + 10 + 10 ppm solution.

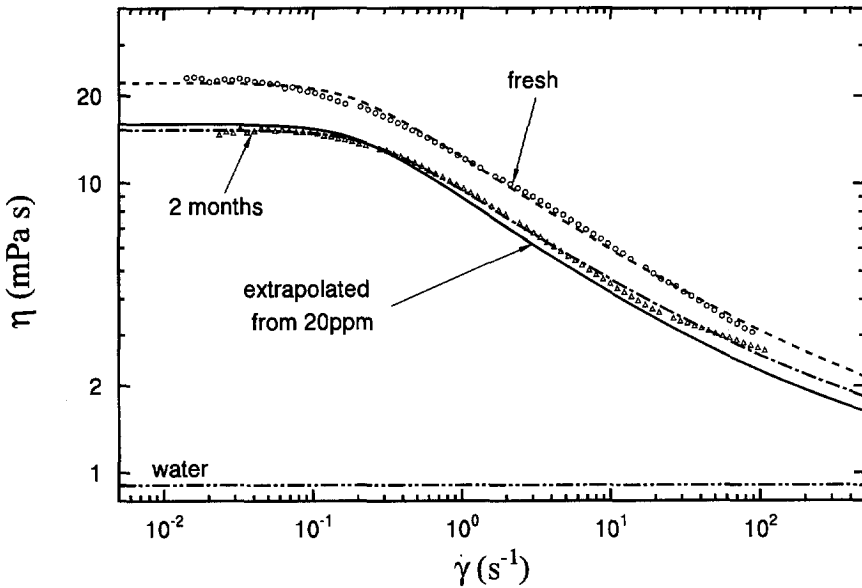


Figure E.5: Viscosity as a functions of steady shear rate for a 20 + 10 + 10 ppm solutions of Superfloc A-110 in demineralized water. The solid line is extrapolated from the viscosity measurements of the 20 ppm solution and represents the equation that has been used to correct the Moody diagram measurements for the 20+10+10 ppm solution.

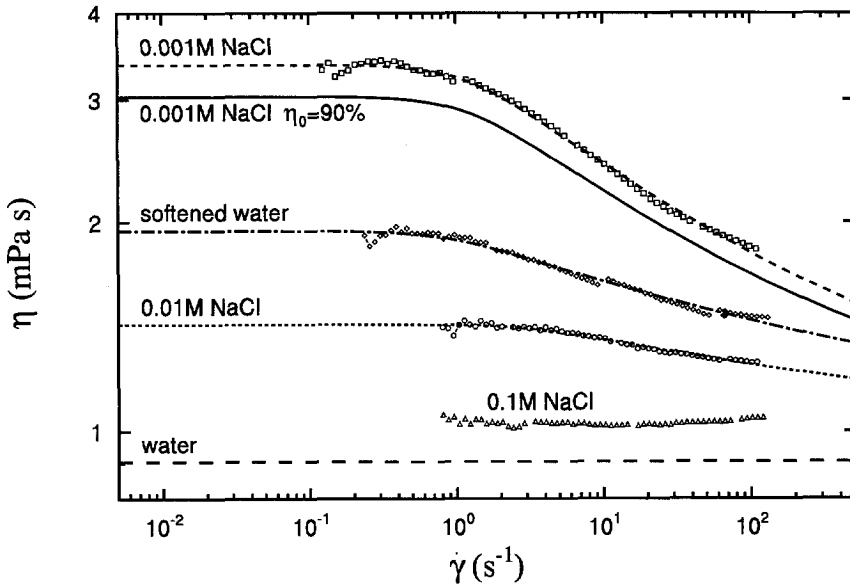


Figure E.6: Viscosity as a function of steady shear rate for the 20 + 10 + 10 ppm solution of Superfloc A-110 in demineralized water with various concentrations of sodium chloride. For comparison, the 40 ppm solution in softened water is plotted.

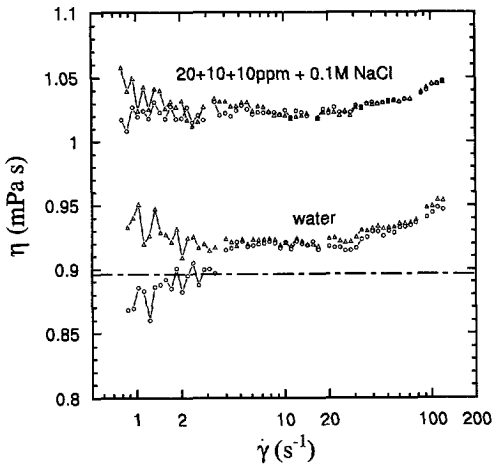


Figure E.7: Steady shear viscosity vs. shear rate for 0.1M NaCl solution and distilled water.

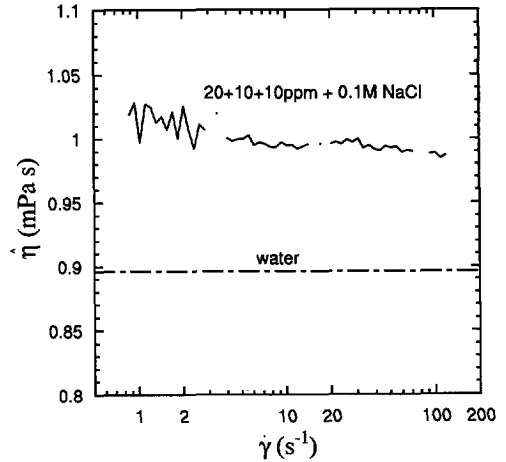


Figure E.8: Steady shear viscosity vs. shear rate for 0.1M NaCl solution and distilled water after normalizing the viscosity with that of water.

onto the Hagen–Poiseuille line. This is most likely caused by aging and fluid samples which are not representative for the fluid in the pipe.

Some of the problems we encountered are:

- From the Moody diagrams for the softened water solutions, figures E.9 and E.10, and that for the 20 ppm solution in demineralized water, figure E.11, it follows from the smaller drag reduction in the turbulent regime that mechanical degradation is present. Thus, mechanical degradation is present when the stability measurements are extended over several days. From stability measurements of the 20 ppm solution in demineralized water, it is shown that mechanical degradation also affects the stability of flow and the minimum transition Reynolds number. Perhaps, the antimicrobial agents which have been reported to prevent aging (Vlassopoulos & Schowalter 1994) could also be of help to reduce mechanical degradation. After all, although the mechanical forces cause the breaking of the polymers, the actual breaking is related to chemical processes. For the 20 ppm Superfloc A-110 solution in demineralized water, shown in figure E.11, the results of day 2 show only slight mechanical degradation. This is not surprising as the 'day 1' results were measured in the afternoon and the 'day 2' results in the early morning. This is due to the preparation and mixing time needed after adding concentrated polymer solution to the water in the system. The third day shows clearly degradation. The degradation seems to have been particularly severe between days 3 and 4. This is due to some experiments that were performed in that period at high flow rates for a relatively long time.
- The Moody data given in figure E.12 for the 20 + 10 + 10 ppm solution have been corrected for viscosity in three different ways. The one far to the left of the Hagen–Poiseuille line is obtained when using the viscosity function derived from the LS-40 measurements performed within a few days of the pipe-flow experiments. Obviously, the viscosity measured by the LS-40 is much higher than that of the fluid in the pipe. As other viscosity measurements matched perfectly with the Moody data, we must assume that the sample taken from the 20 + 10 + 10 ppm experiment most probably contains a higher concentration of polymer than was actually present in the pipe. This may be a result of the method of mixing. Concentrated polymer solution of 640 ppm is added to the reservoir where an impeller mixer enhances the stirring. At the bottom of the vessel the pump extracts fluid and after running through the facility, the fluid is discharged in the vessel just below the free surface. The fluid samples are all obtained at the free surface in the vessel rather than from the discharge opening just below this surface (with the exception of the 20 ppm solution in demineralized water). The fluid at the surface may not have been well mixed as velocities are very low and the distance to the impeller is large. The fluid samples are taken only 1 to 2 hours after adding the concentrated master solution and given the low mixing actions at the free surface, it is throughout possible that the polymer concentration of the sample is too high. The viscosity function found after storage for two months of the sample is quite different (see also table E.1). η_0 has decreased from 22 to 15 mPa s. The time constant λ and power-law exponent n have remained practically the same. Using these values, the laminar flow data shown in figure E.12 are much closer to the Hagen–Poiseuille line but the viscosity is still 15% too high. Furthermore,

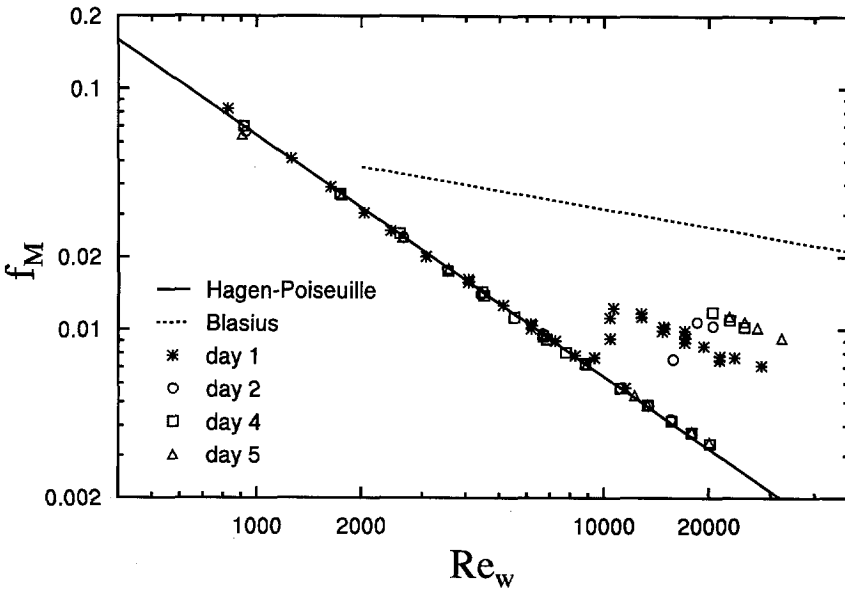


Figure E.9: Moody diagram for 20 ppm A-110 in softened water.

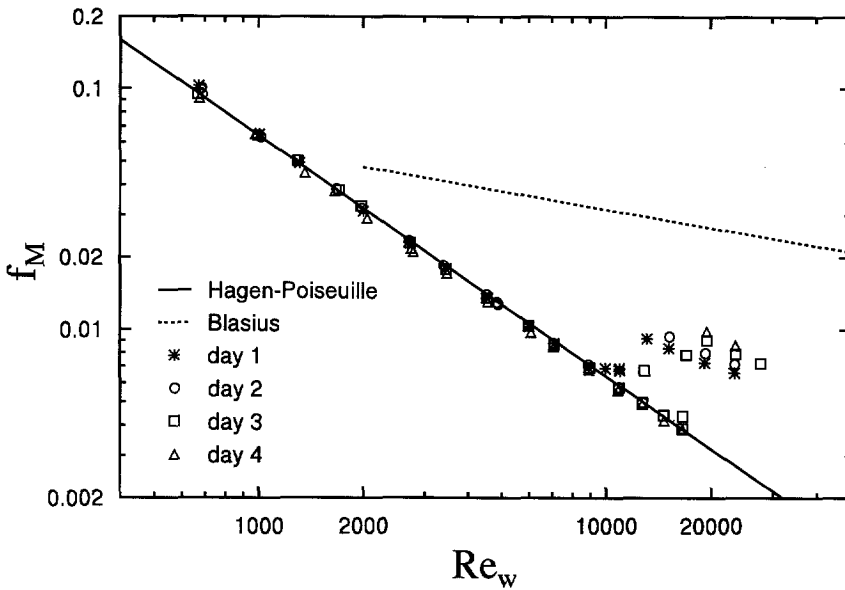


Figure E.10: Moody diagram for 40 ppm A-110 in softened water.

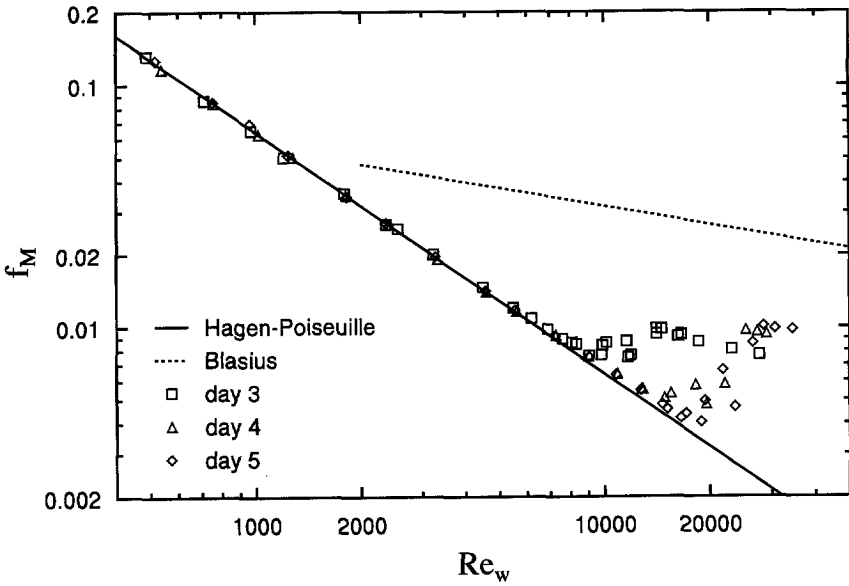
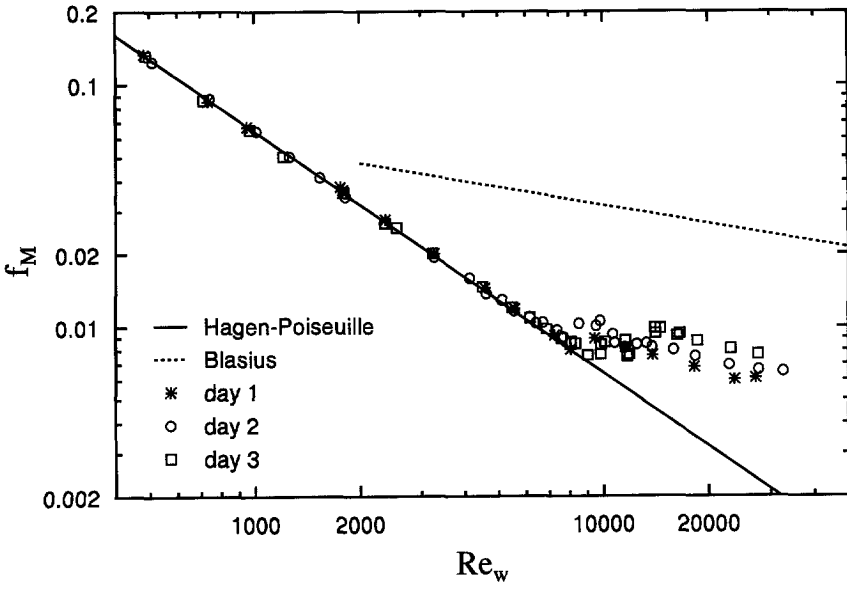


Figure E.11: Moody diagram of 20 ppm solution of Superfloc A-110 in demineralized water after circulation for several days; days 1 to 3 (top) and days 3 to 5 (bottom).

a two months old sample needs no longer be representative for the fluid used in the flow experiments since chemical degradation may have altered its properties.

As none of the viscosity measurements seem to result in a viscosity function which correctly transforms the Moody diagram, another approach has been followed for the 20 + 10 + 10 ppm solution. As both the 20 ppm as well as the 20 + 10 + 10 ppm fresh solutions are very similar in shape and λ and n values are almost identical, the 20 ppm viscosity function was used as a reference for the 20 + 10 + 10 ppm viscosity function. The laminar flow data in the Moody diagram can also be regarded as pipe viscometer data. The increase in viscosity at the lowest flow rates that is needed to shift the Moody data to the Hagen–Poiseuille line can be estimated to be 2.1 and 3.5 times that of water for the 20 ppm and 20 + 10 + 10 ppm solutions respectively. The zero-shear-rate viscosity for the 20 + 10 + 10 ppm solution is then extrapolated from that of the 20 ppm solution by:

$$\eta_0(20 + 10 + 10 \text{ ppm}) = \frac{3.5}{2.1} \eta_0(20 \text{ ppm}) \tag{E.2}$$

This assumes that the viscosity function is changed only through the level of η_0 and that the shape, determined by λ and n , remains unaltered. This viscosity function does a very good job in collapsing the data onto the Hagen–Poiseuille line as is illustrated in figure E.12. For this reason the extrapolated viscosity function is used further on to correct all 20 + 10 + 10 ppm measurements.

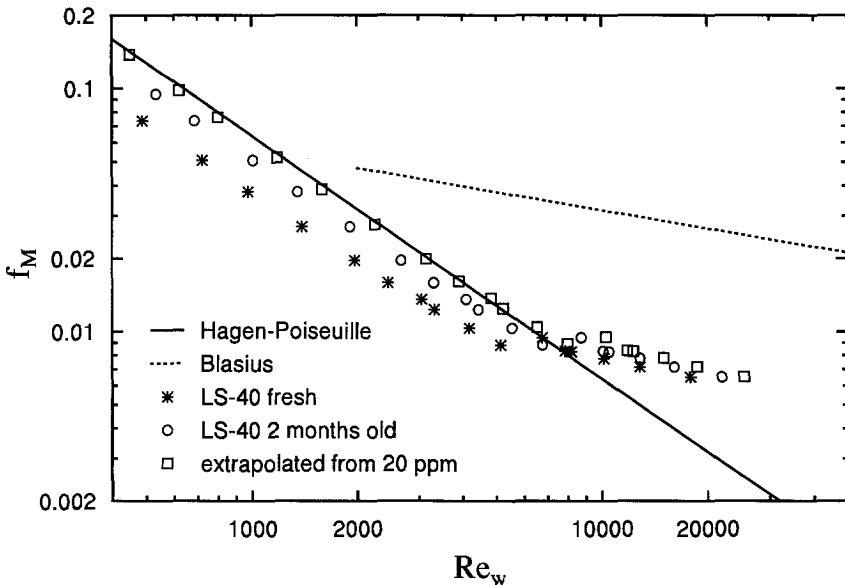


Figure E.12: Moody diagram of fresh 2) + 10 + 10 ppm Superfloc A-110 solution in demineralized water corrected using several viscosity curves measured with the Contraves Low-Shear LS-40 as well as one extrapolated from the 20 ppm solution.

- The viscosity functions of the 20+10 ppm Superfloc A-110 solution in demineralized water and the ones where sodium chloride was added have also been measured two months after the pipe experiments and may therefore be not entirely representative for the actual fluid used in the pipe experiments. The 20 + 10 ppm viscosity data does collapse the laminar flow data fairly well onto the Hagen–Poiseuille line, as we show in figure E.13. However, η_0 is smaller than that of a degraded 20 ppm solution, the power-law exponent $n=0.735$ whereas it ranges from 0.61 to 0.64 for the 20 and 20+10+10 ppm fresh solutions. Thus it is fair to doubt the 20 + 10 ppm viscosity measurements and the sample/mixing problem and chemical degradation may have cancelled each other. Nevertheless, as the Moody diagram data seems to have been properly corrected for viscosity effects, i.e. the viscosity function seems correct in the high shear rate range and this is sufficient for our purposes.
- The viscosity measurements of the 20+10+10 ppm Superfloc A-110 solution with 0.001 M NaCl added also gives a too large viscosity correction in the Moody diagram. For this reason the η_0 value was reduced to 90% of the measured value, for which case the laminar data collapse onto the Hagen–Poiseuille line, as is shown in figure E.14.
- For both the 0.01 M and the 0.1 M NaCl solution, the Moody diagram in figure E.14 shows that particularly at low Reynolds numbers, the measured viscosity is too low. This may be due to incorrect sampling leading to erroneous salt concentrations or to chemical degradation. However, as the largest deviations from the Hagen–Poiseuille line occur for low Re_w , where we did not perform any stability measurements, we used the measured values as listen in table E.1.

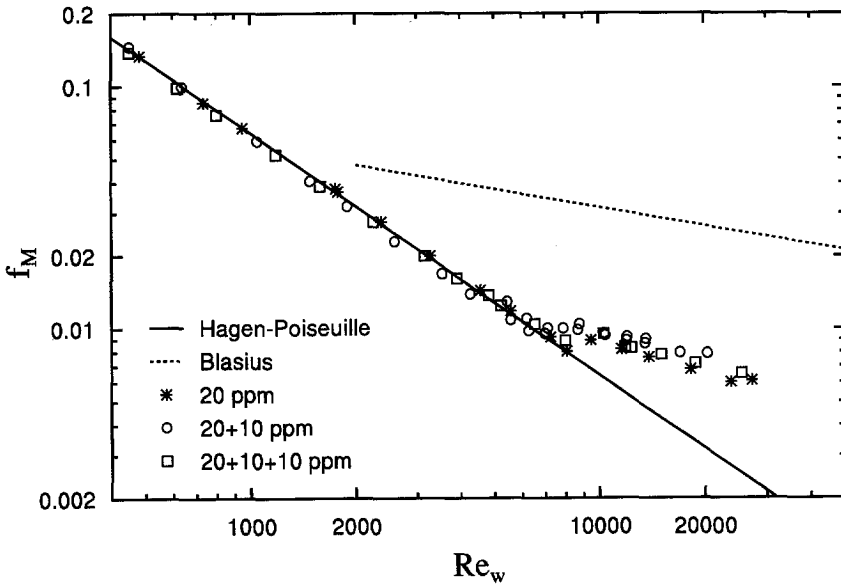


Figure E.13: Moody diagram of fresh Superfloc A-110 solutions in demineralized water at various concentrations.

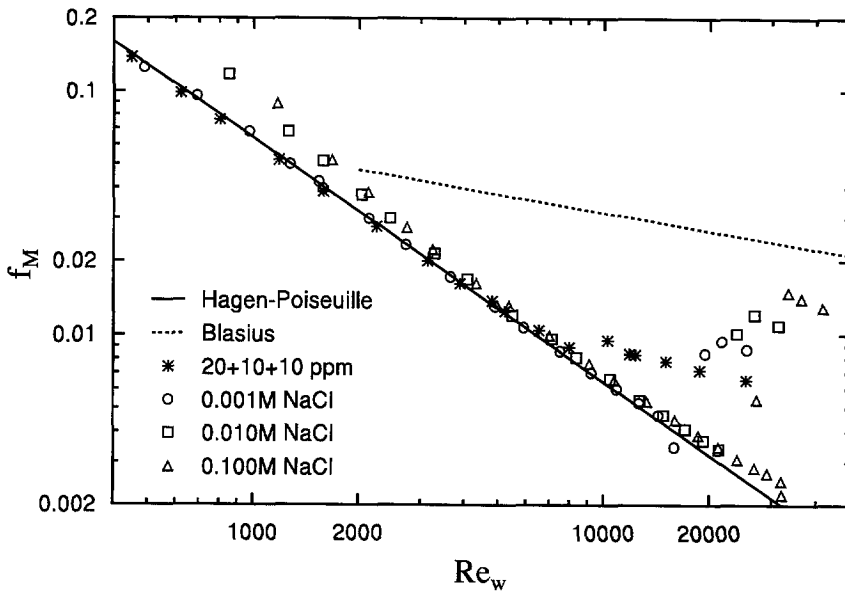


Figure E.14: Dependence of the Moody diagram of 20 + 10 + 10 ppm Superfloc A-110 solution on salt concentration.

Based on the viscosity measurements and the Moody diagram results, one of the most important rules to be followed in future experiments of this kind is that the great care should be taken to make sure that the fluid sample taken is representative for the fluid which was actually used during the Moody diagram measurements. One could think of tapping some fluid through one of the many pressure hole available or at least take a sample right in front of the discharge opening. Another vital aspect is that viscosity measurements should be performed as soon as possible after the fluid has been sampled to eliminate any chemical degradation influence.

Bibliography

- AANEN, L. 1995. *LDA- and DPIV-measurements in a pipe flow under transition*. Master Thesis MEAH-125. Delft University of Technology, Laboratory of Aero- & Hydrodynamics.
- BARK, F.H., & TINOCO, H. 1978. Stability of plane Poiseuille flow of a dilute suspension of slender fibres. *Journal of Fluid Mechanics*, **87**, part 2, 321-333.
- BARKER, S.J., & GILE, D. 1981. Experiments on heat-stabilized laminar boundary layers in water. *Journal of Fluid Mechanics*, **104**, 139-158.
- BATCHELOR, G.K. 1967. *An introduction to fluid dynamics*. Cambridge: Cambridge University Press.
- BAYLY, B.J., ORSZAG, S.A., & HERBERT, TH. 1988. Instability mechanisms in shear flow transition. *Annual Review of Fluid Mechanics*, **20**, 359-391.
- BENTON, G.S. 1956. The effect of the earth's rotation on laminar flow in pipes. *Transactions of the ASME, Journal of Applied Mechanics*, **23**, 123-127.
- BERGER, S.A., TALBOT, L., & YAO, L.-S. 1983. Flow in curved pipes. *Annual Review of Fluid Mechanics*, **15**, 461-512.
- BERGSTRÖM, L.B. 1993. Optimal growth of small disturbances in pipe Poiseuille flow. *Physics of Fluids A*, **5**(11), 2710-2720.
- BERMAN, N.S., & COOPER, E.E. 1972. Stability Studies in Pipe Flows Using Water and Dilute Polymer Solutions. *AIChE Journal*, **18**(2), 312-320.
- BEWERSDORFF, H.W. 1990. Drag reduction in surfactant solutions. *Pages 293-312 of: GYR, A. (ed), Structure of turbulence and drag reduction, IUTAM Symposium Zurich/Switzerland 1989*. Berlin Heidelberg: Springer Verlag.
- BEWERSDORFF, H.W. 1991. Turbulence structure of dilute polymer and surfactant solutions in artificially roughened pipes. *In: 6th European Drag Reduction working meeting*. Eindhoven University of Technology. 21-22 November.
- BEWERSDORFF, H.W., & SINGH, R.P. 1988. Turbulent drag reduction and relaminarisation by Xanthan gum. *Pages 333-348 of: Turbulence Management and Relaminarisation, IUTAM Symposium Bangalore/India 1987*. Berlin Heidelberg: Springer Verlag.
- BIRD, R.B., STEWART, W.E., & LIGHTFOOT, E.N. 1960. *Transport Phenomena*. New York: John Wiley & Sons.
- BIRD, R.B., ARMSTRONG, R.C., & HASSAGER, O. 1987a. *Dynamics of Polymeric Liquids ; Fluid Mechanics*. Second edn. Vol. 1. New York: John Wiley & Sons.
- BIRD, R.B., CURTISS, C.F., ARMSTRONG, R.C., & HASSAGER, O. 1987b. *Dynamics of Polymeric Liquids ; Kinetic Theory*. Second edn. Vol. 2. New York: John Wiley & Sons.
- BOERE, J.W.R.A. 1995. *Frequency and amplitude dependence of laminar-turbulent transition in pipe flow*. Master Thesis MEAH-129. Delft University of Technology, Laboratory of

- Aero- & Hydrodynamics. In Dutch.
- CANUTO, C., HUSSAINI, M.Y., QUATERONI, A., & ZANG, T.A. 1988. *Spectral Methods in Fluid Dynamics*. Springer Verlag.
- CASTRO, W., & SQUIRE, W. 1967. The effect of polymer additives on transition in pipe flow. *Applied Scientific Research*, **18**(September), 81-96.
- CHAN MAN FONG, C.F., & WALTERS, K. 1965. The solution of flow problems in the case of materials with memory. Part II: The stability of plane Poiseuille flow of slightly viscoelastic fluids. *Journal de Mécanique*, **4**(4), 439-452.
- CHEN, T.S., & JOSEPH, D.D. 1973. Subcritical bifurcation of plane Poiseuille flow. *Journal of Fluid Mechanics*, **58**, 337-351. part 2.
- CHRISTIANSEN, E.B., & LEMMON, H.E. 1965. Entrance region flow. *AIChE Journal*, **11**(6), 995-999.
- CHUNG, J.S., & GRAEBEL, W.P. 1972. Laser Anemometer Measurements of Turbulence in Non-Newtonian Pipe Flows. *Physics of Fluids*, **15**(4), 546-554.
- COHEN, M.J., & RITCHIE, N.J.B. 1962. Low-Speed three-dimensional contraction design. *Journal of the Royal Aeronautical Society*, **66**(April), 231-236.
- COLLYER, A.A., & CLEGG, D.W. 1988. *Rheological Measurement*. London: Elsevier Applied Science.
- DARBYSHIRE, A.G., & MULLIN, T. 1995. Transition to turbulence in constant-mass-flux pipe flow. *Journal of Fluid Mechanics*, **289**, 83-114.
- DAVEY, A., & DRAZIN, P.G. 1969. The stability of Poiseuille flow in a pipe. *Journal of Fluid Mechanics*, **36**, 209-218. part 2.
- DAVEY, A., & NGUYEN, H.P.F. 1971. Finite-amplitude stability of pipe flow. *Journal of Fluid Mechanics*, **45**, 701-720. part 4.
- DAVIES, R.E., & WHITE, C.M. 1928. An experimental study of the flow of water in pipes of rectangular section. *Proceedings of the Royal Society London A*, **119**, 92-107.
- DEAN, W.R. 1927. Note on the Motion of Fluid in a Curved Pipe. *Philosophical Magazine and Journal of Science*, **4**(20), 208-223.
- DEAN, W.R. 1928. The Stream-line Motion of Fluid in a Curved Pipe. *Philosophical Magazine and Journal of Science*, **5**(30), 673-695.
- DODGE, D.W., & METZNER, A.B. 1959. Turbulent Flow of Non-Newtonian Systems. *AIChE Journal*, **5**(2), 189-204.
- DRAAD, A.A., & WESTERWEEL, J. 1996. Measurement of temporal and spatial evolution in transitional pipe flow. In: *Proc. 8th Int. Symp. Applications of Laser Techniques to Fluid Mechanics, Lisbon/Portugal, 8-11 July 1996*.
- DRAAD, A.A., KUIKEN, G.D.C., & NIEUWSTADT, F.T.M. 1995. Transition to turbulence in pipe flow. *Pages 103-110 of: KOBAYASHI, R. (ed), Laminar-Turbulent transition, IUTAM Symposium Sendai/Japan 1994*. Berlin/Heidelberg: Springer Verlag.
- DRAZIN, P.G., & REID, W.H. 1981. *Hydrodynamic Stability*. Cambridge University Press.

- DYKE, M. VAN. 1982. *An album of fluid motion*. Stanford, California: The Parabolic Press.
- EGGELS, J.G.M. 1994. *Direct and Large Eddy Simulation of Turbulent Flow in a Cylindrical Pipe Geometry*. Ph.D. thesis, Delft University of Technology, Mechanical Engineering, The Netherlands.
- EGGELS, J.G.M., UNGER, F., WEISS, M.H., WESTERWEEL, J., ADRIAN, R.J., FRIEDRICH, R., & NIEUWSTADT, F.T.M. 1994. Fully developed turbulent pipe flow: a comparison between direct numerical simulation and experiment. *Journal of Fluid Mechanics*, **268**, 175–209.
- FORAME, P.C., HANSEN, R.J., & LITTLE, R.C. 1972. Observations of early turbulence in the pipe flow of drag reducing polymer solutions. *AIChE Journal*, **18**(1), 213–217.
- FOX, J.A., LESSEN, M., & BHAT, W.V. 1968. Experimental investigation of the stability of Hagen–Poiseuille flow. *Physics of Fluids*, **11**(1), 1–4.
- FRIGAARD, I.A., HOWISON, S.D., & SOBEY, I.J. 1994. On the stability of Poiseuille flow of a Bingham fluid. *Journal of Fluid Mechanics*, **263**, 133–150.
- GORDON, G.V., & SHAW, M.T. 1994. *Computer programs for rheologists*. Munich, Germany: Carl Hanser Verlag.
- GROTH, J., & JOHANSSON, A.V. 1988. Turbulence reduction by screens. *Journal of Fluid Mechanics*, **197**, 139–155.
- HANSEN, R.J. 1973. Stability of laminar pipe flows of drag reduced polymer solutions in the presence of high-phase-velocity disturbances. *AIChE Journal*, **19**(2), 298–304.
- HERBERT, TH. 1976. Periodic secondary motions in a plane channel. *Pages 235–240 of: VOOREN, A.I. VAN DE, & ZANDBERGEN, P.J. (eds), Proc. 5th Intl. Conf. on Numerical Methods in fluid dynamics*. Springer Verlag.
- HERBERT, TH. 1983. Secondary instability of plane channel flow to subharmonic three-dimensional disturbances. *Physics of Fluids*, **26**, 871–874.
- HERBERT, TH., & MORKOVIN, M.V. 1980. Dialogue on Bridging Some Gaps in Stability and Transition Research. *Pages 47–72 of: EPPLER, R., & FASEL, H. (eds), Laminar-Turbulent transition, IUTAM Symposium Stuttgart/Germany 1979*. Berlin Heidelberg: Springer Verlag.
- HINZE, J.O. 1975. *Turbulence*. Second edn. Mechanical Engineering. New York: McGraw-Hill Inc.
- HO, T.C., & DENN, M.M. 1978. Stability of plane Poiseuille flow of a highly elastic liquid. *Journal of Non-Newtonian Fluid Mechanics*, **3**, 179–195.
- HULSEN, M.A. 1996. *A discontinuous Galerkin method with splitting applied to visco-elastic flow*. Tech. rept. MEAH-137. Delft University of Technology, Laboratory of Aero- & Hydrodynamics.
- HUSSAIN, A.K.M.F., & RAMJEE, V. 1976. Effects of the axisymmetric contraction shape on incompressible turbulent flow. *Transactions of the ASME, Journal of Fluids Engineering*, March, 58–69.

- JIMÉNEZ, J. 1987. Bifurcations and bursting in two-dimensional Poiseuille flow. *Physics of Fluids*, **30**(12), 3644–3646.
- JIMÉNEZ, J. 1990. Transition to turbulence in two-dimensional Poiseuille flow. *Journal of Fluid Mechanics*, **218**, 265–297.
- JOSEPH, D.D. 1990. *Fluid Dynamics of Viscoelastic Liquids*. Applied Mathematical Sciences, no. 84. Springer Verlag.
- KACHHARA, N.L., WILCOX, P.L., & LIVESEY, J.L. 1974. A theoretical and experimental investigation of flow through short axisymmetric contractions. *Pages 82–89 of: LINDLEY, D., & SUTHERLAND, A.J. (eds), Fifth Australasian conference on Hydraulics and fluid mechanics.*, vol. 1. University of Canterbury, Christchurch/New Zealand. 9–13 December.
- KALASHNIKOV, V.N. 1994. Shear-rate dependent viscosity of dilute polymer solutions. *Journal of Rheology*, **38**(5), 1385–1403.
- KIM, J., & MOSER, D. 1989. On the secondary instability in plane Poiseuille flow. *Physics of Fluids A*, **1**(5), 775–777.
- KLEISER, L., & ZANG, TH.A. 1991. Numerical simulation of transition in wall-bounded shear flows. *Annual Review of Fluid Mechanics*, **23**, 495–537.
- KLINGMANN, B.G.B. 1992. On transition due to three-dimensional disturbances in plane Poiseuille flow. *Journal of Fluid Mechanics*, **240**, 167–195.
- KOZLOV, V.V., & RAMAZANOV, M.P. 1984a. Development of finite-amplitude disturbances in Poiseuille flow. *Journal of Fluid Mechanics*, **147**, 149–157.
- KOZLOV, V.V., & RAMAZANOV, M.P. 1984b. Development of finite-amplitude disturbances in Poiseuille flow. *In: KOZLOV (ed), IUTAM symposium on Laminar-Turbulent Transition*.
- LANDAHL, M.T. 1973. Drag reduction by polymer addition. *Pages 177–199 of: BECKER, E., & MIKHAILOV, G.K. (eds), Theoretical and Applied Mechanics, Proc. 13th Int. Congr. Theor. and Appl. Mech., Moscow 1972*. Springer Verlag.
- LAWS, E.M., & LIVESEY, J.L. 1978. Flow through screens. *Annual Review of Fluid Mechanics*, **10**, 247–266.
- LEE, K-C., & FINLAYSON, B.A. 1986. Stability of plane Poiseuille and Couette flow of a Maxwell Fluid. *Journal of Non-Newtonian Fluid Mechanics*, **21**, 65–78.
- LEITE, R.J. 1959. An experimental investigation of the stability of Poiseuille flow. *Journal of Fluid Mechanics*, **5**, 81–97. part 1.
- LI, T-Q., & MCCARTHY, K.L. 1995. Pipe flow of aqueous polyacrylamide solutions studied by means of nuclear magnetic resonance imaging. *Journal of Non-Newtonian Fluid Mechanics*, **57**, 155–175.
- LIU, C., LIU, Z., & MCCORMICK, S. 1991. Multigrid methods for flow transition in a planar channel. *Computer Physics Communications*, **65**, 188–200.
- LOEHRKE, R.I., & NAGIB, H.M. 1976. Control of free-stream turbulence by means of honeycombs: A balance between suppression and generation. *Transactions of the ASME, Journal of Fluids Engineering*, September, 342–353.

- MASSAH, H., KONTOMARIS, W.R., SCHOWALTER, W.R., & HANRATTY, T.J. 1993. The configurations of a FENE bead-spring chain in transient rheological flows and in a turbulent flow. *Physics of Fluids*, **5**(4), 881–890.
- MATTHYS, E.F. 1987. Rheology, friction, and heat transfer study of a discontinuously shear-thickening antimisting polymers solution. *Journal of Non-Newtonian Fluid Mechanics*, **25**, 177–196.
- MAULIK, B.K. 1989. *Numerical studies of the Oldroyd-B fluid: Stability and transition in planar channels*. Ph.D. thesis, Princeton University, Department of Mechanical and Aerospace Engineering, USA.
- METZNER, A.B., & REED, J.C. 1955. Flow of non-Newtonian fluids – Correlation of the laminar, transition, and turbulent-flow regions. *AIChE Journal*, **1**(4), 434–440.
- MIZUNUMA, H., & KATO, H. 1988. Influence of Polymer additives on Transitional Plane Poiseuille flow. *Japan Society of Mechanical Engineering International Journal, Series II, Volume 31*(2), 209–217.
- NIEUWSTADT, F.T.M. 1992. *Turbulentie, Inleiding in de theorie en toepassingen van turbulente stromingen*. Epsilon Uitgaven. In Dutch.
- NISHIOKA, M., & ASAI, M. 1985. Some observations of the subcritical transition in plane Poiseuille flow. *Journal of Fluid Mechanics*, **150**, 441–450.
- NISHIOKA, M., IIDA, S., & ICHIKAWA, Y. 1975. An experimental investigation of the stability of plane Poiseuille flow. *Journal of Fluid Mechanics*, **72**, 731–751. part 4.
- ORSZAG, S.A. 1971. Accurate solution of the Orr-Sommerfeld stability equation. *Journal of Fluid Mechanics*, **50**, 689–703.
- ORSZAG, S.A., & PATERA, A.T. 1983. Secondary instability of wall-bounded shear flows. *Journal of Fluid Mechanics*, **128**, 347–385.
- O'SULLIVAN, P.L., & BREUER, K.S. 1994a. Transient growth in circular pipe flow. I. Linear disturbances. *Physics of Fluids*, **6**(11), 3643–3651.
- O'SULLIVAN, P.L., & BREUER, K.S. 1994b. Transient growth in circular pipe flow. II. Nonlinear development. *Physics of Fluids*, **6**(11), 3652–3664.
- PARK, J.T., MANNHEIMER, R.J., GRIMLEY, T.A., & MORROW, T.B. 1989. Pipe flow measurements of a transparent non-Newtonian slurry. *Transactions of the ASME, Journal of Fluids Engineering*, **111**(3), 331–336.
- PATEL, V.C., & HEAD, M.R. 1969. Some observations in skin friction and velocity profiles in fully developed pipe and channel flows. *Journal of Fluid Mechanics*, **38**, 181–201.
- PATERSON, R.W., & ABERNATHY, F.H. 1972. Transition to turbulence in pipe flow for water and dilute solution of polyethylene oxide. *Journal of Fluid Mechanics*, **51**, 177–185. Part I.
- PFENNIGER, W. 1961. Boundary layer suction experiments with laminar flow at high Reynolds numbers in the inlet of a tube by various suction methods. *Pages 961–980 of: LACHMANN, G.V. (ed), Boundary layer and flow control. Its principles and applications.*, vol. 2. Pergamon Press.

- PINHO, F.T., & WHITELOW, J.H. 1990. Flow of non-Newtonian fluids in a pipe. *Journal of Non-Newtonian Fluid Mechanics*, **34**, 129-144.
- PORTEOUS, K.C. 1971. *The hydrodynamic stability of viscoelastic fluids in plane parallel flow*. Ph.D. thesis, University of Delaware, Chemical Engineering, USA.
- PORTEOUS, K.C., & DENN, M.M. 1972a. Linear stability of plane Poiseuille flow of viscoelastic liquids. *Transactions of the Society of Rheology*, **16**(2), 295-308.
- PORTEOUS, K.C., & DENN, M.M. 1972b. Nonlinear stability of plane Poiseuille flow of viscoelastic liquids. *Transactions of the Society of Rheology*, **16**(2), 309-319.
- POURQUIÉ, M.J.B.M. 1994. *Large Eddy Simulation of a free turbulent jet*. Ph.D. thesis, Delft University of Technology, Mechanical Engineering, The Netherlands.
- PRENGLE, R.S., & R.R., ROTHFUS. 1955. Transition phenomena in pipes and annular cross sections. *Industrial and Engineering Chemistry*, **47**(3), 379-386.
- PRICE, T., BRACHET, M., & POMEAU, Y. 1993. Numerical characterization of localized solutions in plane Poiseuille flow. *Physics of Fluids A*, **5**(3), 762-764.
- RENARDY, Y.Y. 1993. Private Communication.
- RESHOTKO, E. 1958. *Experimental study of the stability of pipe flow. I. Establishment of an axially symmetric Poiseuille flow*. Tech. rept. Jet Propulsion Laboratory, California Institute of Technology, Pasadena, California, U.S.A. Progress Report No. 20-364.
- REYNOLDS, O. 1883. An experimental investigation of the circumstances which determine whether the motion of water shall be direct or sinuous, and of the law of resistance in parallel channels. *Phil. Trans. Roy. Soc.*, **174**, 935-982.
- ROCHFORT, S., & MIDDLEMAN, S. 1985. Effect of molecular configuration on Xanthan gum drag reduction. *Pages 333-348 of: RABIN, Y. (ed), Polymer-Flow Interaction, American Institute of Physics, Conf. Proc. number 137*.
- ROSENBLAT, S., & DAVIS, H. 1979. Bifurcation from infinity. *SIAM J. Appl. Math. (USA)*, **37**(1), 1-19.
- RUBIN, Y., WYGNANSKI, I., & HARITONIDIS, J.H. 1980. Further observations on transition in a pipe. *Pages 17-26 of: EPPLER, R., & FASEL, H. (eds), Laminar-Turbulent transition, IUTAM Symposium Stuttgart/Germany 1979*. Berlin Heidelberg: Springer Verlag.
- SÁ PEREIRA, A., & PINHO, F.T. 1994. Turbulent pipe flow characteristics of low molecular weight polymer solutions. *Journal of Non-Newtonian Fluid Mechanics*, **55**, 321-344.
- SABADELL, L.A. 1988. *Effects of a drag reducing additive on turbulent boundary layer structure*. Master Thesis. Princeton University, Dept. Mechanical and Aerospace Engineering.
- SALWEN, H., & GROSCH, C.E. 1972. The stability of Poiseuille flow in a pipe of circular cross-section. *Journal of Fluid Mechanics*, **54**, 93-112. part 1.
- SARIC, W.S. 1994. Görtler Vortices. *Annual Review of Fluid Mechanics*, **26**, 379-409.
- SCHMID, P.J., & HENNINGSON, D.S. 1994. Optimal energy density growth in Hagen-Poiseuille flow. *Journal of Fluid Mechanics*, **277**, 197-225.
- SEN, P.K., VENKATESWARLU, D., & MAJI, S. 1985. On the stability of pipe-Poiseuille flow

- to finite-amplitude axisymmetric and non-axisymmetric disturbances. *Journal of Fluid Mechanics*, **158**, 289–316.
- SINGER, B.A., REED, H.L., & FERZIGER, J.H. 1989. The effect of streamwise vortices on transition in the plane channel. *Physics of Fluids A*, **1**(12), 1960–1971.
- SMITH, F.T., & BODONYI, R.J. 1982. Amplitude-dependent neutral modes in Hagen-Poiseuille flow through a circular pipe. *Proceedings of the Royal Society London A*, **384**, 463–489.
- SURESHKUMAR, R., & BERIS, A.N. 1995a. Effect of artificial stress diffusivity on the stability of numerical calculations and the flow dynamics of time-dependent viscoelastic flows. *Journal of Non-Newtonian Fluid Mechanics*, **60**, 53–80.
- SURESHKUMAR, R., & BERIS, A.N. 1995b. Linear stability analysis of viscoelastic Poiseuille flow using an Arnoldi-based orthogonalization algorithm. *Journal of Non-Newtonian Fluid Mechanics*, **56**, 151–182.
- TAHITU, G.J.R. 1994. *The possibilities of LDA measurements in a turbulent pipe flow*. Master Thesis MEAH-117. Delft University of Technology, Laboratory of Aero- & Hydrodynamics. In Dutch.
- TAM, K.C., & TIU, C. 1990. Role of ionic species and valency on the steady shear behavior of partially hydrolyzed polyacrylamide solutions. *Colloid & Polymer Science*, **268**, 911–920.
- TATSUMI, T. 1952. Stability of the laminar inlet-flow prior to the formation of Poiseuille régime, II. *Journal of the Physics Society Japan*, **7**, 495–502.
- TEITGEN, R. 1980. Laminar-Turbulent transition in pipe flow: Development and structure of the turbulent slug. *Pages 27–36 of: EPPLER, R., & FASEL, H. (eds), Laminar-Turbulent transition, IUTAM Symposium Stuttgart/Germany 1979*. Berlin Heidelberg: Springer Verlag.
- TOONDER, J.M.J. DEN. 1995. *Drag reduction by polymer additives in a turbulent pipe flow: Laboratory and numerical experiments*. Ph.D. thesis, Delft University of Technology, Mechanical Engineering, The Netherlands.
- TOONDER, J.M.J. DEN, DRAAD, A.A., KUIKEN, G.D.C., & NIEUWSTADT, F.T.M. 1995. Degradation effects of dilute polymer solutions on turbulent drag reduction in pipe flows. *Applied Scientific Research*, **55**, 63–82.
- TREFETHEN, L.N., TREFETHEN, A.E., REDDY, S.C., & DRISCOLL, T.A. 1993. Hydrodynamic stability without eigenvalues. *Science*, **261**(July), 578–584.
- VASELESKI, R.C., & METZNER, A.B. 1974. Drag reduction in the turbulent flow of fiber suspensions. *AIChE Journal*, **20**(2), 301–306.
- VIRK, P.S. 1975. Drag reduction by collapsed and extended polyelectrolytes. *Nature*, **253**(January 10), 109–110.
- VIRK, P.S., & WAGGER, D.L. 1990. Aspects of mechanisms in type B drag reduction. *Pages 201–213 of: IUTAM Symposium on Structure of Turbulence and Drag Reduction, Zurich/Switzerland 1989*. Berlin Heidelberg: Springer Verlag.
- VIRK, P.S., MERRILL, E.W., MICKLEY, H.S., SMITH, K.A., & MOLLO-CHRISTENSEN,

- E.L. 1967. The Toms phenomenon: turbulent pipe flow of dilute polymer solutions. *Journal of Fluid Mechanics*, **30**, part 2, 305–328.
- VLASSOPOULOS, D., & SCHOWALTER, W.R. 1994. Steady viscometric properties and characterization of dilute drag-reducing polymer solutions. *Journal of Rheology*, **38**(5), 1427–1446.
- WALTERS, K. 1962. The solution of flow problems in the case of materials with memory. Part I. *Journal de Mécanique*, **1**(4), 479–486.
- WANG, C.B. 1972. Correlation of the friction factor for turbulent pipe flow of dilute polymer solutions. *Ind. & Eng. Chem. Fundamentals*, **11**(4), 546–551.
- WARD-SMITH, A.J. 1980. *Internal fluid flow. The fluid dynamics of flow in pipes and ducts*. New York: Clarendon Press, Oxford University Press.
- WESTERWEEL, J. 1993. *Digital Particle Image Velocimetry – Theory and Application*. Ph.D. thesis, Delft University of Technology, Mechanical Engineering, The Netherlands.
- WESTERWEEL, J., DRAAD, A.A., HOEVEN, J.G.TH. VAN DER, & OORD, J. VAN. 1994. A fast data acquisition system for Digital PIV; application to fully-developed and transitional turbulent pipe flow. In: *Proc. 7th Int. Symp. Applications of Laser Techniques to Fluid Mechanics, Lisbon, Portugal, 11-14 July 1994.*, vol. 2.
- WHITE, W.D., & MCELIGOT, D.M. 1970. Transition of Mixtures of Polymers in a Dilute Aqueous Solution. *Journal of Basic Engineering, Trans. of the A.S.M.E.*, September, 411–418.
- WÓJS, K. 1993. Laminar and turbulent flow of dilute polymer solutions in smooth and rough pipes. *Journal of Non-Newtonian Fluid Mechanics*, **48**, 337–355.
- WYGNANSKI, I., SOKOLOV, M., & FRIEDMAN, D. 1975. On transition in a pipe. Part 2. The equilibrium puff. *Journal of Fluid Mechanics*, **69**, part 2, 283–304.
- WYGNANSKI, I.J., & CHAMPAGNE, F.H. 1973. On transition in a pipe. Part 1. The origin of puffs and slugs and the flow in a turbulent slug. *Journal of Fluid Mechanics*, **59**, part 2, 281–335.
- ZAHN, J-P., TOOMRE, J., SPIEGEL, E.A., & GOUGH, D.O. 1974. Nonlinear cellular motions in Poiseuille channel flow. *Journal of Fluid Mechanics*, **64**, 319–345. part 2.
- ZAKIN, J.L., NI, C.C., & HANSEN, R.J. 1977. Laser Doppler velocimetry studies of early turbulence. *Physics of Fluids*, **20**(10, part II), s85–s88.

Curriculum vitae

Aswin (Adrianus Antonius) Draad was born on May 14 1966 in Oss, The Netherlands.

In 1984 he graduated from pre-university education (VWO) at the "Maasland-College" in Oss.

From 1984 to 1990 he studied Mechanical Engineering at the Eindhoven University of Technology. He was secretary of the committee in Eindhoven, that organized a study-tour to the USA in April 1988 in cooperation with their colleagues of the Twente University of Technology. From May to July 1989, he did a summer assignment with Shell Offshore Inc. in New Orleans, USA. The subject was *Laminar pressure drop calculations of drilling fluids in axial annular flows*. From October 1989 to September 1990, he continued this work for his Master's Thesis at the "Koninklijke Shell Exploratie en Productie Laboratorium" in Rijswijk, The Netherlands, under supervision of prof. dr. ir. W.M.J. Schlösser. On June 19 1990 he graduated cum laude.

On November 1 1990, he started his Ph.D.-study at the Laboratory for Aero- and Hydrodynamics under the supervision of prof.dr.ir. F.T.M. Nieuwstadt and dr. ir. G.D.C. Kuiken. His assignment was to shed more light on laminar-turbulent transition for non-Newtonian fluids, the application being improvement of pressure drop predictions for drilling-fluid flows in oilwells. The emphasis has been on performing stability experiments, but also numerical techniques have been used extensively. Some of the work reported in this thesis has been presented at the Fifth European Turbulence Conference in Siena, Italy in July 1994 and at the IUTAM symposium on Laminar-Turbulent Transition in Sendai, Japan in September 1994.

On March 1 1996, he started working at the Research & Development laboratory of Océ in Venlo, The Netherlands. Océ designs and manufactures copiers, printers, and plotters.

Laboratory for Aero- & Hydrodynamics
Delft University of Technology
Rotterdamseweg 145
2628 AL Delft
tel.: +31 15 278 2904
FAX: + 31 15 278 2947